Investigations of the direction-driven water and ion transport along the interfaces and through polymer networks

Dissertation

zur Erlangung des Grades eines Doktors der Naturwissenschaften

der Fakultät für Naturwissenschaften der Universität Paderborn

vorgelegt im Mai 2017

von

Melanie Reichinger

geb. Rademacher

Eidesstattliche Erklärung

Ich versichere hiermit an Eides statt, dass ich die vorgelegte Arbeit selbstständig, ohne fremde Hilfe und ohne die Benutzung anderer als die in der Arbeit angegebenen Hilfsmittel angefertigt habe.

Alle Stellen, die wörtlich oder sinngemäß aus veröffentlichten und nicht veröffentlichten Quellen entnommen wurden, sind als solche in der Arbeit kenntlich gemacht.

Die vorliegende Arbeit hat in dieser oder ähnlicher Form oder auch auszugsweise im Rahmen einer anderen Prüfung noch nicht vorgelegen.

Neuss, 05.05.2017

Melanie Reichinger

Unterschrift

Erstgutachter:	Prof. Dr. Bremser
Zweitgutachter:	Prof. Dr. Dornbusch
Drittgutachter:	Prof. Dr. Warnecke
Vorsitzender:	Prof. Dr. Henkel
Tag der Verteidigung:	14.02.2018

Danksagung

Die vorliegende Arbeit wurde während meiner Tätigkeit als wissenschaftliche Mitarbeiterin an der Hochschule Niederrhein in Kooperation mit der Universität Paderborn im Zeitraum von Mai 2014 bis Mai 2017 angefertigt.

Prof. Dr. Dornbusch gilt mein besonderer Dank für die Themenstellung, die Betreuung und Diskussionsbereitschaft sowie die finanzielle Unterstützung der Arbeit. Prof. Dr. Bremser möchte ich danken für die Kooperationsbereitschaft und die Hilfestellungen.

An der Hochschule Niederrhein möchte mich beim Laborteam des Lacks für die Einführung, die Hilfestellung bei der Lackapplikation und allen kleinen Gefälligkeiten des Alltags bedanken. Insbesondere ist dieser Dank an A. Biniek, M. Bering, T. Krawczyk sowie an alle N_2-Lieferanten gerichtet. Maßgeblich für den Raman-SKP-Aufbau war die Unterstützung aus den Werkstätten der verschiedenen Fachbereiche. Ich danke allen Beteiligten für Ihr Engagement und Ihre unbürokratische Arbeitsweise.

An der Universität Paderborn möchte ich mich ganz besonders bei Nadine Buitkamp für Ihren Einsatz am FIB bedanken sowie des AK Grundmeier für die Möglichkeit zur Erprobung unterschiedlicher Raman-Laser. An dieser Stelle sei auch Dr. Björn Fischer des AK Bettermann der Universität Düsseldorf gedankt.

Für die Lackmaterialien möchte ich bei der Axalta Coating Systems, insbesondere bei Dr. Benfer, Dr. Beiring, Dr. Richter, Dr. Cornelsen sowie deren Laborteams, bedanken. Darüber hinaus gilt mein Dank dem Henkel-Team für den Austausch und die Vorbehandlungen. Dr. Steinhage von Netzsch sei gedankt für die Elektrodenmuster sowie Lackwerke Peters für die Isolierlacke.

Besonders möchte ich mich bei M. Wicinski, den EA Gutachtern sowie allen weiteren Diskussionspartnern, den ich begegnet bin, bedanken. Jeder Austausch hat diese Arbeit in irgendeiner Weise geformt.

Den Proofreadern, P. Göttert und M. Jones, danke ich für Ihren Einsatz.

Schließlich möchte ich Josef für seine anhaltende Unterstützung und Geduld herzlichst danken.

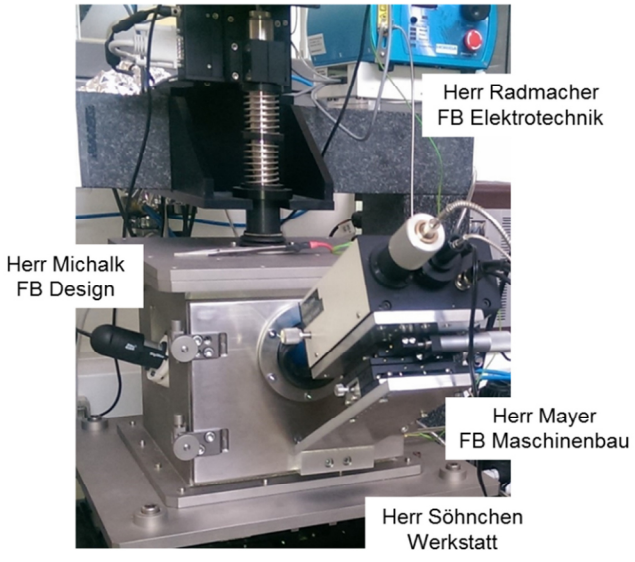

Helfer des Raman-SKP-Aufbaus

Abstract

The omnipresence of paints and adhesives in contact with metals requires a detailed knowledge of water diffusion and the ionic pathways through their polymer networks and along their interfaces. The E-coat, for example, generally shows uniform water diffusion. However, the substrate dissolves during film formation and enriches the E-coat. Iron ions in particular block the interfacial ion transport and normal water diffusion compared with zinc and aluminium ions. Moreover, Raman-SKP investigations show that the ions move through the E-coat in parallel to the aluminium interface. The pH-value immediately changes at the interface and the Volta potential increases with the pH-value, whereupon the interfacial dipole changes from ionic bonds to hydrogen bonds. Indeed, selective dealloyings or micro-galvanic couplings can cause the breakdown of the aluminium oxide and then the ion transport also takes place at the interface. Furthermore, various impedance approaches quantify the in-plane water and ion diffusion through various automotive polymer-metal systems. Concomitantly, the degree of plasticising, internal stress and topographical changes are assessed to clarify the core issue surrounding the Fickian and non-Fickian treatment. All in all, the methods and results developed offer several links for further paint and adhesive developments.

Kurzfassung

Die Omnipräsenz von Lacken und Klebstoffen in Kontakt mit Metallen erfordert detaillierte Kenntnisse über die Wasserdiffusion und die Wege der Ionen durch das Polymernetzwerk und entlang der Grenzflächen. Die kathodische Tauchlackierung zum Beispiel zeigt generell eine gleichmäßige Wasserdiffusion. Das metallische Substrat löst sich jedoch während der Abscheidung auf und die Tauchlackierung reichert sich mit Metallionen an. Insbesondere die Eisen-Ionen hemmen den Grenzflächentransport und die Wasserdiffusion in Substratrichtung - im Vergleich zu Zink- und Aluminium-Ionen. Raman-SKP-Untersuchungen zeigen darüber hinaus, dass sich der Ionentransport am Aluminium-Substrat hauptsächlich durch die Tauchlackierung vollzieht. Gleichzeitig ändert sich der pH-Wert an der intakten Grenzfläche, das Volta-Potenzial steigt mit dem pH-Wert und die Dipole an der Grenzfläche gehen von ionischen Bindungen in Wasserstoffbrückenbindungen über. Selektive Metallauflösungen oder mikrogalvanische Interaktionen verursachen mit der Zeit allerdings den Zusammenbruch des Aluminiumoxides, wodurch der Ionentransport dann direkt an der Grenzfläche stattfindet. Die Wasser- und Ionendiffusion durch verschiedene Automobillacke parallel zur Metallgrenzfläche werden durch diverse Impedanz-Spektroskopische Ansätze quantifiziert. Der Grad der Plastifikation, des inneren Stresses und die topographischen Änderungen durch die Salzwasser-Aufnahme werden herangezogen, um die Diffusion Fickischen oder Nicht-Fickischen Bedingungen zuzuordnen. Insgesamt eröffnen die entwickelten Methoden und die Ergebnisse eine Vielzahl von Anknüpfungspunkte für weitere Lack- und Klebstoffentwicklungen.

Table of Contents

Appendix

Glossary of applied techniques

Electrochemical Impedance Spectroscopy (EIS):

Perturbation of an electrode surface by small periodic signals and detection of the electrochemical response for the appraisal of corrosion mechanism and kinetics.

Potentiodynamic Analysis:

Potential changing at the working electrode and monitoring the current which is produced as a function of time or potential.

Scanning Kelvin Probe (SKP):

Vibrating capacitor technique at which the Kelvin Probe vibrates micrometres above the sample surface while the Fermi level of the SKP needle tries to reach the Fermi level of the metallic sample. The detected Volta potential provides information about the electron transfers from the metal to the needle and is usually used to observe the progress of corrosion processes at polymer-metal interfaces. An extension of the SKP technique is a height control whereby a further circuit adjusts a constant distance of the needle to the surface before the Volta potential is measured via the vibrating capacitor technique.

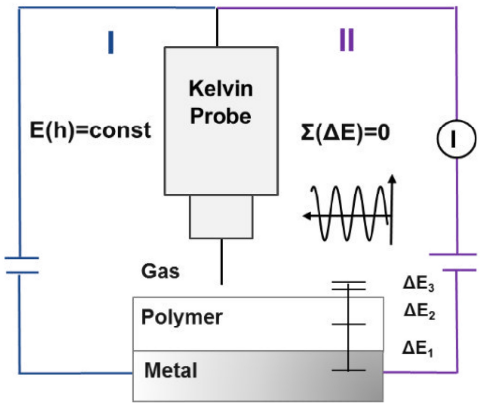

Height control (I) and vibrating capacitor technique (II)

Source: Leng et al. (1999), Wapner et al. (2005)

Infrared Spectroscopy (IR):

Triggering molecular vibrations through irradiation with infrared light. The resulting IR spectra provides information about the antisymmetric stretching and bending of the molecules.

- *Attenuated Total Reflectance (IR-ATR):*

  IR light undergoes multiple internal reflections in a crystal which is in direct contact with the sample.

- *IR-Reflection:*

  IR light is reflected at the metal surface while the light passes through layers with a high level of transparency.

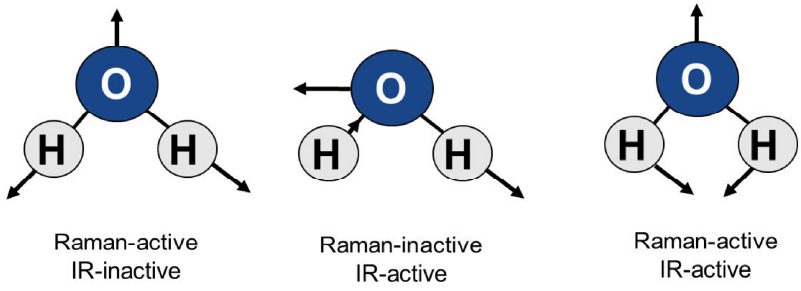

Confocal Raman Spectroscopy:

Light scattering technique that can be thought of in its simplest form as a process where a photon of light interacts with a sample to produce scattered radiation of different wavelengths:

- *Rayleigh scattering*
  Elastic push, photon emission at constant frequency
- *Stokes scattering*
  Inelastic push, photon emission at low frequency
- *Anti-Stokes scattering*
  Hyperelastic push (weak), dislocation of stimulated molecules, photon emission with sum frequency of causative and molecular vibrations

Due to this, Raman spectra provide information about the symmetric stretching and bending vibrations. Additionally, the confocal technique has the ability to spatially filter the analysis volume of the sample, in the XY (lateral) and Z (depth) axes.

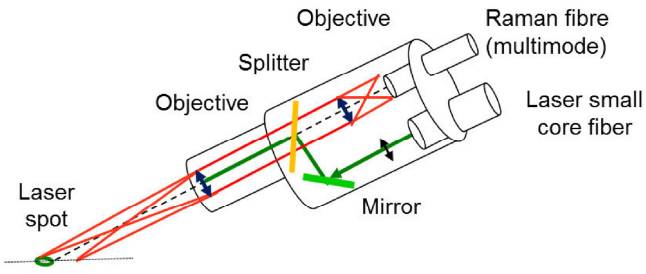

Confocal Raman setup with slope (spatial filter)

Source: Horiba handbook, Hesse (2012), Larkin (2011)

Dynamic-Mechanical Analysis (DMA):

Measurement of material's properties as a function of temperature, time, frequency, stress, atmosphere or a combination of these parameters.

Atomic Force microscopy (AFM):

Nanoscale imaging of topographical, electronical and mechanical properties due to a surface scan by a tip/cantilever in various modes (contact, non-contact, trapping) dependent on the issue.

Force Modulation Microscopy (FMM):

Extension of atomic force microscopy (AFM) imaging at which the AFM tip is scanned in contact with the sample surface, and the Z feedback loop maintains a constant cantilever deflection. In addition, a periodic signal known as the 'driving signal' is applied to a bimorph piezo and vibrates either the tip or the sample. The resulting tip motion is converted to an electrical signal. This electrical signal is separated into AC and DC components for analysis. The amplitude of the AC signal is sensitive to the elastic properties of the sample surface, while the DC signal represents the topography of the sample surface.

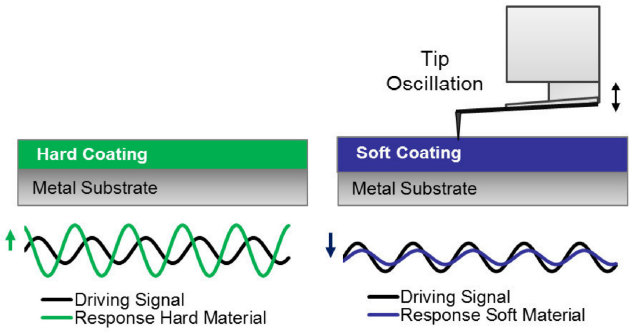

Mechanical behaviour of the AC signal

Source: www.parkafm.com

Nanoindentation:

A load is applied to an indenter in contact with the sample measuring the depth of penetration at the same time. Mechanical properties such as hardness and elasticity are determined in the nanoscale of the sample surface.

Multi-angle Spectrophotometer:

Measurement of the total colour impression by different viewing angles and viewing conditions to assess the appearance of effect finishes. Light/dark flops, colour shifts and special sparkling effects are determined as two tone, graininess, brightness, sparkle intensity/area, gloss and colour coordinates.

Source: Byk handbook

Scanning Electron Microscope (SEM):

Technique that scans a sample with a focused electron beam and delivers images with information about the samples' topography and composition.

Energy Dispersive X-ray Spectroscopy (EDX):

Elemental analysis due to the interaction of some source of X-ray excitation and a sample and the determination of the unique set of peaks in the electromagnetic emission spectrum of each element.

Focused Ion Beam Scanning Electron Microscope (FIB-SEM):

Tomography and fabrication of a specimen surface in the nanoscale and observation via SEM, often used for the creation of cross sections from 3D-objects.

1 General introduction

Diffusion of corrosive species through polymer coatings and the transport along their metal interfaces play a fundamental role in the lifetime of coating-metal systems [1-2]. The polymer permeability for water molecules and solvated ions causes a swelling, in which water acts as a plasticiser. The chemical properties of the coating change and the polymer network passes on to an amorphous state. The salt-water transport occurs at the polymer-metal interface either after the water penetrates through the whole polymer or due to substrate-deep defects in the coating. Solvated ions such as chloride or sulphate increase conductivity, which in turn increases the corrosion rate. Combined with a humid oxygen atmosphere, these conditions are the perfect environment for cathodic delamination [3], filiform corrosion [4-5], blistering [5] and, lastly, the complete deterioration of the coating.

The water-borne cataphoretic paintings (E-coats) in particular have the major function of resisting corrosion and de-adhesion. They are the first protective shield of automobile bodies. The slow degradation of the E-coat due to the addition of functional additives, pigments and fillers makes it harder to determine the water diffusion and the ion transport. Steel and hot-dip galvanised (HDG) steel are usually protected by the E-coat. Additionally, light metals such as aluminium alloys are increasingly being used as they reduce vehicle weight [7-8]. Their technical surfaces are very heterogeneous with several intermetallic particles (IMPs) and insulating oxides. Due to this, the interface of aluminium alloys can only accessed with difficultly. Chromate-free conversion coatings such as titanium or zirconium layers with various additives are used to protect the aluminium alloys. Moreover, polymer coatings are heterogeneous as well. The salt water ingress in the normal and in plane direction can conspicuously differ through the coating. The direction-driven nature, the so-called anisotropy, of a polymer system depends on its peculiarities such as the binder systems, the pore structures, the functional pigments or polymer-polymer interfaces.

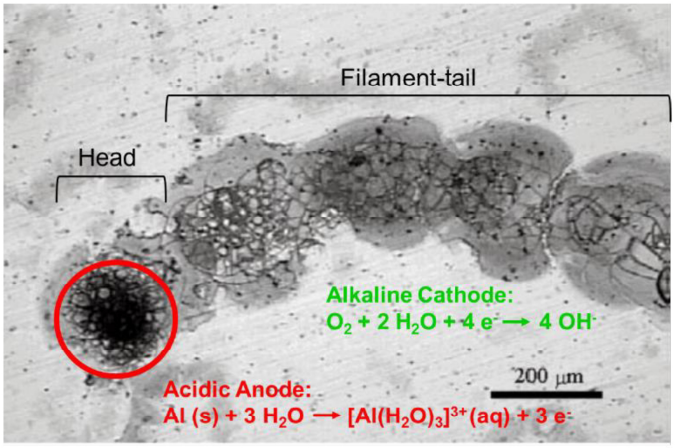

Fig. 1.1 PH-driven filiform corrosion at the aluminium alloy [6]

Recent research has focused on the characterisation of the coating barrier normal to the metal surface via the electrochemical impedance spectroscopy (EIS) [9-10] and the interfacial ion transport along the polymer-metal interfaces by means of the scanning Kelvin probe (SKP) [11-13] or scanning Kelvin probe force microscopy (SKPFM) [14-16] in a humid oxygen atmosphere. The water uptake is further monitored by means of in-situ atomic force microscopy (AFM) combined with an infrared spectroscopy

(IR) at single layers [17], nuclear magnetic resonance (NMR) on the basis of the GARfield approach [18] or various electrochemical approaches with embedded electrodes [19-21] at multilayers. Moreover, metals with a zirconium conversion layer are polarised to mimic the cataphoretic deposition with in situ Raman studies [22], or the Kelvin probe technique is coupled with the Raman spectroscopy [23-25] to gain the structural and electrochemical information about the polymer-metal interface. Often, ideal Fickian behaviour is assumed and, at the same time, the plasticising of the polymer [9, 10, 17], hydrolyse reactions [9, 17-18], stress [18] and the osmotic pressure [18] are discussed. Only a few studies consider non-Fickian circumstances [9]. Quantification data about the water diffusion and the ion transport is rare and a comparative study about the substrate dependencies at the E-coat has not been available until now. In particular, the insulating character of the aluminium oxide forces researchers only to assess the consequences of the ion transport, e.g. due to the observation of the filiform progression [6]. The cause, the ion transport, is quasi invisible for the Kelvin probe, which is why studies about any kinetics at the aluminium interface rarely exist.

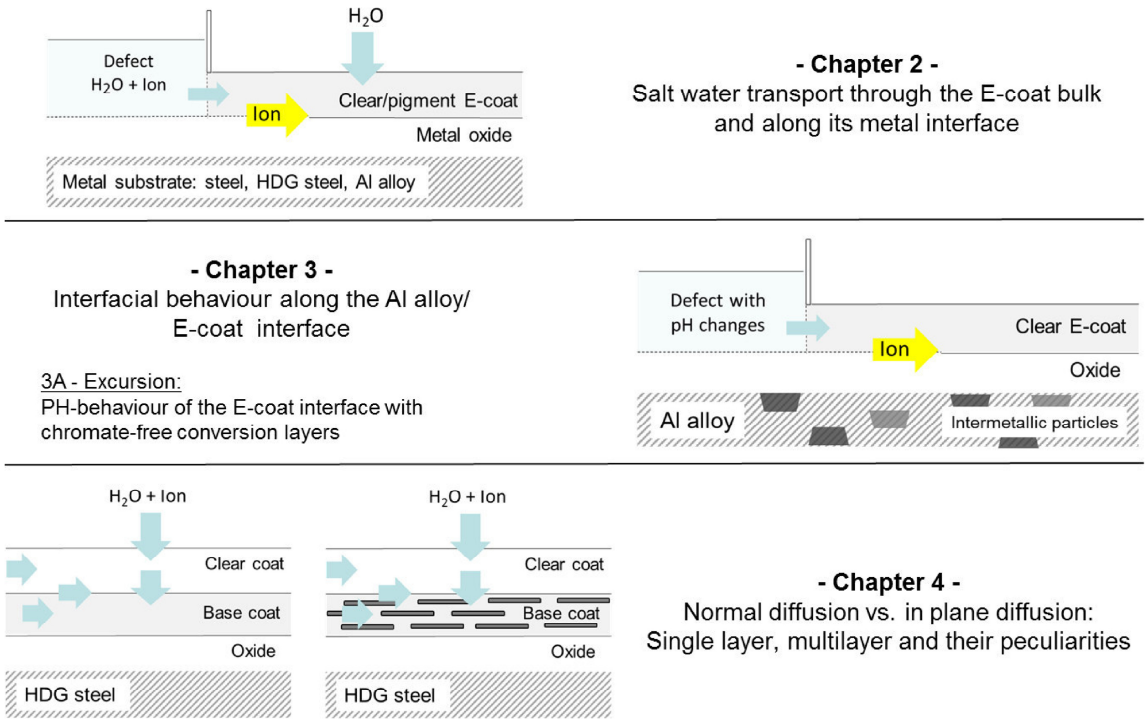

Fig. 1.2 Diagram of the approach followed in the study at hand

This work is introduced with a comprehensive study about the interface and the normal water diffusion on a technical E-coat with a focus on pigmentation and substrate effects, see Figure 1.2. Beyond the kinetics, the physicochemical aftermaths due to the salt water uptake are analysed by the degree of plasticising and topographical changes to clarify the core issue surrounding the Fickian and non-Fickian treatment.

Due to the difficulties at the aluminium interface, a new approach is pursued by changing the prevailing pH-value at the interface and simultaneous Raman-SKP-analysing in a humid oxygen-deficiency. Using the generated data base, the detectability of the pH-activities underneath the E-coat is assessed across the Volta potential as a result of bond modifications. This approach is additionally proven at titanium and zirconium conversion layers with the addition of a pickling inhibitor, a self-assembly and a polymer.

In the last part of this work, the direction-driven nature of the E-coat and various other single and multilayers is highlighted to understand the transport mechanisms completely. The in plane diffusion of water is compared with the in plane ion diffusion in a wet-dry-wet cycle and the role of the base coat – clear coat interface is pointed out during the salt water ingress. The changes in the glass transition, the Deborah number as a degree of elasticity, the effect finish and the stress and strains present are related to the deviations of the water sorption from the ideal Fickian law.

All in all, the results identify the rate-determined water/ion transport pathways through various polymer-metal systems and the simultaneously physicochemical processes at and in these coatings. With regard to the type of the polymer coatings, their pigmentation, their formation, their conversion layer and their type of substrate, this work provides a holistic view of later corrosion and de-adhesion due to all types of electrolyte ingress.

References

[1] Z. W. Wicks, F. N. Jones, S. P. Pappas, D. A. Wicks, Organic coatings: science and technology, Vol. 3, Wiley, New Jersey, 2007.

[2] G. Grundmeier, M. Stratmann, Adhesion and de-adhesion mechanisms at polymer/metal interfaces: mechanistic understanding based on in situ studies of buried interfaces, Ann. Rev. Mat. Res. 35 (2005) 571.

[3] E. L. Koehler, The influence of contaminants on the failure of protective organic coatings on steel, Corros. Nace 33 6 (1977) 209.

[4] A. Bautista, Filiform corrosion in polymer-coated metals – review paper, Prog. Org. Coat. 28 (1996) 49.

[5] W. Funke, Blistering of paint films and filiform corrosion, Prog. Org. Coat. 9 (1981) 29.

[6] G. Williams, H. N. McMurray, D. Hayman, P.C. Morgan, Time-lapse potentiometric imaging of active filiform corrosion using a scanning Kelvin probe technique, PhysChemComm 6 (2001) 1.

[7] N. Birbilis, T. Muster, R. G. Buchheit, Corrosion of aluminium alloys. Corrosion mechanisms in theory and practice, Ed. P. Marcus, 3rd Edition, CRC Press, London (2011) 705.

[8] O. Engler, E. Brünger, Microstructure and texture of aluminium alloys for autobody applications, Matériaux & Techiques 5-6 (2002) 71.

[9] V. N. Nguyen, F. X. Perrin, J. L. Vernet, Water permeability of organic/inorganic hydrid coatings prepared by sol-gel method: A comparison between gravimetric and capacitance measurements and evaluation of non-Fickian sorption models, Corros. Sci. 47 (2005) 397.

[10] Q. Zhou, Y. Wang: Comparison of clear coating degradation in NaCl solution and pure water, Prog. Org. Coat. 76 (2013) 1674.

[11] W. Fürbeth, M. Stratmann, The delamination of polymeric coatings from electrogalvanized steel – a mechanistic approach. Part 1: Delamination from a defect with intact zinc layer, Corros. Sci. 43 (2001) 207.

[12] W. Fürbeth, M. Stratmann, The delamination of polymeric coatings from electrogalvanized steel – a mechanistic approach. Part 2: Delamination from a defect down to steel, Corros. Sci. 43 (2001) 229.

[13] S. M. Cambier, R. Posner, G. S. Frankel, Coating and interface degradation of coated steel, Part 1: Field exposure, Electrochim. Acta 133 (2014) 30.

[14] C. Senöz, S. Borodin, M. Stratmann, M. Rohwerder, In situ detection of differences in the electrochemical activity of Al_2Cu IMPs and investigation of their effect on FFC by scanning Kelvin probe force microscopy, Corros. Sci. 58 (2012) 307.

[15] C. Senöz, M. Rohwerder, Scanning Kelvin probe force microscopy for the in situ observation of the direct interaction between active head and intermetallic particles in filiform corrosion on aluminium alloy, Electrochim. Acta 56 (2011) 9588.

[16] P. Leblanc, G. S. Frankel, A study of corrosion and pitting initiation of AA2024-T3 using atomic force microscopy, J. Electrochem. Soc. 149 6 (2002) B239.

[17] S. Morsch, S. Lyon, S. R. Gibbon, The degradation mechanism of an epoxy-phenolic can coating, Prog. Coat. 102 Part A (2017) 37.

[18] V. Bankh, H. P. Huinink, O. C. G. Adan, S. J. F. Erich, L. G. J. van der Ven, NMR imaging of water uptake in multilayer polymeric films: stressing the role of mechanical stress, Macromolecules 43 (2010) 3382.

[19] K. N. Allahar, B. R. Hinderliter, D. E. Tallman, G. P. Bierwagen, Water transport multilayer organic coatings, J. Electrochem. Soc. 155 8 (2008) F201.

[20] A. Miszczyk, T. Schauer, Electrochemical approach to evaluate the interlayer adhesion of organic coatings, Prog. Org. Coat. 52 (2005) 298.

[21] V. Upadhyay, K. N. Allahar, G. P. Bierwagen, Environmental humidity influence on a topcoat/Mg-rich primer system with embedded electrodes, Sensors and Actuators B 193 (2014) 522.

[22] A. Sarfraz, R. Posner, A. Bashir, A. Topalov, K. J.J. Mayrhofer, K. Lill, A. Erbe, Effect of polarisation mimicking cathodic electrodeposition coating on industrially relevant metal substrates with ZrO_2-based conversion coating, ChemElectroChem 3 (2016) 1415.

[23] R. Posner, A. M. Jubb, G. S. Frankel, M. Stratmann, H. C. Allen, A simultaneous Kelvin Probe and Raman spectroscopy approach for in situ surface and interface analysis, Electrochim. Acta 76 (2012) 34.

[24] R. Posner, A. M. Jubb, G. S. Frankel, M. Stratmann, H. C. Allen, Simultaneous in situ Kelvin probe and Raman spectroscopy analysis of electrode potentials and molecular structures at polymer covered salt layers on steel, Electrochim. Acta 83 (2012) 327.

[25] D. Verreault, A. M. Jubb, G. S. Frankel, M. Stratmann, H. C. Allen, R. Posner, Laser effects on Volta potential transients recorded by a Kelvin probe, ECS Electrochem. Letters 2 5 (2013) H19.

2 Interface and volume transport on technical E-coats: A comparison of steel, hot-dip galvanised steel and AlMg(Mn)

2.1 Introduction

The water-borne cataphoretic paintings (E-coats) – the first protective shield of automobile bodies – have the major function of resisting corrosion and de-adhesion. Commonly, a conversion of an epoxy resin with amino alcohol forms a polyamine with hydroxyl groups. The resulting resin is cross-linked by a blocked aromatic isocyanate and forms a polyurethane network. During electrophoresis, the positively charged amine is neutralised to the metal cathode and therefore the resin is deposited homogeneously on the metal substrate [1]. In spite of the excellent corrosion resistance of these paintings, de-adhesion on steel and zinc substrates in the form of blistering is observed along the interface and far away from any defects. By contrast, anodic undermining dominates on the boundaries of aluminium and low-alloyed steel [2]. The complex interactions at the different polymer-metal interfaces, coupled with the plasticising of the pure coating, hinder a simple explanation of the practical corrosion and infiltration phenomena.

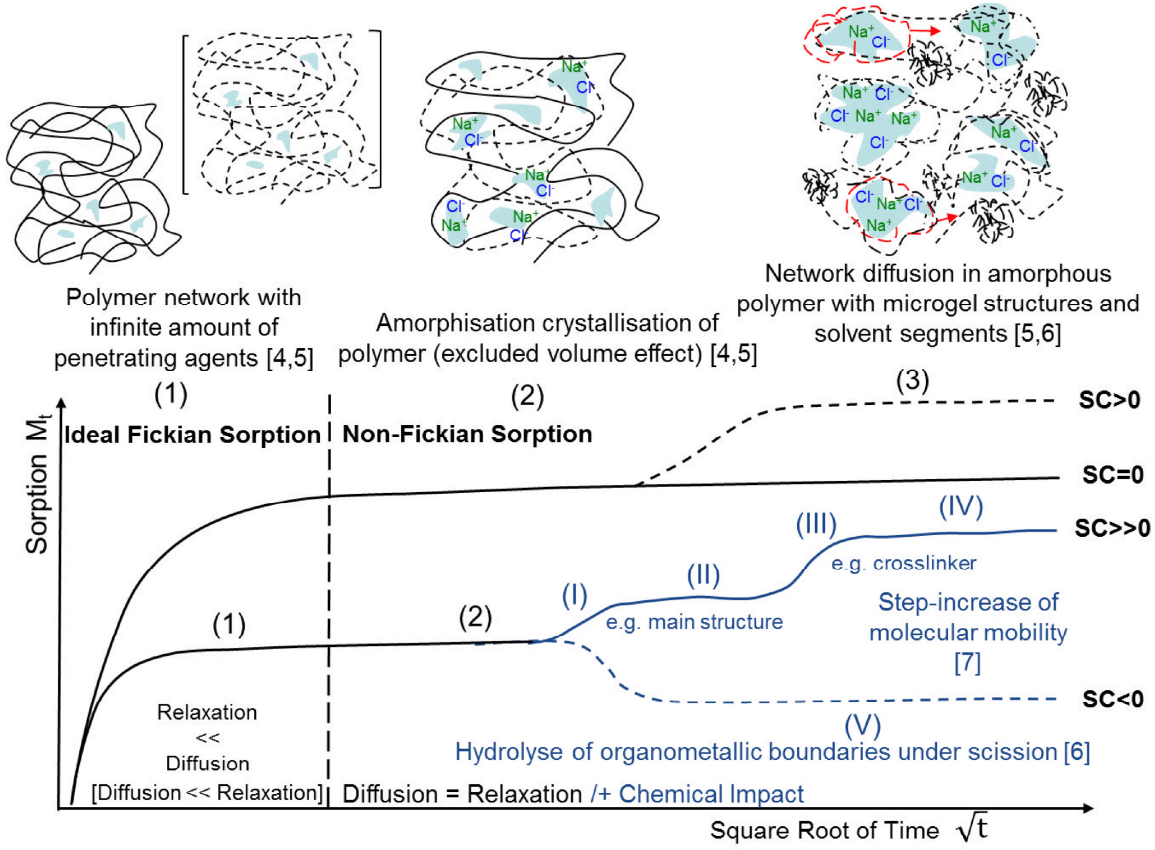

Fig. 2.1 Review of the polymer mechanism (top) and the diffusion kinetic (bottom) during the moisture swelling referred to [4, 5-7]

Actual research is focused on typical failure by corrosion with assumed Fickian swelling in an oxygen atmosphere. The barrier coating properties are modelled via electrochemical impedance spectroscopy

(EIS), which characterises the failure due to interstitial stagnant moisture [3]. Unfortunately, only a few EIS studies consider the transition from Fickian to non-Fickian behaviour during water uptake as summarised in Figure 2.1. First, the relaxation or the diffusion is rate-determined (1), then, the amorphisation crystallisation of the polymer (2) starts and the transport processes get disordered [4, 5-7]. Dependent on the coating, microgel structures and solvent segments diffuse in networks [8] and/or the molecular mobility increases in steps on account of the different interactions of the backbone and cross-linkers to water molecules [7]. Scission is also possible due to hydrolysing of organometallic boundaries in the presence of titanium dioxide pigments [6]. With regard to stone-chipping defects, time-dependent Volta potential changes – measurable via *scanning Kelvin Probe* (SKP) – describe the failure progress along the polymer-metal interface. Anodic and cathodic undermining is intensively studied on model coatings excluding functional additives, pigments or fillers on steel [8-12], electro-galvanised steel [13-15] and aluminium alloys [16-18]. Indeed, transport quantification data is rare and a comparative study about the substrate dependencies, especially on technical coatings including pigments, has not been available until now. Due to the omnipresence of technical coatings, robust studies about de-adhesion of these coatings are necessary.

This work will point out the substrate-dependent water and ion transport with a focus on the polymer-pigment bulk and the polymer-metal interfaces by quantifying the transport rates. The general coating properties of technical clear and pigment E-coats were characterised by infrared spectroscopy in attenuated reflection (IR-ATR) and energy dispersive X-ray (EDX) on profile cuts via focused ion beams (FIB). Current density-potential curves are used to describe the substrate behaviour of steel, hot-dip galvanised (HDG) steel and aluminium alloy AlMg(Mn) in various pH buffers. The water diffusion through the coating volume is quantified via Fickian and non-Fickian approaches using extensive EIS data. Independent resistance and confidence analyses support the diffusion determination with the applied circuit. The level of polymer plasticising and the roughness changes are described via Force modulation microscopy (FMM) to identify the Fickian state after salt-water uptake. The SKP is used to compare the interfacial ion transport at the clear and pigment E-coat in a humid nitrogen atmosphere. Further, the metal-dependent kinetic data was assessed on the pigment E-coat, with 0.1 M, 0.5 M and 1 M NaCl defects. In brief, the results clarify the general differences between technical clear and pigment coating-metal systems, as well as the substrate-dependent circumstances for later corrosion and de-adhesion due to electrolyte ingress on an E-coat.

2.2 Experimental

2.2.1 Metal preparation and coating application

Steel, HDG steel and AlMg(Mn) samples (Gardabond E HDG, C and F (5005A), Chemetall GmbH) were cleaned by soaking them in toluene, acetone and ethanol, followed by submerging them in alkaline cleaner Gardoclean® 855/1 (20 g/L, Chemetall GmbH) and stirring them at 500 rpm at 60 °C for 5 min. Then, the samples were soaked and jetted with distilled water and dried in recirculated air at 40 °C for 120 min. The clear and pigment E-coats (Aqua EC3000, Axalta Coating Systems Germany GmbH) were deposited at 32 °C and with an initial voltage of 260 V (Wächter GLT 400/20), the metal substrate served as a counter electrode. Film thicknesses of 20 µm ±1.5 µm were deposited on steel, HDG steel and AlMg(Mn) and were measured with PHYNIX® Surfix after hardening at 180 °C for 20 min.

2.2.2 Sample characterisation

The alkaline-cleaned metal substrates were analysed by the Zeiss Neon® 40 system with a SE2 detector to observe the surface topography. The current density-potential curves were recorded on the Zennium workstation (Zahner-Elektrik GmbH) with a three-electrode arrangement. The metal sheets (Gardabond E HDG, C and F (5005A), Chemetall GmbH) were degreased in toluene, acetone and ethanol and masked with an electrical and chemical resistant lacquer except for a defined analysis surface. A calomel electrode as a reference and a Pt sheet as a counter electrode were used to complete the setup. Various pH buffers were prepared with p.a. quality chemicals (Sigma-Aldrich), pH($H_2PO_4^-$/H_3PO_4)=2, pH(HPO_4^{2-}/$H_2PO_4^-$)=6, pH($B(OH)_4^-$/$B(OH)_3$)=10, pH(CO_3^{2-}/HCO_3^-)=11, pH(PO_4^{3-}/HPO_4^{2-})=13, and used as electrolytes.

Next, the metals were polarised at -1.2 V for 3 minutes and, when the potential stabilised, the current-potential curves were recorded with a scan rate of 5 mV/s at 25 °C. The IR spectra of the clear and pigment E-coat were measured via the Bruker Vector in attenuated total reflection between 500 and 4000 cm^{-1} (100 scans), with a resolution of 4 cm^{-1}. Element profile analyses were operated by the Zeiss Neon® 40 with an ultra-dry X-ray detector from Thermo Fisher Scientific. The SEM images of the FIB cuts were made with an Inlens detector. For minimising the subsequent sample removal, the coating thicknesses were slightly reduced to around 12-18 µm. Then, the samples were sputtered with Au/Pd (80/20) and finally deposited by the Ga emitter with 2 nA and 30 kV across a length of 30 µm down to the substrate. The first element detection was done in the mapping mode at 20 kV. Further, the acceleration voltage was decreased to 5 kV due to the lower interaction volume, and three line scans were taken for each sample by quantifying the relevant elements.

2.2.3 Impedance and resistance measurements

The EIS analyses on the E-coat were performed in a 0.5 M NaCl solution with a Zennium workstation (Zahner-Elektrik GmbH) and a two-electrode setting [19], in which a platinum mesh wire (HMT, Heraeus) acted as a counter electrode. The use of a NaCl solution has the advantages of being similar to practical applications of salt contaminations and being comparable to other publications. From a start frequency of 1 kHz the single run was continued up to 100 kHz and returned to 100 mHz with 10 points per decade. The first course from 1 kHz to 100 mHz served only as a transient oscillation to avoid artefacts in the fitting region and was later disregarded in the evaluation. Three runs per substrate were started every 5 min with each run lasting up to 72 h. The test-coated surfaces (12.6 cm²) were perturbed with an amplitude of 20 mV and coupled on the initial open circuit potential of the metal in electrolyte [20]. The spectra were fitted between 10-100 kHz by Randles circuit (see Figure 4.2) [21], containing the coating resistance, $R_{coat,}$ parallel to the capacitance, $C_{coat,}$ and an electrolyte resistance, $R_{el,}$ in series. This physical model assumes ideal coating behaviour, which is only given up to 10 kHz [22]. The capacitance, $C_{t,}$ was further calculated about the impedance Z_{im} at f=10 kHz [23, 24]:

$$C_t = \frac{1}{2\pi f Z_{im}} \tag{2.1}$$

The resistance measurements were recorded between a highly resistive ring electrode (FE 50, diameter d=60 mm) on the top of the coating and the contacted metal of the coated samples with a TeraOhmmeter TO-3 (H.-P. Fischer Elektronik GmbH & Co.) according to DIN IEC 60093. First, this resistance, $R_{x,}$ was measured ten times, then, the EIS measurements were taken for 72 h and the resistance analysis repeated. Finally, the first resistances, $R_{Coat,}$ of the chosen circuit were compared to the resistances, $R_{x,}$ of the original and swollen coating (repeat determination).

2.2.4 Force modulation microscopy and nanoindentation

The plasticising behaviour of the polymer was reviewed with an atomic force microscope (Park XE7, Park Systems Corp.) in *FMM mode*. A Fort Silicon cantilever with a spring constant k_L of 2.81 N/m and a q-factor of 175 mapped the original and swollen coating surface in an area of 90 µm x 90 µm with an amplitude of Δz of 7 nN, T=296 K; the results were extracted by XEI and the amplitude responses were calibrated by a five-fold nanoindentation measurement on the E-coated steel samples.

The nanoindentation tester (CSM Instruments) with a Berkovich diamond indenter initially loaded with 100 mN/min up to 50 mN, which was held for 10 s and then relieved again with 100 mN/min. *The Oliver & Pharr method* was used to calculate the Young's modulus E, assuming a Poisson ratio of 0.22 for epoxides [25].

Referring to the force modulation, the surface deforms by an amount, δ, which expresses the deviation of the constant amplitude *Δz,* and the resulting cantilever deflection amplitude, *Δd*. The dynamic force *ΔF* is found by ΔF=kδ [26], where k presents the contact stiffness. The counterforce, given by $\Delta F=k_L\Delta d$, is introduced from the cantilever. Due to the balances of forces, *k* was determined by:

$$k = \frac{\Delta F}{\Delta z - \Delta d} = \frac{k_L}{\frac{\Delta z}{\Delta d} - 1} \tag{2.2}$$

for the FMM samples. Further, there is a linear connection (2.3) between the stiffness *k,* and the Young's modulus *E* [27], where the parameter *a* expresses the contact radius between the tip/indenter and the sample.

$$k = 2aE \tag{2.3}$$

Hence, the Young's modulus can be calculated as a function of the resulting amplitude *Δd,* and the constant but technique-shifted contact radius *a'*.

$$E = \frac{k_L}{2a\prime\left(\frac{\Delta z}{\Delta d} - 1\right)} \tag{2.4}$$

Finally, the Young's modulus was calculated from the common areas and the roughness parameters were assessed from the achieved topography images (dpi=96) according to ISO 14755.

2.2.5 Scanning Kelvin Probe measurements

For the SKP analyses, the samples were prepared with a stone-chipping defect filled with NaCl solution which is comparable to realistic car damage (see Figure 3.5). To facilitate this, a metal deep defect area was masked during the cataphoretic deposition with a sharp-cut frontier to the coating area. This preparation differs from the typical practice as described in [28]. Further, a self-made reservoir with a size of 15 mm x 20 mm x 15 mm was placed on the coating-free area and filled with a 1 mL NaCl solution to initialise the water and ion transport underneath the coating. The filling of the reservoir was done at standard atmosphere conditions, and, because of this, the solutions were alkalised at the beginning of the exposure. For the comparison of the clear and pigment E-coat, steel samples were placed in anaerobic pots in a humid oxygen atmosphere for a duration of 525 h and were then suspended in the SKP chamber under a humid nitrogen purge. After a constant atmospheric setting (relative humidity (rH) of 84-86 %, O_2≤3 %), the samples were suspended further for 48 h in a humid, oxygen-deficient environment before the SKP measurement were started. For the concentration-dependent measurements on the pigment E-coat, steel, HDG steel and AlMg(Mn) were directly placed and measured in a humid nitrogen atmosphere (rH=88-91%, O_2≤2 %). The height-controlled SKP from Wicinski & Wicinski GbR [29], with a 120 µm thick Ni/Cr needle, was calibrated with saturated $CuSO_4$,

adjusted to a standard hydrogen electrode (SHE) and finally, potential and height profiles (DH=160 mV, x/y-steps=20 µm) were measured in the humid nitrogen atmosphere.

2.3 Theory – Ideal-Fickian and non-Fickian approach

Assumed ideal Fickian water sorption *through a supported polymer volume* is represented by the following equation [4]:

$$\frac{M_t}{M_s} = \frac{log(C_t/C_0)}{log(C_s/C_0)} = \left(1 - \frac{8}{\pi^2}\sum_{n=0}^{\infty}\frac{1}{(2n+1)}exp\left[\frac{-(2n+1)^2 D\pi^2 t}{4L^2}\right]\right) \quad (2.5)$$

where M_t acts as water amount at time *t*, M_s as water amount at saturation, *D* as diffusion coefficient and *L* as layer thickness. This calculation assumes an initial dry and homogeneous single layer with a constant penetrate activity and layer thickness. The Brasher & Kingsbury (BK) water uptake [30] (6) can be expressed by the capacitances and the dielectric constant of water (ε_w=78.3):

$$BK = \frac{log(C_t/C_0)}{log\varepsilon_w} \quad (2.6)$$

The non-Fickian approach, based on Berens [31] and Van Westing and co-workers [32], adds the linear swelling and the corresponding thickness increases by an adsorption coefficient *SC* to equation (5). Applied to EIS data it is defined as:

$$\frac{M_t}{M_s} = \frac{log(C_t/C_0)}{log(C_s/C_0)} = \left(1 - \frac{8}{\pi^2}\sum_{n=0}^{\infty}\frac{1}{(2n+1)}exp\left[\frac{-(2n+1)^2 D\pi^2 t}{4L^2}\right]\right) + SC \cdot t \quad (2.7)$$

where the *SC* coefficient expresses negative or positive deviations of the ideal Fickian sorption with time (see Figure 2.1). The *SC* coefficient relates to the polymer rearrangement and additionally includes phenomena such as [6]:

- Slower ion diffusion compared to water
- Practical dissolution and leaching out of organic fragments
- Change in the distribution and/or the state of water during long exposure times

The ideal Fickian ion diffusion *along the polymer-metal interface* is described by a linear isotropic and semi-infinite transport processes according to [4, 8-9]:

$$\frac{c^*}{K} = 0{,}1\ M\left[1 - erf\left(\frac{A_{0,1}}{2\sqrt{D}}\right)\right] = 0{,}5\ M\left[1 - erf\left(\frac{A_{0,5}}{2\sqrt{D}}\right)\right] = 1{,}0\ M\left[1 - erf\left(\frac{A_{1,0}}{2\sqrt{D}}\right)\right] \quad (2.8)$$

with *c** as the threshold concentration, K as equilibrium constant, the initial ion concentrations and their slopes, $A_{0,1}$, $A_{0,5}$ and $A_{1,0,}$ resulting from the movement of the potential front plotted against the square root of time.

2.4 Results and discussion

This chapter provides an overview of the interface and volume transport on a technical E-coat with focus on pigmentation and substrate effects. The first subsection presents the peculiarities of the technical substrates and their E-coats. The volume transport through the E-coat is characterised by diffusion parameters and analyses of the physicochemical aftermaths – the degree of the plasticising and topographical changes – to clarify the core issue surrounding the Fickian and non-Fickian treatments. The interfacial transport from the incubation to the sub-surface flux is described to understand the overall kinetics. The defect is initialised in an oxygen atmosphere whereupon the ion flux is recorded under humid oxygen-deficiency. The uniqueness of this SKP approach is specified and the additional benefits are demonstrated.

2.4.1 General properties of the technical substrates and E-coats

A topographical impression of the substrates is given in Figure 2.2. Steel has a homogeneous surface with roundish recesses. The surface of HDG steel is more edged with larger recesses compared to the steel surface, and the AlMg(Mn) surface has the flattest and most homogeneous finish.

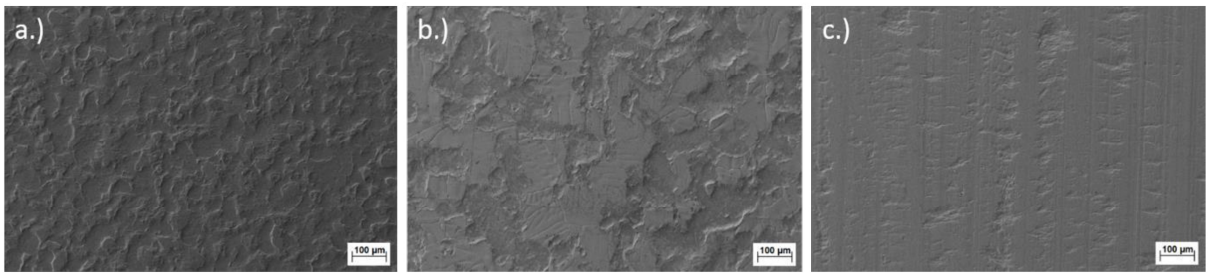

Fig. 2.2 SEMs of the alkaline-cleaned metal surfaces before the cataphoretic deposition: a.) steel, b.) HDG steel, c.) AlMg(Mn)

The oxygen-driven natures of these substrates show the current density-potential curves at different pH values (see Figure 2.3). The logarithmic limiting current density ln (j_L) is noticeably lower with HDG steel compared to the other metals at higher pH values. AlMg(Mn) and steel have ln (j_L) higher than -4, whereas ln (j_L) of HDG steel reaches values of -5 at a pH of 13 and -5.5 at a pH of 10. The amphoteric zinc seems to be stabilised due to several thermodynamic equilibriums in the pH range between 8 and 14 [33]. A passive range between the pH values of 12 and 13 has already been found whereby it is assumed that the zinc surface is protected by a HO-Zn-(O-Zn)$_x$-OH cover [34]. These reasons lead to the increased corrosion resistance of HDG steel compared to the other metals. Furthermore, the amphoteric character of the aluminium alloy AlMg(Mn) is visible by the highest ln (j_L) at pH=2 followed by the ln (j_L) at pH=11 and the lowest value around -3.5 at pH=6 in the passive range of the alloy. Note that these potentials are not comparable to the SKP-potentials in humid oxygen-deficiency.

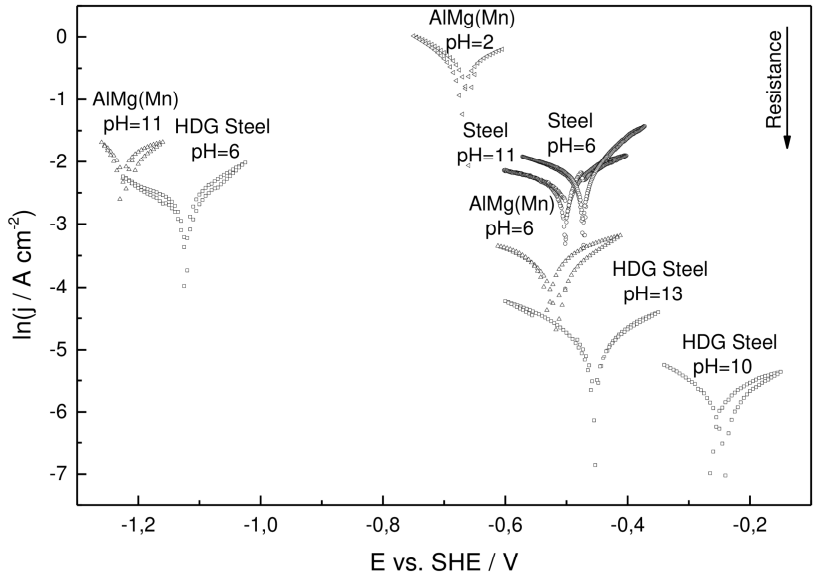

Fig. 2.3 Current density-potential curves of steel, HDG steel and AlMg(Mn) in different pH buffers, pH($H_2PO_4^-/H_3PO_4$)=2, pH($HPO_4^{2-}/H_2PO_4^-$)=6, pH($B(OH)_4^-/B(OH)_3$)=10, pH(CO_3^{2-}/HCO_3^-)=11, pH(PO_4^{3-}/HPO_4^{2-})=13, dE/dt=5 mV/s, T=298 K in O_2-atmosphere

The chemistry of the clear and the pigment E-coat is displayed by the IR spectra in Figure 2.4. The absorbance of the pigment E-coat is less than the clear E-coat due to a lower amount of functional groups per area. The coating itself is characterised by the urethane stretching vibrations at 1740-1690 cm^{-1}(O-CO-N), the amine bending at 1580-1490 cm^{-1} (NH) and 1650-1560 cm^{-1} (NH_2), the stretching vibrations of C-OH at 1150-1040 cm^{-1} as well as the alkyl groups at 2990-2860 cm^{-1} and hydroxyl/amine vibrations in hydrogen bonds between 3600 cm^{-1} and 3200 cm^{-1}. Further, the aromatic CH bonding at 863 cm^{-1}, =C-O-C stretching vibrations at 1180 cm^{-1} and C-O-C bending at 1220 cm^{-1} are present in the fingerprint region.

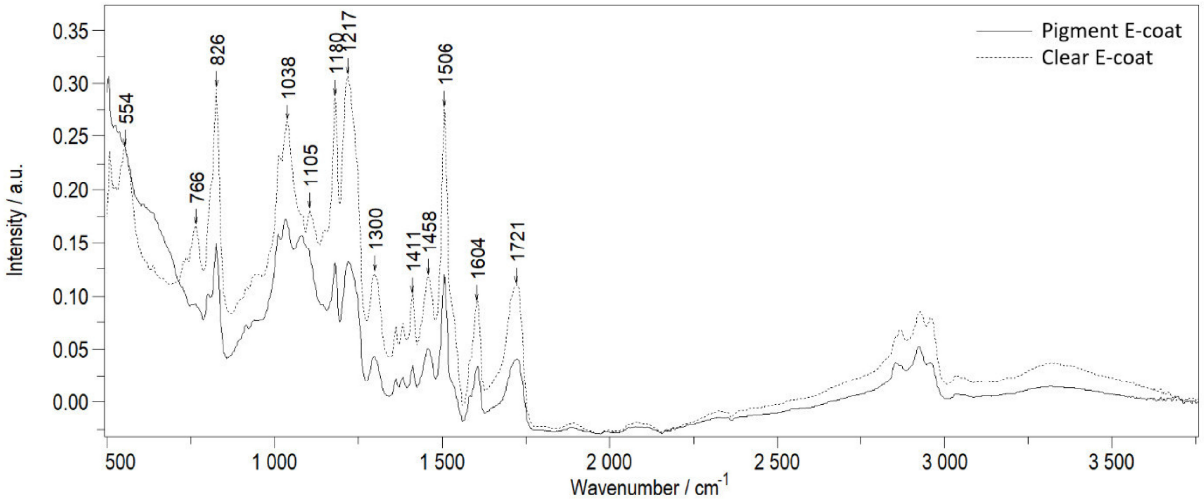

Fig. 2.4 IR-ATR spectra of the clear and the pigment E-coat; spectral resolution: 4 cm^{-1}

Typically, the E-coat matrix contaminates due to the dissolved substrate during the cataphoretic deposition (see Figure 2.5). The complete element analysis is placed in Appendix A1, which is why Figure 2.6 presents only the metal content of the polymer layer through the coating profile. The polymer matrices of the amphoteric metals have up to 10 at% aluminium or zinc with a slight increase in the interface region. The polymer matrix of steel contains even more than 20 at% of iron. These results are independent of the clear or the pigment deposition. The substrate alkalises at up to a pH of 14 during the film formation at the cathodic polarised substrate. Zinc and aluminium dissolve but steel is generally passive in such an environment. However, the reaction is highly exothermic - the substrate temperature increases especially due to the great deposition voltage/current of 260 V/~10 As. The amount of free secondary amines should stimulate dissolution by chelate formation. Further, Serebrennikova and co-workers [35] have proven that iron loses its passivity by transpassive iron dissolution in 40 % KOH solutions at temperatures of 333 K so the increased iron content compared to zinc and aluminium is a likely result.

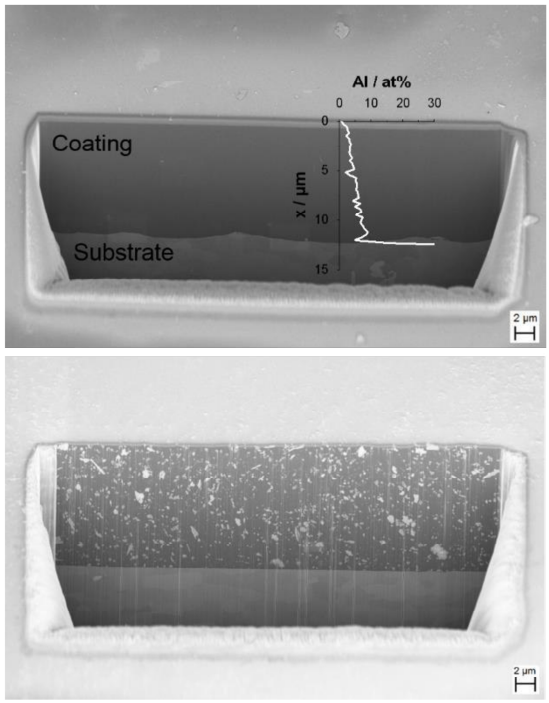

Fig. 2.5 FIB cuts of the clear and the pigment-coated AlMg(Mn) samples

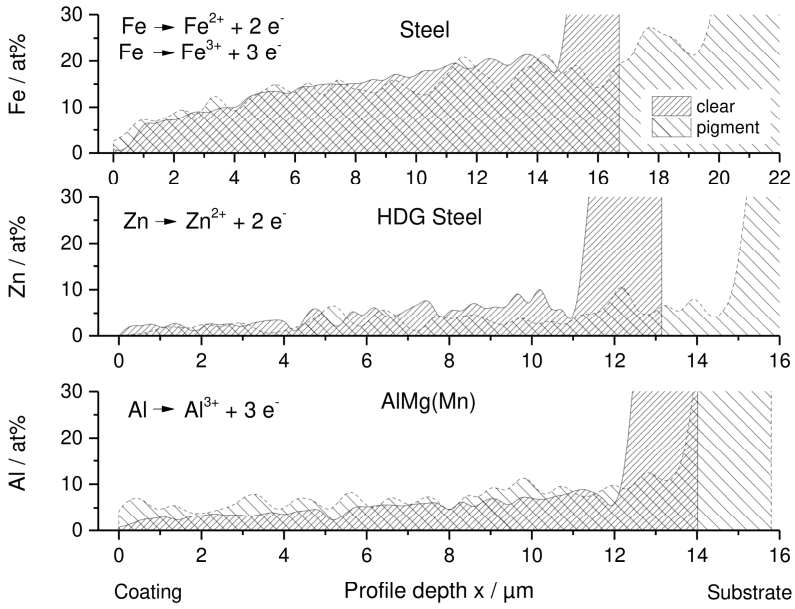

Fig. 2.6 Metal ion concentrations in the clear and pigment coating profile

2.4.2 Water diffusion through the clear and pigment E-coat volume

This part is centred on the EIS data, the validation of the raw data and the applied Randle circuit as well as the proceeding how the diffusion coefficients D and the adsorption coefficients SC are determined. The results identify reliable velocity trends and deviations of physicochemical properties via the SC parameter assuming non-Fickian behaviour.

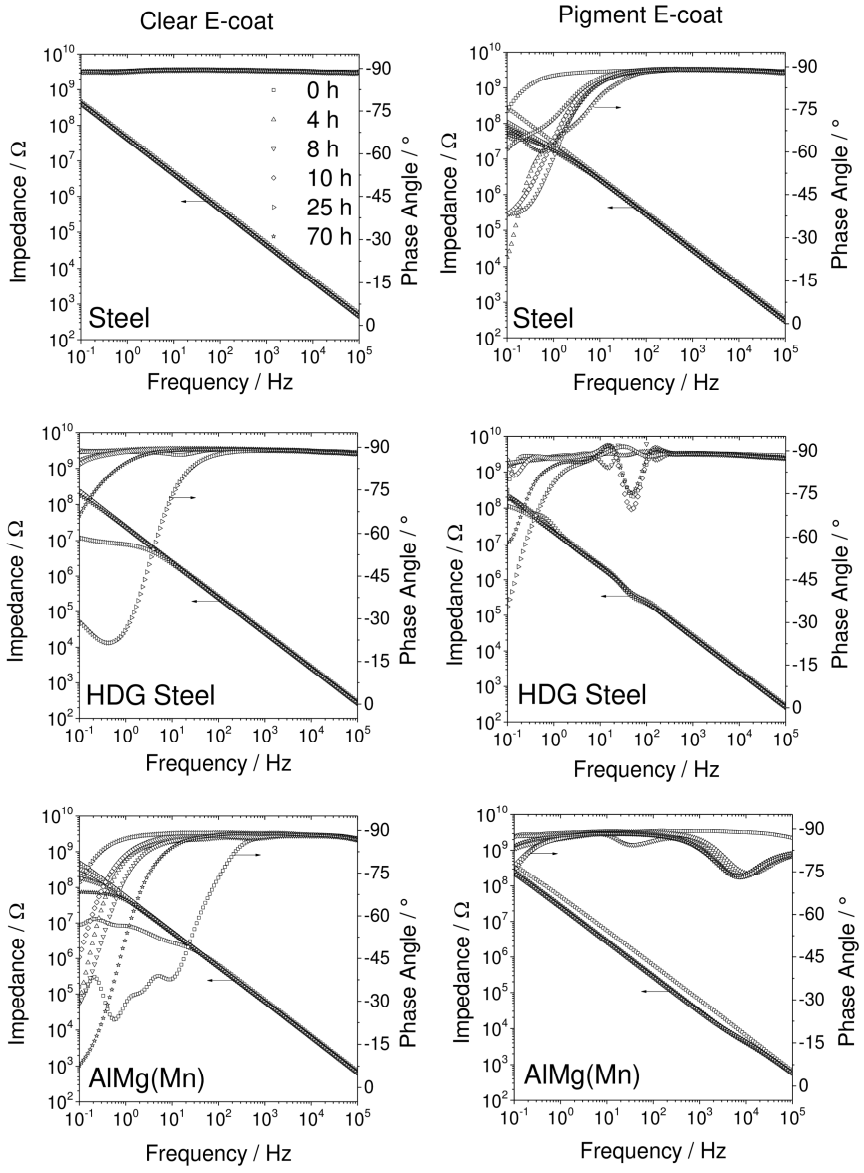

Fig. 2.7 Bode plots of the 20 µm thick clear and pigment E-coat on steel, HDG steel and AlMg(Mn) during the salt water uptake up to 70 h, frequency range: 10 kHz to 100 mHz, start: OCP (metal), amplitude: 20 mV

First, the substrate and pigmentation differences, as seen in Figure 2.7, are made clear via the Bode plots of the clear (left) and the pigment E-coat (right). The clear system on steel shows linear capacitive behaviour, especially at low frequencies and phase angles of -90 ° during the whole 72 h. All observations express ideal coating circumstances and affirm the used RC circuit. Meanderings of this

state occur on HDG steel and are even larger on AlMg(Mn). The phase angles and impedances decrease significantly between 100 mHz and 50 Hz. The Bode plots of the pigment E-coat are quite similar to each other with slight phase angle variations dependent on the type of metal. Steel and HDG steel show a phase decrease at low frequencies, whereas the phase angle on AlMg(Mn) decreases at higher frequencies. However, the ideal capacitive behaviour is present in the used fitting range from 10 to 100 kHz except for the deviations at the AlMg(Mn) due to the slight phase decrease to -75°.

Appendix A2.2 contains more details relating to the data quality and validation. Briefly, the raw impedances are reproducible at 10 kHz and the independent resistances, R_X, confirm the coating resistance, R_{Coat}, of the applied Randle circuit before and after the salt-water uptake of 72 h. For this EIS study, the Randle circuit is proven and the procedure/process is continued.

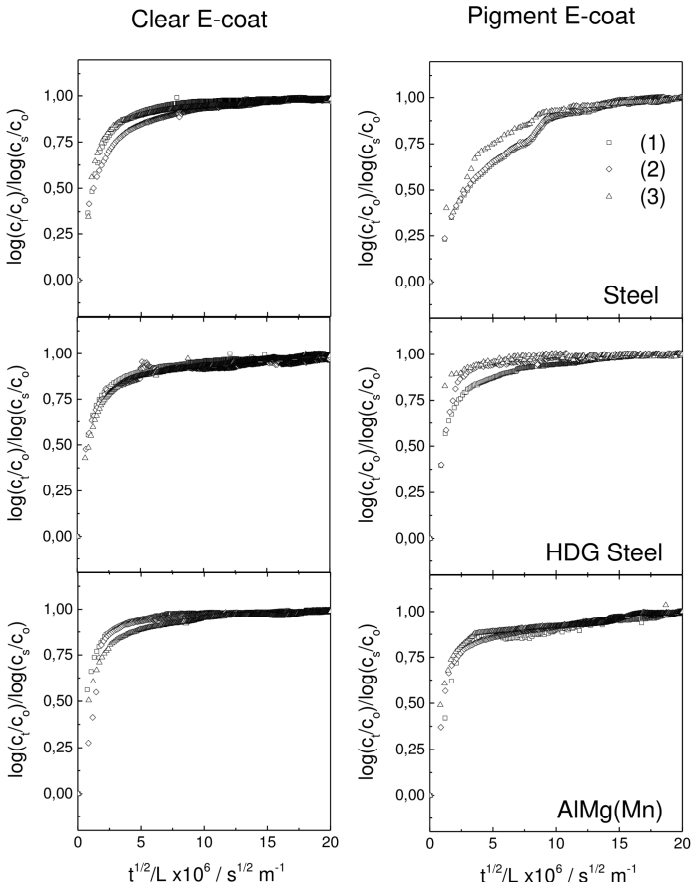

Fig. 2.8 E-coat capacitances on steel, HDG steel and AlMg(Mn) calculated with RC fit applied between 10 kHz-100 kHz and extracted at a frequency of 10 kHz

Next, the capacitance was estimated, logarithmised and displayed against the square root of time to calculate the diffusion kinetics. The results of the threefold analysis are shown in Figure 2.8. The curves are widely superimposable. Variations of curve progression are noticeable on steel and HDG steel with pigment E-coat in the initial stage. The curve slopes seem to be equal, and only the pigment coated steel samples have a more moderate capacitance gain with a small step at 8.5E6 $s^{1/2}$/m (98 min). Thickness fluctuations are always a problem on polymer coatings, which is why proper samples were selected from the bulk and only presented in this case study. However, if the layer thickness of the pigment E-coated steel increases up to 25 µm, the observed capacitance step in the initial zone disappears. Roy and co-workers [36] have modulated such curve progress in an infinite element approach including creep

during anomalous moisture swelling in polymer composites. Nevertheless, creep or thickness increase caused by swelling is expressed by the non-Fickian approach with the adsorption coefficient SC, which will be discussed later.

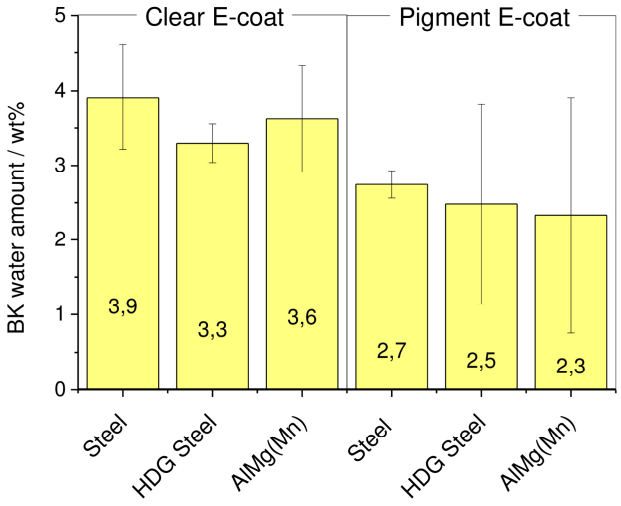

Fig. 2.9 BK water contents of the clear and the pigment E-coat on steel, HDG steel and AlMg(Mn)

Typically, the BK water amounts are presented in Figure 2.9 assuming ideal Fickian conditions. The results of the clear and pigment E-coat are based on the raw capacitances from the start and the end of the salt-water uptake. The water content is slightly higher in the clear E-coat with 3.6 % to 2.5 % on average but there are no prominent discrepancies among the substrates. Especially, the error bars of HDG steel and AlMg(Mn) with the pigment E-coat are large and fluctuate with standard deviations of 1.3 and 1.6 %, as indicated in the impedance diagram (Figure A2.2.1). In general, the error bars of the BK values decrease while coating thickness increases, due to the higher capacitances and the E-coats are relatively thin layer of 20 µm. The quality of the start value additionally depends on the velocity of the operator to start the experiment. In this case, the BK determination does not reflect dominant substrate or pigmentation differences.

Furthermore, the capacitance curves have to be fitted as an exponential function to determine the diffusion parameters of the different approaches [37]. A number of degrees of freedom exists to fit these curves in an adequate way and only the short slope region dominates the results with a small amount of raw data as described in [38]. Therefore, three curves of each type of sample were averaged to gather a higher amount of available data for the early stages and the variation values of the averaged curve were produced from the raw data. From these resulting variations, negative and positive curve progressions were created and fitted to get a confidence interval for the diffusion parameters. As a general fitting standard, the curves have to converge and the chi² tolerance value has to reach 1E-9. The initial fitting parameters were not changed or fixed and the initial SC coefficient was set to zero.

All kinetic results of this process are shown in Appendix A2.3 and are summarised in Figure 2.10 which shows the confidence intervals of the diffusion and SC coefficients for the clear (white) and pigment E-coat (dashed). In detail, the Fickian data of the clear E-coat indicates a reliable difference between steel and HDG steel as shown by the mean diffusion coefficient of steel (1.5E-13 m²/s) and HDG steel (3.1E-13 m²/s). Due to the large confidence interval of AlMg(Mn) from 1.3 to 4.6E-13 m²/s, there is no reliable method of comparison to the other substrates. The Fickian results of the pigment E-coat are almost equal though large error bars exist on the steel and the AlMg(Mn) samples. However, the non-Fickian results give nearly the same picture of the diffusion for the clear and the pigment E-coats. The slowest water transport process is shown to be on steel followed by HDG steel and AlMg(Mn), with a constant overlap of the HDG steel and AlMg(Mn) interval. The calculated means point to a slightly higher diffusion coefficient on AlMg(Mn). This trend is further in an agreement with the found metal concentrations in the E-coats. The high iron content of around 20 at% seem to protect the E-coat against the water ingress while a blocking of the ingress of sodium and chloride ions is probable due to osmotic forces.

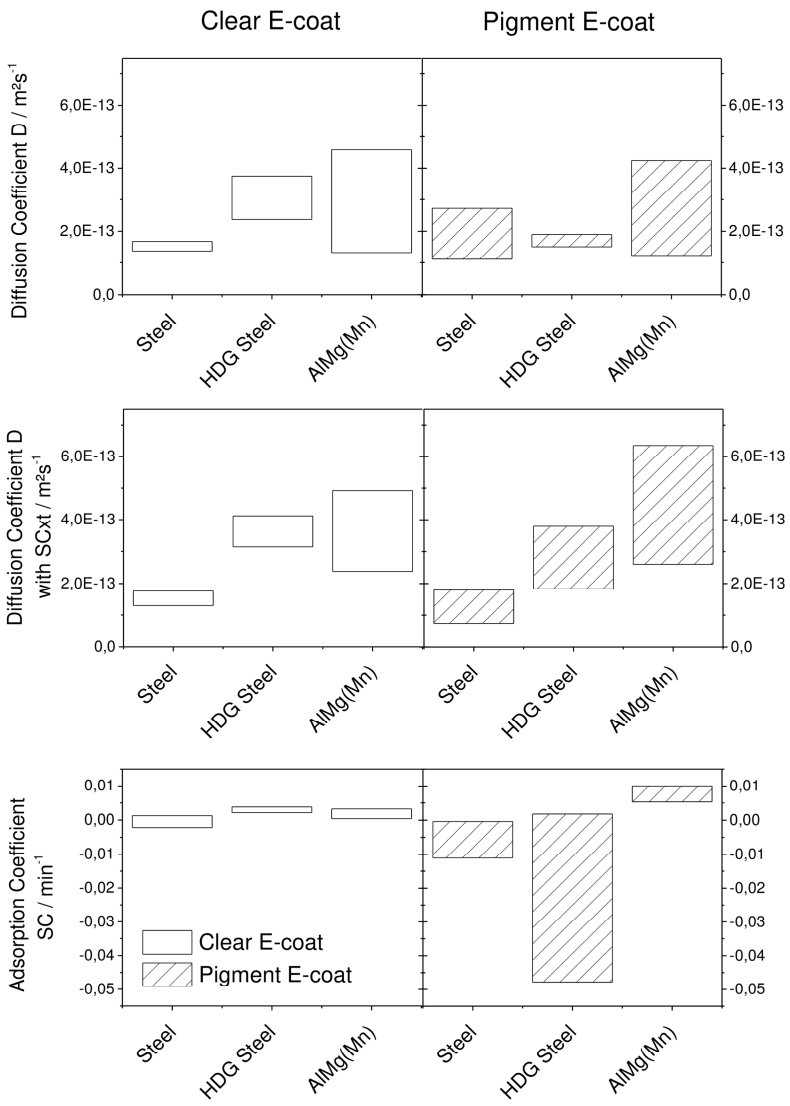

Fig. 2.10 Fickian and non-Fickian diffusion coefficients with SC of the clear E-coat (white) and the pigment E-coat (dashed) for the different metal substrates

The SC coefficients of the clear E-coat hover around zero which implies a substrate-independent ideal Fickian behaviour (see Figure 2.1). The results of the pigment E-coat reflect a tendency towards negative SC coefficients on steel and HDG steel up to -0.048 min^{-1}. If the pigment E-coat plasticises, the negative SC coefficient would hint to bounded water in the polymer bulk due to the smaller

permeability constant (ε_W=60) compared to free water (ε_W=78.3). By contrast, the SC coefficients on AlMg(Mn) are positive with values between 0.005 and 0.010 min^{-1}, which would indicate network diffusion and/or electrolyte segments through an increased disorder.

After reviewing all diffusion data, the diffusion coefficients show a slight increase from steel, HDG steel to AlMg(Mn) with the exception of the Fickian data of the pigment E-coat. However, the SC coefficients of the pigment E-coat also diverge from zero in contrast to the clear E-coat. Consequently, the clear E-coat can be fitted with the Fickian or the non-Fickian approach, both are equivalently suitable. The substrate-dependencies are nearly the same when comparing the non-Fickian results of the pigment E-coat to the results of the clear E-coat. If a non-Fickian process exists, the E-coat would pass to an amorphous state with polymer segments and microgel structures, which is why the following section sheds light on the viscoelasticity and the topography of the pigment E-coat after salt-water uptake.

2.4.3 Physicochemical characteristics of the 'swollen' pigment E-coat

The degree of the plasticising and topographical changes indicate the creation of polymer segments, microgel structures and pigment moves, and offers the first hint of non-Fickian processes through the E-coat volume. The extraction of this information is shown by FMM results of the pigment E-coated steel. The substrate differences are pointed out by Young's modulus distributions and roughness changes, which clarify the Fickian states.

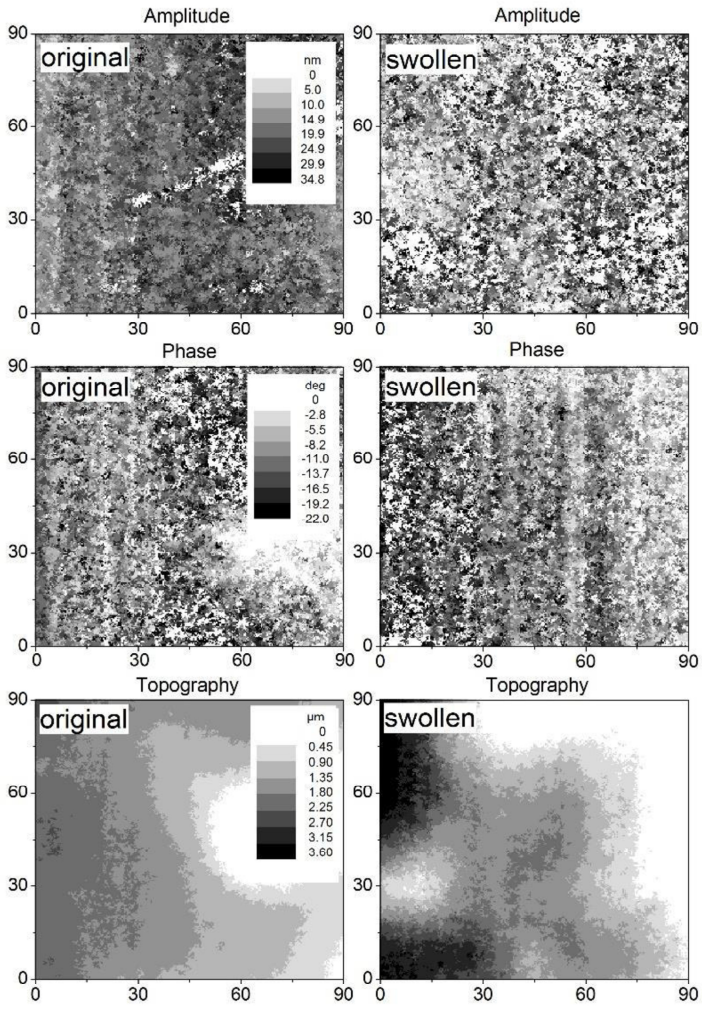

Fig. 2.11 Force amplitude, phase and topography images (top to bottom) of the original (left) and the swollen E-coat (right) on steel, load: 7.9 mL/cm² 0.5 M NaCl, duration: 50 days

The pigment E-coated steel is loaded with a 7.9 mL/cm² 0.5 M NaCl solution for 50 days. Figure 2.11 shows the corresponding amplitude, phase and topography images of the original (left) and the swollen surface (right). The amplitude is more homogeneous on the original E-coat than on the

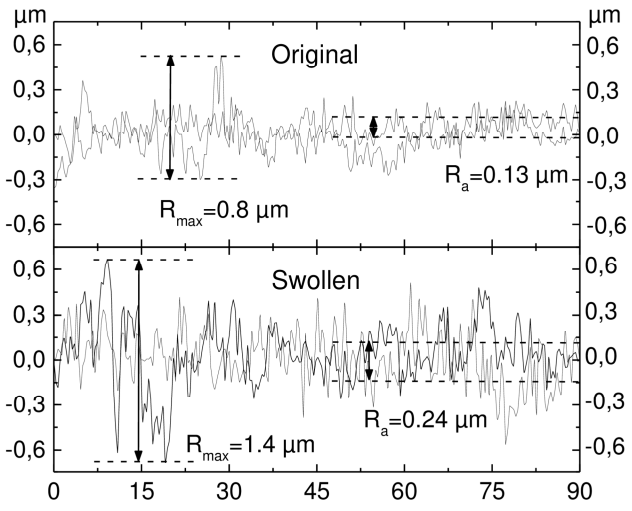

Fig. 2.12 Exemplified profile diagrams of the original (top) and the swollen E-coat surface (bottom) and their roughness parameters on steel after 50 days

swollen one. The median amplitude increases from 14.1 nm to 16.9 nm after salt-water uptake. Both phase distributions are nearly equivalent. The median phase shifts slightly from -16.1 ° to -14.1 ° due to the salt-water. More distinct differences between the samples are evident by the topography. The images indicate smaller original hills of approximately 2.0 µm, whereas the hills of the swollen surface increased to 3.6 µm. After the elimination of form deviations (e.g. skewness, sphericity) and waviness, roughness parameters such as the arithmetic roughness, R_a, and the maximal roughness depth R_{max} are accessible. Figure 2.13 presents exemplified profile diagrams of the original (top) and the swollen surface (bottom). Their roughness parameters have been analysed by fourteen measured lines with a length of 90 µm. The original E-coat surface has an arithmetic roughness of 0.13 µm with a maximal roughness depth of 0.8 µm. In comparison to the original E-coat, the swollen E-coat is significantly rougher. After 50 days of salt-water uptake without

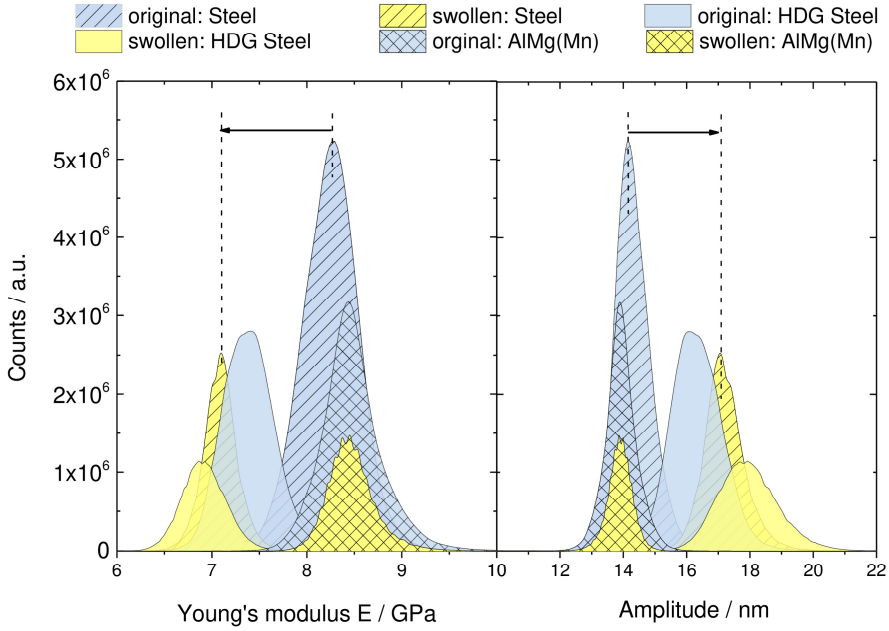

Fig. 2.13 Young's modulus (left) and amplitude (right) distributions of the original (white) and the swollen E-coat (grey), swollen coatings loaded with 7.9 mL/cm² 0.5 M NaCl on steel for a duration of 50 days, on HDG steel and AlMg(Mn) for 75 days

visible corrosion processes, the E-coat almost doubles its roughness parameters, the arithmetic roughness amounts to 0.24 µm and the maximal depth is 1.4 µm.

The substrate dependencies are shown in Figure 2.13 as amplitude/hardness (right) and Young's modulus distributions (left) of the original (white) and the swollen E-coats (grey) on steel (dashed) as well as on HDG steel and AlMg(Mn) (squared) after 75 days of salt-water uptake. The median amplitude increases slightly on the steel and HDG steel from 14 nm to 16-17 nm, whereas the AlMg(Mn) amplitude does not change due to soaking. The amplitude gain is accompanied by a Young's modulus drop. The Young's modulus reaches values between 6.5 and 9.5 GPa. If the E-coat achieves its glass transition point (~90 °C) and passes on to an amorphous state, a logarithmical abatement of the Young's modulus of epoxy films according to [39] would be expected. Rather, the amount of decrease suggests the first sign of free volume increase so that localised bond movements such as bending and stretching, as well as side chain movements, can occur [39]. However, this so-called 'gamma transition' may also involve associations with water [40].

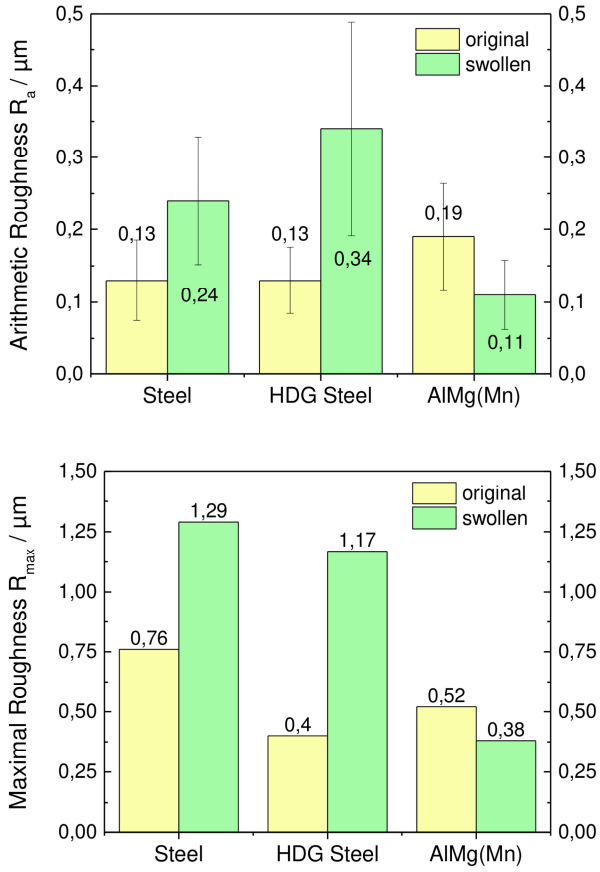

Fig. 2.14 Substrate-dependent arithmetic roughness, R_a, (top) and maximal roughness, R_{max}, (bottom) of the original (white) and the swollen E-coats (dashed); swollen E-coats loaded with 7.9 mL/cm² 0.5 M NaCl on steel for a duration of 50 days, on HDG and AlMg(Mn) for 75 days

The attendant roughness parameters are presented in Figure 2.14. The arithmetic roughness parameters double on steel and HDG steel, but are halved on AlMg(Mn). The roughness gains are accompanied by a rise of the mean variations. The bar chart of the maximal roughness depths support these findings. The swollen E-coat surfaces excluding AlMg(Mn) have visible orange peeling. Corrosion, lifting or other de-adhesion phenomena were not observed but the finish of the metal surfaces (Figure 2.2) differs noticeably, as seen in the section 2.4.1.

Due to the salt-water uptake, the polymer mobility increases and the E-coat becomes more like a liquid, which is why the pigment-polymer bulk fills the available valleys of the metal surface. E-coats

are renowned for their well-defined layer thicknesses. This benefit gets lost due to an inhomogeneous substrate structure such as those of steel and HDG steel. Contrarily, a liquid-like bulk will homogenously disperse on a flat substrate and level the coated surface as shown on AlMg(Mn). Additionally, an amplitude/hardness increase, coupled with a roughness gain, can only occur due to an increased surface ratio of brittle components such as pigments and fillers. The spatial orientation of the E-coat seems to be modified due to the water uptake on steel and HDG steel. The pigments in the E-coat enrich on the top of the E-coat during the water uptake, whereas the AlMg(Mn) surface causes only a levelling with a constant particle distribution in the topmost E-coat section.

In brief, FMM results show that the E-coat does not plasticise during water uptake but the embedded particles cause a disorder in the polymer network dependent on the substrate finish. This behaviour seems to be comparable to the disorder of plasticising processes and clarifies the good suitability of the non-Fickian model for the pigment E-coat.

2.4.4 Ion transport along the metal interface

The previous results showed that the metal has an influence on the volume diffusion independent of the type of coating but it is doubtful whether these results are in line with the interface mechanisms. The following subsection should clarify this question using the SKP approach, by comparing the interfacial transport on clear and pigment-coated steel, and concentration-dependent measurements on the pigment E-coat for the different substrates with a special regard to the E-coated AlMg(Mn).

2.4.4.1 SKP approach at semi-conductive and insulating metal oxides

Typically, the cathodic delamination is investigated along the interfaces of semi-conductive metal oxides such as those of zinc or steel in a humid oxygen ambience. The oxygen reduction promotes the migration of solvated ions underneath the polymer while the metal substrate dissolves as the anodic counter reaction in the defect. The measurable Volta potential $\Delta\psi$ is dominated by the electron transfer of the redox reaction, the mobile charge carriers and the interaction of corrosion product with the interfacial layer [2]. As a result, the time-dependent potential scan shows a cathodic progress to the intact polymer area with continuous failure.

In the present case, the ambience is changed to oxygen-deficient conditions under N_2 purge. This procedure causes an inhibition of the electron transfer of the redox reaction and a blocking of the creation of corrosion products. The Volta potential then is dominated by the charge carriers whereupon the smallest one, e.g. Na^+, move ahead due to their highest mobility. These charge carriers strongly impact the Galvani potential $\Delta\Phi^{MeOx}$ of the semi-conductive metal oxides *MeOx*. The initial

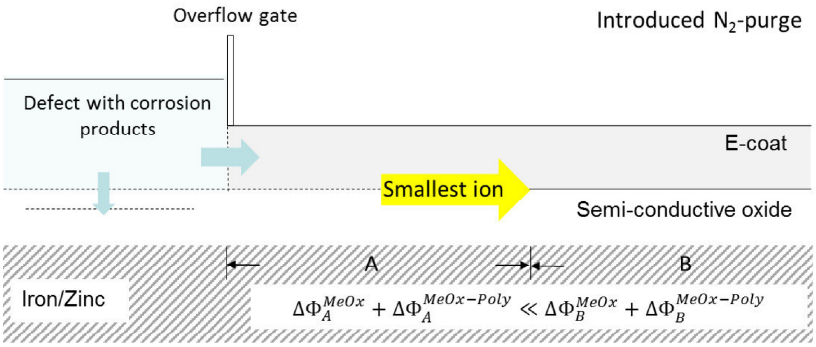

Fig. 2.15 Mechanistic understanding of the applied SKP approach on the semi-conductive oxide interfaces under nitrogen purge

produced corrosion products may also affect the Galvani potential $\Delta\Phi^{MeOx-Poly}$ of the interfacial layer MeOx-Poly in a small amount. In detail, the Volta potential is a function of the sum of the Galvani potentials and constant parameters such as the chemical potential μ, the work function W, the Faraday constant F (96485.3 C/mol) and the electric surface potential χ^{Poly} of the polymer [41, 42]:

$$\Delta\psi = \Delta\Phi^{Me} + \Delta\Phi^{MeOx} + \Delta\Phi^{MeOx-Poly} - \frac{\mu}{F} - \frac{W}{F} + \chi^{Poly} \tag{2.9}$$

In contrast to the cathodic delamination along the interfaces of conductive metal oxides, the insulating *aluminium* oxide is well-known for the filiform corrosion with an anodic head and a cathodic tail. The ions of the acidic aluminium dissolution move ahead followed by the corrosion products resulting from the alkaline oxygen reduction in the tail. However, the transported charge carriers have no bearing on the Galvani potential of an intact aluminium oxide due to its low rate of electron transfer (ETR). The ion incorporation is quasi invisible to the Kelvin probe. The introduced N_2 purge stabilises the aluminium oxide and avoids the complete breakdown. Similar to the conductive oxides, the redox reaction and the corrosion products are blocked but the resulting Volta potential is just dominated by the interfacial dipole layer *MeOx-Poly*.

Of course, the metal oxides can be stabilised or destabilised by the initial oxygen exposure and due to the sample preparation, the charge carriers additionally move through the polymer in parallel to the polymer-metal interface (see Figure 2.15). However, these circumstances recreate the usual problem caused by stone damage, especially for wetness due to dammed-up water. The N_2 purge stabilises and preserves this running process (approx. after 48 h) whereupon the Volta potential is mainly driven by the charge carriers at semi-conductive oxides (steel and HDG steel) and the state of the interfacial dipole layer at intact insulating oxides (AlMg(Mn)).

2.4.4.2 Comparison of the clear and pigment E-coat

The described SKP approach is applied to analyse the pigmentation effect on the interfacial transport of the clear and the pigment E-coat on steel with the use of a 0.5 M NaCl solution. Therefore, the samples were stored for 525 h in a humid oxygen atmosphere followed by the N_2 purge.

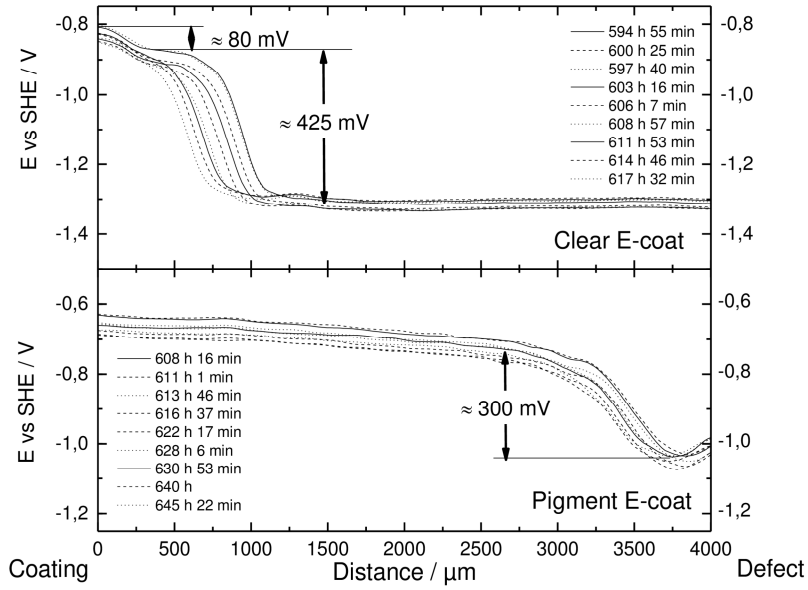

Fig. 2.16 Potential lines of clear (top) and pigment E-coat (bottom) on steel with 0.5 M NaCl defect, atmosphere: rH=86-84 %, O_2≤3 %

Figure 2.16 presents the movement of the sharp potential fronts for the clear and pigment-coated steel interfaces in oxygen-deficient atmosphere from 594 to 645 h after the electrolyte addition to the defect. This time-sequence results from the fact that the first movement at the pigment-coated steel interface was observed after three weeks. However, both samples started at the same time, have the same defect distance and the same atmosphere histories so there are comparable despite these differences.

Evidently, the charge carriers along the clear E-coat move earlier and many times faster than the charge carriers at the pigment E-coat. The potential drop of the pigment sample amounts to 300 mV. However, the clear E-coat has a major potential drop of 425 mV followed by a second delayed rise of round 80 mV. The initial delays of three weeks on the pigment E-coat and one week on the clear E-coat express the incubation time

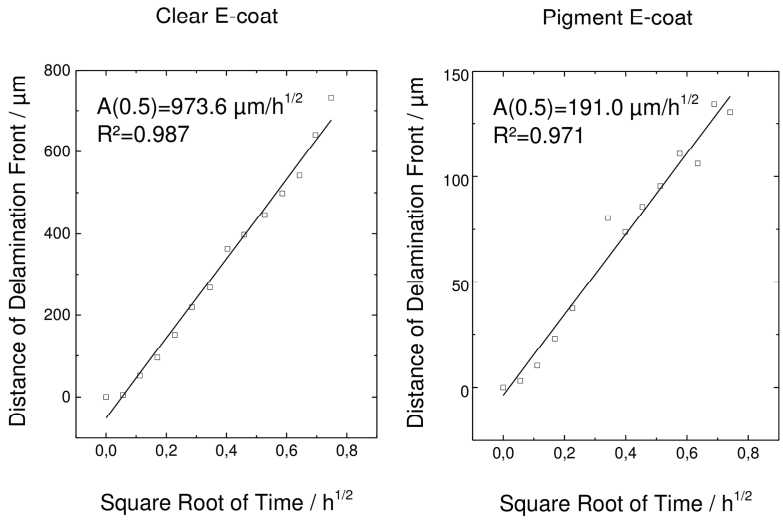

Fig. 2.17 Interface kinetics of the clear (left) and the pigment E-coat (right) on steel presented as distance to defect against the square root of time

to achieve the boundary conditions for the sub-surface flux without detectable transport activities. Consequently, the time is reset at 594 h to calculate only the assumed transport-controlled process as the basis for the applied square root law. Figure 2.17 presents the kinetic results across these 51 h from 594 to 645 h. The data shows linear behaviour. The observed potential drops are further in line with the calculated slopes *A* with a value of 974 µm/h$^{1/2}$ at the clear E-coat and 191 µm/h$^{1/2}$ at the pigment E-coat. Compared to the volume diffusion data, the interface differences between the pigment and the clear E-coat are prominent, whereby the sub-surface flux on the clear system is five times faster compared to the flux of the pigment system.

Referring to the SKP approach, the measured flux j_{Na^+} is composed of diffusion j_{diff} and migration processes j_{mig} and expressed in the Nernst-Planck equation [4]:

$$j_{Na^+} = j_{diff} + j_{mig} = \left(-D_{Na^+} \frac{\partial C_{Na^+}(x,t)}{\partial x}\right) + \left(-\frac{F}{RT} D_{Na^+} C_{Na^+} \frac{\partial E(x)}{\partial x}\right) \quad (2.10)$$

With the assumption of a linear concentration gradient and $\alpha = \frac{\Delta E}{\Delta x}$, the relation of the transport terms [15] is illustrated by the equation (2.11) and calculated for the clear E-coat with a potential drop of 425 mV across 1073 µm:

$$\frac{j_{diff}}{j_{mig}} = \frac{RT}{Fc_0\alpha}\frac{\Delta c}{\Delta x} = \frac{8.31451\,\frac{J}{mol\,K}\cdot 298.15\,K\cdot 0.5\,\frac{mol}{L}\cdot 1073\,\mu m}{9.64853\cdot 10^4\,\frac{C}{mol}\cdot 0.5\,\frac{mol}{L}\cdot 0.425\,V\cdot \Delta x} = \frac{64.9\,\mu m}{\Delta x} \quad (2.11)$$

As a result, the migration should dominate after 65 µm on the clear and after 92 µm on the pigment E-coat. The measured flux is mainly driven by migration due to the electrical field and secondary by diffusion caused by the concentration gradient. The SKP approach primarily provides the kinetic information about the present galvanic coupling of conductive metal oxides in a humid nitrogen ambience.

In brief, the pigmentation effect of the E-coat is prominent along the steel interface. The charge carriers start earlier and move five times faster at the clear E-coat interface compared to the pigment one. According to the Nernst-Planck equation, the measured flux is driven by migration and should not be comparable with the EIS data as is often suggested [43, 44].

2.4.4.3 Metal- and concentration-dependent effects

An initial oxygen exposure of 525 h seem to cause a migration-driven ion flux at the steel interface in a humid oxygen-deficient ambience. For the following results, the samples were directly placed and measured in a humid nitrogen atmosphere, rH=88-91% and O_2≤2 % after filling the defect. The metal

and concentration differences are presented at the pigment E-coat, with regard to the manner of the interfacial transport.

Figure 2.18 shows the sub-surface flux at the steel interface for 1.0 M, 0.5 M and 0.1 M NaCl solutions in the time frame of 513 h to 640 h after the electrolyte addition to the defect. The potential front moves faster whereupon the potential barrier decreases from approximately 350 mV to 270 mV, with increased ion concentration. This trend is also observed on the HDG steel samples which exhibit a potential barrier decrease from ca. 320 mV to 270 mV. This seems be a contradiction because the potential drop is the driving force for migration. The dominance of the migration is basically proven by the observed cation and anion separation along the interface in earlier works [15]. However, an equal flux of potassium and bromine ions was already detected at the water-borne epoxy steel interface in the humid air [11]. Water-filled interfacial voids are discussed as transport highways for the bromine ions. The low oxygen permeability of the E-coat and the present oxygen deficiency inhibit the migration while the diffusion might be

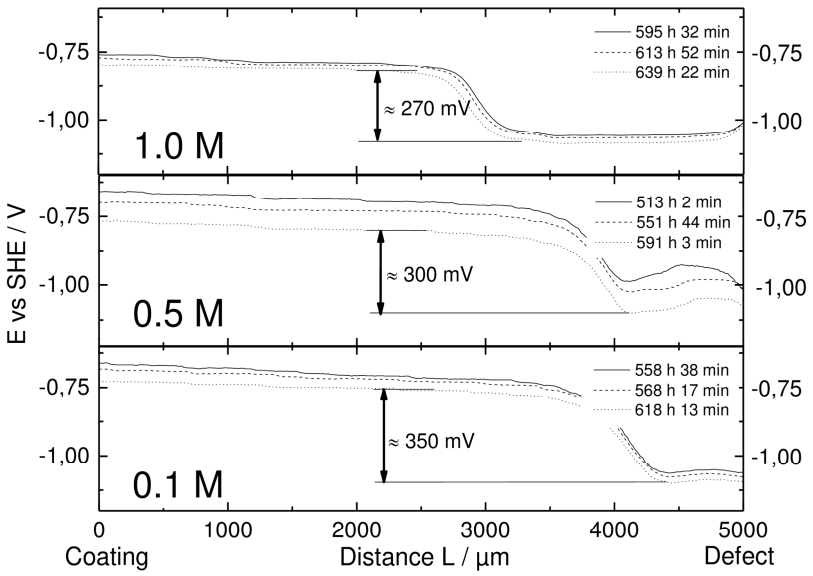

Fig. 2.18 Potential lines of E-coated steel with defect concentrations of 1.0 M, 0.5 M and 0.1 M NaCl (top to bottom), atmosphere: rH=88-91 %, O_2≤2 %

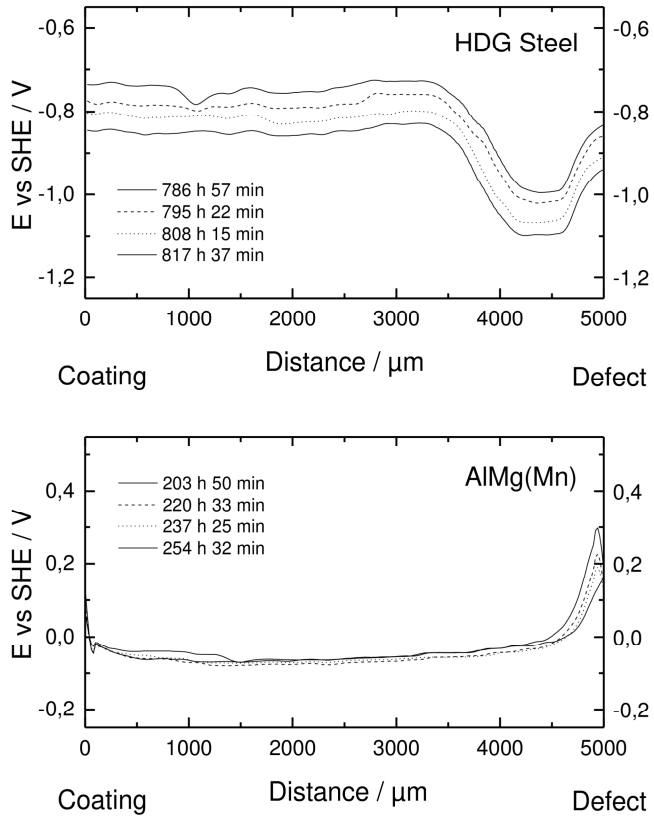

Fig. 2.19 Potential lines of a pigment E-coated HDG steel (top) and AlMg(Mn) (bottom) with 1 M NaCl defect, atmosphere: rH=88-91 %, O_2≤2 %

more prominent on the water-borne E-coat. The sample characterisation further showed that there is an increased amount of iron ions in the polymer network, which may also affect the potential drop.

While the oxides of steel are stable, the oxides of zinc and aluminium destabilise, in the alkaline environment at the beginning of the experiment. Impressively, Figure 2.19 illustrates the instability of the amphoteric substrates, HDG steel and AlMg(Mn), due to an anodic behaviour in the defect area. It is still conspicuous that for all HDG samples the first detected move happens at least one week after the first movement signs along the steel interface. Unfortunately, a parallel detection of steel and HDG steel did not succeed due to the different starting times and the finite sample length. It is assumed that the initial anodic behaviour of zinc plays the major role in causing the delay, because the anodic flux underneath the coating is generally many times slower than the cathodic flux. Further, Figure 2.3 (section 2.4.1) already indicated the increased corrosion resistance of HDG steel compared to the other substrates in the oxygen environment. Posner and co-workers [45, 46] analysed the coated iron and galvanic zinc interfaces in a single sample due to the partial dissolution of the zinc layer. In a humid oxygen-deficient atmosphere, the iron oxide interface showed a cathodic shifted potential combined with a XPS/ToF-SIMS-proven potassium ion flux. Contrary to the iron oxide, no ion ingress was observed at the covered zinc oxide after 60 h, which is in line with present results across 820 h.

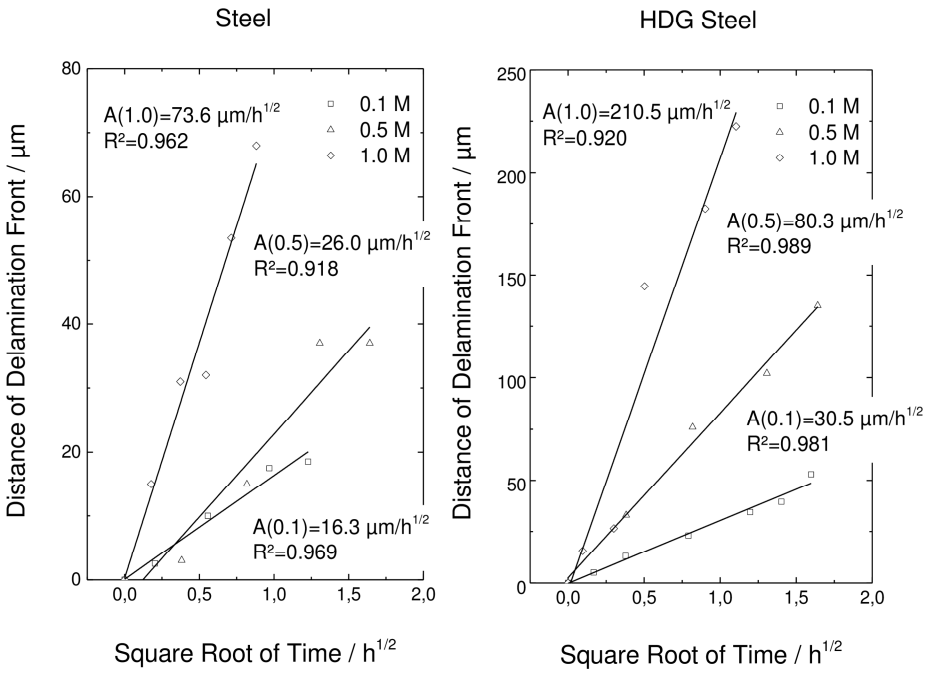

Fig. 2.20 Interface kinetics of the E-coated steel with defect concentrations of 0.1 M, 0.5 M and 1.0 M NaCl presented as distance to defect against the square root of time

Tab. 2.1 Interface kinetic data of steel and HDG steel calculated after Leng et al. [8] in which the mean transport coefficient expresses the assumption of concentration-independent behaviour; [1)] Requirement of sub-surface flux: $c_{bulk} > c^*/K$

Substrate	Conc. c / mol L^{-1}	Slope A / µm $h^{-1/2}$	Transport coefficient / m^2 s^{-1}	Mean transport coefficient / m^2 s^{-1}	Mean[1)] critical bulk conc. c^*K^{-1} / mol L^{-1}
Steel	0.1	16.3	0.4E-13	2.6E-13 ±3.6E-13	0.030 ±0.009
	0.5	26.0	1.2E-13		
	1.0	80.2	6.3E-13		
HDG Steel	0.1	30.5	0.9E-13	16.8E-13 ±26.2E-13	0.016 ±0.000
	0.5	80.3	6.3E-13		
	1.0	210.5	43.3E-13		

Accordingly, the concentration-dependent transport rates were quantified for the conductive oxides of steel and HDG steel (see Figure 2.20). The recordings started at ca. 512 h for steel and 786 h for HDG steel dependent on the defect concentration. In general, it was difficult to linearise the movement, the transport occurs very slowly and the inflexion point detection about the second potential deviation does not always express the measured movement due to the natural potential course of the technical E-coat. Nevertheless, the data generated regression coefficients above 0.9 and it showed that the sub-surface flux at the zinc interface is approximately two times faster than the transport on steel. However, the overall transport is twice as slow along the zinc interface (≈1.5 µm/h at 815 h) compared to the steel interface (≈3.4 µm/h at 596 h) due to the delayed start of zinc. The undermining threshold concentration, c*/K for steel is twice that of the threshold concentration of zinc with 0.016 mol/L (see Table 2.1). The determined transport coefficients reach values of 0.4E-13 m²/s to 6.3E-13 m²/s for steel and 0.9E-13 m²/s to 43.3E-13 m²/s for HDG steel with a rising trend coupled to the NaCl concentration. Generally, the coefficients have to be determined irrespective of the ion concentration. Possible reasons for the deviations are the poor linearization and the results of any mathematic operation of erf(x)-function. Further, the included particles can interact on the oxidised metal, the amines can form chelate complexes with metal ions [47] or cluster water can accumulate at the interface [48]. The results indicate non-Fickian interface behaviour as was already discussed with the EIS and FMM data.

As shown in Figure 2.19, the AlMg(Mn) interface does not develop potential drops under oxygen-deficient conditions. The potential curve has an anodic region at the beginning of the defect up to 0.3 V and flattens continuously to -0.05 V with a 1.0 M NaCl solution. Referring to these potentials, investigations of the surface oxide properties on the aluminium/epoxy interfacial bonding [42, 49-50]

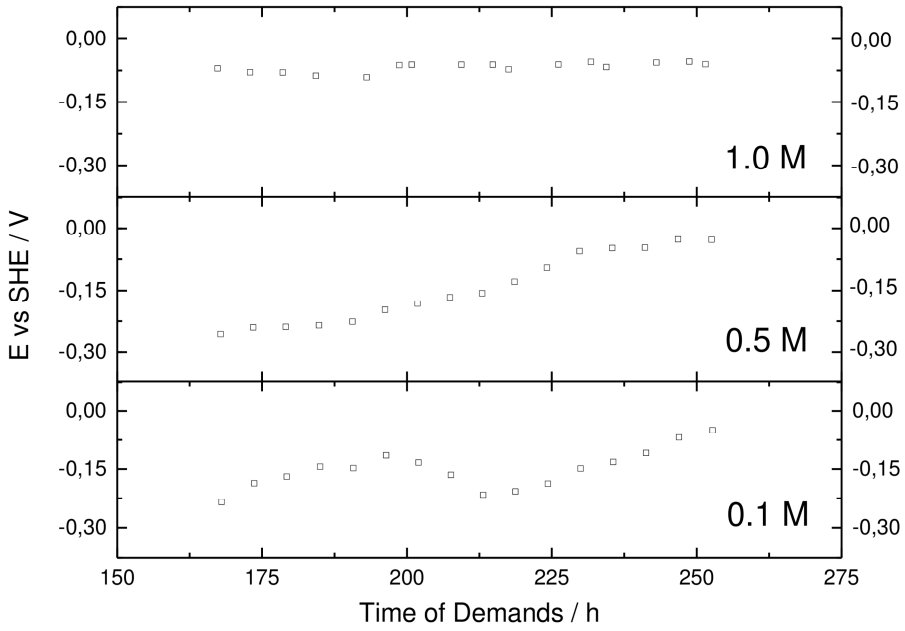

Fig. 2.21 Time-dependent potentials of the E-coated AlMg(Mn) at 1 M (top), 0.5 M (middle) and 0.1 M NaCl (bottom), measured 2500 µm away from defect, atmosphere: rH=88-91 %, $O_2 \leq 2$

show that the alkaline-cleaned aluminium has a potential of -0.05 V as amide and -0.30 V as amine bonding, correlated via X-ray photoelectron spectroscopy (XPS). Correspondingly, Figure 2.21 presents the concentration-dependent potentials 2500 µm away from the initial defect in the time frame of 150 h to 275 h. As seen before, the potential of the 1 M NaCl solution is constant at -0.05 V. The potential of the 0.5 M NaCl solution shifts from -0.05 V to -0.30 V and the potential of the 0.1 M NaCl electrolyte flips between -0.30 V and -0.05 V in this time range. These initial results were unexpected, which is why the measurement was repeated to avoid artefacts. The impact of atmospheric conditions can be excluded due to the same treatment of samples. The potential was freshly calibrated before recording and the samples were directly measured in an area of 5000 µm x 300 µm with a step length of 20 µm in succession. Lastly, the results hint at a flip between two different boundary states at the interface.

All things considered, the interfacial transport starts a week earlier on steel than on HDG steel whereupon the velocity along the interface is then twice faster on HDG steel. With increased defect concentration, the transport rates increase while the potential barriers decrease. Due to this fact, migration seem to be inhibit and diffusion gains in importance. Additionally, the AlMg(Mn) interface shows a time- and concentration-dependent potential flip which hint at two different interfacial boundaries. However, it has to be clarified, whether a transport takes place and the potential flip provides any kinetic information.

2.5 Conclusion

This comprehensive study shows that clear and pigment E-coated steel, HDG steel and AlMg(Mn) differ conspicuously in their transport behaviours and during their film formation. The substrates dissolve due to the extreme cathodic polarisation under high alkaline conditions, which is why the E-coat is contaminated by the solvated metal on zinc and aluminium and – contrary to expectations – with its highest content on steel. Therefore, the E-coated steel shows the slowest water diffusion through the polymer bulk followed by HDG steel and AlMg(Mn), see Figure 2.22. The high iron content of around 20 at% seem to protect the E-coat against the water ingress while a blocking of the ion ingress is probable due to osmotic forces. The polymer matrix reveals a slight Young's modulus drop and an increased disorder in the pigment-polymer network on rough substrates after 50 days of salt-water uptake. Further signs of plasticising are not observed but these circumstances already require a non-Fickian approach. Moreover, a noticeable influence of the pigmentation is not reflected in the EIS diffusion data but is prominent in the SKP findings. The time lines of the interfacial results are summarised in Figure 2.23. The ion transport at the clear E-coat starts earlier and is five times faster than the ion transport at the pigment version on steel. On the other hand, at the pigment E-coat, the ion transport starts a week earlier on steel than on HDG steel whereupon the velocity along the interface is then faster on HDG steel. Additionally, the AlMg(Mn) interface shows a time- and concentration-dependent potential flip which hints at two different interfacial boundaries.

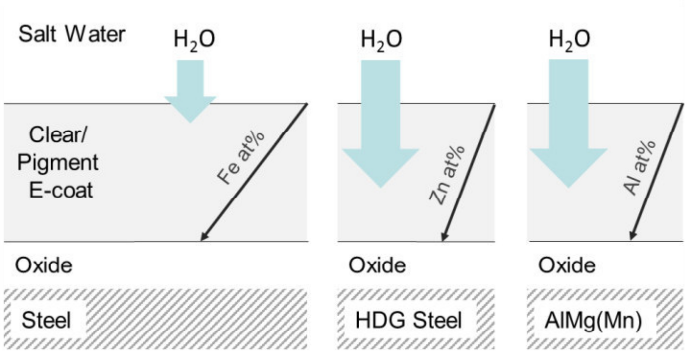

Fig. 2.22 Scheme of the water diffusion through the E-coat bulk

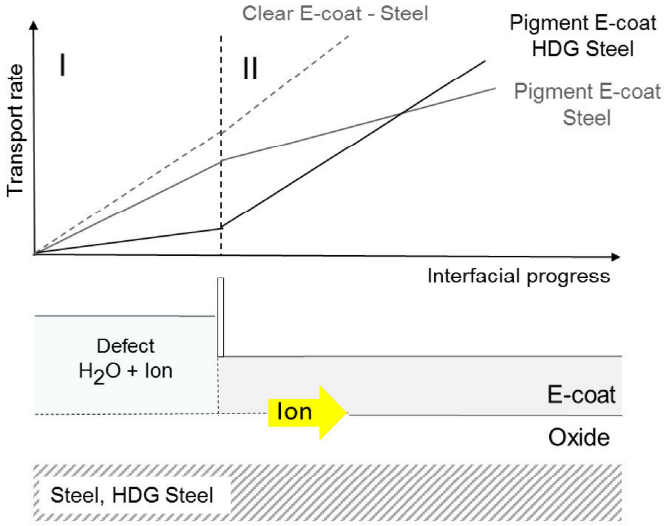

Fig. 2.23 Interfacial results at the time line, I) incubation, II) ion transport

References

[1] Z. W. Wicks, F. N. Jones, S. P. Pappas, D. A. Wicks, Organic coatings: science and technology, Vol. 3, Wiley, New Jersey, 2007.

[2] G. Grundmeier, M. Stratmann, Adhesion and de-adhesion mechanisms at polymer/metal interfaces: mechanistic understanding based on in situ studies of buried interfaces, Ann. Rev. Mat. Res. 35 (2005) 571.

[3] A. Schönberger, Prognose des Steinschlags und der induzierten Korrosion am Fahrzeug, Doctoral thesis, Alexander-Friedrich-University Erlangen-Nürnberg, 2012.

[4] J. Crank, The mathematics of diffusion, Clarendon Press, Oxford, 1975.

[5] Y. Osada, K. Kajiwara, T. Fushimi, O. Irasa, Y. Hirokawa, T. Matsunaga, T. Shimomura, L. Wang, H. Ishida, Gels Handbook, Academ. Press, London, 2001.

[6] V. N. Nguyen, F. X. Perrin, J. L. Vernet, Water permeability of organic/inorganic hydrid coatings prepared by sol-gel method: A comparison between gravimetric and capacitance measurements and evaluation of non-Fickian sorption models, Corros. Sci. 47 (2005) 397.

[7] H. Zhu, H. P. Huinink, O. C. G. Adan, K. Kopinga, NMR study of the microstructures and water–polymer interactions in cross-linked polyurethane coatings, Macromolecules 46 (2013) 6124.

[8] A. Leng, H. Streckel, M. Stratmann, The delamination of polymeric coatings from steel. Part 1: Calibration of the Kelvin probe and basic delamination mechanism, Corros. Sci. 41 (1999) 547.

[9] A. Leng, H. Streckel, M. Stratmann, The delamination of polymeric coatings from steel. Part 2: First stage of delamination, effect of type and concentration of cations on delamination, chemical analysis of the interface, Corros. Sci. 41 (1999) 579.

[10] A. Leng, H. Streckel, K. Hofmann, M. Stratmann, The delamination of polymeric coatings from steel. Part 3: Effect of the oxygen partial pressure on the delamination reaction and current distribution at the metal/polymer interface, Corros. Sci. 41 (1999) 599.

[11] R. Posner, M. Santa, G. Grundmeier, Wet- and corrosive de-adhesion processes of water-borne epoxy film coated steel, J. Electrochem. Soc. 158 3 (2011) C29.

[12] M. Santa, R. Posner, G. Grundmeier, Wet- and corrosive de-adhesion processes of water-borne epoxy film coated steel II. The influence of γ-glycidoxypropyltrimethoxysilane as an adhesion promoting additive, J. Electrochem. Soc. 158 3 (2011) C36.

[13] W. Fürbeth, M. Stratmann, The delamination of polymeric coatings from electrogalvanized steel – a mechanistic approach. Part 1: Delamination from a defect with intact zinc layer, Corros. Sci. 43 (2001) 207.

[14] W. Fürbeth, M. Stratmann, The delamination of polymeric coatings from electrogalvanized steel – a mechanistic approach. Part 2: Delamination from a defect down to steel, Corros. Sci. 43 (2001) 229.

[15] W. Fürbeth, M. Stratmann, The delamination of polymeric coatings from electrogalvanized steel – a mechanistic approach. Part 3: Delamination kinetics and influence of CO_2, Corros. Sci. 43 (2001) 243.

[16] A.-P. Romano, M.-G. Olivier, A. Nazarov, D. Thierry, Influence of crosslinking density of a cataphoretic coating on initiation and propagation of filiform corrosion of AA6016, Prog. Org. Coat. 66 (2009) 173.

[17] A. Nazarov, A.-P. Romano, M. Fedel, F. Deflorian, D. Thierry, M.-G. Olivier, Filiform corrosion of electrocoated aluminium alloy: role of surface pretreatment, Corros. Sci. 65 (2012) 187.

[18] C. Senöz, M. Rohwerder, Scanning Kelvin Probe Force Microscopy for the in situ observation of the direct interaction between active head and intermetallic particles in filiform corrosion on aluminium alloy, Electrochim. Acta 56 (2011) 9588.

[19] J. Vogelsang, W. Strunz, Electrochemical investigations of organic, corrosion protective barrier coatings – limiting factors of small signal perturbation techniques, Mater. Corros. 52 (2001) 462.

[20] EN ISO 16773-2:2007

[21] J. E. B. Randles, Kinetics of rapid electrode reactions, Discuss. Faraday Soc. 1 (1947) 11.

[22] R. G. Kelly, J. R. Scully, D. W. Shoesmith, R. G. Buchheit, Electrochemical techniques in corrosion science and engineering, New York, Marcel Dekker, 2003.

[23] R. Vlasak, I. Kueppel, G. Grundmeier, Combined EIS and FTIR–ATR study of water uptake and diffusion in polymer films on semiconducting electrodes, Electrochim. Acta 52 (2007) 8075.

[24] E. L. Koehler, The influence of contaminants on the failure of protective organic coatings on steel, Corros. Nace 33 6 (1977) 209.

[25] M. S. Kiasat, L. J. Ernst, G. Q. Zhang, R. Bressers, Philips, Time and temperature dependent thermo-mechanical characterization and modeling of a packaging molding compound, EuroSIME 2001, Paris.

[26] K. L. Johnson, Contact mechanics, Cambridge University Press, Cambridge, 1985.

[27] J. J. Vlassak, W. D. Nix, Measuring the elastic properties of anisotropic materials by means of indentation experiments, J. Mech. Phys. Solids 42 (1994) 1223.

[28] W. Fürbeth, M. Stratmann, Scanning Kelvin probe investigations on the delamination of polymeric coatings from metallic surfaces, Prog. Org. Coat. 39 (2000) 23.

[29] K. Wapner, B. Schönberger, M. Stratmann, G. Grundmeier, Height-regulating scanning Kelvin probe for simultaneous measurement of surface topology and electrode potentials at buried interfaces, J. Electrochem. Soc. 152 (2005) E114.

[30] D. M. Brasher, A. H. Kingsbury, Electrical measurements in the study of immersed paint coatings on metal. I. Comparison between capacitance and gravimetric methods of estimating water-uptake, J. Appl. Chem. 4 (1954) 62.

[31] A. R. Berens, H. B. Hopfenberg, Diffusion and relaxation in glassy polymer powders: 2. Separation of diffusion and relaxation parameters, Polymer 19 (1978) 489.

[32] E. P. M. Van Westing, G. M. Ferrai, J. H. W. de Wit, The determination of coating performance with impedance measurements—II. Water uptake of coatings, Corros. Sci. 36 (1994) 957.

[33] M. Pourbaix, Atlas d'Équilibres Elektrochimiques, Gauthiar-Villar & Cie, Paris, 1963.

[34] J.C. Fenster, Zinkkorrosion in alkalisch wässrigen Lösungen, Doctoral thesis, Heinrich-Heine-University Düsseldorf, 2009.

[35] I. Serebrennikova, I. Paramasivam, P. Roy, W. Wei, S. Virtanen, P. Schmuki, Steel corrosion in alkaline batteries, Electrochim. Acta 54 (2009) 5216.

[36] S. Roy, Modeling of anomalous moisture diffusion in polymer composites: a finite element approach, J. Compos. Mater. 33 14 (1999) 1318.

[37] Z. Hens, W. P. Gomes, On the diffusion impedance at semiconductor electrodes, J. Phys. Chem. 101 (1997) B 5814.

[38] L. Aktas, Y. K. Hamidi, M. C. Altan, Combined edge and anisotropy effects on Fickian mass diffusion in polymer composites, J. Eng. Mater. & Technol. 126 (2004) 427.

[39] K. P. Menard, Dynamic mechanical analysis: a practical introduction, 2nd Edition, CRC Press, Boca Raton, 2008.

[40] N. McCrum, G. Williams, B. Read, Anelastic and dielectric effects in polymeric solids, Dover, New York, 1967.

[41] M. Rohwerder: Scanning Kelvin Probe and Scanning Kelvin Probe Force Microscopy and their application in corrosion science. In: Corrosion science and technology: Mechanism, mitigation and monitoring, Eds. U. K. Mudali, B. Raj, Taylor & Francis, London, 2008, 468.

[42] B. Salgin, Ö. Özkanat, J. Mol, H. Terryn, M. Rohwerder, Role of surface oxide properties on the aluminium/epoxy interfacial bonding, J. Phys. Chem. C 117 (2013) 4480.

[43] R. Posner, P.E. Sundell, T. Bergman, P. Roose, M. Heylen, G. Grundmeier, P. Keil, UV-curable polyester acrylate coatings: Barrier properties and ion transport kinetics along polymer/metal interfaces, J. Electrochem. Soc. 158 6 (2011) C185.

[44] S. M. Cambier, R. Posner, G. S. Frankel, Coating and interface degradation of coated steel, Part 1: Field exposure, Electrochim. Acta 133 (2014) 30.

[45] R. Posner, K. Wapner, M. Stratmann, G. Grundmeier, Transport processes of hydrated ions on oxide covered iron and zinc surfaces and interfaces. Part 1: Transport at polymer/oxide/metal interfaces, Electrochim. Acta 54 3 (2009) 891-899.

[46] R. Posner, T. Titz, K. Wapner, M. Stratmann, G. Grundmeier, Transport processes of hydrated ions at polymer/oxide/metal interfaces. Part 2: Transport on oxide covered iron and zinc surfaces, Electrochim. Acta 54 33 (2009) 900-908.

[47] A. Nazarov, D. Thierry, P. Volovitch, K. Ogle, The application of SKP and EIS to study the adsorption of amines on zinc oxide surfaces, Europ. Corros. Congr. Sept. 13-17 2010, Moscow, 3 (2010) 2207.

[48] G. K. van der Wel, O.C.G. Adan, Moisture in organic coatings – a review, Prog. Org. Coat. 37 (1999) 1.

[49] Ö. Özkanat, B. Salgin, M. Rohwerder, J. Mol, J. Wit, H. Terryn, A combined macroscopic adhesion and interfacial bonding study of epoxy coatings on pretreated AA2024-T3, J. Phys. Chem. C 116 (2012) 1805.

[50] C. R. Kemnitz, M. J. Loewen, Amide resonance correlates with a breadth of C-N rotation barriers, J. Am. Soc. 129 (2007) 2521.

3 Interfacial behaviour along the AlMg(Mn)/E-coat interface

3.1 Introduction

During the last decades, the global application of aluminium alloys has increased to the second position in terms of usability behind ferrous alloys due to their good formability and due to the rising importance to lowering vehicle weight [1, 2]. Because of their increased importance, additional attention has to be paid to avoiding corrosion in forms of pitting, selective dissolutions, intermetallic particle etchants, intergranular attacks and exfoliation – especially when covered by an E-coat. However, the technical surface of aluminium alloys tend to be as heterogeneous as the alloy itself with various intermetallic particles (IMPs) and oxides. Great efforts were done to explain the micro-galvanic interactions of the alloys by electrochemical studies [3-5], scanning Kelvin probe force microscopy (SKPFM) approaches [6-8] and Finite element methods (FEM) [9]. A lot of filiform corrosion studies were performed in the macroscopic scale via SKP in a humid oxygen ambience [10-13] but the investigation of the sub-surface flux of polymer-coated aluminium alloys stagnates due to the insulating aluminium oxides. Salgin and co-workers [14] developed a setup with an external electrical field whereby the SKP mapped the potential change along a differently pre-treated aluminium alloy during and after the application of high voltages. They also clarified the surface oxide properties on the aluminium/epoxy interfacial bonding [15]. Both studies focused on an intact aluminium oxide or an intact interfacial bonding but an investigation about an active sub-surface flux, which changes the interfacial bonding, has not been available until now.

The E-coat contains urethane, ether, amine and hydroxyl groups, whereas urethane is nearly comparable to the described amide of Salgin and co-workers [15] regarding the polarity tendencies and the formation of hydrogen boundaries. Both functional groups are sluggish in their reactions, thus, the molecules are resonance-stabilised and react neutrally in aqueous solutions. A potential drop due to protonation or deprotonation is improbable. Mostly, hydrogen boundaries originate between the basic polymer groups and the hydroxyl groups of the aluminium oxide, illustrated in Figure 3.1 on the

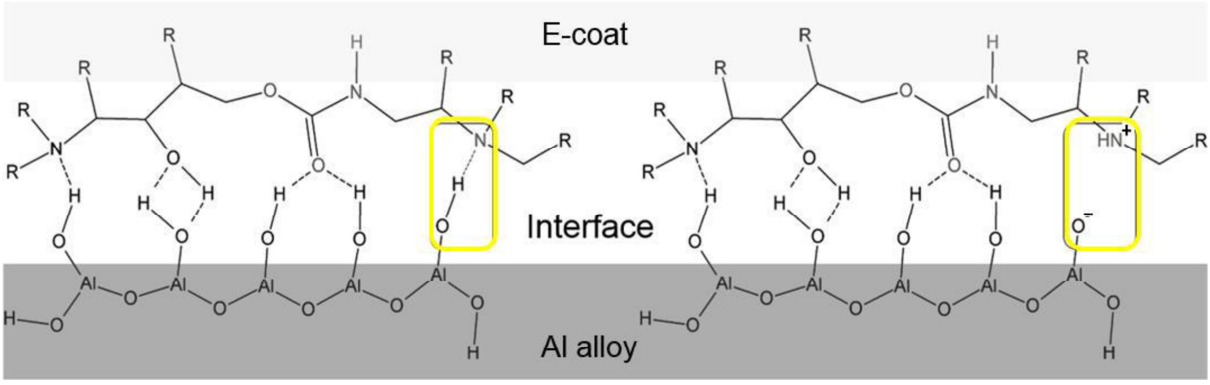

Fig. 3.1 Schematic of the boundary characteristics of the E-coat on aluminium alloy by exceeding (left) and undercutting (right) the IEP of the interfacial dipole

left hand. However, amines can protonate and shift the potential to the cathodic range (see Figure 3.1, right). The amine protonation is promoted in an acidic environment by undercutting the isoelectric point (IEP) of the bonding dipole. This characteristic has the potential to be used to detect the pH-activities underneath the E-coat.

Supported by the results of the last chapter, this work should prove this theory. It focuses on the existence of the sub-surface flux itself and the manner of the interfacial bonds under oxygen-deficient conditions. The pH- and concentration-dependent peculiarities as well as the impact of the intermetallic particles (IMPs) are picked out as central themes in which the interfacial dipole changes are investigated and linked with the Volta potential.

The in situ observation of the interfacial processes is generally challenging. All peel-off, tensile and shear efforts failed to remove the E-coat of the substrates which is why non-destructive methods are the preferred choice. Referring to [15, 16], Volta potential measurements are used to describe the interfacial bonding of the aluminium oxide of an AlMg(Mn) alloy with a 10 µm thick clear E-coat. A confocal Raman with 785 nm laser is coupled on to the SKP chamber to simultaneously analyse the interface in humid oxygen-deficiency and to detect the ions, the structural changes and the interfacial dipole layer via the Volta potential. Such a Raman-SKP setup was firstly described by Posner and co-workers (2012) with a 532 nm laser in dry/humid air and in dry nitrogen [17, 18]. This short-wave laser causes an irreversible potential shift with a partial relaxation while the 785 nm laser shows a reversible potential transient [19]. Additionally, the long-wave laser reduces the fluorescence signal caused by the presence of interfacial water, this advantage allows measurements during an active sub-surface flux. The findings are supported by local infrared spectra based on reflection and cross sections of the interfaces made by focus ion beam (FIB) and analysed by SEM/EDX. All in all, this study clarifies the detectability of the pH-activities underneath the E-coat of aluminium alloys via the Volta potential under humid oxygen-deficient conditions.

3.2 Experimental

3.2.1 Sample preparation

All experiments were carried out using AlMg(Mn) alloy – composition by weight: 0.3 % Si, 0.7 % Fe, 0.2 % Cu, 0.2 % Mn, 0.5-1.1 % Mg, 0.1 % Cr, 0.25 % Zn, 0.15 % other elements, remainder Al – supplied by Chemetall GmbH (Gardabond F (5005A)). The AlMg(Mn) sheets (70 mm x 30 mm) were cleaned by soaking them in toluene, acetone and ethanol, followed by submerging them in the alkaline cleaner Gardoclean® 855/1 (20 g/L, Chemetall GmbH) and stirring them at 500 rpm at 60 °C for 5 min. Then, the sheets were soaked and jetted with distilled water and dried in recirculated air at 40 °C for 120 min. The clear E-coats (Aqua EC3000, Axalta Coating Systems Germany GmbH) were deposited at 32 °C and with an initial voltage of 260 V (Wächter GLT 400/20), the same substrate served as counter electrode. Film thicknesses of 10 µm ±1.0 µm were deposited and were measured with PHYNIX® Surfix after hardening at 180 °C for 20 min. During the deposition of the clear E-coat, an area was masked with a sharp-cut frontier to the coating side to prepare the substrate-deep defect. Further, the self-made reservoir with a size of 15 mm x 20 mm x 15 mm was placed on the coating-free area, as seen in Figure 2.15. Phosphate-based buffers were prepared with a pH=1.6 (conductibility at 25 °C, $\chi(H_2PO_4^-/H_3PO_4)$=23.5 mS/cm), a pH=6.1 ($\chi(HPO_4^{2-}/H_2PO_4^-)$=16.6 mS/cm) and a pH=12.2 ($\chi(PO_4^{3-}/HPO_4^{2-})$=28.5 mS/cm) as stock solutions for 1 M, 0.5 M and 0.1 M KBr or Na_2SO_4 electrolytes, p.a. quality (Sigma-Aldrich). Lastly, the defect reservoirs of the 10 µm thick clear E-coat/AlMg(Mn) samples were filled with the pH- and concentration-varying electrolytes to initialise the water and ion transport along the aluminium interface.

3.2.2 Raman-SKP setup

A height-controlled SKP from Wicinski & Wicinski GbR [20] was coupled with a modular Raman spectrometer of Horiba Jobin Yvon GmbH. As seen in Figure 3.2, the door of the SKP chamber was replaced by a self-made mount for the Raman ConfHead (RB07020601, Horiba Jobin Yvon GmbH). The utilised 785 nm continuous-wave diode laser (Innovative Photonic Solutions) sent the laser light across a

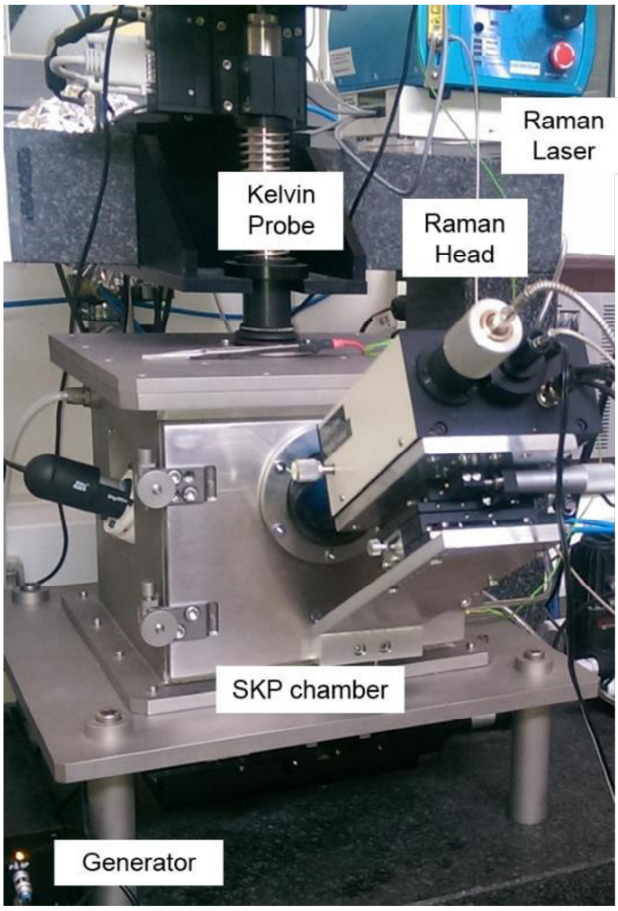

Fig. 3.2 Overview of the Raman-SKP setup

fibre optic cable to the ConfHead. The objective of the ConfHead had to be extended due to its limited focal length of 10.6 mm. The used tube was jacketed by a crease collar to achieve relative moistures up to 92 % and low oxygen concentrations smaller than 3 % in the chamber inside. The laser light with a power of 20-25 mW hit the sample at an angle of 30 ° from surface normal with a beam diameter of 2-3 µm at the focal spot underneath the 120 µm thick Ni/Cr needle of the SKP setup (see Figure 3.3). The ConfHead itself was placed on an yz-table with a driving motor to define the height regulation (z) and to adjust the focal spot at each surface position. The light scattered from the substrate surface was collected by the ConfHead and sent via a fibre optic cable to the spectrometer (iHR 320, Horiba Scientific) equipped with a 1800 groove/mm grating, with a spectral resolution of 0.6 cm^{-1}.

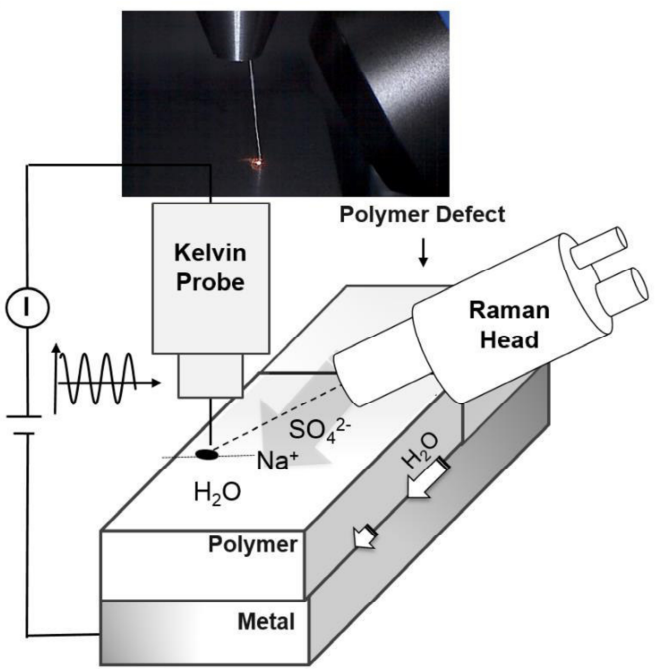

Fig. 3.3 Principle of the Raman-SKP measurement

Preliminary studies showed that a 532 nm laser with a power of 200 mW reduces the E-coat to ashes, illustrated by the large vibrations at 1344 and 1597 cm^{-1}. No laser-induced degradation of the E-coat was observed via a 633 nm laser (max. 17.5 mW) and the used 785 nm laser with a maximal power of 300 mW. However, any laser energy will dry the wet samples which is why a small power of 20-25 mW is applied during the acquisition time of 300 s. The impact a laser power of 20 mW has on the SKP potential during a long-term exposure at a clear E-coat/AlMg(Mn) sample is shown in Figure 3.4. The potential decreases in an amount of 10 mV followed by a rising up to 60 mV after around 18 h. At the pigment E-coat, the potential changes up to 250 mV. A potential drift of 60 mV is already noteworthy. Additionally, the local focusing of the interface is very time-consuming in spite of the driving

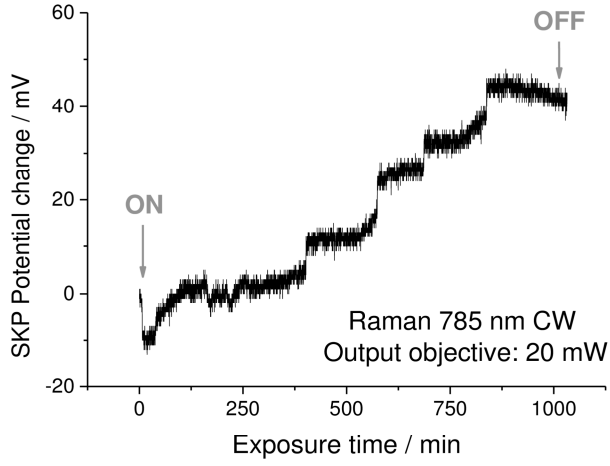

Fig. 3.4 Potential changes during a long-term laser exposure

motor. The low time-resolution of the Raman system paired with the high speed of the Kelvin Probe contradict each other, hence, the Raman spectra were recorded only at certain instances between 100 and 1800 cm^{-1}.

For the potential scans, the samples were directly placed in a humid nitrogen atmosphere (rH=90-92%, O_2≤3 %). The experiments were visualised by an external camera at the left side of the chamber. The SKP needle was calibrated with saturated $CuSO_4$, adjusted to a standard hydrogen electrode (SHE) and potential and height profiles (DH=160 mV, x/y-steps=20 µm) were measured in the humid nitrogen atmosphere.

3.2.3 Attendant analytics

Selected samples were dried at 40 °C in vaccum for 20 min to stop the transport process. Then, the E-coat surface was mapped via EDX with the Hitachi TM 3000 system at 15 kV. Local points of interest were analysed via infrared spectroscopy between 500 and 4000 cm^{-1} (100 scans) in reflection through the E-coat by a Lumos FT-IR-Microscope ECL 10 of Bruker, with a resolution of 4.0 cm^{-1}. Moreover, FIB cuts were operated by the Zeiss Neon® 40 with an ultra-dry X-ray detector from Thermo Fisher Scientific. The SEM images of the FIB cuts were made with an Inlens detector. The samples were sputtered with Au (pH=6) and Au/Pd (80/20) (pH=12) and deposited by the Ga emitter with 2 nA and 30 kV across a length of 30 µm down to the substrate. The first element detection was done in the mapping mode at 20 kV. Finally, the cross sections were mapped again with a decreased acceleration voltage of 5 kV due to the lower interaction volume.

3.3 Results and discussion

This chapter focuses on the existence of the sub-surface flux itself and the manner of the interfacial bonds under oxygen-deficient conditions. It is assumed that the interfacial dipole can vary between pure hydrogen bonds above the IEP of the dipole and protonated amines with anionic charged aluminium oxides at lower pH-values. PH- and concentration-dependent investigations should prove this theory by analysing their changes during the electrolyte transport, as well as the impact of the IMPs of the aluminium alloy. Using the generated data base, the detectability of the pH-activities underneath the E-coat is assessed across the Volta potential changes as a result of the dipole modifications.

3.3.1 Interfacial changes in humid oxygen-deficiency

A survey of the pH-activities at the E-coated AlMg(Mn) interface should clarify the existence of the sub-surface flux and the manner of the interfacial bonds of the dipole as fundamentals of the theory.

KBr-containing phosphate-buffers with pH-values of 2, 6 and 12 are used as defect solutions to change the interfacial conditions. During the experiment, bubbles at the top of the E-coat occur at a pH-value of 2 and 12 more than 5 mm away from the defect. Figure 3.5 shows the SEM images of the dried E-coat surfaces after the long-term exposure in humid nitrogen atmosphere. The corresponding EDX images prove the existence of the buffer components – K, Br and P – in the bubble areas (see Appendix

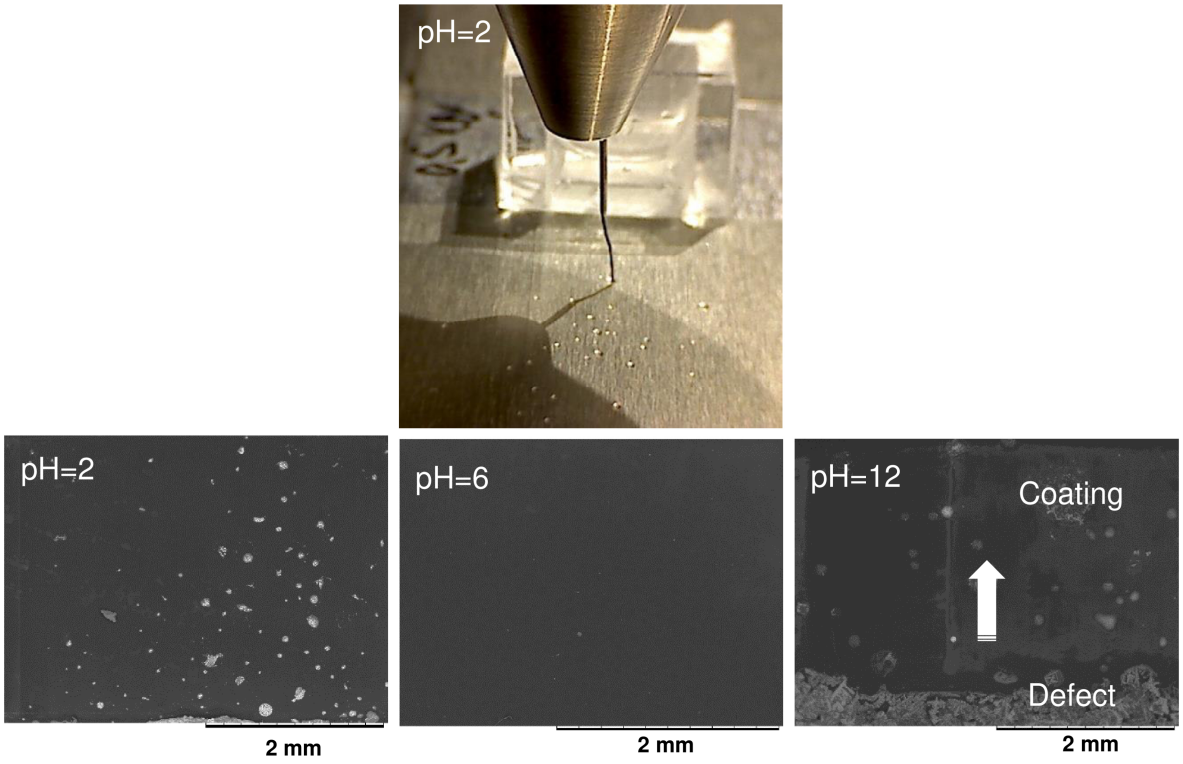

Fig. 3.5 SEMs of the clear E-coated AlMg(Mn) with defect buffers of a pH=12 (PO_4^{3-}/HPO_4^{2-}) plus 1 M KBr, 6 (HPO_4^{2-}/$H_2PO_4^-$) plus 1 M KBr and 2 ($H_2PO_4^-$/H_3PO_4) plus 0.5 M KBr, stored in humid oxygen-deficiency for 650 h, excepting pH=2 with 100 h

A3.1). It impressively illustrates the amphoteric character of the aluminium oxide by hydrogen-induced crevice corrosion. The oxygen-driven corrosion is blocked due to the nitrogen purge. Nonetheless, aggressive media such as pH-buffers of 2 or 12 break down the nominally passive and corrosion-resistant aluminium oxide film at weak locations of the heterogeneous AlMg(Mn) surface as illustrated in Figure 3.6. The buffers enable micro galvanic couplings which cause a dissolution at the anode and hydrogen evolution at the cathode. As a result, transport channels are formed from the AlMg(Mn) surface to the top of the E-coat. These channels transport the infiltrated electrolytes out of the layer. Aluminium is well-known for its localised attacks in an oxygen-rich atmosphere. However, the results prove a pH-dependent sub-surface flux at the E-coat/AlMg(Mn) interface and an ion transport through the E-coat in parallel to the interface in humid oxygen deficiency.

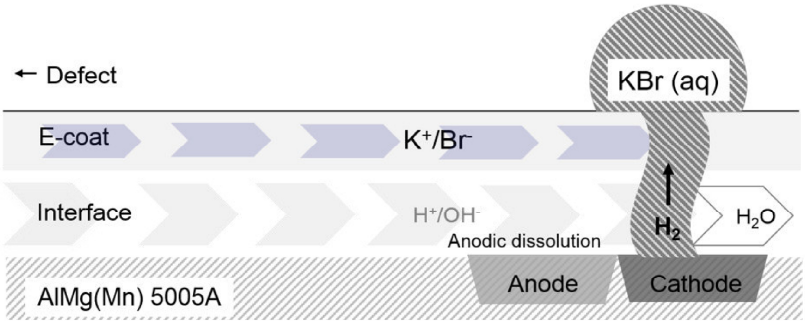

Fig. 3.6 Transport model based on the observations at the AlMg(Mn)E-coat samples referred to Fig. 3.5 in humid oxygen-deficiency

The interfacial bonds can be verified by using XPS, but all peel-off, tensile and shear efforts failed to remove the E-coat of the substrate, which is why XPS was not possible. EDX-mappings of the cross sections are a poor choice due to the overlapping of the X-ray production volumes in the interfacial nanoscale [21]. However, local points of the bubble and the closed E-coat area were analysed by infrared spectroscopy in reflection to record structure information from the E-coat bulk to the AlMg(Mn) surface. The spectra are given in Figure 3.7. The clear E-coat is represented by the urethane stretching vibrations at 1740-1690 cm^{-1} (O-CO-N), the amine bending at 1580-1490 cm^{-1} (NH) and 1650-1560 cm^{-1} (NH_2), the stretching vibrations of C-OH at 1150-1040 cm^{-1} as well as the alkyl groups at 2990-2860 cm^{-1} and hydroxyl/amine vibrations in hydrogen bonds between 3600 cm^{-1} and 3200 cm^{-1}. Further, aromatic CH bonds at 3035 cm^{-1}, 767 cm^{-1}/830 cm^{-1}, =C-O-C stretching vibrations at 1185 cm^{-1} and C-O-C bending at 1257 cm^{-1} characterise the clear E-coat in the fingerprint region [22]. The vibration in the zone of the phosphates shifts from 1038 cm^{-1} at pH=12, 1046 cm^{-1} at pH=6 to 1053 cm^{-1} at pH=2. These vibrations show the used buffer solutions in the E-coat bulk and/or at the AlMg(Mn) interface. By comparing the bubble and the closed area, the spectra of the bubbles show larger hydroxyl vibrations (3600-3200 cm^{-1}), which have a slight shift to lower wavenumbers. In spite of the drying, these changes hint at higher and loosely bonded water content [23, 24]. Moreover, protonated

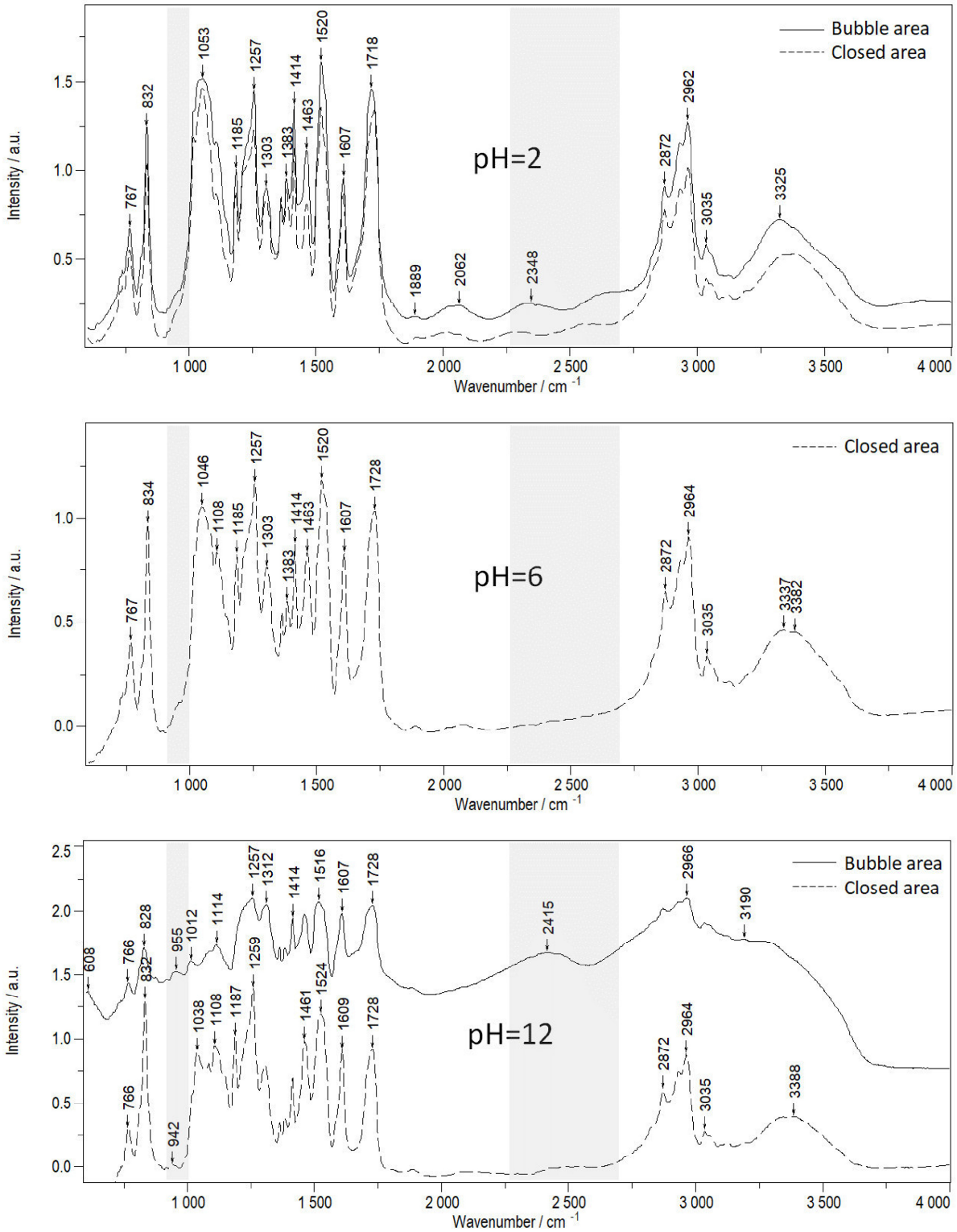

Fig. 3.7 IR-Reflection spectra of the clear E-coat after the KBr-buffer transport; average of min. three spots of the bubble/intact area, spectral resolution: 4 cm^{-1}

amines are visible at 2700-2250 cm^{-1} [22] in the bubble areas at pH=12 and 2 as well as in the closed area at pH=2. An anodic attack resulting in the bubble will continue to propagate into the alloy due to acidification of the solution. When the dissolved metal ions migrate away from this pit, the aluminium alloy precipitates as a membrane, further isolating and intensifying local acidity [1]. Due to this, the bubble areas show an increased amount of protonated amines. Using a buffer of pH=2, protonated amines are generally present. Beyond, the spectra of the alkaline-produced bubbles show strongly reduced vibrations lower than 1200 cm^{-1}, which indicate local disbondments. Interestingly, Al-O stretching vibrations at 950 cm^{-1} [24-26] are found everywhere when using the pH-buffer of 12. These stretching vibrations describe the barrier aluminium oxide [27, 28] and are not visible at pH-values of 6 or 2, which means that the interface termination of the aluminium oxide changes between a prevailing pH-value of 6 and 12. Theoretically, the IEP of the interfacial dipole has to be the mean of the IEP of the aluminium oxide (7-10) [14] and the IEP of the amines (8-10) [29] and this is in line with the results.

The infrared spectra measured in reflection provide information about the sum of the bulk material and the interface, while the confocal Raman spectroscopy allows the investigation at the wet interface under a humid nitrogen-purge. The Raman spectra is only based on the symmetric stretching and bending [30], which are generally a small number of signals compared to the infrared spectra including the antisymmetric stretching and bending vibrations. However, the scissoring (1650-1590 cm^{-1}) and the wagging vibrations of the primary amine (around 800 cm^{-1}) are Raman-active. The protonation and the hydrogen bonding of the amine are thus detectable around the vibration shifts. These shifts depend on the bonding energy of the amine, while the ionic bonding is generally energy-rich with 600 to 1000 kJ/mol, the hydrogen bonding is energy-low with <50 kJ/mol [31].

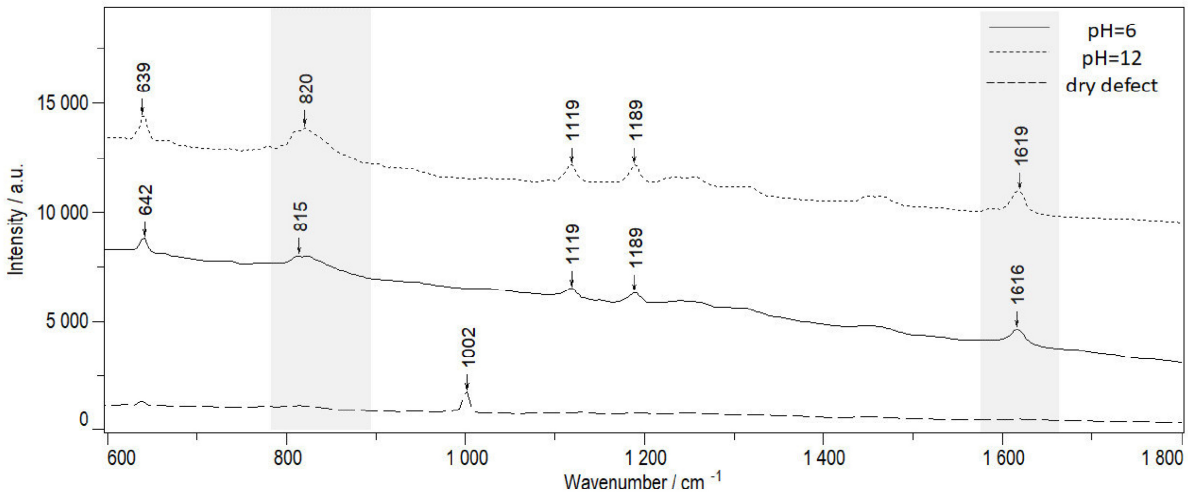

Fig. 3.8 Confocal Raman spectra of the dry defect and the clear E-coated AlMg(Mn) with substrate-deep defect filled with pH=6 ($HPO_4^{2-}/H_2PO_4^-$) and pH=12 buffers (PO_4^{3-}/HPO_4^{2-}) and added with 1 M KBr after 650 h stored in humid oxygen deficiency; spectral resolution: 0.6 cm^{-1}

Figure 3.8 shows the Raman results at the clear E-coated AlMg(Mn) between 600 and 1800 cm^{-1} for the pH-value of 6 and 12. Note that further vibrations lower 600 cm^{-1} were invisible for the used 785 nm layer due to its low energy compared to 532 nm or 633 nm laser. Evidently, the wide wagging and the scissoring vibrations shift slightly with 5 and 3 cm^{-1} to lower wavenumbers at a pH of 6. These results dominate across the total interfaces. The spectra were not manipulated by baseline corrections and the peaks were mathematically identified by the Gauß-Lorentz distribution. Due to a spectral resolution of 0.6 cm^{-1}, the measured shifts are proper and the primary amine protonates by undercutting the IEP of the interfacial dipole. Besides these effects, the phosphate vibrations are absent at around 1000 cm^{-1}, phosphate precipitations at the interface can be excluded but the spectra are affected by the fluorescence due to the wet measuring conditions. As mentioned before, the electrolyte transport can occur along the interface and through the E-coat volume parallel to the interface. At the interface, no phosphate ions were found even though an anodic-driven transport would promote phosphate movements. The phosphate vibration could be covered by the fluorescence of water, but then phosphate would have to be found at the dry interface. The self-evident explanation is that there is simply no phosphate transport along the interface. In this case, the detected amine protonation is supported by the electrolyte ingress through the E-coat parallel to the interface, as summarised in Figure 3.9.

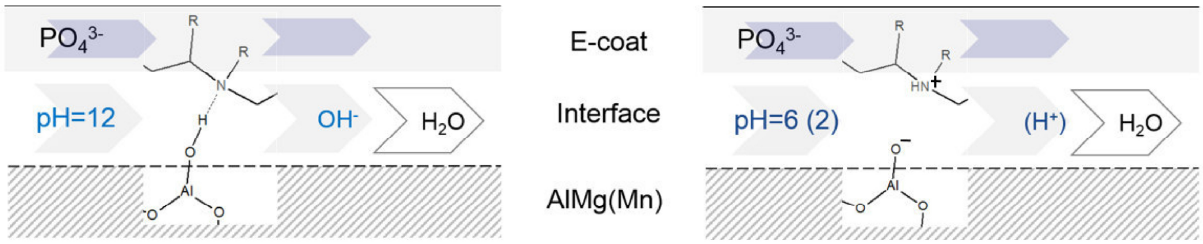

Fig. 3.9 Transport model including the interfacial bonding at the AlMg(Mn)/E-coat samples in humid oxygen-deficiency

In brief, the main flux at the AlMg(Mn) occurs in parallel to the interface through the E-coat while the flux causes a pH-change at the interface. At pH-values of 6 and 2, the interfacial amine groups protonate. Conversely, at a pH-value of 12, the termination of the aluminium oxide changes and the amine bond energy decreases which hints at interfacial hydrogen bonds.

3.3.2 PH- and concentration-dependent sub-surface flux

The systematic change of the pH-value and the salt concentration should describe and verify the dependency of the interfacial bonding on the Volta potential and identify the role of the IMPs of the AlMg(Mn).

As seen in Figure 3.5 before, the AlMg(Mn) interface acidifies under hydrogen evolution with a pH-buffer of 2. The corresponding SKP findings are shown in Figure 3.10 with 0.1 M, 0.5 M and 1.0 M KBr.

The potentials are obviously flatten across the total line-scans and are very low up to -1.5 V. A concentration-dependent trend is not reflected in the data. The low potentials exclude the adsorption of H^+ which would lead to the formation of a cationic charge ($AlOH_2^+$); this is why an amine protonation has to be favoured. The potential levelling further excludes galvanic cells underneath the E-coat at the heterogeneous AlMg(Mn) surface. However, Mg_2Si particles are found underneath the bubbles in the material inside (see Figure 3.11) and the magnesium dissolves as Mg^{2+} with hydrogen evolution in acidic solution. The selective magnesium dealloying is independent of the present potentials [5] and explains the smooth potentials. Moreover, a cathodic underminining is observed in parallel to the defect breadth against the rolling direction after around 100 h, as illustrated in Figure 3.12. The potential changes from -0.7 V to -1.5 V. The great potential drop of 0.8 V hints at a high driving force which promotes the ion migration.

At neutral conditions, the aluminium is generally passive with aresistant oxide film according to the Pourbaix diagram [32]. The Volta potentials are described by constant behaviour at -0.6 V up to 0.1 V, as seen in Appendix A3.2. No concentration effects are observed.

Compared to the acidic and neutral series, the alkaline series show potential increases which are steeper with rising concentrations and stabilise at around 0.4 V. The details are given in Figure 3.13.

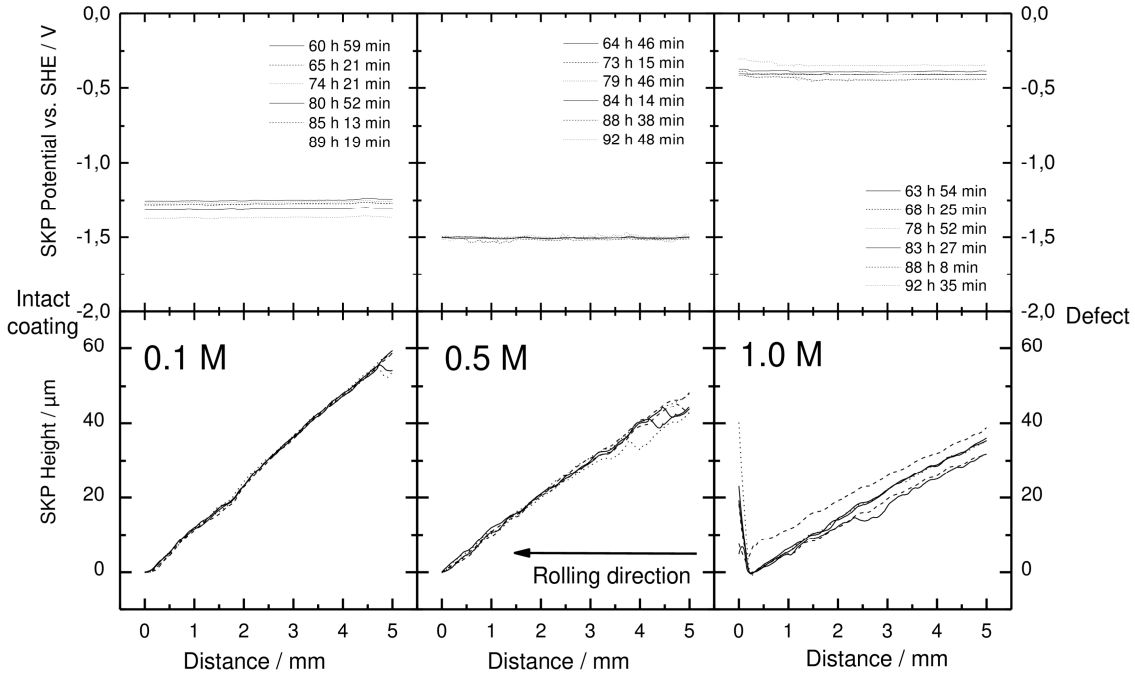

Fig. 3.10 Potential and height scans of the AlMg(Mn) alloy covered with a 10 µm thick E-coat between 60 h and 93 h after the addition of a buffer pH=2 to a substrate-deep defect in humid N_2-atmosphere, rH=90-92%, $O_2 \leq 3$ %

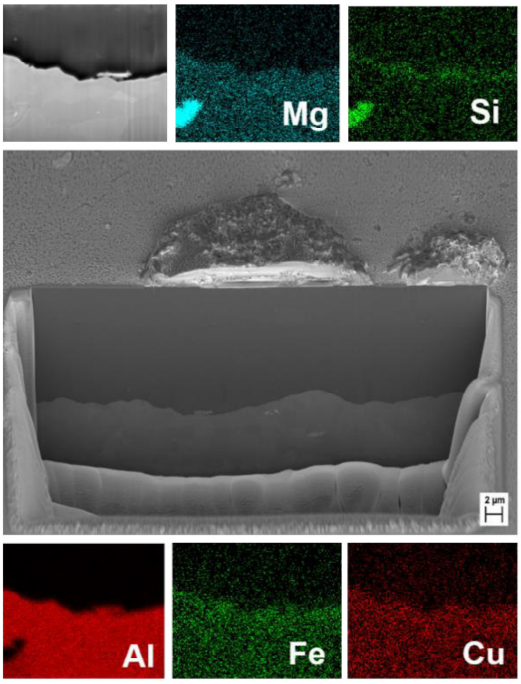

Fig. 3.11 FIB cut at a bubble caused by the buffer pH=2 under humid oxygen-deficient conditions

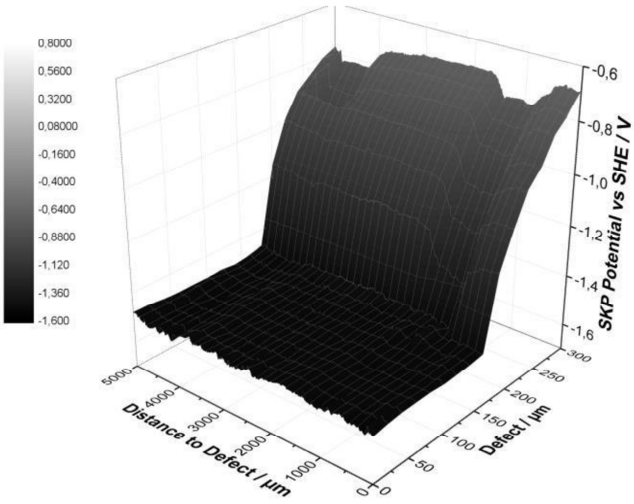

Fig. 3.12 Cathodic undermining at the E-coat/AlMg(Mn) interface in parallel to the defect breadth (pH=2, 0.5 M KBr)/against the rolling direction after ~100 h under humid N_2-purge

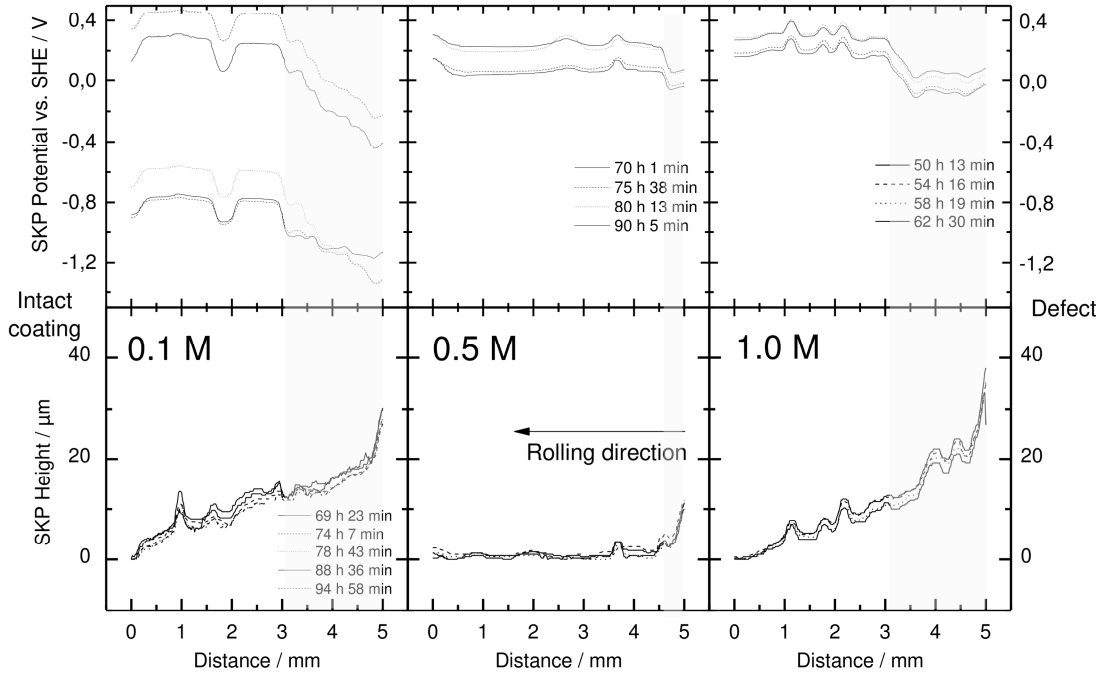

Fig. 3.13 Potential and height scans of the AlMg(Mn) alloy covered with 10 µm thick E-coat between 50 h and 95 h after the buffer addition pH=12, rH=90-92 %, O_2≤3 %

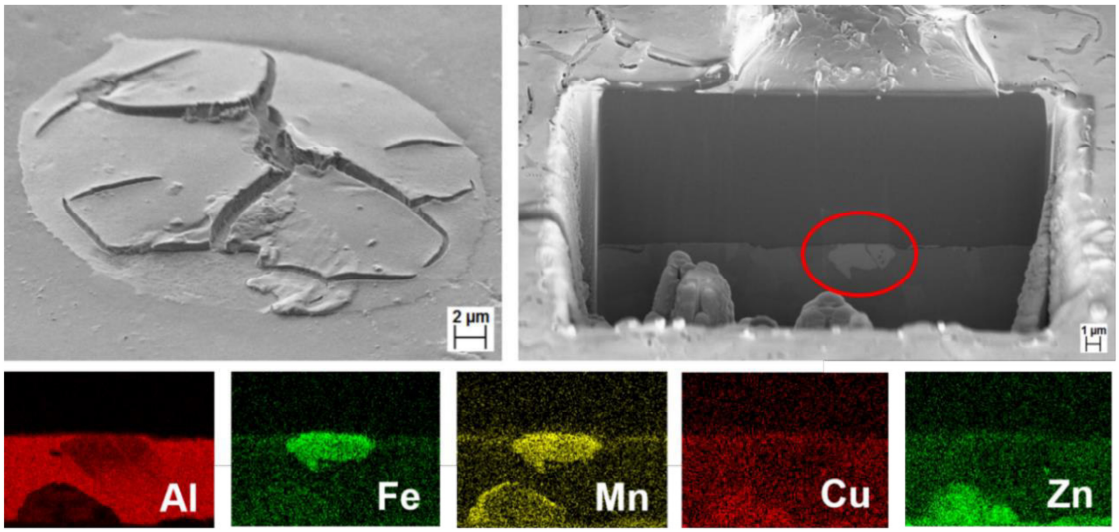

Fig. 3.14 FIB cut at a bubble caused by the buffer pH=12 under humid oxygen-deficient conditions

The line scans are further characterised by cathodic potential decreases in the defect area but these underminings have an independent progress of the defect concentration. The height profiles display irregularities while the correspondingly local potentials slightly increase or decrease from the potential baseline. An anionic surface charge ($Al(OH)_2^-$), via OH^- adsorption, and an amine protonation cannot be favoured due to the cathodic potentials. The amines seem to build hydrogen bonds due to their free electron pairs. The hydrogen bonds cause a neutral charging of the aluminium oxide which will increase its Galvani potential and the Volta potential. Further, the potential and height irregularities are placed at the observed bubble areas and seem to express the micro-galvanic interactions and their corrosion products. The FIB cut through the bubble (in Figure 3.14) prove that the causes of the hydrogen evolution are the Al6MnFe particles at the top of the AlMg(Mn) surface. The cathodic undermining near the defect express the weakness/break down of the aluminium oxide film. Interestingly, the alkaline undermining is oriented in the rolling direction (see Figure 3.15) while the acidic

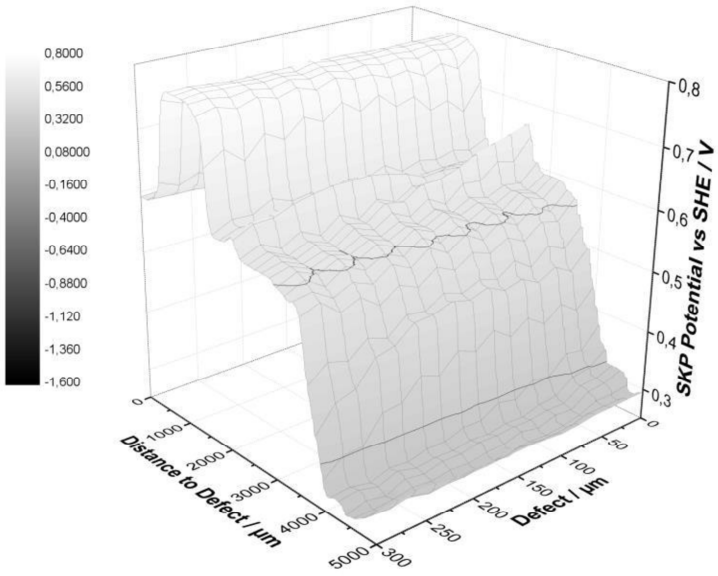

Fig. 3.15 Cathodic undermining at the E-coat/AlMg(Mn) interface with progress away from the defect (pH=12, 1 M Na_2SO_4)/in the rolling direction under humid N_2-purge after ~250 h

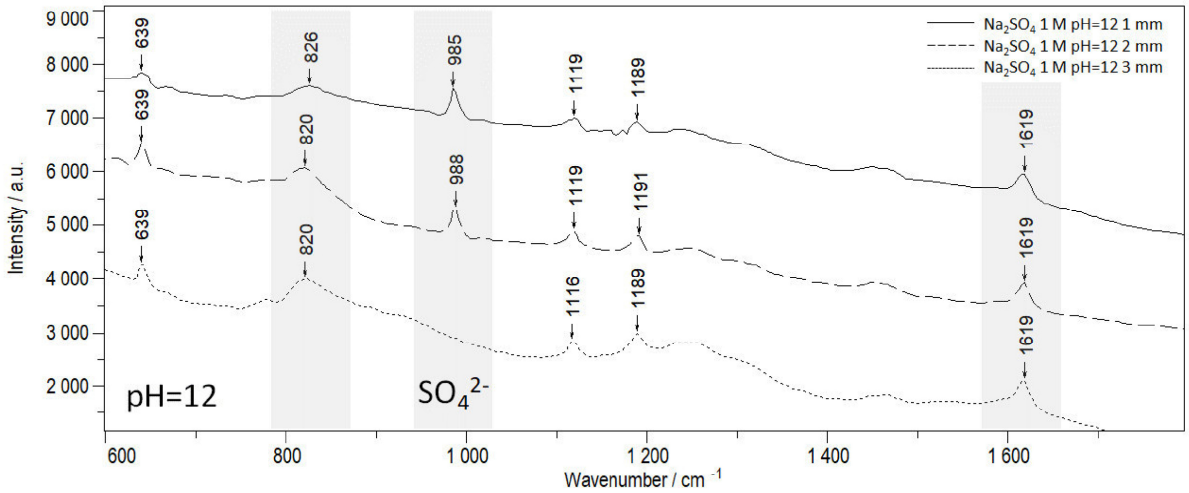

Fig. 3.16 Confocal Raman spectra of the clear E-coated AlMg(Mn) with substrate-deep defect filled with pH=12 (PO_4^{3-}/HPO_4^{2-}) and added with 1 M Na_2SO_4 after ~250 h stored in humid oxygen deficiency; spectral resolution: 0.6 cm^{-1}

undermining shows the progress against the rolling direction. AlMg(Mn) is hot-rolled while hot-rolling deforms the original cast structure and the as-cast grains are elongated in the rolling direction [1]. This fact implies an alkaline attack along the as-cast grains in the form of exfoliation. Besides, the potential difference of 0.3 V between the anodic and the cathodic area is low in comparison to the acidic potential change of 0.8 V. Consequently, the acidic-induced migration is many times faster than the alkaline-induced one. This ion migration takes place directly at the aluminium oxide, as proven at pH=12 in Figure 3.16. The galvanic coupling (or selective Mg de-alloying at pH=2) seem to weaken the oxide film until it breaks down. Then, the ions reach the interface and promote the progressive de-adhesion and corrosion (see Figure 3.17). As a result, the transport at the insulating aluminium oxide is driven by two transport mechanisms, through the polymer layer in parallel to the interface and at the interface itself.

An overview of the results at different pH-values shows that there is a stable potential at pH-values of 2 and 6, after which the potential increases until it stabilises at a pH-value of 12. This cathodic shift stabilises faster with increased ion concentration but further concentration dependencies are not

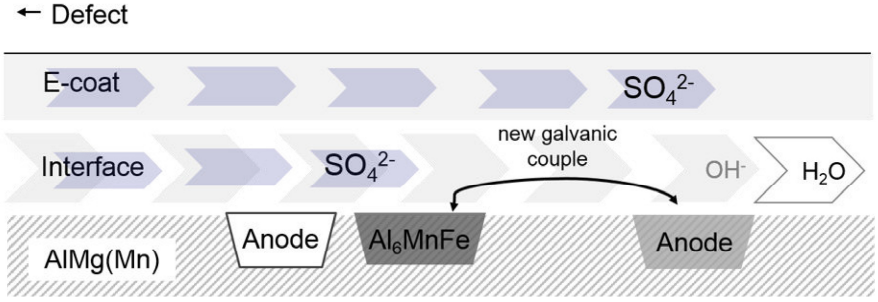

Fig. 3.17 Transport model after the break down of the aluminium oxide at pH=12

observed. Additionally, the acidic Mg dealloying and the alkaline galvanic coupling at the Al_6MnFe particles weaker the aluminium oxide until it breaks down which directly promote a second ion transport at the interface.

3.3.3 PH-detectability via the Volta potential in humid oxygen deficiency

Based on the generated data, the measurability of the pH-activities underneath the E-coat should be assessed across the Volta potential changes. Therefore, Figure 3.18 shows the Volta potentials of the intact areas after the potential stabilisation. The potentials are averaged up to the observation time of 93 h after the addition of the buffers with 0.1 M, 0.5 M and 1.0 M KBr.

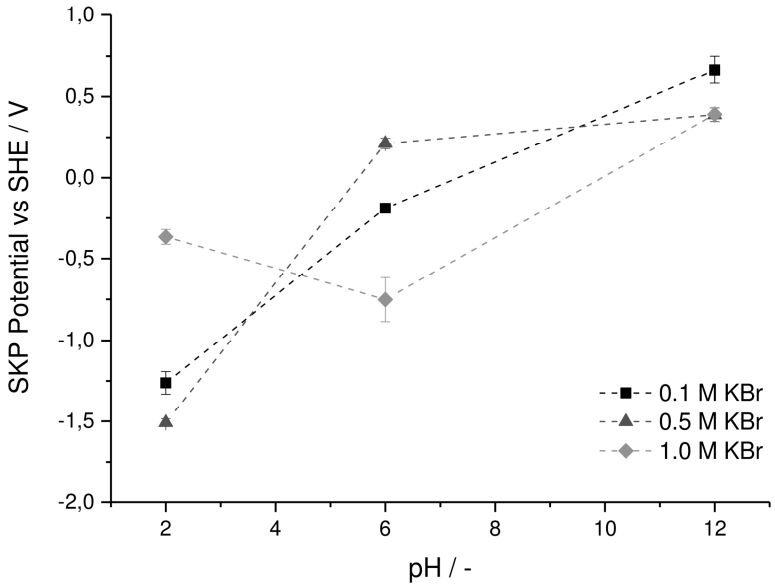

Fig. 3.18 PH- and concentration-dependent Volta potentials 2500 µm away from the defect, extracted after potential stabilisation and averaged up to the observation time of 93 h after the addition of the buffers

The diagram illustrates a large potential differences up to 2.0 V, after which the Volta potential shows a linear gain with the increase of the pH-value. More negative charge carriers have to rest at the aluminium oxide at low potentials while the degree of protonated dipoles increases with the decrease of the pH-value. However, the number of outliers increases with higher KBr-concentrations, which decreases the solubility and promotes the tendency to precipitations of $AlBr_3$ (or $AlPO_4$). Such side effects seem to affect the Volta potential. The general trend is an agreement with the theory of the ad-atom charge of Gross et al. [33] and Salgin's finding, where alkaline-produced oxide exhibits higher potentials with respect to the acidic oxide [14]. However, the potentials are affected by micro-galvanic cells and underminings which is why the local potential resolution – present resolution: 160 µm – has to be increased e.g. via SKPFM to detect the pH-activities around the IMPs.

3.4 Conclusion

This Raman-SKP study focuses on the changes of the interfacial bonds at the AlMg(Mn)/E-coat interface due to a sub-surface flux in humid oxygen deficiency. By the initiation of the flux at the AlMg(Mn) substrate, the main flux occurs in parallel to the interface through the E-coat. Media such as pH-buffers of 2 and 12 cause a hydrogen-induced crevice corrosion, which illustrates the pH-changes at the interface. At a pH-value of 12, the hydrogen evolution is caused by a galvanic coupling of the Al_6MnFe particles at the top of the AlMg(Mn) substrate. The interface at neutral conditions is displayed by a resistant oxide of the AlMg(Mn). At a pH-value of 2, the selective Mg dealloying occurs under hydrogen evolution at the Mg_2Si particles in the material inside, independently of the present potential. Moreover, the interfacial amine groups protonate at pH-values of 6 and 2 while the termination of the aluminium oxide change at a pH-value of 12, shown by Al-O stretching vibrations at 950 cm^{-1}. The Volta potential, which indirectly represents the charge carriers of the interfacial dipole, shows stable potentials at pH-values of 2 and 6, while the potential increases until it stabilises at a pH-value of 12. This cathodic shift stabilises faster with increased ion concentration but further concentration dependencies are not observed. In general, the Volta potentials show a linear gain from -1.7 V up to 0.8 V with the increase of the pH-value. More functional groups change their orientation at the E-coat/AlMg(Mn) interface and the Volta potential increases due to the change of ionic bonds to hydrogen bonds between the aluminium oxide and the amine groups. This general effect, the dependency of the interfacial pH-value with the Volta potential, can be used to detect the pH-activities at the epoxy-covered aluminium oxide.

References

[1] N. Birbilis, T. Muster, R. G. Buchheit, Corrosion of aluminium alloys. Corrosion mechanisms in theory and practice, Ed. P. Marcus, 3rd Edition, CRC Press, London (2011) 705.

[2] O. Engler, E. Brünger, Microstructure and texture of aluminium alloys for autobody applications, Matériaux & Techiques 5-6 (2002) 71.

[3] J. A. Lyndon, R. K. Gupta, M. A. Gibson, N. Birbilis, Electrochemical behaviour of the ß-phase intermetallic (Mg_2Al_3) as a function of pH as relevant to corrosion of aluminium-magnesium alloys, Corros. Sci. 70 (2013) 290.

[4] N. Birbilis, R. G. Buchheit, Electrochemical characteristics of intermetallic phases in aluminium alloys: an experimental survey and discussion, J. Electrochem. Soc. 152 (2005) B140.

[5] E. Linardi, R. Haddad, L. Lanzani, Stability analysis of the Mg_2Si phase in AA 6061 aluminium alloy, 11th International congress on metallurgy & materials SAM/CONAMET 2011, Rosario, Argentina.

[6] C. Senöz, S. Borodin, M. Stratmann, M. Rohwerder, In situ detection of differences in the electrochemical activity of Al_2Cu IMPs and investigation of their effect on FFC by scanning Kelvin probe force microscopy, Corros. Sci. 58 (2012) 307.

[7] C. Senöz, M. Rohwerder, Scanning Kelvin probe force microscopy for the in situ observation of the direct interaction between active head and intermetallic particles in filiform corrosion on aluminium alloy, Electrochim. Acta 56 (2011) 9588.

[8] P. Leblanc, G. S. Frankel, A study of corrosion and pitting initiation of AA2024-T3 using atomic force microscopy, J. Electrochem. Soc. 149 6 (2002) B239.

[9] L. Yin, Y. Jin, C. Leygraf, J. Pan, A FEM model for investigation of micro-galvanic corrosion of Al alloys and effects of deposition of corrosion products, Electrochim. Acta 192 (2016) 310.

[10] G. Williams, H. N. McMurray, D. Hayman, P.C. Morgan, Time-lapse potentiometric imaging of active filiform corrosion using a scanning Kelvin probe technique, PhysChemComm 6 (2001) 1.

[11] G. Williams, H. N. McMurray, Inhibition of filiform corrosion on organic-coated AA2024-T3 by smart-release cation and anion-exchange pigments, Electrochim. Acta 69 (2012) 287.

[12] A.-P. Romano, M.-G. Olivier, A. Nazarov, D. Thierry, Influence of crosslinking density of a cataphoretic coating on initiation and propagation of filiform corrosion of AA6016, Prog. Org. Coat. 66 (2009) 173.

[13] A. Nazarov, A.-P. Romano, M. Fedel, F. Deflorian, D. Thierry, M.-G. Olivier, Filiform corrosion of electrocoated aluminium alloy: role of surface pretreatment, Corros. Sci. 65 (2012) 187.

[14] B. Salgin, R. F. Hamou, M. Rohwerder, Monitoring surface ion mobility on aluminium oxide: effect of chemical pre-treatments, Electrochim. Acta 110 (2013) 526.

[15] B. Salgin, Ö. Özkanat, J. Mol, H. Terryn, M. Rohwerder, Role of surface oxide properties on the aluminium/epoxy interfacial bonding, J. Phys. Chem. C 117 (2013) 4480.

[16] M. Rohwerder: Scanning Kelvin Probe and Scanning Kelvin Probe Force Microscopy and their application in corrosion science. In: Corrosion science and technology: Mechanism, mitigation and monitoring, Eds. U. K. Mudali, B. Raj, Taylor & Francis, London (2008) 468.

[17] R. Posner, A. M. Jubb, G. S. Frankel, M. Stratmann, H. C. Allen, A simultaneous Kelvin Probe and Raman spectroscopy approach for in situ surface and interface analysis, Electrochim. Acta 76 (2012) 34.

[18] R. Posner, A. M. Jubb, G. S. Frankel, M. Stratmann, H. C. Allen, Simultaneous in situ Kelvin probe and Raman spectroscopy analysis of electrode potentials and molecular structures at polymer covered salt layers on steel, Electrochim. Acta 83 (2012) 327.

[19] D. Verreault, A. M. Jubb, G. S. Frankel, M. Stratmann, H. C. Allen, R. Posner, Laser effects on Volta potential transients recorded by a Kelvin probe, ECS Electrochem. Letters 2 5 (2013) H19.

[20] K. Wapner, B. Schönberger, M. Stratmann, G. Grundmeier, Height-regulating scanning Kelvin probe for simultaneous measurement of surface topology and electrode potentials at buried interfaces, J. Electrochem. Soc. 152 (2005) E114.

[21] R. Castaing, Application of electron probes to local chemical and crystallographic analysis, PhD Thesis, University of Paris, 1951.

[22] M. Hesse, H. Meier, B. Zeeh, Spektroskopische Methoden in der organischen Chemie, 8th Edition, Thieme, Stuttgart (2012) 39.

[23] P. Sutandar, D. J. Ahn, E. I. Franses, FTIR ATR analysis for microstructure and water uptake in poly(methyl methacrylate) spin cast and Langmuir-Blodgett thin films, Macromolecules 27 (1994) 7316.

[24] M. Öhman, D. Persson, C. Leygraf, In-situ ATR-FTIR studies of the aluminium/polymer interface upon exposure to water and electrolyte, Prog. Org. Coat. 57 (2006) 78.

[25] V. D. Farmer, The infrared spectra of minerals, Mineralogical Society Monograph, Mineralogical Society, London (1974).

[26] A. J. Maeland, R. Rittenhouse, W. Lahar, P. V. Romano, Infrared reflection-absorption spectra of anodic oxide films on aluminium, Thin Solid Films 21 (1974) 67.

[27] R. W. Hannah, An optical accessory for obtaining the infrared spectra of very thin films, Appl. Spectroscopy, 17 (1963) 11.

[28] T. Takamura, H. Kihara-Morishita, U. Moriyama, Infrared reflectance spectra of barrier-type anodic oxide films formed on pure aluminium, Thin Solid Films, 6 (1970) R17.

[29] A. Nazarov, D. Thierry, P. Volovitch, K. Ogle, The application of SKP and EIS to study the adsorption of amines on zinc oxide surfaces, Europ. Corros. Congr. Sept. 13-17 2010, Moscow, 3 (2010) 2207.

[30] P. Larkin, Infrared and Raman Spectroscopy – Principles and spectral interpretation, Elsevier, Amsterdam, 2011.

[31] J. Gähde, Adhesion characteristics of polyurethanes on steel, Farben & Lacke 101 (1995) 689.

[32] M. Pourbaix, Atlas d'Équilibres Elektrochimiques, Gauthiar-Villar & Cie, Paris, 1963.

[33] L. Gross, F. Mohn, P. Liljeroth, J. Repp, F. J. Giessibl, G. Meyer, Measuring the charge state of an adatom with noncontact atomic force microscopy, Science 324 (2009) 1428.

3A Excursion: PH-behaviour of the E-coat interface with chromate-free conversion layers

3A.1 Introduction

Corrosion and adhesion protection is the central issue of the conversion layers in the transport industry. However, typical phosphate-based conversion layers have a weak performance with aluminium alloys, while the successful chromate systems are restricted by environmental policies – e.g. the well-known "End of Life Vehicles Directive" of the European Community [1]. Zirconium, vanadium, titanium or silane-based compounds with or without organic or inorganic polymerisation are used as environmentally friendly solutions [1-3]. Most of these technologies function similarly to create a surface conversion coating, by means of fluoro-based chemistry. H_2ZrF_6 and H_2TiF_6 are common systems. In principle, a fluoride etching dissolves the surface of the aluminium alloy under hydrogen evolution and the solvated aluminium ions build a complex with the fluoride. The interface alkalises with time due to the water decomposition, which causes a subsequent precipitation of Zr/Ti oxyhydroxides [2-4]. The reactions are summarised in the following equation:

$$Al^{3+} + Zr^{4+} + F^- + 4\ H_2O \longrightarrow Al(OOH)Zr(OOH)F + 6\ H^+ \qquad (3A.1)$$

The structure of the resulting conversion layer is disputed in the literature [2, 3, 5]. A consent may exists about a two layer formation which is illustrated in Figure 3A.1 and confirmed by the GDOES/XPS-AES profile results [6-8]. The strong electronegativity and the free electron pairs of the fluorine combined the hydroxyl groups promote several hydrogen bonds with the top coat. The deposition of the conversion is driven by the prevailing pH-value at the interface which is why cathodic IMPs with their alkaline surrounding cause a favourable precipitation of the Zr/Ti oxyhydroxides as an island growth [2-4]. Additionally, self-assemblies (SAs) can be added to the conversion coating. For aluminium alloys, these SAs are mainly based on phosphonic acids [9], which condensate with the hydroxyl groups of the conversion network (R^1=Zr/Ti/Al) [9], as seen in (3A.2), and are often linked with organic compounds R such as the diethylenetriamine penta(methylene phosphonic acid) (DETPMPA) or the 3-phenylpropen phosphonic acid (PPPA) [10].

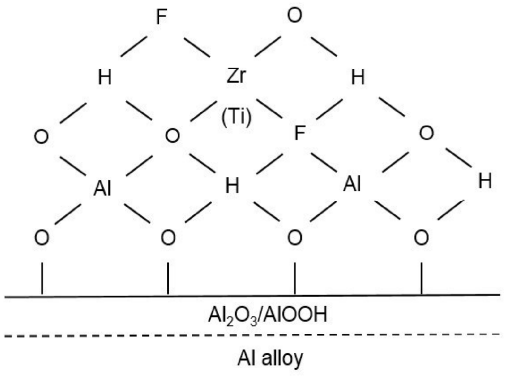

Fig. 3A.1 Model sequence of the Zr/Ti conversion coating on aluminium alloy; all bonds are not illustrated.

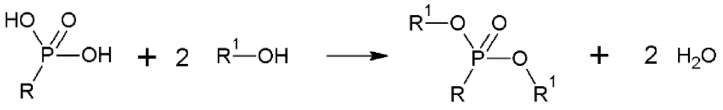

(3.2)

For an improved functionality, the organic side chain of the phosphonic acids can further cross-linked or polymeric acids can be directly blended into the bath. Some examples are acrylic acids, Mannich product of polyalkenyl phenol [10], polyhydroxy phenol (tannin) [10], acryl amide [3] and several more [10-13].

Recent research is focused on the protection of multi metal interfaces using different strategies [7, 14-17]. One approach is the improvement of the conversion layers by the addition of copper particles [7, 16-17], which covers the IMPs and improves the homogeneity [6] and the film growth of the subsequent Zr/Ti layers. Other groups improve the organic coating at the top to avoid or eliminate the conversion step. Smart-release cation and anion-exchange pigments incorporated within an organic polymer binder [15] are promising as inhibitors and sequesters of aggressive ions. On the other hand, chromate-free silane-based primers can be an alternative due to their strong adhesion properties [18, 19]. However, the performance of the aluminium interface is always determined by the acid-base interactions underneath the top coat – the coupling of IMPs or grains with hydroxyl groups of the conversion layer or the aluminium oxide, as well as the bonds of self-assemblies or polymers.

In the automotive section, chromate-free conversion layers are actually usual as an underground for the E-coat which is why the scope of this chapter leans on the pH-activities underneath the clear E-coat at the AlMg(Mn) with conversion films. Ti- and Zr-based conversion coatings were investigated with the addition of a pickling inhibitor, a self-assembly and a polymer. The interfacial pH-values are changed and the corresponding Volta potentials are measured under a humid nitrogen purge. The merit of the results is assessed by means of the structural changes, the corrosion and de-adhesion processes.

3A.2 Experimental

3A.2.1 Deposition and analysis of chromate-free conversion layers

AlMg(Mn) sheets (70 mm x 30 mm) – composition by weight: 0.3 % Si, 0.7 % Fe, 0.2 % Cu, 0.2 % Mn, 0.5-1.1 % Mg, 0.1 % Cr, 0.25 % Zn, 0.15 % other elements, remainder Al, Chemetall GmbH (Gardabond F (5005A)) – were used as substrates. The pre-treatment started by submerging the sheets in an alkaline cleaner for 5 min at 60 °C. After rinsing with water, the samples were deoxidised for 60 s at 30 °C and rinsed again with de-ionised water. Then, three common passivation baths were applied by Henkel, their products are listed in A3.3. The *bath A* is based on H_2TiF_6 with a pickling inhibitor to block the hydrogen evolution. The other baths contain H_2ZrF_6 and are improved by a self-assembly (*bath B*) and by the addition of a polymer (*bath C*). The chosen Ti- and Zr-based conversion coatings were deposit for 60 s at 30 °C and finalised by rinsing and drying.

The surface topography and the coverage of the conversion layers were analysed by the Zeiss Neon® 40 system with a SE2 detector. The electrochemical performance was measured via potential-dynamic curves and impedance spectra, which were recorded on the Zennium workstation (Zahner-Elektrik GmbH) with a three-electrode arrangement. For this purpose, the pre-treated AlMg(Mn) sheets were masked with an electrical and chemical resistant lacquer except for a defined analysis surface. A calomel electrode was the reference and a Pt sheet acted as a counter electrode. A neutral buffer solution, pH(HPO_4^{2-}/$H_2PO_4^-$)=5.7 - χ(HPO_4^{2-}/$H_2PO_4^-$)=2.78 mS/cm, p.a. quality chemicals (Sigma-Aldrich), completed the setup. The current-potential curves were recorded with a scan rate of 1 mV/s (5 mV/s) at 25 °C. For the impedance spectra, the sample surface (12.6 cm^2) were polarised at 1 V and perturbed with an amplitude of 20 mV. With a start frequency of 1 kHz, the run was continued up to 100 kHz and returned to 100 mHz with 10 points per decade. The first course from 1 kHz to 100 mHz served only as a transient oscillation to avoid artefacts and was later disregarded in the evaluation.

3A.2.2 Investigations of the E-coated conversion layers during and after sub-surface flux

For the cataphoretic deposition, the pre-treated AlMgMn sheets were moistened in de-ionised water and the clear E-coat (Aqua EC3000, Axalta Coating Systems Germany GmbH) was deposit at 32 °C with an initial voltage of 260 V (Wächter GLT 400/20), countered to the substrate. Film thicknesses of 10 µm ±1.0 µm were reached and were measured with PHYNIX® Surfix after hardening at 180 °C for 20 min. During the deposition of the clear E-coat, an area was masked with a sharp-cut frontier to the coating side to prepare the defect up to the conversion layer. Lastly, a reservoir with a size of 15 mm x 20 mm x 15 mm was placed on the E-coat-free area and filled with the same phosphate-based buffers from the previous study – with a pH=1.6 (conductibility at 25 °C, χ($H_2PO_4^-$/H_3PO_4)=23.5 mS/cm) and a

pH=12.2 ($\chi(PO_4^{3-}/HPO_4^{2-})$=28.5 mS/cm), p.a. quality (Sigma-Aldrich) – to initialise a defect at the conversion coating of the AlMg(Mn). Directly after the addition of the electrolyte, the samples were purged with humid nitrogen (rH=86-88 %, $O_2 \leq 2$ %) in the SKP chamber of the SKP-Raman setup, which was already described in Chapter 3. The SKP needle was calibrated with saturated $CuSO_4$, adjusted to a standard hydrogen electrode (SHE) and, potential and height profiles (DH=160 mV, x/y-steps=20 µm) were measured for 516 h after the start of the experiment. Next, Raman spectra (785 nm) were recorded in the "intact" areas with an 1800 groove/mm grating, a power of 20-25 mW and an acquisition time of 300 s (spectral resolution: 0.6 cm^{-1}). No bubbles were observed with the naked eye which is why the scans were continued until 709 h in a humid oxygen ambience (rH=86-88 %).

Additionally, the samples were dried at 40 °C in vaccum for 20 min to stop the transport process. Then, the E-coat surface was mapped via EDX with the Hitachi TM 3000 system at 15 kV. Local points of interest were analysed via infrared spectroscopy between 500 and 4000 cm^{-1} (100 scans) in reflection through the E-coat by a Lumos FT-IR-Microscope ECL 10 of Bruker, with a resolution of 4.0 cm^{-1}. Moreover, FIB cuts were operated by the Zeiss Neon® 40 with an ultra-dry X-ray detector from Thermo Fisher Scientific. The SEM images of the FIB cuts were made with an Inlens detector. The samples were sputtered with Au and deposited by the Ga emitter with 2 nA and 30 kV across a length of 30 µm down to the substrate. The first element detection was done in the mapping mode at 20 kV. Finally, the cross sections were mapped again with a decreased acceleration voltage of 5 kV due to the lower interaction volume.

3A.3 Results and discussion

The acid-base interactions at chromate-free conversion layers of AlMg(Mn) underneath the E-coat are the central theme of this chapter. The influence of a pickling inhibitor, a self-assembly and a polymer in the conversion layer are pointed out by interfacial pH-changes in a humid nitrogen/oxygen atmosphere. Therefore, the peculiarities of the conversion layers are presented and an alkaline and acidic flux are initiated at the conversion layer under the E-coat. The corresponding Volta potential and structural results clarify the role of the conversion coatings in protecting the bonds of the E-coat with the aluminium substrate.

3A.3.1 Characterisation of chromate-free conversion layers

An overview of the surface topography and the coverage of the conversion layers at the AlMg(Mn) substrate is given in Figure 3A.2, with a magnification at the bottom. All coatings show a high degree of the coverage but they differ in their surface structure. The Ti- (A) and Zr-based conversion layers (B) are characterised by a homogeneous surface with some dark spots and grooves along the rolling direction. The dark spots result from lower secondary electron emission due to locally topographical inhomogeneity. The smoothest impression makes the Zr-based conversion with the polymer (C). No grooves of the AlMg(Mn) substrate are visible. In the magnification, the Ti-based coating with the inhibitor shows a fine structured topping, additionally, the Zr-based layer has several small plates at the top, which close the surface. At the third layer, the polymeric parts seem to protrude out of the coating. In general, the acidic deposition of the conversion layers causes a favourable island growth in the alkaline surrounding of cathodic IMPs [2-4]. This causes the observed dark spots in the topography, while the visibility of the groove depends on coating thicknesses lower than 100 nm. Moreover, the

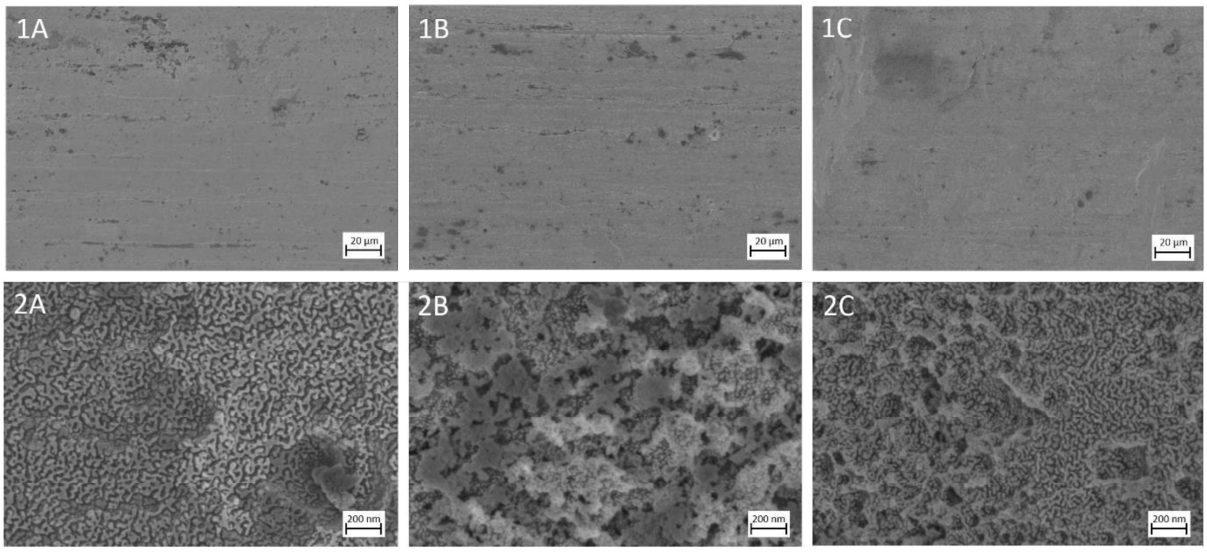

Fig. 3A.2 SEMs of the pre-treated AlMg(Mn) before the cataphoretic deposition: A) Ti-based, B) Zr-based, C) Zr+Polymer-based conversion layers

self-assembly of the Zr-based layer seems to be cross-linked with a covering organic compound, as shown in forms of small plates, which have further anchors to the substrate. The smooth impression of the polymer-based layer is also reported by Deck et al. [3]. The polymer forms a real monolayer above the stable oxide to protect the substrate [9] while the structural inhomohgenities decrease with the increase of the coating thickness.

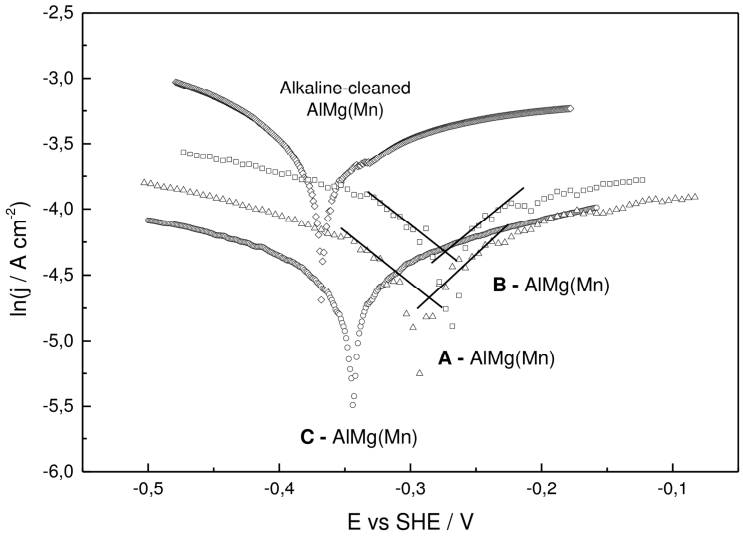

Fig. 3A.3 Tafel diagrams of the AlMg(Mn) alloy and the conversion layers - A) Ti+inhibitor, B) Zr+SA, C) Zr+Polymer – measured at pH=5.7, $\chi(HPO_4^{2-}/H_2PO_4^-)$=2.78 mS/cm; dE/dt=1 mV/s, except for A/B with 5 mV/s; T=25 °C in O_2-atmosphere

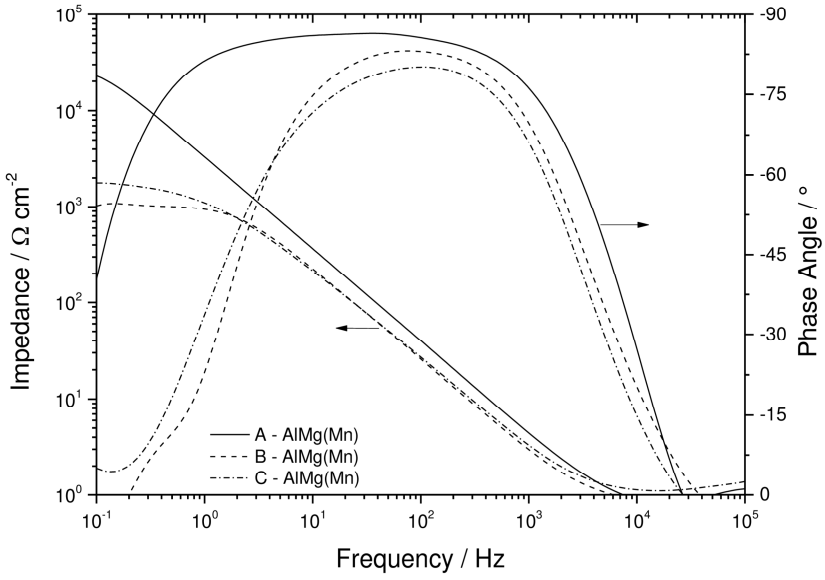

Fig. 3A.4 Bode diagrams of the AlMg(Mn) alloy and the conversion coatings – A) Ti+inhibitor, B) Zr+SA, C) Zr+Polymer – measured at pH=5.7, $\chi(HPO_4^{2-}/H_2PO_4^-)$=2.78 mS/cm; frequency range: 10 kHz to 100 mHz, start at 1 V, amplitude: 20 mV; T=25 °C in O_2-atmosphere

The oxygen-driven nature of the conversion coatings in neutral buffer solution is illustrated by the potential-dynamic curves in Figure 3A.3. The logarithmic limiting current densities $\ln(j_L)$ are significantly lower for all types of conversion layers compared to the pure substrate. The smallest $\ln(j_L)$

with a value of -4.8 and the best corrosion resistance is shown by the conversion layer C with the polymeric compound, which increase the barrier properties of the sample. The next one is the Ti-based conversion layer with the inhibitor (A) with a value of -4.6, whereas the Zr-based conversion layer B reaches a $\ln(j_L)$ of -4.3. In the same order, the corrosion potential slightly shifts from -0.35 V to -0.27 V.

Intact barrier conversion coatings behave as capacitor, which is characterised in the Bode plots of Figure 3A.4. Interestingly, the Ti-based conversion coating A is displayed by the largest capacitance range from 10 kHz up to 0.1 Hz with a maximal impedance of 2E4 Ω/cm² (0.1 Hz). A nearly ideal phase spreads from 0.5 Hz to 1.2 kHz with values between -75 ° and -90 °. The coating does not exhibit signs of breakdown. This performance is comparable to a $CeCl_3$-treated 7075-T6 during the immersion in 0.5 NaCl solution [20]. However, degradation signs are obvious at the conversion coatings B and C due to an increased resistance at low frequencies and a small area of a phase around -90 °. The Zr-based conversion coating with the polymer (C) reaches 1.8 E3 Ω/cm² and the Zr-based conversion coating with the SA (B) 1.1 E3 Ω/cm² at 0.1 Hz. The corresponding Nyquist diagrams are given in Figure 3A.5.

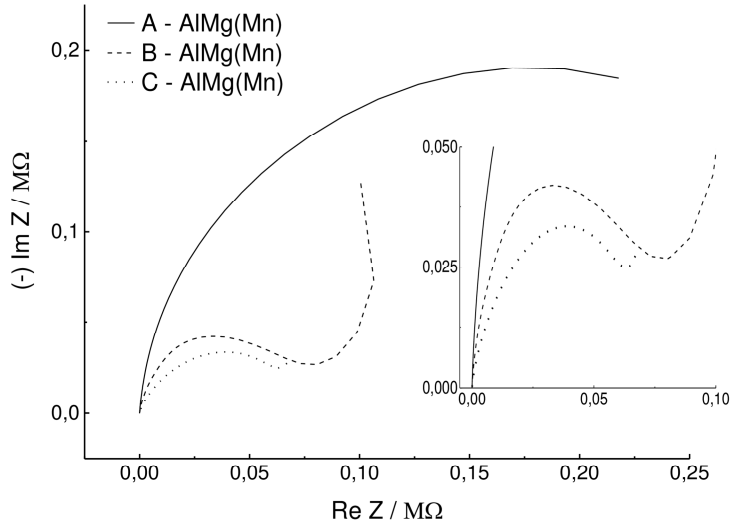

Fig. 3A.5 Nyquist diagrams of the AlMg(Mn) alloy and the conversion coatings – A) Ti+inhibitor, B) Zr+SA, C) Zr+Polymer – measured at pH=5.7, $\chi(HPO_4^{2-}/H_2PO_4^-)$=2.78 mS/cm; frequency range: 10 kHz to 100 mHz, start at 1 V, amplitude: 20 mV; T=25 °C in O_2-atmosphere

While the Ti-based conversion layer shows a semicircle, the Zr-based conversion layers have a semicircle with a linear slope of approx. 45° such as a Warburg. This slope is further continued by a normal progress such as a simple inductance at the Zr-based conversion layer with SA. Accordingly, the electrolyte has to reach the interfaces to form a double layer at the Zr-based conversion layer, expressed by the Warburg and the SA has to act as a dielectric, which weakens the capacitor of the Zr-network.

Note that all investigated conversion coatings show an improvement of their corrosion resistance as well as their barrier properties by anodization up to 3 V.

Briefly, under neutral conditions, the polymer conversion coating (C) has the best corrosion resistance, but the polymer and the SA conversion coatings (C+B) are permeable for the electrolyte. Due to this fact, their barrier resistance decrease while the Ti-based conversion coating with the inhibitor (A) is stable against the electrolyte ingress. However, an overview of the real protection potential of the conversion layers has to include their behaviour against aggressive media which is why the next section is focused on the acidic and alkaline attack at the conversion coating.

3A.3.2 Acidic and alkaline sub-surface flux at the E-coat-covered conversion layers

The acid-base interactions underneath the E-coat are pointed out by interfacial pH-changes in humid nitrogen and oxygen atmosphere. The corresponding Volta potential and structural results clarify the protection and failure mechanism at the conversion coatings.

First, an acidic and alkaline flux are initiated at the different conversion layers along the E-coat-conversion-interface and the atmosphere was purged with humid nitrogen for 519 h. Appendix A3.4 contains the corresponding SKP scans to the experiment. In general, the potential profiles show a comparable behaviour as the pure AlMg(Mn) substrate (see Figure 3.13 and 3.10). The acidic flux causes flat potentials because the local Mg dealloying has no bearing on the potentials, as discussed in Chapter 3. Interestingly, the conversion layers A and C have distinctively anodic areas, which express the first degradation signs near the defect. However, no anodic area is seen at the covered conversion layer B with the SA. The alkaline flux causes typically local potential increases in the SKP scans due to the micro-galvanic of the Al_6MnFe.

The averaged Volta potentials present Figure 3A.6 at an intact area 2500 µm away from the defect after the potential stabilisation. In general, the potential increases from the conversion layer A, B to C. This observation hints at a higher amount of functional groups [21] from the titanium (A) to the zirconium plus SA (B) and lastly to the zirconium plus polymer (C). However, no prominent pH-differences are observed by comparing the data with the pure AlMg(Mn). The Volta potential slightly decreases by 0.2 V from pH=12 to pH=2 at the Ti- and the Zr-based conversion coating with polymer. Conversely, the potential increases around 0.1 V at the Zr-based conversion coating. With the naked eye, no bubbles were visible after 519 h which is why the experiment was continued in humid oxygen atmosphere. Due to the change of the ambience, the potentials decrease rapidly. The slight potential shift at the Ti-based conversion disappears while the potential increases to 0.2 V at the Zr-based conversion layer with the SA. At the Zr-based conversion layer with the polymer, the surface is roughed up during the acidic flux. Due to that reason, the height control of the SKP was very time-consuming and the measurement of this sample was stopped to increase the time resolution of the other samples.

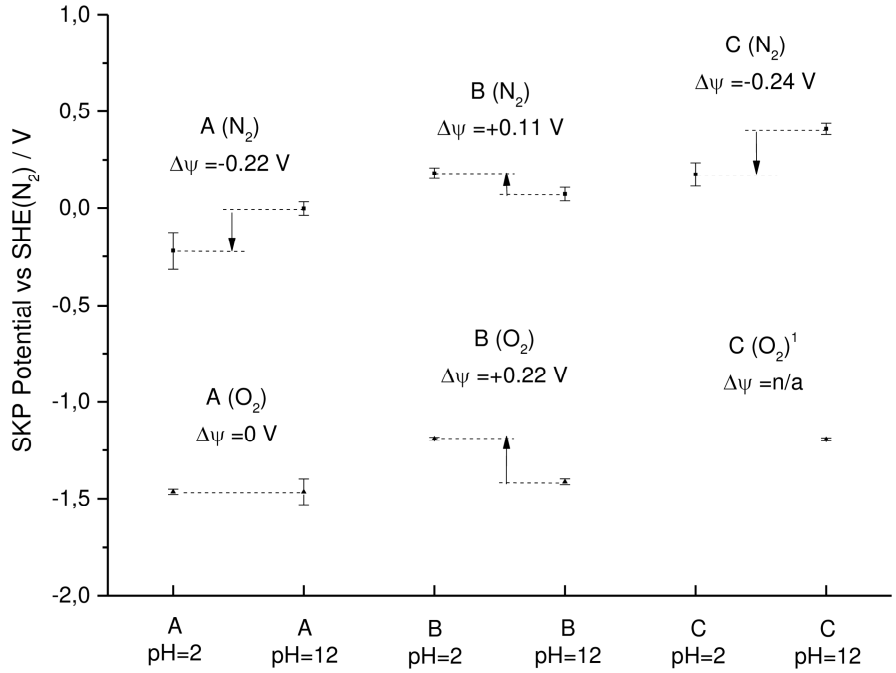

Fig. 3A.6 Volta potentials of the Cr-free conversion layers – A) Ti plus inhibitor, B) Zr plus SA, C) Zr plus polymer – covered with a 10 µm thick E-coat 2500 µm away from the defect (intact areas), extracted after potential stabilisation – averaged from 293 h to 519 h in humid N_2 and up to 709 h in humid O_2 ambience

In general, the potential changes are slight and can also be a result of precipitations, mechanical stress [22] and the observed roughness changes. Although, the ZrO_2 is an ionic conductor [16-17], there is a very low bearing of the charge carriers on the sum of the Galvani potentials and the Volta potential. All conversion layers seem to neutralise developing potential gradients and this mechanism protects the interface from an electrochemical point of view. Additionally, the TiO_2 and ZrO_2 have a larger passivation range in the alkaline direction compared to the aluminium [23]. At the aluminium, the potential increase is prominent at a pH-value of 12, which seems to not be enough for the TiO_2 and the ZrO_2. However, the results of the Zr-based conversion layer with SA (B) are uncommon. Sarfraz and co-workers [16] analysed the behaviour of a Zr-based conversion coating with copper while mimicking the strongly alkaline conditions with the high voltages during the cataphoretic deposition. They started in a neutral solution und alkalised the interface, getting a slight potential increase of 0.1 V and showing the chemical stability of the conversion layer, via Raman analyses and photoluminescence (PL) spectroscopy – unfortunately, the complete composition of this layer is unknown.

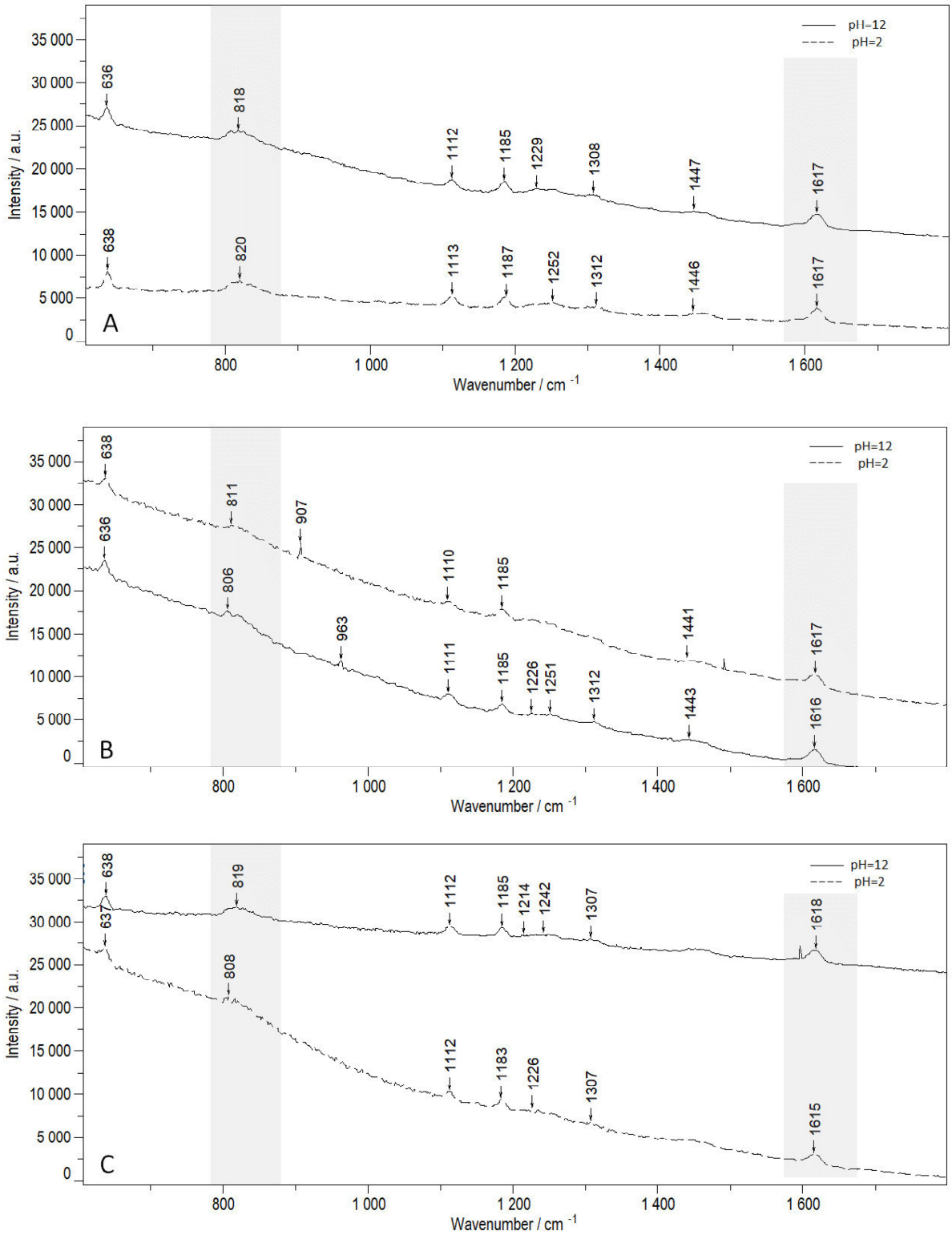

Fig. 3A.7 Raman spectra of the Cr-free conversion layers – A) Ti plus inhibitor, B) Zr plus SA, C) Zr plus polymer – at an intact area during the transport of the phosphate-based pH-buffers 2 and 12 under humid nitrogen purge, spectral resolution: 0.6 cm^{-1}

Next, the interfacial pH-behaviour and the manner of the ion transport should be clarified by analysing the confocal Raman spectra in Figure 3A.7 during the acidic and alkaline flux. The used pH-buffers are based on phosphates, due to this, an ion transport at the interface would be visible by vibrations around 1000 cm^{-1}. These vibrations are not found in the spectra, consequently, the general transport has to occur through the E-coat in parallel to the interface, as already found at the AlMg(Mn) interface. Interestingly, at the Zr-based conversion with SA (B), two new vibrations appear at 907 cm^{-1} (pH=2) and 963 cm^{-1} (pH=12), which could characterise different P-OR esters (900-1050 cm^{-1}) – a pH-interaction of the SA.

The interfacial pH-behaviour is given by the scissoring (1650-1590 cm^{-1}) and the wagging vibrations of the amines (around 800 cm^{-1}). A shift to higher wavenumbers characterises loose bonds such as hydrogen bonds between the hydroxyl groups and the amines of the E-coat while a shift to lower wavenumbers hints at an amine protonation due to strongly ionic bonds.

- At the Ti-based conversion with the inhibitor (A), the vibrations are nearly equal at high wavenumbers, which express an alkaline state at the AlMg(Mn) interface for both buffers.
- The Zr-based conversion coating with the SA (B) has generally stronger amine bonds than the Ti-based conversion (A) while the ionic bonds are slightly weaker with a flux of pH=12. The results express a more acidic state compared to AlMg(Mn).
- The Zr-based conversion coating with the polymer (C) shows the strongest bonds with vibrations at 808 cm^{-1} and 1615 cm^{-1} during the acidic flux but the loosest bonds with vibrations at 818 cm^{-1} and 1618 cm^{-1} in alkaline environment. This tendency is typical for the pure AlMg(Mn), too.

A classic pickling inhibitor is the hexamethylen tetramine which acts as a buffer solution around a pH-value of 5 and blocks the occurrence of the hydrogen evolution. In an acidic environment, the hexamethylen tetramine decomposes to formaldehyde and ammonium ions. The effect of the inhibitor explains the marginally interfacial changes at the Ti-based conversion coating. Of course, the SA and the polymer of the other conversion coatings can also interact with the acidic or alkaline environment but for any explanations, the chemical structures have to be analysed.

For further information about the structural changes, the samples were dried. The corresponding SEM and EDX (P) images are presented in Figure 3A.8. With an alkaline defect, the performance of the conversion layer is weaker compared to the acidic one. Especially, the conversion layer with the polymer (C) shows numerous small bubbles at the top of the E-coat surface. The Ti-based conversion with the inhibitor (A) shows a high number of bigger bubbles while the Zr-based conversion with the SA (B) only shows some little bubbles due to the hydrogen evolution. With the acidic defect, the Zr-

based conversion layers (B+C) show only single bubbles. This corrosion resistance seems to be rooted in an increased molecular weight and an improved adhesion of the E-coat at the Zr-based conversion layer [24]. Conversely, the Ti-based conversion layer (A) has a singularly big bubble followed by a large tail of little bubbles. These observations are in line with the results of the bond strength between the amines and the hydroxyl groups of the conversion layers

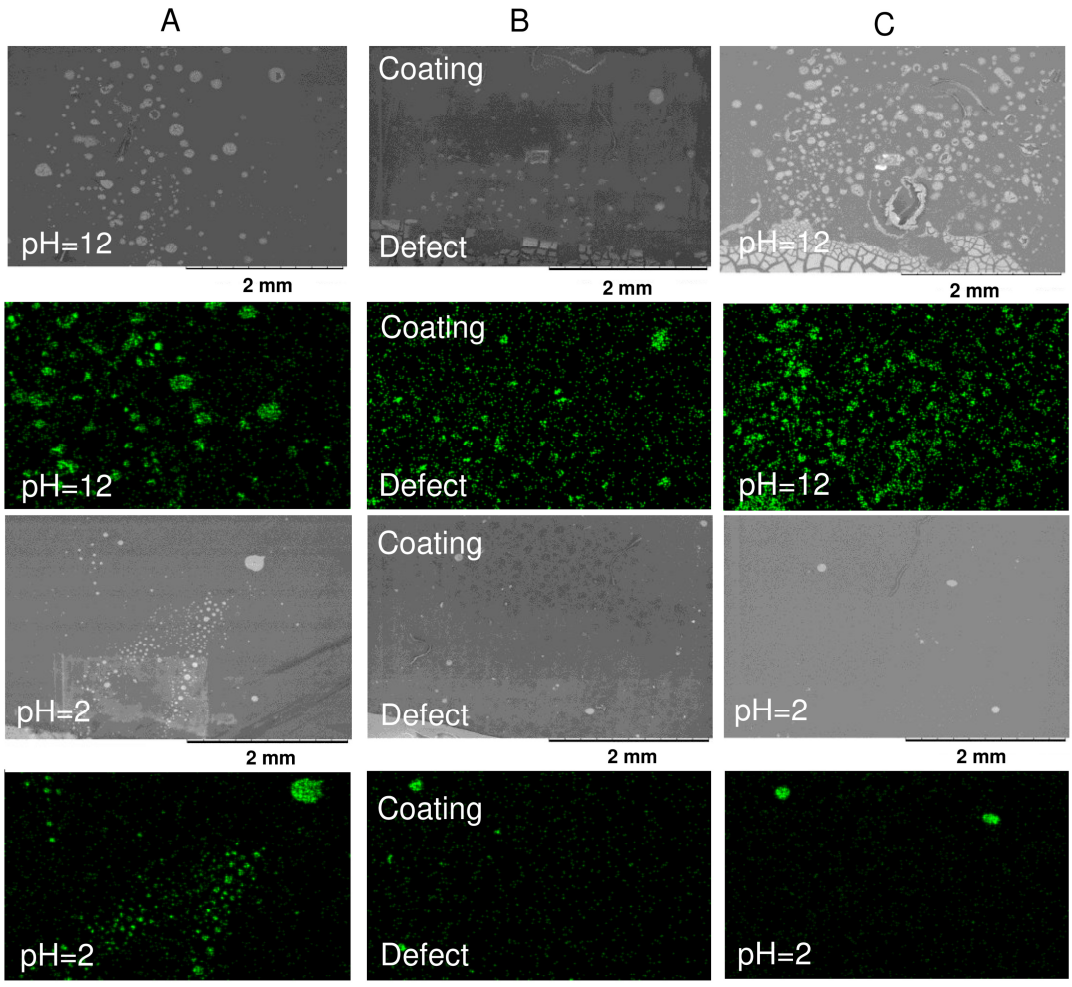

Fig. 3A.8 Overview (REM/EDX(P)) of the E-coat surface behind the defect at 709 h after the addition of the defect buffers with a pH=12 (PO_4^{3-}/HPO_4^{2-}) and pH=2 ($H_2PO_4^-$/H_3PO_4); A) Ti plus inhibitor, B) Zr plus SA, C) Zr plus polymer, same size as in Figure 3.5

Additionally, Appendix A3.5 shows the IR spectra in reflection of all samples in the intact and bubble areas. In principle, the increase of the water vibration of the intact areas supports the findings of Figure 3A.7. Interestingly, the Al-O stretching vibration around 950 cm^{-1} is visible at the conversion layers with inhibitor (A) and SA (B) but this vibration disappears at the conversion layer with SA (B) in an alkaline environment. The Al-O-change at the SA layer is converse to the change at the untreated AlMg(Mn), however, the Volta potential shifts are converse, too.

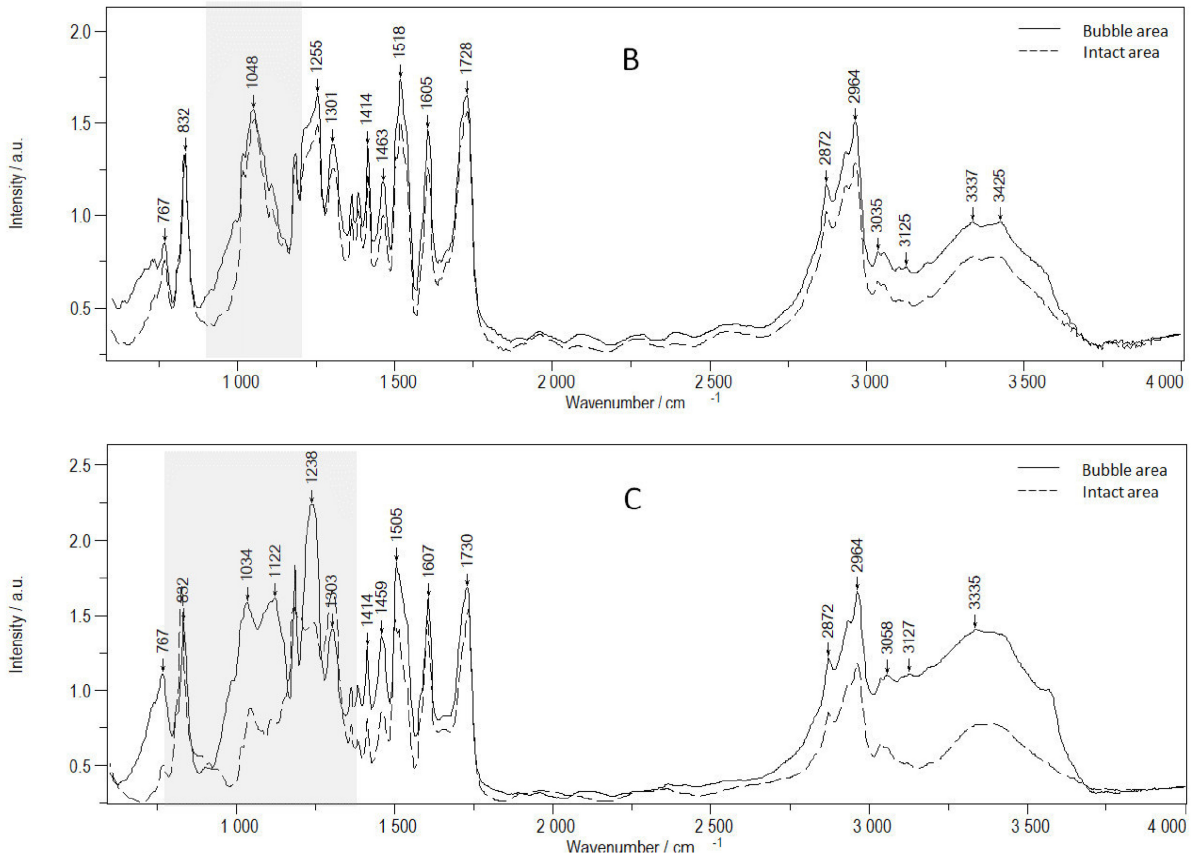

Fig. 3A.9 IR spectra in reflection of the Zr-based conversion coatings with the SA (B) and the polymer (C) after the alkaline flux; average of min. three spots, spectra resolution: 4 cm^{-1}

The previous study (see Figure 3.7 in Chapter 3) demonstrated that the local acidity is very distinctive under alkaline conditions, due to this reason, the structural changes are obvious here. The locally acidic bubble areas and the alkaline intact areas of the Zr-based conversion coatings (B+C) are presented in Figure 3A.9, via IR spectra in reflection after the alkaline treatment. The Zr-based conversion coating with the SA (B) gets an expanded vibration at 1048 cm^{-1} in the acidic area compared to the alkaline area. The conversion coating with the polymer (C) shows converse behaviour to the untreated AlMg(Mn). In the acidic bubble area, the polymer is stable but the vibrations are strongly reduced to lower wavenumbers than 1200 cm^{-1} in the alkaline region. The loose bonds cause a loss of adhesion.

Typically, the SAs for aluminium are phosphonic acids, which condensate with the hydroxyl groups of the conversion layer and form an ester. However, the phosphate/phosphonate chemistry can be further used to protect the aluminium alloy against acidic attacks due to precipitation:

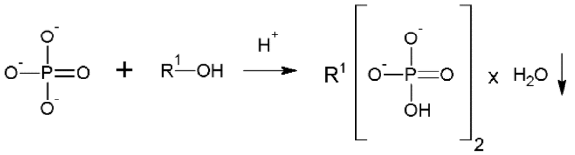

(3A.3)

The incorporation of phosphates or phosphonates in the conversion layer causes their dissolution in the pit, where insoluble salts with the metal ions R^1 of the conversion layer are formed, effectively sealing the pit [12, 25]. The jellylike salts such as the $Zr[HPO_4]_2$ x H_2O will cover the protruding Al-O groups so that they disappear in the IR spectra. Cross-linkers of phosphonates will embedded in the salt and guarantee a further adhesion. This scenario is likely due to the vibration increase at 1255 cm^{-1} (phosphonate) and the expansion at 1048 cm^{-1} (phosphate at 1000 cm^{-1}) at the SA sample.

Under an alkaline attack, the SA ester and an ester of the polymer can hydrolyse at the anchor groups, as expressed in the next reactions:

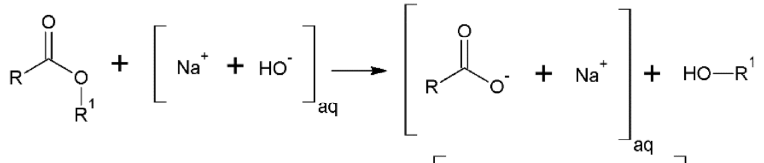

(3A.4)

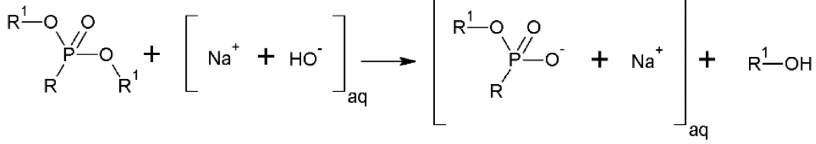

(3A.5)

In regard to the water content, the bond strength and the pits, the reaction at the polymeric ester has to be favoured, the vibrations of the polymeric ester (1034 cm^{-1} and 1112 cm^{-1}) distinctively decrease while the ester of the phosphonate (900-1050 cm^{-1}) is stable and protects the substrate.

Note that the results of the alkaline behaviour of the conversion layer also reflect the conditions during the cataphoretic deposition. At high voltages, a transpassive dissolution of ZrO_2 under zirconate formation was not found [16]. The AlMg(Mn) dissolves slightly due to the deposition (see Figure 2.6) but, in this case, it is protected by the conversion coating. Impressively, the electrochemical stability of this system is shown by the nearly constant Volta potentials in comparison to the single AlMg(Mn). Due to this fact, the electrochemical effects can be disregarded in this example.

Moreover, Figure 3A.10 and 3A.11 show the cross sections at the bubbles of the Zr-based conversion coating with the polymer. All cross sections are given in Appendix A3.6. In general, the IMPs are found 1-2 µm deep in the inside of the AlMg(Mn). The IMPs are leached out by deoxidation step during the pre-treatments. However, this distance alone does not protect the AlMg(Mn) sufficiently. The charge cloud of the IMPs overcomes it. Further, the top of the bubbles makes a fur-like impression at the Zr-based conversion layers (B+C) compared to the Ti-based conversion layer (A) and the untreated AlMg(Mn) (see Figure 3.11/3.14). The organic compounds seem to be flushed out of the Zr-based conversion layers.

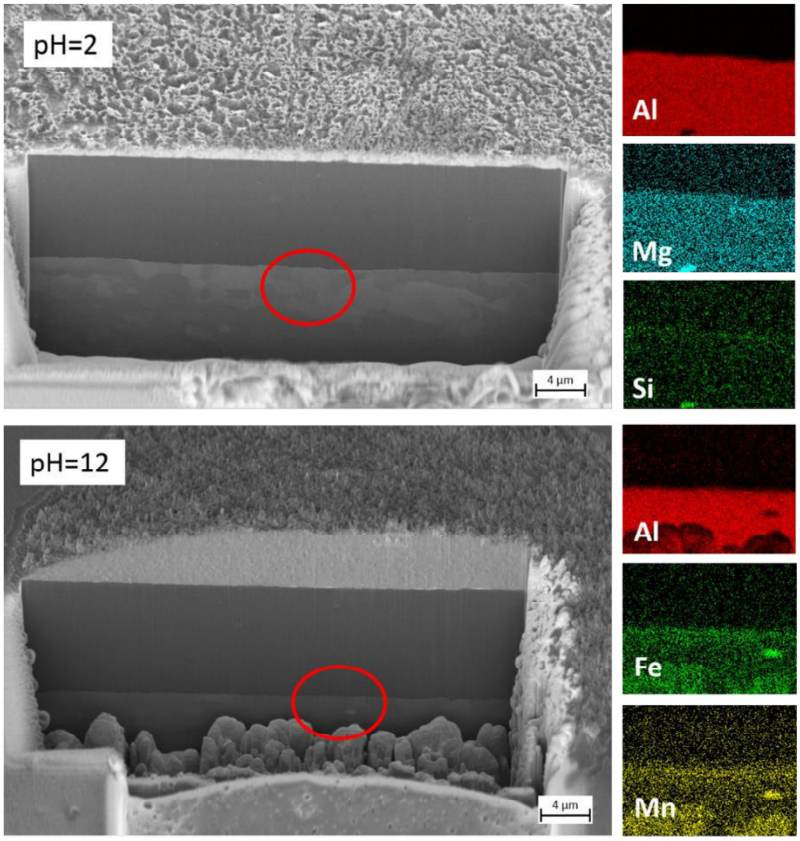

Fig. 3A.10 FIB cuts at the bubbles of the Zr-based conversion coating with polymer after the acidic and the alkaline sub-surface flux

The overview of the acid-base interactions at the interface of the E-coat-covered conversion layers showed that there are three general modes of action to protect the aluminium substrate. The pickling inhibitor buffers the pH-value at the interface but it weakens the bonds to the AlMg(Mn). Alternatively, the addition of a polymer compound shows a strong resistance under the acidic flux whereby its bonds hydrolyse and loss their adhesion at alkaline conditions. The self-assembly has a good performance in both environments due to the acidic precipitation of insoluble salts and their high amount of anchor groups to the substrate. These results correlate well with the Raman shifts of the amine groups. However, the mechanisms are chemically driven and balance the interface activities. The TiO_2 and the ZrO_2 have a high electrochemical stability when compared to the AlMg(Mn), which might be the reason why the pH-activities do not influence the Volta potential, significantly.

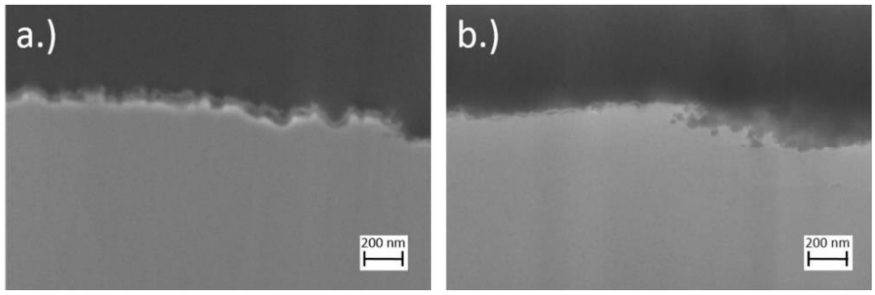

Fig. 3A.11 Nanoscale of the interface in the cross section of the Zr-based conversion coating (C) after the acidic sub-surface flux underneath a bubble; (a) and (b) are different areas.

3A.4 Conclusion

In this study, the pH-activities underneath the clear E-coat were investigated at the Ti- and Zr-based conversion coatings with the addition of a pickling inhibitor, a self-assembly (SA) and a polymer at the AlMg(Mn). Three different modes protect the substrate and work very efficiently in acidic environments, while they weaken under alkaline conditions, as illustrated in Figure 3A.12.

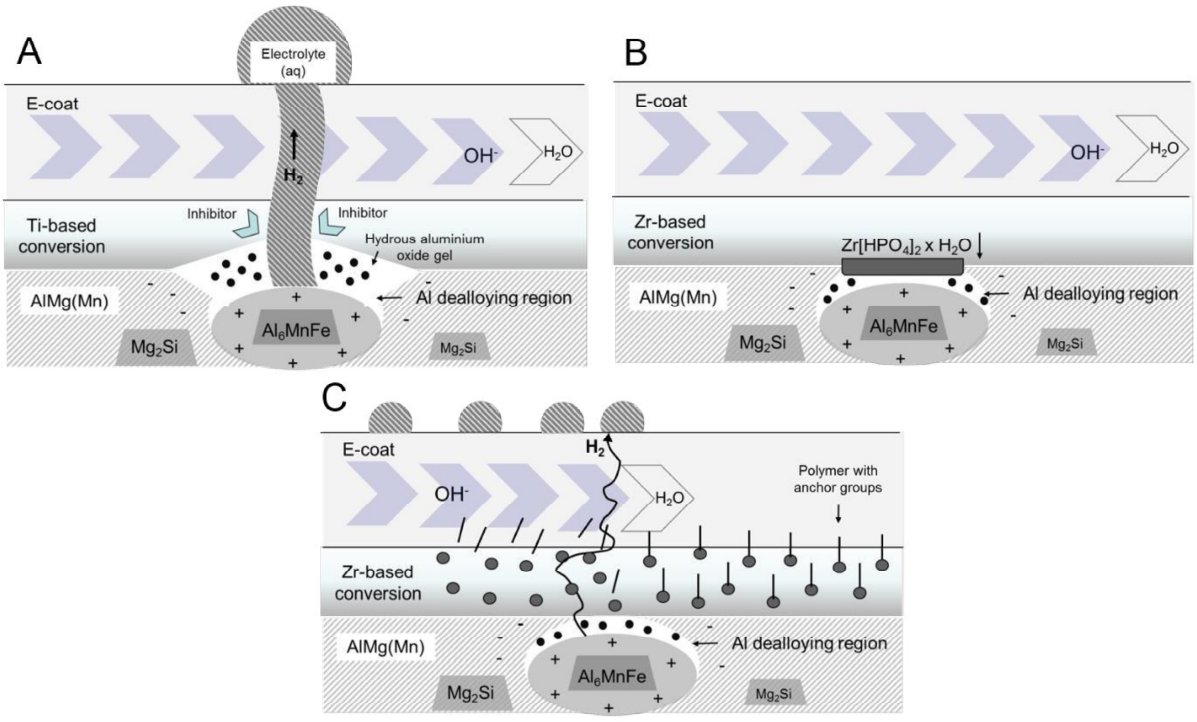

Fig. 3A.12 Schemes about the actions at the chromate-free conversion layers – A) Ti plus inhibitor, B) Zr plus self-assembly, C) Zr plus polymer – during the alkaline flux underneath the E-coat.

At the Ti-based conversion coating (A), the inhibitor buffers the interfacial pH-value and reduces the hydrogen evolution to avoid the further dissolution of the aluminium. This layer is stable against the electrolyte ingress but it has a weak adhesion to the E-coat. The self-assembly (B) has a good performance in both environments due to the precipitation of insoluble salts and their high amount of anchor groups to the substrate. Under acidic and neutral conditions, the conversion coating with the polymer (C) shows the best corrosion resistance combined with the strongest adhesion. However, the organic compounds of the conversion layer are permeable for the electrolyte and can hydrolyse during an alkaline flux. This scenario weakens the conversion layer by flushing the organic compound out of the layer. Especially, the polymer conversion coating loses its bonds with the E-coat, due to this, numerous of small bubbles occur across the E-coat.

Although, the bond strength of the amines changes, the Volta potentials are nearly stable at the conversion layers. The TiO_2 and ZrO_2 have an increased electrochemical resistance, due to their larger passivation range when compared to the AlMg(Mn), and the addition of chemical ingredients to the

conversion system balances the interfacial pH-value. These reasons seem to avoid the change of the charging of the metal oxides and the interfacial dipole of the oxide with the polymer, which is why the Volta potential has no significant merit of information about the interfacial processes at the conversion layers. However, the results present impressively the protection behaviour of the conversion layers at the AlMg(Mn) due to the decrease of the potential gradient from 2.5 V to 0.2 V, by an interfacial pH-change from 12 to 2.

References

[1] G. Bockmair, Non-chromate surface protection for aircraft maintenance, Advanced materials Research 38 (2008) 7.

[2] A. Nylund, Chromium-free conversion coatings for aluminium surfaces, Aluminium Transactions 2 1 (2000) 121

[3] P. D. Deck, M. Moon, R. J. Sujdak, Investigation of fluoroacid based conversion coatings on aluminium. Prog. Org. Coat. 37 (1998) 39.

[4] J. H. Nordlien, J.C. Walmsley, H. Østerberg, K. Nisancioglu, Formation of a zirconium-titanium based conversion layer on AA 6060 aluminium, Surf. Coat. Technol. 153 (2002) 72.

[5] N. J. Newhard, Corrosion Control Coating, Ed. H. Leidheiser, Science Press (1979) 225.

[6] O. Lunder, Chromate-free pre-treatment of aluminium for adhesive bonding, Doctoral thesis, Norwegian University of Science and Technology, 2003.

[7] J. M. Cerezo Palacios, Zr-based conversion coatings for multi-metal substrates, Doctoral thesis, Technical University Delft, 2014.

[8] C. Stromberg, P. Thissen, I. Klueppel, N. Fink, G. Grundmeier, Synthesis and characterisation of surface gradient thin conversion films on zinc coated steel, Electrochim. Acta 52 (2006) 804.

[9] M. Rohwerder, M. Stratmann, G. Grundmeier, Corrosion prevention by adsorbed organic monolayers and ultrathin plasma polymer film, Ed. P. Marcus, 3rd Edition, CRC Press, London (2011) 617.

[10] U. Harm, W. Fürbeth, K.-M. Mangold, Crosslinked molecular films for corrosion protection of galvanized steel surfaces, Jahrbuch Oberflächentechnik 66 (2010) 149.

[11] D. Narayan, Coating composition and method for the treatment of formed metal surfaces, US Patent No. 5139586 (1992).

[12] D. Hauffe, T. Kolberg, G. Müller, H. Gehmecker, W. Rausch, P. Schubach, T. Wendel, Process for a passivating postrinsing of conversion layers, US Patent No. 5294266, 1994.

[13] S. E. Dolan, Compositions and processes for forming a solid adherent protective coating on metal surfaces, US Patent No. 5342456 (1994).

[14] T. Lostak, A. Maljusch, B. Klink, S. Krebs, M. Kimpel, J. Flock, S. Schulz, W. Schuhmann, Zr-based conversion layer on Zn-Al-Mg alloy coated steel sheets: insights into the formation mechanism, Electrochimica Acta 137 (2014) 65.

[15] G. Williams, H. N. McMurray, Inhibition of filiform corrosion on organic-coated AA2024-T3 by smart-release cation and anion-exchange pigments, Electrochim. Acta 69 (2012) 287.

[16] A. Sarfraz, R. Posner, A. Bashir, A. Topalov, K. J.J. Mayrhofer, K. Lill, A. Erbe, Effect of polarisation mimicking cathodic electrodeposition coating on industrially relevant metal substrates with ZrO_2-based conversion coating, ChemElectroChem 3 (2016) 1415.

[17] A. Sarfraz, R. Posner, M. M. Lange, K. Lill, A. Erbe, Role of intermetallics and copper in the deposition of ZrO_2 conversion coatings on AA6014, J. Electrochem. Soc. 161 12 (2014) C509.

[18] A. Seth, W. J. van Ooij, P. Puomi, Z. Yin, A. Ashirgade, S. Bafna, C. Shivane, Novel, one-step, chromate-free coatings containing anticorrosion pigments for metals – An overview and mechanistic study, Prog. Org. Coat. 58 (2007) 137.

[19] P. Puomi, Z. Yin, W. an Ooij, A. Seth, Chromate-free silane-containing primer technology, 5 (2009) 181.

[20] F. Mansfeld, S. Lin, S. Kim, H. Shih, Corrosion protection of Al alloys and Al-based metal matrix composites by chemical passivation, Corrosion 45 (1989) 615.

[21] M. Rohwerder: Scanning Kelvin Probe and Scanning Kelvin Probe Force Microscopy and their application in corrosion science. In: Corrosion science and technology: Mechanism, mitigation and monitoring, Eds. U. K. Mudali, B. Raj, Taylor & Francis, London (2008) 468.

[22] A. Nazarov, V. Vivier, D. Thierry, F. Vucko, B. Tribollet, Effect of mechanical stress on the properties of steel surfaces: scanning Kelvin probe and local electrochemical impedance study, J. Electrochem. Soc. 164 2 (2017) C66.

[23] M. Pourbaix, Atlas d'Équilibres Elektrochimiques, Gauthiar-Villar & Cie, Paris, 1963.

[24] N. Khun, G. Frankel, J. Zimmerman, Investigation of surface morphology, wear resistance, and adhesiveness of AA6061-T6 treated in a hexafluorozirconic acid-based solution, Corrosion 69 (2013) 259.

[25] C. E. Tomlinsion, Conversion coatings including alkaline earth metal fluoride complexes, US Patent No. 5380374, 1995.

4 Normal diffusion vs in plane diffusion: Single layer, multilayer and their peculiarities

4.1 Introduction

The previous studies identified the influence of the E-coat bulk on the interface. For example, the pigments in the E-coat bulk decrease the velocity of the interfacial ion transport or the pH-activities along the aluminium oxide are dominated by the flux through the E-coat bulk. These results show the direction-driven nature, the so-called anisotropy, of the layer systems for the electrolyte. In general, the intramolecular conformations of the polymer must be anisotropic in the directions parallel and normal to the surface, while they must be varied with the distance normal to the surface [1]. Currently, the water diffusion normal to the interface and the ion transport at the interface are investigated, but there is no information about the ion and water diffusion/transport in parallel to the interface. However, the quantification of this characteristic plays a key role in assessing the complete diffusion processes. Peculiarities of the layer systems such as solvated ions in the E-coat, functional pigments such as aluminium flakes, which act as diffusion barrier, or polymer-polymer interfaces will impact the transport paths.

In the actual research, the water sorption and the diffusion in polymer coatings are monitored by fluorescence [2], nuclear magnetic resonance (NMR) [3] and electrochemical techniques [4-7]. An overview of further techniques is given elsewhere [8]. The fluorescence techniques are based on extrinsic molecular rotor probes, whose sense changes in the mobility of the polymer matrix as it is plasticised by water [2]. Bankh and co-workers [3] imaged the water uptake and the mechanical stress in multilayer films via the GARfield approach, whereby the magnetic field varies linearly with the position. Electrochemical approaches use embedded electrodes to detect the water accumulation in the polymer bulk and in the interlayer [4-7], or various electrolyte holders with electrodes were mounted at different coating levels for EIS measurements [9]. However, all studies unify the one-dimensional view of the transport through the polymer; a comparison study of the normal and in plane water and ion transport is not available, until now.

This chapter highlights the direction-driven nature of single layers and multilayers. Therefore, the E-coat, a base coat and a clear coat were selected and the impact of the aluminium flakes and the base coat-clear coat interface have been highlighted as a central theme. The quantitative study is based on a standard EIS setup with a single electrolyte holder and an EIS setup with two electrolyte holders, in which the counter and the working electrode are placed in such a way that they can measure the in plane water diffusion (see Figure 4.2). The results of the in plane water diffusion are compared with the in plane ion diffusion measured via embedded electrodes in a wet-dry-wet cycle (see Figure 4.3). Additionally, the Fickian and the non-Fickian approaches are applied while the changes in the glass

transition, the Deborah number as a degree of elasticity and the stress and strains present are determined via dynamic-mechanical analyses (DMA).

Ultimately, the results demonstrate the rate-determined diffusion paths through single and the multilayers and characterise the physicochemical circumstances during the electrolyte ingress. The study presents the relation between water and the ion diffusion as well as the relation between the adsorption coefficients of the non-Fickian law and various physicochemical factors and will complete the total diffusion investigations.

4.2 Experimental

4.2.1 Sample preparation: coatings and their application

Various HDG steel samples (150 mm x 75 mm/75 mm x 60 mm, Gardabond E HDG, Chemetall GmbH) were cleaned by soaking them in toluene, acetone and ethanol, followed by submerging them in alkaline cleaner Gardoclean® 855/1 (20 g/L, Chemetall GmbH) and stirring them at 500 rpm at 60 °C for 5 min. Then, the samples were soaked and jetted with distilled water and dried in recirculating air at 40 °C for 120 min. The pigment *E-coats (CP)* were deposited at 32 °C and with an initial voltage of 260 V (Wächter GLT 400/20), while a HDG steel sheet served as a counter electrode. Coating thicknesses of 22.7 µm±1.3 µm were deposited and measured with the PHYNIX® Surfix after hardening at 180 °C for 20 min. The water-borne *base coats (BC/BCs)* are acrylic core-shell systems with a grey pigment paste, in which 90 % of the pigments are smaller than 5.5 µm. As illustrated in Figure 4.1, a base coat was modified by the addition of silver dollars and cornflakes as non-leafing pigments with a quantile Q_{90} of 32.5 µm, measured via laser diffraction. The chosen 2-pack *clear coat (CC)* is based on a solvent-borne polyester/isocyanate resin. All coating materials were supplied by Axalta Coating Systems Germany GmbH, which is why the structural information about the single layers is additionally given by infrared spectra in Appendix A4.1. After the viscosity adjustment and the mixing, the base coats and the clear coat were sprayed on the alkaline-cleaned HDG steel with a SATA LP90 gun in an automatic spraying machine, with flash-offs of 5 min after two cycles. Coating thicknesses of 30.3±1.2 µm for the base coat and 28.6±2.9 µm for the base coat with Al flakes were reached after an intermediate curing at 70 °C for 5 min and a final curing at 145 °C for 20 min, measured with the PHYNIX® Surfix. The clear coat was further sprayed on electrodes (DEA 28800A59. 010-00, Netzsch)

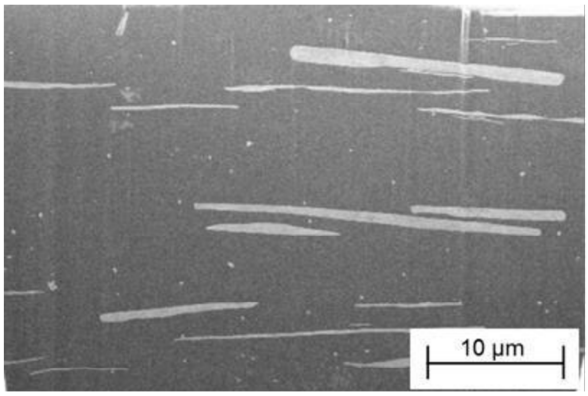

Fig. 4.1 Cross section of the base coat with silver dollars and cornflakes

Tab. 4.1 Single and double layers and their thicknesses for normal and in plane diffusion experiments

Sample Abbr.	Cataphoretic Painting CP	Base coat BC	Base coat plus Al flakes BCs	Clear coat CC	Base coat – Clear coat BC-CC	Base coat plus Al flakes – Clear coat BCs-CC
1st layer	22.7±1.3	30.3±1.2	28.6±2.9	52.9±4.1	29.2±2.1	29.9±3.5
2nd layer					26.6±2.0	18.7±1.9

which were placed at a steel, see Figure 4.3. The thicknesses of the clear coats average 52.9±4.1 µm after the curing at 145 °C for 20 min to cover the electrodes completely. The double layers exhibit base coat thicknesses of 29 µm and clear coat thicknesses of around 23 µm after the intermediate curing and the final curing at 145 °C. All layer thickness are summarised in Table 4.1.

4.2.2 Water diffusion: normal and in plane measurement

All EIS experiments were carried out using a 0.5 M NaCl solution, a Zennium workstation (Zahner-Elektrik GmbH) and a two-electrode setting [10]. The normal diffusion measurements were done by a standard EIS setup with a single electrolyte holder and a platinum mesh wire (HMT, Heraeus) as a counter electrode. The in plane diffusion was measured by an EIS setup with two electrolyte holders, in which platinum mesh wires were placed as counter and working electrodes. Due to this, the setup represents the normal water ingress into the polymer and the in plane ingress through the polymer. The electrolyte reservoirs had a diameter of 40 mm while the distance between the holders amounted 35 mm. Figure 4.2 shows the differences of the setups.

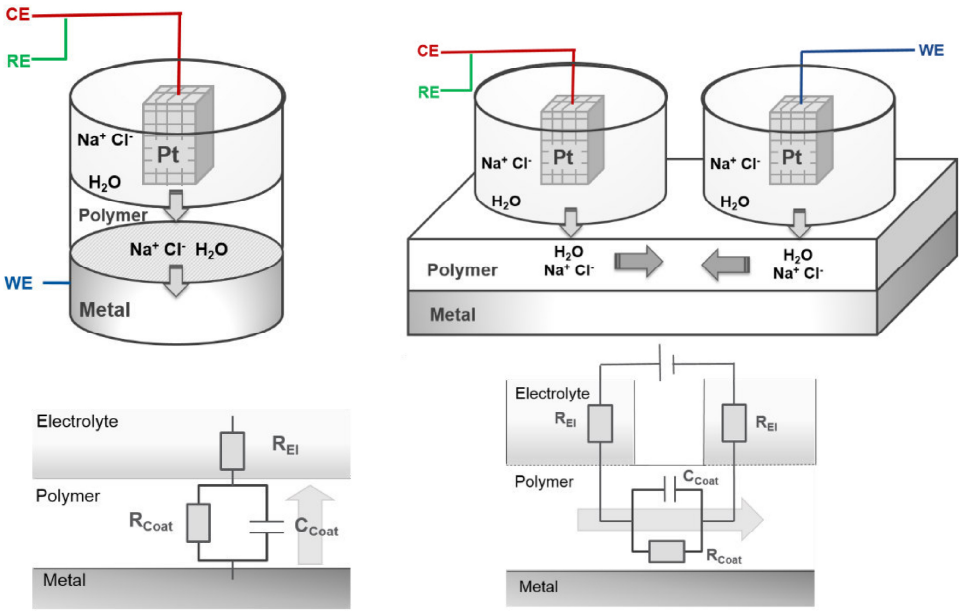

Fig. 4.2 Normal and in plane EIS setups and their circuits to calculate the water diffusion rates

Similar to the EIS investigations in Chapter 2, the runs started at a frequency of 1 kHz, were continued up to 100 kHz and returned to 100 mHz with 10 points per decade. The first course from 1 kHz to 100 mHz served only as a transient oscillation to avoid artefacts in the fitting region and was later disregarded in the evaluation. Three runs per sample were started every 4 min, with each run lasting up to 72 h. The working electrodes were perturbed with an amplitude of 20 mV and coupled on the initial open circuit potential of the metal in the electrolyte [11]. The spectra of the normal and the in plane direction were fitted between 10-100 kHz by Randles circuit [12], containing the coating resistance, $R_{coat,}$ parallel to the capacitance, $C_{coat,}$ and an electrolyte resistance, $R_{el,}$ in series. This treatment is additionally useful for the in plane spectra, because the two resistances of the electrolyte

reservoirs can be added together. Finally, the ideal Fickian and the non-Fickian approach were applied. The details about the approaches and the standards for the data treatment were already presented in sections 2.3 and 2.4.2. All samples were measured three times.

4.2.3 Ion diffusion: in plane measurement with embedded electrodes

As mentioned during the sample preparation, comb electrodes as counter electrodes and the working electrode (DEA 28800A59.010-00, Netzsch) were covered by a 52.9±4.1 µm thick clear coat. Then, electrolyte reservoirs were placed at the end of the electrodes at the top of the clear coat to initialise the ion ingress, as illustrated in Figure 4.3. The distance between the single electrodes amounts around 80 µm, while the distance between the last electrode of the comb and the working electrode amounts around 500 µm, with an accuracy of ±10 µm. The EIS measurement was directly started after the addition of 0.5 M NaCl solution to the reservoirs, under standard atmosphere conditions. The spectra were recorded from 100 kHz to 100 mHz, starting at 1 kHz, while the return from 100 kHz to 100 mHz was used for the examination. The runs were repeated every 4 min until the end of the experiment.

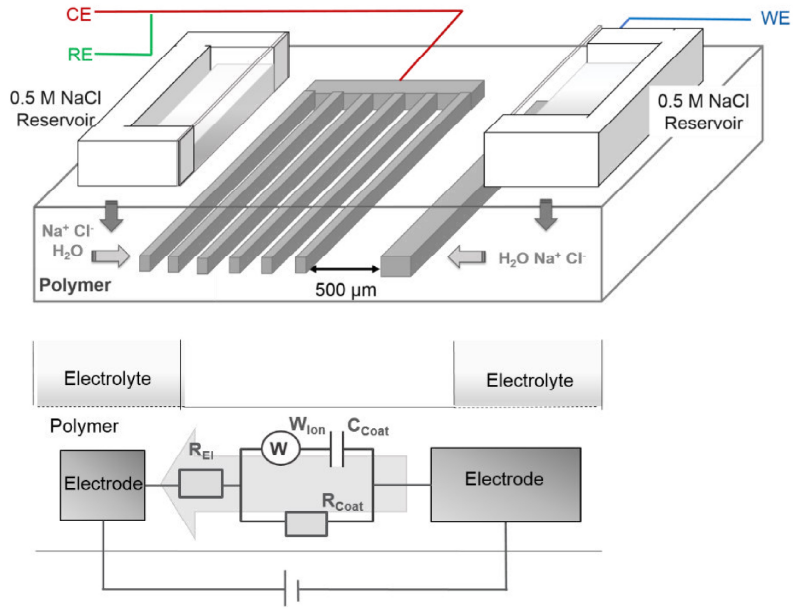

Fig. 4.3 In plane EIS setup and the applied circuit for the calculation of the ion diffusion rates

This setup is comparable to the in plane setup with the two electrode holders. First, the electrolyte has to find its way into the polymer and when the ions reach the electrodes, the transport in the polymer and parallel to the interface is measurable. The examination of the results was done by a Randles circuit with a Warburg element.

4.2.4 Dynamic-mechanical analyses of free films

Several free films were measured with the dynamic-mechanical analyser Q800 of TA Instruments and a tension clamp. The base coats were coated with a doctor knife of 250 µm on a glass plate and were

cured at 70 °C for 5 min and at 145 °C for 20 min. The clear coats were sprayed on a sheet in the same manner as described in 4.2.1 for the HDG steel. Thicknesses of 90 µm were reached after the curing. For the double layer, the base coats were coated again with the doctor knife (250 µm) on a glass plate, were cured at 70 °C for 5 min and coated with the clear coat and a doctor knife of 500 µm and were finished after a curing at 145 °C for 20 min. The dry samples were directly peeled off the sheets and the glass plates, while the wet samples were first stored in 0.5 M NaCl solution before they were peeled off. Then, the films were cut to a size of 10-15 mm x 13 mm and measured with an amplitude of 20 µm (f=1 Hz) and an initial load of 0.01 N with a constant force track of 125 %. The temperature program was divided into eight steps:

(1) 5 °C/min gradient to 0 °C
(2) 3 min isotherm at 0 °C
(3) 1 °C/min gradient to 125 °C
(4) 3 min isotherm at 125 °C
(5) 1 °C/min gradient to 0 °C
(6) 3 min isotherm at 0 °C
(7) 1 °C/min gradient to 125 °C
(8) 3 min isotherm at 125 °C

The films of the single layers were heated from 0 °C to 125 °C (1-4) while the films of the double layers were heated from 0 °C to 125 °C followed by a cooling down to 0 °C and a second heating up to 125 °C (1-8). Two measurements per sample were done as a repeat determination.

4.2.5 Attendant analyses

The IR spectra of the base coats and the clear coat were measured via the Bruker Vector in attenuated total reflection between 500 and 4000 cm^{-1} (100 scans), with a resolution of 4 cm^{-1}.

The multi-angle spectrophotometry was carried out with a Byk-mac (Byk-Gardner GmbH) at the base coat and the base coat-clear coat on glass plates, which were prepared as described in the previous section 4.2.4. The data were averaged of three different spots on the samples.

4.3 Theory – Deborah number as a degree of elasticity

According to the law of conversion of energy, temperature effects on elasticity are given in the following equation:

$$\left(\frac{\partial l}{\partial T}\right)_{f,V} = \frac{1}{f}\left(\frac{\partial U}{\partial T}\right)_{f,V} - \frac{T}{f}\left(\frac{\partial S}{\partial T}\right)_{f,V} \tag{4.4}$$

with the length l, the temperature T, the constant tensile force f, the energy U and the entropy S. The first term expresses the energy elasticity and the second term represents the entropy elasticity, while volume changes dV have to be very small at constant pressure. This thermodynamic relation can be displayed by dynamic-mechanical analyses [13-14]. If stress is introduced to a polymeric film by a temperature gradient, the film will be expanded or compressed and the length of the film will change. Exemplarily, Figure 4.4 shows the stress and the length behaviour of a clear coat during a temperature increase with time.

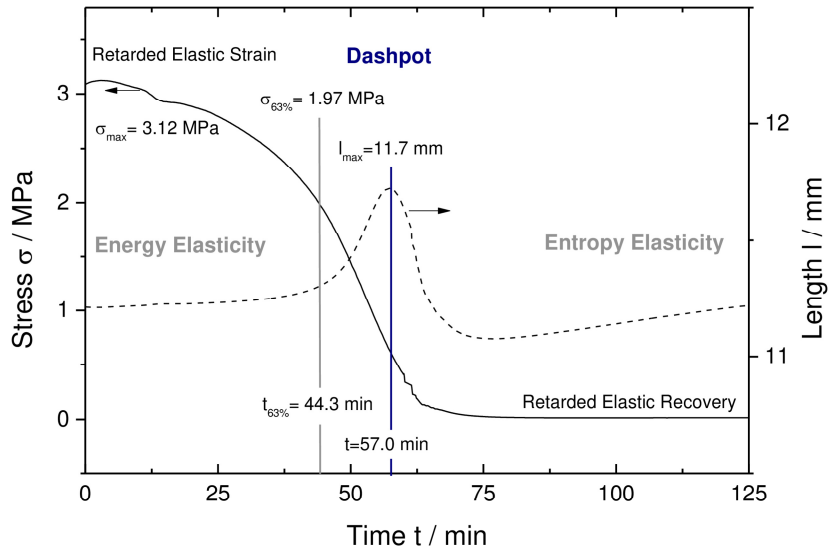

Fig. 4.4 Example: stress relaxation on free films illustrated by the stress and length behaviour of a clear coat during a temperature increase with time

Based on the four parameter model, the following analogies may be drawn [13]:

- *Energy elasticity* represents the elastic straining of bond angles and lengths. All bonds in polymer chains have equilibrium angles and lengths. The deformation involves interatomic bonds, which occur essentially from a macroscopic point of view.
- The *dashpot* represents the resistance of the polymer chains to uncoiling and coiling, caused by temporary mechanical entanglements of the chains and molecular friction during these processes.

- The area of *entropy elasticity* represents the restoring force brought about by the thermal agitation of the chain segments, which tend to return chains oriented by stress to their random, or highest entropy, configuration.

Generally, the dashpot is described by the maximum of the tan delta [13]. This method is suitable for the pure system. However, the water content in the polymer shifts the maximum of the tan delta curve to higher values when the glass transition point T_g is lower than 100 °C. The water evaporates on account of temperature increase during a typically dynamic-mechanical analysis. Therefore, the length is more suitable as a temperature-independent parameter to indicate the dashpot of samples.

Moreover, the Deborah number (De) is strictly defined as the ratio of the time scale of the material response to the time scale of the measurement process or in other words [13-14]:

$$De = \frac{time\ of\ relaxation}{time\ of\ observation} \tag{4.5}$$

When the time of relaxation expresses the time of observation (De=1), the material shows viscoelastic behaviour. If the relaxation time is lower than the time of observation (De<<1), the material will be viscous, and in the case, where the relaxation time is higher (De>>1), the material will be elastic. However, the concept of a single relaxation time applies to first-order response and thus is not applicable to real materials [13-14]. Figure 4.5 illustrates the behaviour of clear coat films with various times of salt water uptake in a Wicket plot. The loss modulus against the storage modulus has to form an ideal semicircle when the clear coat films give a first-order response. However, the response of the clear coats show wide and misshapen semicircles. Nevertheless, the characteristic time for any material can be defined as the time required for the material to reach 1-1/e or 63.2 % of its ultimate retarded elastic response to a step change [14]. This empirical approach can be transferred to the example in Figure 4.4. The ultimate retarded elastic response is equal to the maximal stress (σ_{max}=3.12 MPa) and the approximate time of relaxation is 44.3 min at a stress of 1.97 MPa (=63.2 % of σ_{max}). The time of observation is given by the maximal change of the length. As a result, the clear coat film has a Deborah number of 0.78, which expresses a viscous behaviour.

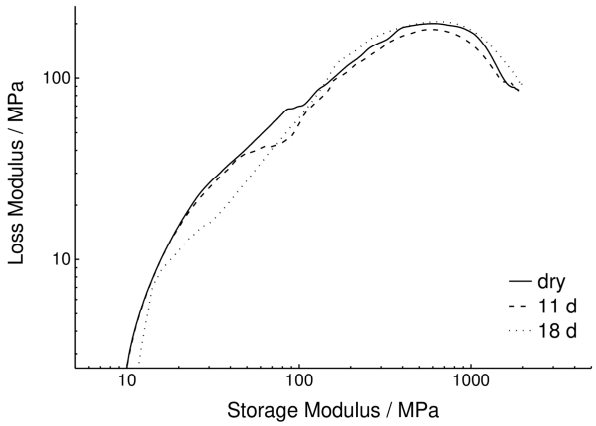

Fig. 4.5 Wicket plot of 90 µm thick clear coat films with various times of salt water uptake (0.5 M NaCl)

4.4 Results and discussion

This chapter characterises the rate-determined transport paths of water in the substrate-containing E-coat, a base coat with and without Al flakes and a clear coat. Moreover, the in plane diffusion of water is compared with the in plane ion diffusion in a wet-dry-wet cycle and the role of the base coat-clear coat interface is highlighted during the salt water ingress. For the interpretation of the data, the ideal Fickian circumstances are assessed by the changes in the effect finish, the glass transition, the Deborah number as a degree of elasticity and the stress and strains present. Thereupon, the adsorption coefficients SC of the non-Fickian law are related to various parameters to estimate the physicochemical expressiveness of this coefficient.

4.4.1 Direction-driven water diffusion at various single layers

Previously, the transport investigations of Chapter 2 and 3 indicate an influence of the in plane flux through the E-coat bulk on the metal interface. Next, the dominance of the normal to the in plane water diffusion through various single layers – the pigment E-coat, the base coat with/without Al flakes and the clear coat – is identified via the normal and the in plane EIS setups. The peculiarities of the layers are pointed out and are related to their anisotropic behaviour and their degree of plasticising.

The anisotropic characteristic of the single layers were analysed during the ingress of the 0.5 M NaCl solution up to 72 h. All normal and in plane EIS results are summarised in the Bode diagrams in Figure 4.6. The diffusion parameters and the water contents are displayed in Figure 4.7, while Appendix A4.2 provides the corresponding Nyquist diagrams and the fitting data.

4.4.1.1 Pigment E-coat

The Bode plot of the 23 µm thick and pigment E-coat (1) shows nearly ideal capacitive behaviour with a linear impedance up to 2.1E8 Ω and phase angles of -90 ° with decreases to -38 ° lower than 1 Hz during the normal electrolyte ingress (1A). More dominant degradation signs of the E-coat are visible in the in plane direction (1B) starting at 10 Hz with an impedance abatement from 2.8E8 Ω to 3.1E7 Ω as well as the phase angle decrease from -90 ° to -7.4 °. The slightly decreased BK water content support the in plane trend with values between 3.0 wt% and 1.2 wt% compared to the normal values in a range between 3.8 wt% and 1.1 wt%. The normal and the in plane diffusion coefficients calculated via the ideal Fickian law overlap at around 1.4 E-13 m²/s, while the non-Fickian values overlap around 2.5 E-13 m²/s. However, the normal adsorption coefficient is strongly negative with up to -0.05 1/min compared to 0.002 1/min for the in plane direction.

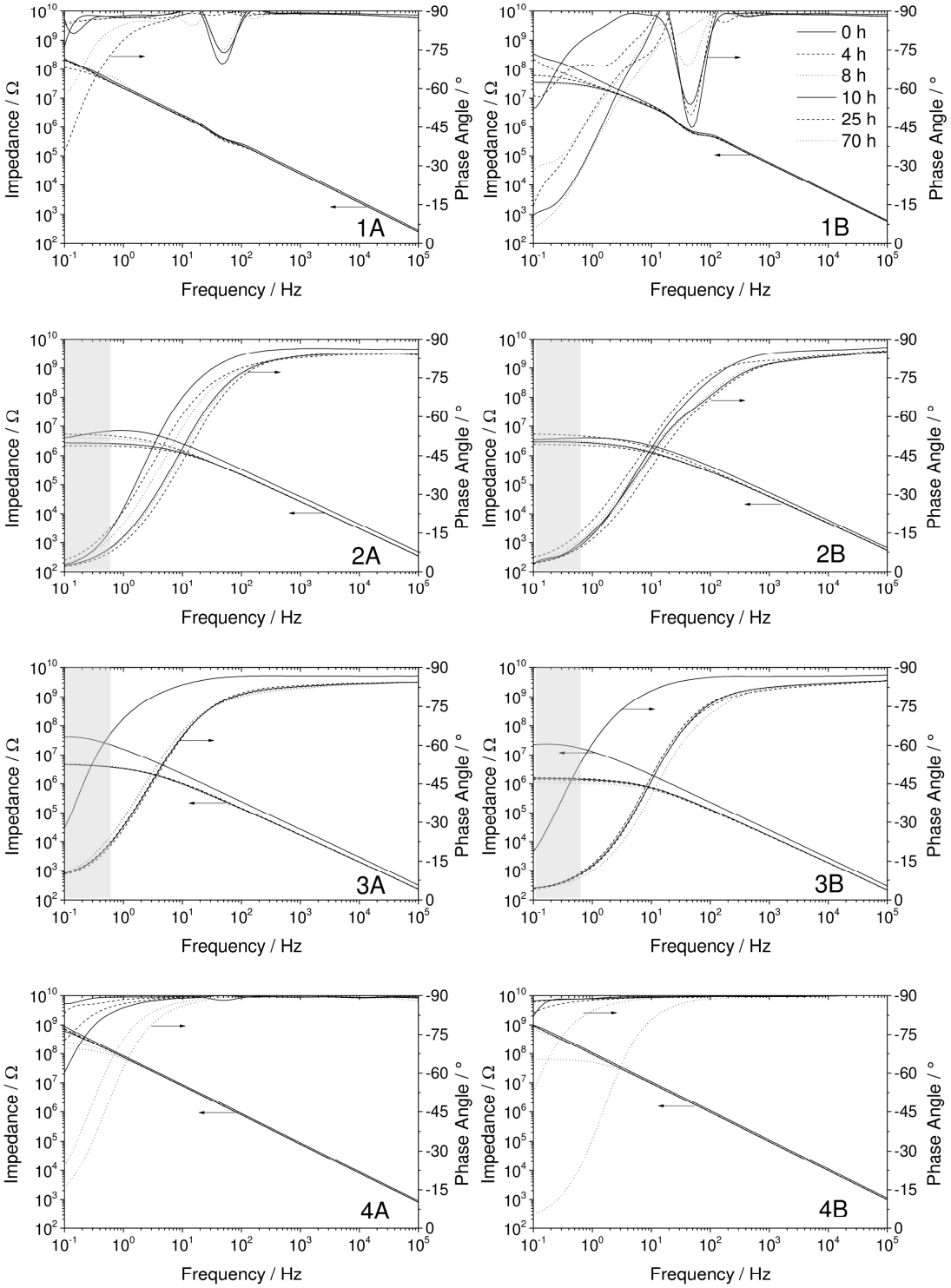

Fig. 4.6 Bode plots of the E-coat (1), the base coat (2), the base coat with Al flakes (3) and the clear coat (4) at HDG steel during the electrolyte ingress up to 70 h measured in normal (A) and in plane direction (B), frequency range: 10 kHz to 100 mHz, start: OCP, amplitude: 20 mV

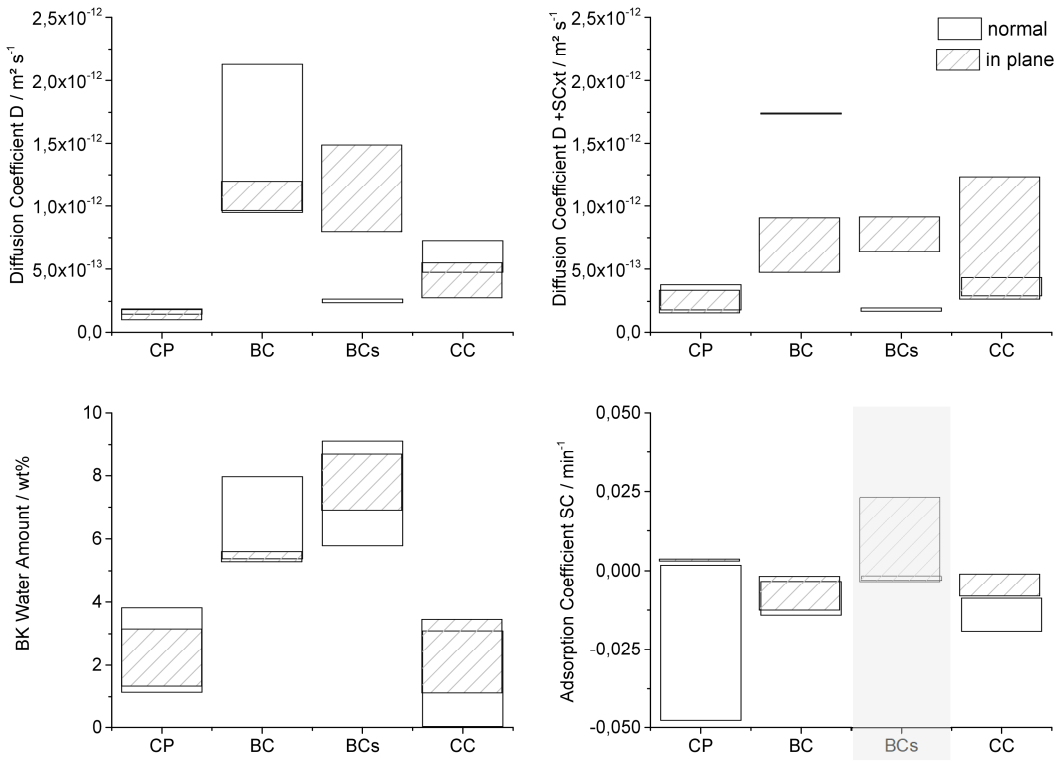

Fig. 4.7 Fickian and non-Fickian diffusion coefficients with the adsorption coefficient SC and the BK water content for the E-coat (CP), the base coat (BC), the base coat with Al flakes (BCs) and the clear coat (CC) in normal (white) and in plane direction (dashed) of the water transport corresponding to Figure 4.6

Previous results of Chapter 2 prove a non-Fickian behaviour of the pigment E-coat and solvated substrate ions in the E-coat due to a transpassive dissolution, while an increased substrate content decreases the normal water diffusion coefficient and the interfacial ion transport. The new results show ideal Fickian behaviour during the in plane ingress due to the hovering of the adsorption coefficient around zero but a strongly negative deviation of the ideal Fickian law during normal ingress. Consequently, it has to be assumed that the non-Fickian deviations are rooted in the normal direction.

During the transpassive dissolution of steel, various scenarios are possible in which hydrated ions and/or complex ions will be formed. Possible scenarios are illustrated in Figure 4.8. According to Elmore [15], the gradient of the ion concentration between the valleys and peaks/mountains of the substrate surface causes a diffusion of the substrate ions through the Nernst double layer and this causes a levelling of the peaks at the substrate surface (a). Additionally, Lewis bases such as amines from the bulk can form complexes with the substrate ions, which cause a mass control at the double layer [16]. If a diffusion- and a mass-controlled transport is existent, then micro-roughness will be embedded like electropolishing with a high gloss (b) [17].

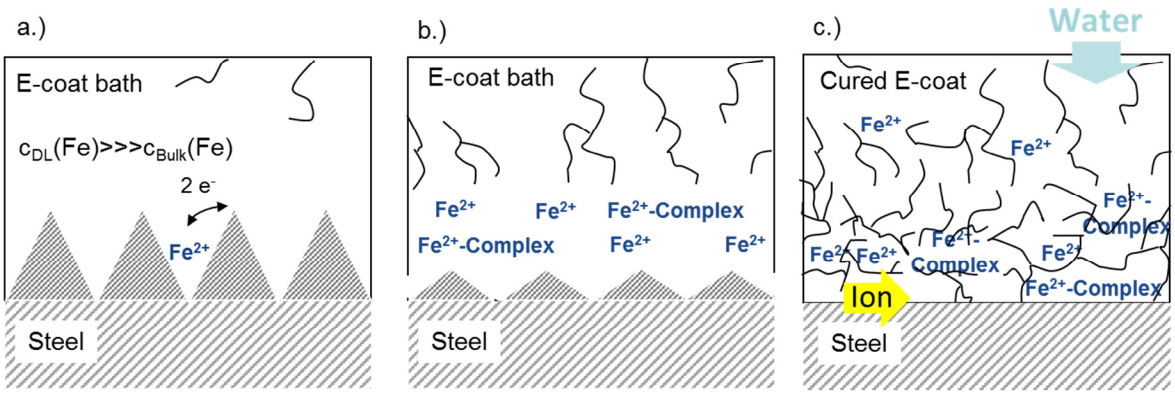

Fig. 4.8 Possible scenarios during the cataphoretic deposition on steel: a) Diffusion-controlled dissolution, b) Diffusion- and mass-controlled dissolution, c.) Fe as a catalyst to increase the cross-linking and the integration of Fe-complexes in the E-coat matrix

Furthermore, some ions such as iron or cobalt can act as a catalyst and increase the cross-linking of the E-coat, especially at the interface (c). The alkaline metal ions can form polyoxometalates via olation or oxolation and template complexes with the saturated amines [18] and/or the triphenylphosphine (E-coat catalyst) [19] as ligands to change the E-coat distribution in favour of specific macrocyclic compounds. Interestingly, the pigment paste of the E-coat bath contains triphenylphosphine [20] as well, while the pigment E-coat was eye-catching due to the five times lower sub-surface flux compared to that of the clear E-coat, see section 2.4.4.1. In addition, it has to be assumed that a higher concentration of the ligand will support the cross-linking. A levelling due to the deposition or/and an increase of the cross-linking improves the corrosion protection of the E-coat. Metal complexes in the polymeric network will have advantages and disadvantages. While metal complexes tend to various colours and dye the coating, an enrichment of substrate ions at the interface decreases the driving force of the interfacial ion migration. The ion concentration of the bulk aligns with the metal substrate, the potential gap decreases and the interfacial ion velocity decreases with the increase of the substrate content in the coating, as verified at the E-coat/steel interface in section 2.4.4.3. Williams and co-workers [21] additionally prove a significant decrease of the sub-surface flux at the zinc interface due to embedded zinc particles. Intelligent developments of surface treatments or E-coats can use this effect by a specific dissolution of active species at the surface or in the substrate during the deposition and/or the curing procedure. However, with the exception of the interface, no significant anisotropy is reflected in the diffusion data through the E-coat on HDG steel.

4.4.1.2 Base coat without Al flakes

The Bode plots of the 30 µm thick base coat without Al flakes (2) show nearly the same curves with a resistance behaviour at low frequencies and a capacitor behaviour at higher frequencies for the normal (2A) and the in plane direction (2B). The impedance reaches values of 5.4E6 Ω at 100 mHz. Slight differences are obvious at the impedance resistance, which ranges up to 4 Hz for the normal and to 10 Hz for the in plane ingress. The phase angles decrease from around to 85 ° to -2 ° (normal) and -7 ° (in plane) during the change of the capacitive to the resistant course. The BK water content amounts 7.9-5.1 wt% while the results of the normal measurements tend to higher water contents than the results of the in plane measurements. This tendency is reflected in the ideal diffusion coefficients with values of around 1.3E-12 m²/s, too. However, the normal non-Fickian diffusion coefficient is significantly higher with 1.7E-12 m²/s than the in plane one at 6.7E-13 m²/s. The adsorption coefficients are nearly equal at -0.009 1/min.

The change of the glass transition temperature T_g during the salt water uptake is given in Figure 4.9. The base coat film (BC - grey) was measured in the dry state, after 12 days and 19 days of soaking between 0 °C and 125 °C. The flat courses of the storage modulus up to 535 MPa and tan delta with a maximum of 0.38 are obvious. The loss moduli are disregarded in favour of clarity. Of course, these films have to be cooled down more until -15 °C with a small temperature gradient of 0.5 °C/min, for a detailed analysis. However, the results of the base coats should be comparable to the clear coat and the double layer with two heating cycles. Due to this, the temperature span of these systems is very large and a single measurement is very time-

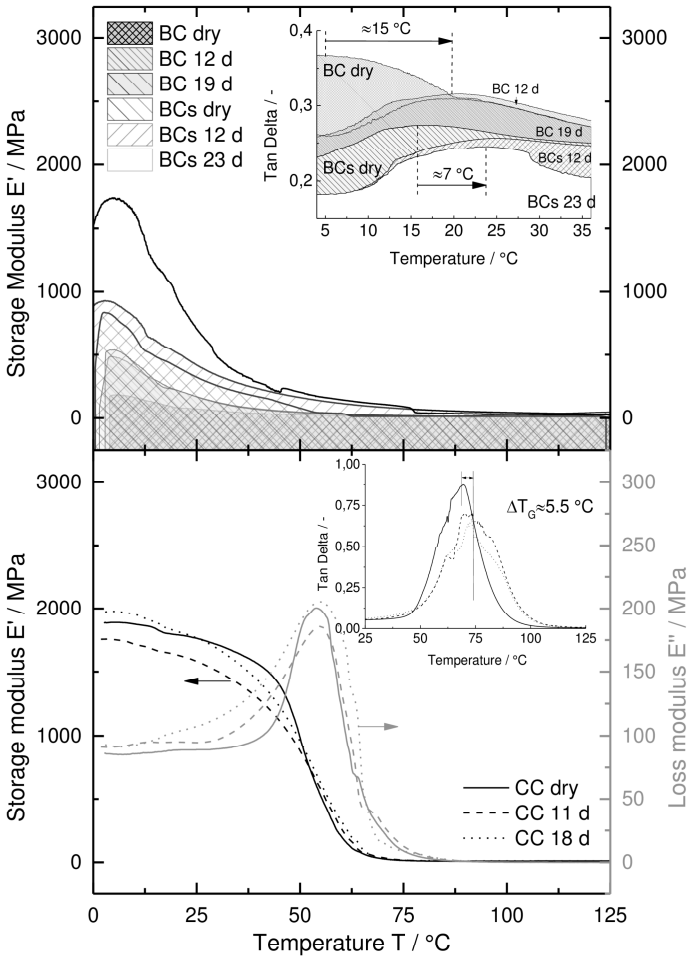

Fig. 4.9 Dynamic behaviour of the base coats (BC), the base coats with Al flakes (BCs) and the clear coat films (CC) after various days of soaking in 0.5 M NaCl solution; Conditions: T=0-125 °C, dT/dt=1 °C/min, f=1 Hz, averaged curves of repeat determination

consuming, especially as a repeat determination, which is why the chosen procedure only allows a vague assessment of the glass transition points at the base coat systems. The dry base coat shows a maximum tan delta of around 5 °C, while the maximum shifts to 20 °C after 12/19 days of soaking.

Typically, the main binder of the base coat dries physically at low temperatures, while another part of the binder initiates the plasticising of the physically dried binder and further cross-linking [20]. Therefore, core-shell dispersions are used with a high inner glass transition temperature of the acrylic resin of around 20 °C [3] and an low outer glass transition temperature of the polyurethane of around 0 °C [3]. As a result, the base coat is viscoelastic and has a low glass transition temperature of 5 °C ($T_{g\ Coat}$), which is necessary to ensure a planar orientation of the Al flakes. The salt water uptake causes an increase in the glass transition temperature to 20 °C. In general, it would be expected that water acts as a plasticiser and the glass transition temperature of the base coat shifts to a glassy state as it is often reported for thermal ageing. However, the increase of the glass transition temperature can be understood comprehensible when one uses the Fox equation [22]:

$$\frac{1}{T_g} = \frac{w_{Coat}}{T_{gCoat}} + \frac{w_{Water}}{T_{g\,Water}} \tag{4.6}$$

This equation based on the theory of interstitial free volumes and occupied volumes in the polymer [23] and assumes that contributions of the components are additive [22]. The glass transition point of water amounts to -134 °C to -138 °C ($T_{g\ Water}$) using differentially thermal analyses and other methods [24-25]. Assuming a water content of 5 wt% (w_{Water}), the glass transition temperature of the soaked base coat film would achieve an increase from 5.0 °C to 5.3 °C, which conforms to the measured trend. Moreover, the water will evaporate on account of the temperature increase and will shift the tan delta to higher values. A decrease in the glass transition temperature of the base coat has to be present in the absence of water. Due to the high degree of viscoelasticity and the pigments, a non-Fickian behaviour has to be concluded, in which the normal water diffusion of the base coat is faster than the in plane water diffusion. One self-evident reason for the anisotropy seems to be the evaporation of the solvent during the curing procedures, result in pores that act as the entrance point for the electrolyte.

4.4.1.3 Base coat with Al flakes

The 29 µm thick base coat with Al flakes (3) shows a conspicuous picture in its normal (3A) and in plane Bode diagrams (3B, Figure 4.6). The curves are characterised by a resistance at low frequencies and a capacitor at higher frequencies. The transitions from the resistance to the capacitor are equal to the pure base coat at 4 Hz in the normal direction and at 10 Hz in the in plane direction. However, impedances are higher with values of 4.2E7 Ω (normal) and 2.3E7 Ω (in plane) compared to the base

coat without Al flakes (5.4E6 Ω for both) at 100 mHz. Conversely, the water content is slightly increased from the normal to the in plane ingress and is generally higher compared to base coat without Al flakes. Interestingly, the diffusion results reflect impressively the consistency of the in plane diffusion data visualised by equal Fickian and non-Fickian diffusion coefficients for the in plane water uptake. Furthermore, the normal diffusion coefficients of the base coat with the Al flakes are always decreased in comparison to the in plane diffusion coefficients. With regard to the viscoelasticity, the storage moduli increase from the dry state, 12 days to 23 days of soaking up to 1750 MPa, while the dash pot, tan delta, decreases with a shift to increased glass transition temperatures from approx. 16 °C to 23 °C. Additionally, residual water is found in the IR-ATR spectra at 3200-3600 cm^{-1} after having been heated up to 125 °C (see Figure 4.10 bottom).

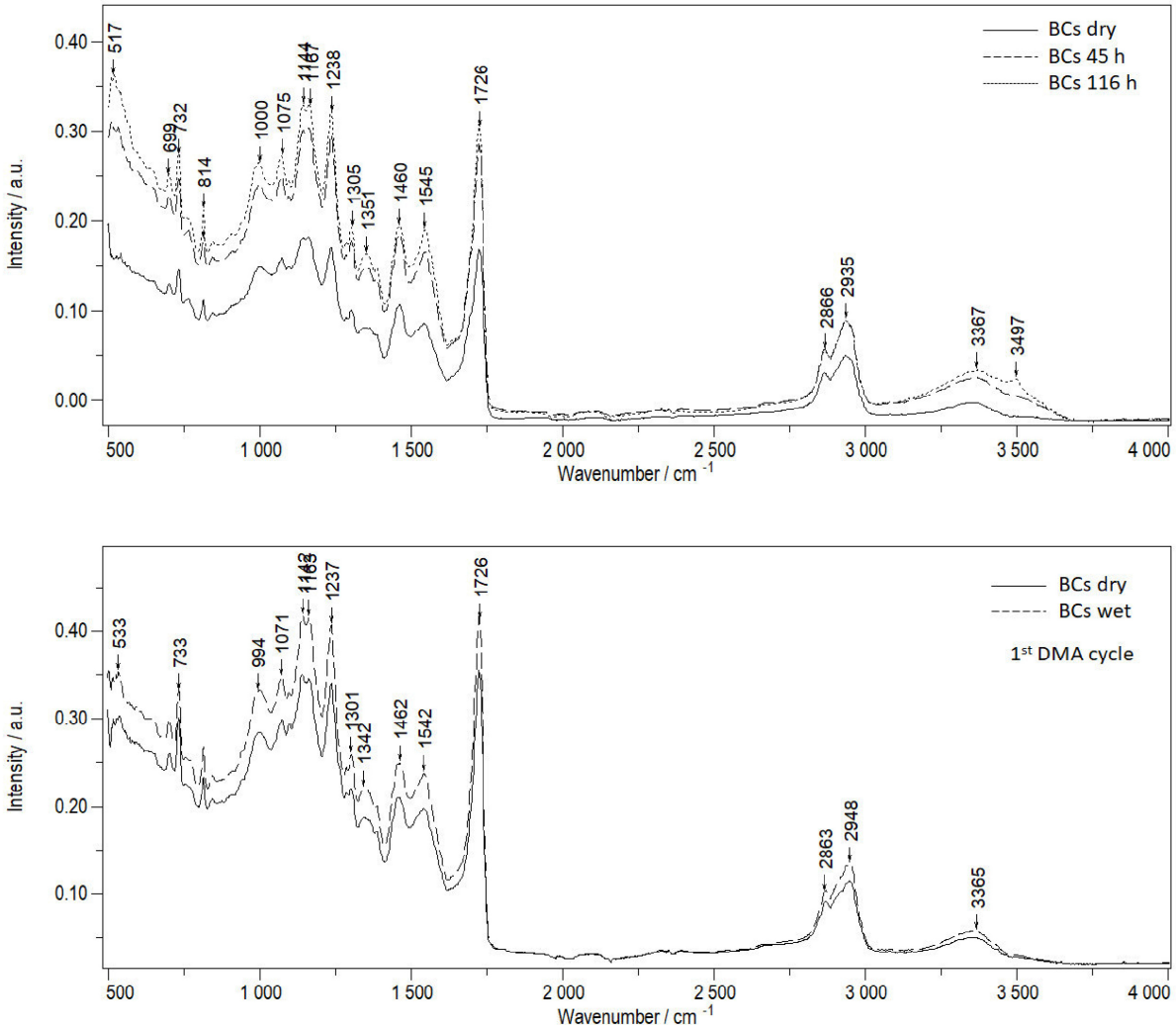

Fig. 4.10 IR-ATR spectra of the base coat with Al flakes (BCs) in the dry state, after 45 h and 116 h of salt water uptake (top) and in the dry and wet state after the first heating up to 125 °C (bottom), spectral resolution: 4 cm^{-1}

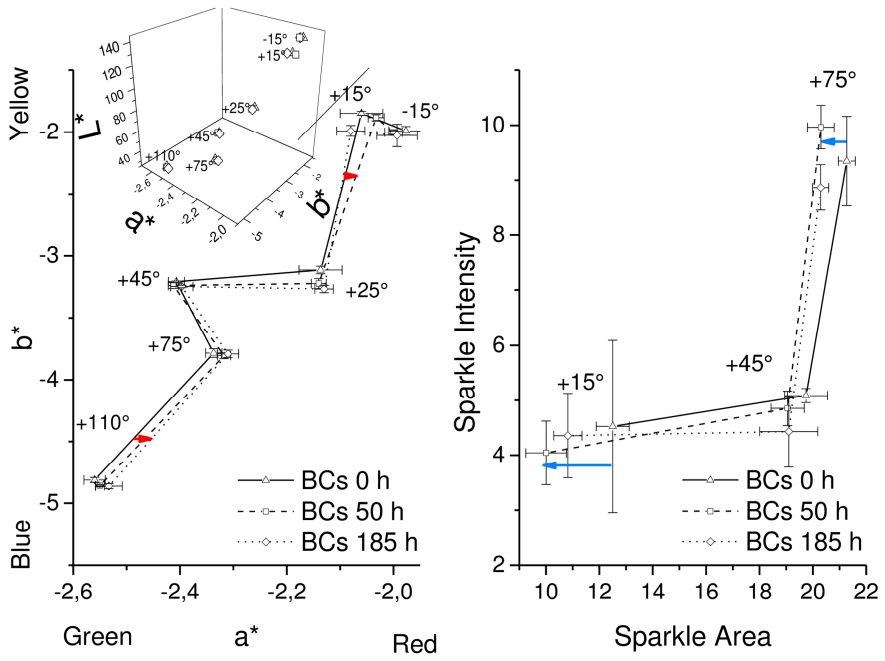

Fig. 4.11 Results of the multi-angle spectrophotometry of the base coat with Al flakes in a dry state, after 50 h and 158 h of salt water uptake.

The influence of the salt water ingress on the effect finish is determined by IR-ATR spectroscopy and multi-angle spectrophotometry on the dry sample and after 45 h and 185 h of salt water ingress. The results are displayed in the top diagram of Figure 4.10 and Figure 4.11. Additional material is given in Figure A4.3.1 of the appendix. The IR-ATR spectra show increased water vibrations in the wet states, as anticipated, but the water vibration exhibits two amplitudes at 3367 cm^{-1} and 3497 cm^{-1}. The results of the multi-angle spectrometry show a constant brightness L* and a nearly constant blue-yellow axis b* while the green-red axis a* slightly shifts towards the red. The decrease of the sparkle area at 15 ° and 75 ° is more prominent compared to the colour changes.

When the Al flakes come into contact with water, acid or alkaline media, they will be attacked and dissolved under hydrogen evolution [26, 27]. Inorganic or organic compounds should protect the Al flakes like phosphoric ester, chromate and phosphate conversion layers by a good corrosion resistance and an interlacing to the binder [20]. Nonetheless, the flakes are a weakness in the coating and are able to bound water due to their high polarity. The IR spectra already point to bound (3367 cm^{-1}) and free water (3497 cm^{-1}). As a result, the water content increases compared to the base coat without the Al flakes. The higher brittleness due to the addition of the Al flakes causes a shift to a more rubbery-like state expressed in increased glass transition temperatures. Additionally, the plate-like shape of the Al flakes oriented parallel to the substrate forms itself a diffusion barrier in the inner base coat, while the decreased sparkle area points to a disorientation of these diffusion barriers with time. The free length of path increases in the normal direction which is why the in plane water diffusion is four times

faster than the normal water diffusion – assuming non-Fickian conditions based on the viscoelasticity, the high water content and the pigment content. The differences rendered conspicuous by the comparison of both base coats and their normal water diffusion coefficients. Here, the water diffusion of the pure base coat is ten times faster than the water diffusion with Al flakes.

4.4.1.4 Clear coat

The normal (4A) and the in plane Bode plots (4B) of the 53 thick clear coat in Figure 4.6 illustrate ideally capacitive behaviour across the total range of the frequency. At 100 mHz, the highest impedances were detected with 8E8 Ω (normal) and 8.4E8 Ω (in plane) of the complete study of the single layers. Meanderings are obvious for both directions in phase angle decreases at low frequencies, while these slight degradation signs are more prominent at the normal distance. The clear coat contains up to 3.3 wt% water. The normal and the in plane diffusion coefficients overlap when using the Fickian and the non-Fickian approach, while the normal adsorption coefficient SC tends towards more negative deviations as the in plane coefficient. Figure 4.9 (bottom) shows the results of the dynamic-mechanical analyses in the dry state, after 11 days and 18 days of salt water uptake. The clear coat shows a classic curve progression during the temperature scans. A little step of the storage moduli at around 16 °C indicates the ß-transition which smears over at the wet clear coats. With continuous heating, the storage modulus rapidly decreases, whereby the slope of the wet samples are more flattened compared to the dry samples. Conversely, the loss modulus increases faster at the wet samples until the glass transition is reached. The tan delta shifts from 68.5 °C to approx. 74 °C, whereupon the value of the tan delta decrease due to the salt water uptake. No residual water is found after this heating, see Figure A4.2.2.

The intention of the clear coat is to protect against the influences of weather and mechanical wear and tear and this is reflected in the results, too. The high resistance to dammed-up water is supported by the high impedances at 100 mHz and the ideally capacitive behaviour. The curing of the clear coat at 145 °C reduces the water content compared with the physically dried base coats [28], while curing above the dry glass transition temperature (T_g(CC)~68 °C) generally causes the increased adhesion of the clear coat [29]. Additionally, no anisotropy is confirmed by the diffusion data. This result will be rooted in the high flexibility and the excellent intercoat adhesion of the clear coat which is necessary to reduce the damage caused by chippings. The toughness [30] which is empirically expressed by the storage modulus of the ß-transition (< 16 °C) changes insignificantly due to the salt water. Moreover, there are three techniques to determine the glass transition point – using the maximum of the tan delta curve, the maximum of the loss modulus or the intersection of the tangents of the storage modulus – with three different results for the clear coat. The glass transition temperature increases by

the tan delta, whereby it is nearly stable with the loss modulus and it slightly decreases via the tangents of the storage modulus. As a result, it has to be assumed that the clear coat does not plasticise significantly after 18 days of soaking and the Fickian and the non-Fickian law have to be equally applicable to the isotropic water diffusion.

4.4.1.5 Relation between the adsorption coefficient SC and the physiochemical parameters

For the assessment of the physicochemical expressiveness of the adsorption coefficients SC, the maximal stress, the length and the tan delta were extracted and the changes in these parameters from the dry state to the state of the longest salt water uptake were determined. Figure 4.12 presents the results, while the raw data are attached in Table A4.2.5. Note that the dynamic-mechanical analysis with the tension clamp used only provides a one-dimensional view of the stress and the length of the film – given a supported film, it will be the in plane direction. Regardless, the means of the in plane and the normal adsorption coefficients SC are correlated with the other parameters. The adsorption coefficients of the base coat and the clear coat show negative deviations of the ideal Fickian law with -0.009 1/min (BC both) and -0.006/-0.011 1/min (CC in plane/normal) while the base coat with the Al flakes deviates more positively from the law with 0.009/-0.002 1/min (BCs in plane/normal). The length decreases at the base coat with Al flakes and the clear coat, but the length increases at the pure base coat due to the salt water uptake. Interestingly, the changes in the tan delta tend to the SC-order of the single layers. The tan delta decreases by the water ingress. The smallest change of the tan delta is displayed in the base coat with Al flakes followed by the base coat and the clear coat. This layer order is further found in the BK water contents, as presented in Figure 4.7. However, the stress confirms the

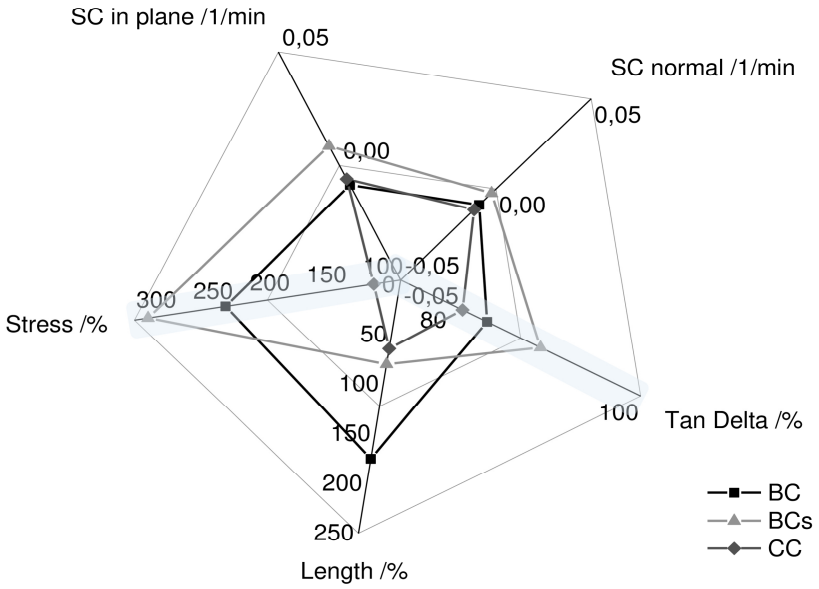

Fig. 4.12 Relation between the adsorption coefficients SC and the changes in the maximal stress, tan delta and length from the dry state to the longest salt water uptake for the base coat (BC), the base coat with Al flakes and the clear coat films (CC)

converse trend, whereupon the stress at the base coat with Al flakes is three times and the pure base coat two-and-a-half times higher compared to the clear coat.

Regardless of the binder types, the main difference between the three coatings is the degree of pigmentation. The clear coat can act in a flexible manner. It can freely expanse/strain which is why the internal stress is strongly reduced compared the base coats. In the base coat, the water transport and the expansion are hindered by the colour particles. Stress occurs in the layer. The addition of the plate-like Al flakes strengthens the internal stress, as illustrated in Figure 4.13. However, the dominance of stress and strain depends on the amount of water, which further depends on the binder system. Conversely, the tan delta as a quotient of the loss modulus and the storage modulus expresses the abatement of water in the layer due to heating. Due to this, the BK water amount conversely acts to the tan delta. As a result, the adsorption coefficients represent the trend to stress and stored water in the investigated layer.

Note that this conclusion is representative for the results at hand. However, the water content and the kinetic data were determined at supported coatings (on HDG steel), while the viscoelasticity, the stress and the strain were measured at free films. These films were cured and soaked in salt water on a glass plate or sheet to avoid changes in solvent evaporations, boundary conditions or the promotion of selective crystallisation in the layer. Nonetheless, stress and strain will change on a supported coating due to the interfacial bonds. Thus, these results only reflect the general trend of the coating system disregarding the metal interface.

4.4.1.6 Conclusion of single layers

The E-coats show neither a plasticising nor an anisotropy through the layer during the salt water uptake. However, the interfacial activities are prominent while the substrate ions can have the potential to increase the cross-linking at the interface due to their dissolution during deposition. Conversely, the base coats react via plasticising and anisotropy. The coloured base coat has a faster normal diffusion, which is rooted in its opened pores that act as an entrance for the salt water. The addition of the Al flakes blocks normal diffusion, while the normal diffusion is then ten times slower compared the base coat without the Al flakes. At the clear coat, no significant plasticising is proven which is why the Fickian and the non-Fickian laws are equally suitable for the isotropic diffusion present. Moreover, the adsorption coefficients tend to relate to the stored water and the stress present of the layer system, whereby the stress at the base coat with Al flakes is three times and the base coat two-and-a-half times higher compared with the clear coat.

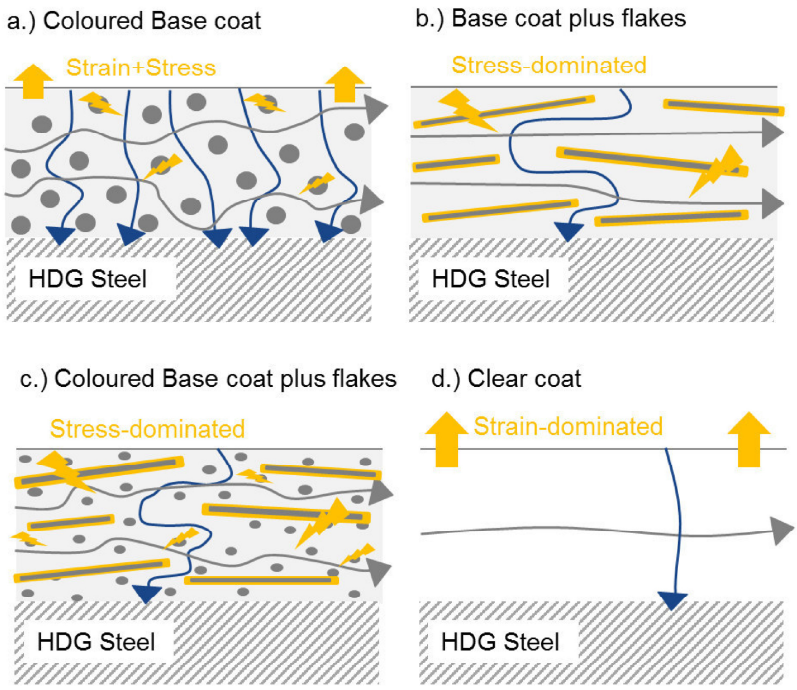

Fig. 4.13 Transport models of the investigated single layers during the salt water uptake

4.4.2 In plane ion diffusion in a wet-dry-wet cycle

The previous section focuses on water diffusion but corrosion and de-adhesion are additionally promoted by ions such as chlorides or sulphates. Therefore, the in plane diffusion of water is compared with the in plane ion diffusion at the 53 µm thick clear coat in a wet-dry-wet cycle via embedded electrodes.

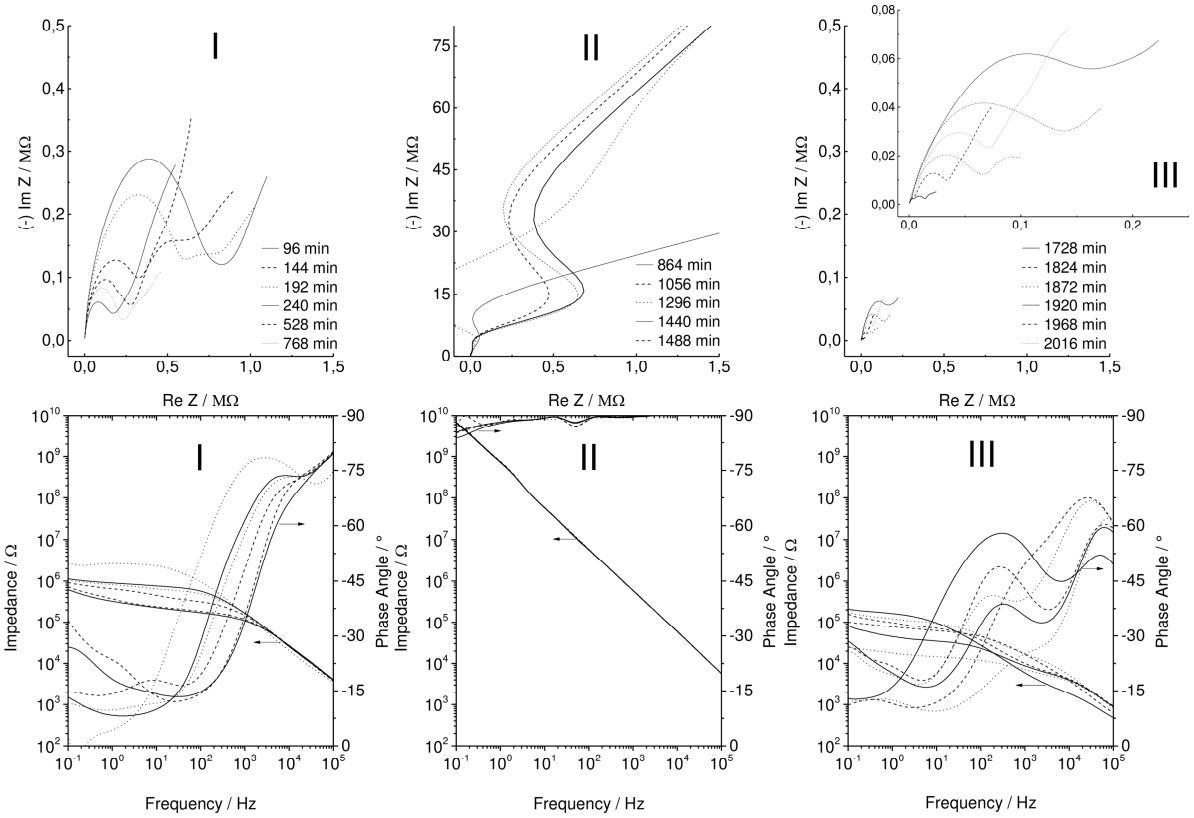

Fig. 4.15 Nyquist and Bode plots of the in plane measurement via embedded electrodes; I) after the 1st addition of 0.5 M NaCl solution, II) during the dry section, III) after the 2nd addition of 0.5 M NaCl solution; frequency range: 10 kHz to 100 mHz, start: OCP, amplitude: 20 mV

Figure 4.15 presents the Nyquist and Bode plots after the first addition of 0.5 M NaCl solution (I), during the dry section (II) and after the second addition of the NaCl solution (III). In the first wet section (I), the Nyquist diagrams were displayed by growing and decreasing semi-circles with linear slopes in an imaginary dimension up to -0.4 MΩ and a real extent up to 1.2 MΩ. The Bode diagrams show a large resistive range of around 1 MΩ up to 5 kHz, followed by a capacitive descent. At low frequencies, the phase angles indicate irregularities in range lower than -32 °, while the phase angles continues with an increase up to -80 °, accompanied by a small step at around 1-10 kHz. During the dry section (II), the Nyquist diagrams exhibit inductances up to imaginary -75 MΩ and real 1.5 MΩ and the Bode diagrams are characterised by an ideal capacitor with phase angles of -90 ° and a linear impedance course up to 10 GΩ. In the second wet section (III), the Nyquist diagrams show growing and decreasing semi-circles

with linear slopes similar to those observed during the first wetting. However, the impedances significantly decrease to imaginary -0.08 MΩ and to real 0.25 MΩ. The Bode diagrams have large resistance areas with capacitive slopes and resistive plateaus at intermediate frequencies and the phase responses are minimally displayed by two time constants with a maximal phase angle of -70 °.

The observed semi-circles characterise a kinetic control due to the formation of a double layer which indicates that water reaches the embedded electrodes in the first and the second wet sections. Note that if the semi-circles are caused by the E-coat, they would have been found in the dry section. More than a single semi-circle leads to the assumption that kinetic processes/charge transfers overlap with individual time constants – for example, as a result of the achievement of the next single comb electrode. This case is very plainly observed during the second wetting. Each of these semi-circles is presentable by an RC element in the circuit. Additionally, a diffusion of an ion species exhibits a linear slope with an angle of -45 ° as found in the Nyquist diagrams. This Warburg impedance is small at higher frequencies, because the ion species has to move a small pathway, while the Warburg impedance increases with the decreasing of the frequency due to the longer pathway. However, the calculation of the ion diffusion by the Warburg element will be manipulated because the linear slopes sometimes deviate from -45 °. Conversely, the dry section can be easily assessed by isolative properties due to the inductances and the high resistances.

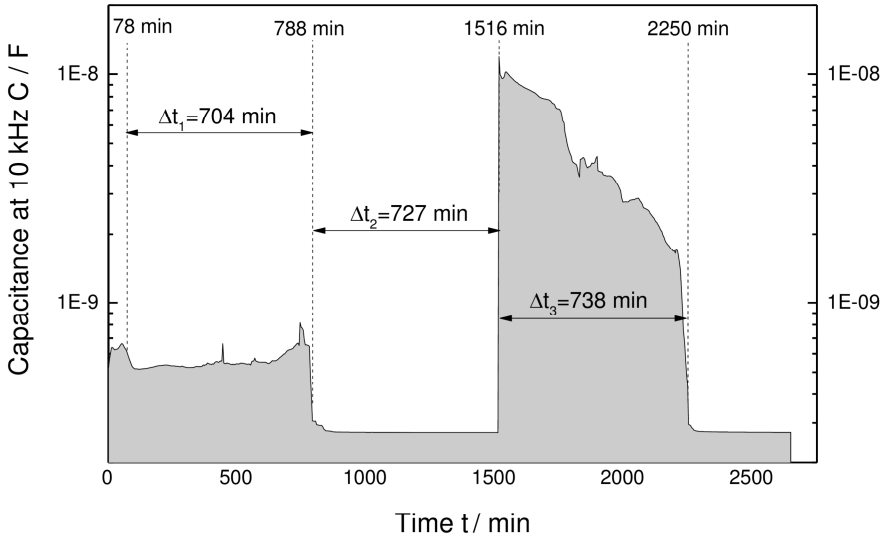

Fig. 4.16 Capacitance at 10 kHz during the in plane measurement with embedded electrodes in a wet-dry-wet cycle, addition of 0.5 M NaCl at t=0 min and t=1516 min, Δt_1 and Δt_3 indicate the time spans with linear slopes in the Nyquist diagrams.

An impression of the time line of the experiment is given by Figure 4.16 which presents the development of the capacitance at 10 kHz. The diagram shows four stages of the capacitance. After the first addition of the 0.5 M NaCl solution, the capacitance rapidly increases and levels off at approx. 5E-10 F up to 788 min while linear slopes in the Nyquist diagrams occur after 78 min until the end of this stage. Then, the capacitance decreases to 2.7E-10 F for a while. This stage is dominated by the inductance and is defined as the dry section. Next, the reservoirs were filled again with 0.5 M NaCl solution for around 1510 min. Thereupon, the capacitance increases very fast to a magnitude of 9.6E-9 F (at 1516 min), then, the capacitance continually falls down to 1.6E-9 F in 738 min before it completely reduces to 2.7E-10 F and stabilises there.

Numerous studies [31-32] assume that the coating capacitance is negligibly affected by accompanying processes at and above 10 kHz and it is dominated by the water uptake. As a result, the water saturation has to be reached very quickly, while the ion diffusion occurs around 78 min later than the water transport during the first wet section. After the second addition of the 0.5 M NaCl solution, the water transport and the ion diffusion are similarly observed. The high initial capacitance of 9.6E-9 F suggests that the water content in the clear coat is significantly higher than that of the first wet section, but it decreases with time until the sample is dried again.

By means of the Nyquist and Bode plots (Figure 4.15), the difficulties in determining the ion diffusion coefficients become apparent. When the water achieves the next electrode with time, a new RC element has to be considered. Moreover, the linear slopes of the Nyquist diagram sometimes differ from -45 °, which is why the ion diffusion determination will be manipulated via the slope deviations. Therefore, an analytical approach was followed based on the Warburg element in which the equation (4.7) [33, 34] has to be fulfilled:

$$ReZ = R_{El} + R_{Coat} - \left(\frac{RT}{z^2F^2A\sqrt{D_{Ion}}}\left(\frac{1}{c^0}\right)\right)^2 C_{Coat} \qquad \text{at} \quad \frac{\partial ImZ}{\partial ReZ} = \tan(-45°) = -1 \tag{4.7}$$

As already mentioned, the ion diffusion is defined by a linear slope of -45 ° in the Nyquist plot due to this, all events were selected in which the first derivation accounts for -1. The sum of the electrolyte resistance R_{El} and the coating resistance R_{Coat} is given by the impedance at low frequencies (100 mHz) [34], while the coating capacitance C_{Coat} is represented at 10 kHz [31-32]. Additionally, the equation is completed by the universal gas constant (R=8.31451 $JK^{-1}mol^{-1}$), the temperature (T=298.15 K), the number of molar electron transfers (z=1), the Faraday constant (F=96485.3329 C), the electrolyte concentration (c_0=0.5 $molL^{-1}$) and the area (A=80.1 µm x 2000 µm=1.6E-7 m^2).

Figure 4.17 presents the results in which the time domains express all events in the time spans of the wettings. During the first wetting (I), the ion diffusion coefficient D_{W1} hovers at around 1.5E-14 m²/s. Due to the second wetting (III), the ion diffusion coefficient D_{W3} is strongly increased with approx. 7.3E-13 m²/s, while the coefficient steeply declines to 2.0E-15 m²/s ($D_{W3.1}$) later on.

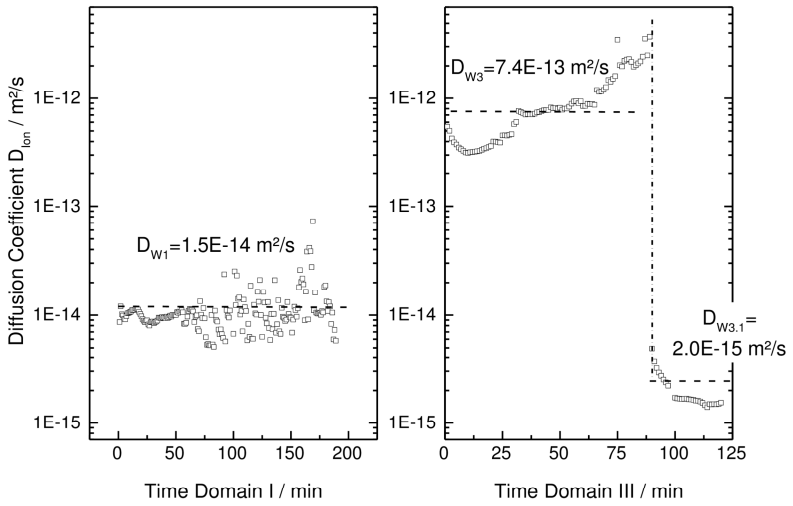

Fig. 4.17 In plane ion diffusion coefficients of the clear coat during the first wetting (I) and the second wetting (III) analytically calculated via the Warburg element.

Compared to the in plane water diffusion results in the section 4.3.1, water is a potency faster than the solvated ions during the first wetting. At the beginning of the second wetting, the diffusion coefficients nearly equalise, while the ion diffusion is then two potencies slower than water. It has to be concluded that the ionic transport pathways are introduced by the action of water during immersion [35]. Alkaline hydrolysis reactions, leaching out of unreacted material or else cause a damage in the polymer matrix [35-37]. These local failures gradually form hydrophilic channels traversing the film [35], which are the transport pathways for the ions, as illustrated in Figure 4.18. When the ions completely conquer the channels of the first wetting, new channels have to be formed by water. As a result, the ion transport is blocked until new channels are developed by water. Additionally, it is discussed that cations contribute to the polymer degradation by inducing localised morphological changes via ion exchange reactions or mass actions [38, 39]. The findings are further supported by an EIS/UV-vis

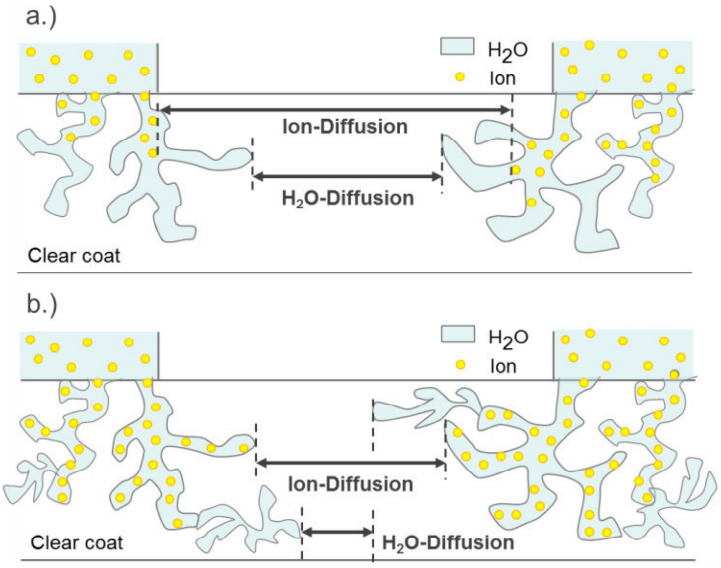

Fig. 4.18 In plane water and ion diffusion model in a wet-dry-wet cycle: a.) First wetting, b.) Second wetting

study at acrylic dispersions [40] and a study in which pure water is faster compared to salt water by a normal uptake through a clear coat [41].

Briefly, an initial salt water uptake leads to a fast saturation of the clear coat, while the ions diffuse a potency behind the water. After a drying section followed by a next initiation of salt water, the ions diffuse faster and in a way that is comparable to water due to the water-induced damage caused by the first wetting. However, later on, the ions are blocked around two potencies because new hydrophilic channels through the clear coat have to be formed by water.

4.4.3 Direction-driven transport at polymer-polymer interfaces

The base coat and the clear coat are completely different systems with regard to their plasticising and their anisotropic behaviour during the salt water ingress. At the auto bodies, the clear coat has to protect the base coat, whereby they were applied wet in wet to avoid any intermediate curing. Due to this, the double layers of the base coat and the clear coat have to fulfil strict requirements, which is why this section focuses on the characteristic of this double layer with and without Al flakes.

4.4.3.1 Normal and in plane water diffusion

The rate-determined transport pathway of water through the double layers, base coat – clear coat (BC-CC) and base coat with Al flakes – clear coat (BCs-CC), should be assessed by the results via the normal and the in plane EIS measurements during the ingress of the 0.5 M NaCl solution up to 72 h. Therefore, the Bode diagrams are given in Figure 4.19, which is supported by Figure 4.20 with the diffusion and water data, while Appendix A4.3 presents the corresponding Nyquist diagrams and the raw fitting data.

In general, the Bode plots negligibly differ from each other. They show ideally capacitive behaviour up to the GΩ-range and phase angles between -80 ° and -90 °. Slight variations become obvious by a look at the impedance at 100 kΩ, whereby the normal impedances (A) are always lower than the in plane impedance (B). The Nyquist plots display no classic circuit elements due to the overlapping of various time constants, especially at the double layer with the Al flakes. A more distinct picture of the results is provided by Figure 4.17. According to the ideal Fickian approach, the double layer shows an anisotropy with a dominating normal diffusion of 5.4E-12 m²/s. Due to the addition of Al flakes, the trend to an increased normal diffusion is also exhibited, but the normal and the in plane diffusion coefficients overlap in a small range. By using the non-Fickian approach, the results are converse. The diffusion coefficients of the pure double layer are comparable at around 2.1E-13 m²/s, while the Al

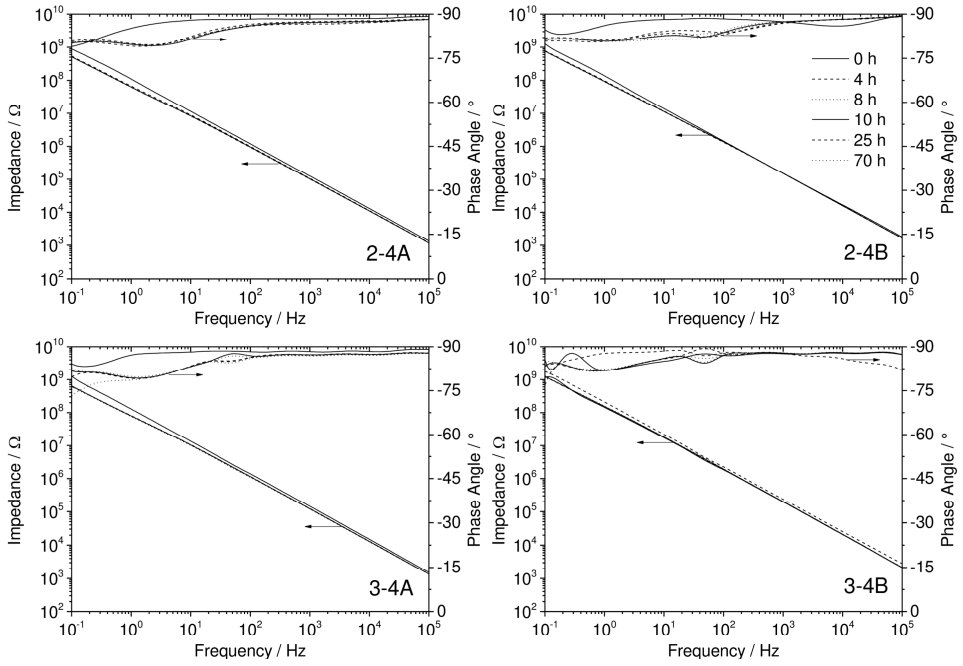

Fig. 4.19 Bode plots of the double layers: base coat – clear coat (2-4) and base coat with Al flakes – clear coat (3-4) during the electrolyte ingress up to 70 h measured in normal (A) and in plane direction (B), frequency range: 10 kHz to 100 mHz, start: OCP, amplitude: 20 mV

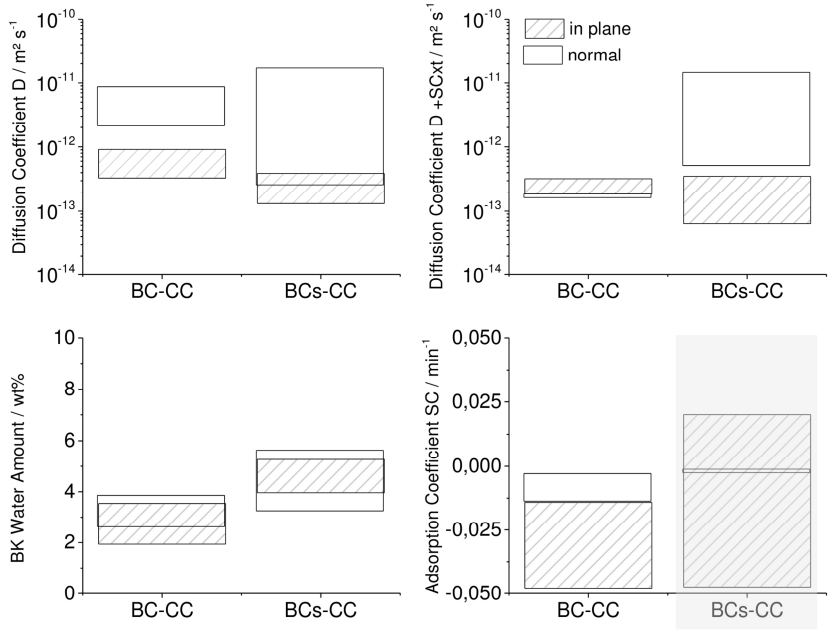

Fig. 4.20 Fickian and Non-Fickian diffusion coefficients with the adsorption coefficient SC and the BK water content for the base coat – clear coat (BC-CC) and the base coat with A flakes - clear coat (BCs-CC) in normal (white) and in plane direction (dashed) of the water transport corresponding to Figure 4.16

flakes cause a significant dominance of the normal diffusion with 7.5E-12 m²/s to the in plane diffusion with 2.1E-13 m²/s. The corresponding adsorption coefficients show a tendency to negative deviations which is especially distinct in the in plane direction. The water content is decreased with values around 2.85 wt% at the BC-CC system compared to 4.4 wt% at the BCs-CC system. However, no direction-driven dominance is reflected in the data of the water contents.

The previous study about the performance of the single layers (see section 4.1.1) verified a faster normal diffusion at the base coat, while the Al flakes inhibit the normal diffusion about the decuple, assuming non-Fickian conditions. The clear coat behaves the same in both directions. However, these characteristics seem to smear out due to the double layer system. The dominance of the top coat is often discussed [42, 43]. On the other hand, it is reported that the water diffusion depends on the thickness of the multilayer [42, 43, 3] and is independent of the layer compositions [42, 43]. The theory of the thickness-dependency is rooted in the simplest case, the unidirectional sorption of multilayers, which is defined by the following equation [44]:

$$\frac{L}{D} = \frac{L_1}{D_1} + \frac{L_2}{D_2} + \cdots \frac{L_n}{D_n} \tag{4.8}$$

with the total diffusion coefficient D, the total coating thickness L and their monolayer 1,2…n. Table 4.2 compares the experimental results of the double layers with the calculations via the unidirectional sorption across the results of the single layers to assess the dependencies. An overlap of the confidence intervals, which is found at the IF diffusion data of the double layer without Al flakes for both directions, is marked grey. The interface between the base coat and the clear coat smears out, due to the wet in wet application. The solvent of the clear coat diffuses into the base coat during application, which improves the intercoat adhesion [20] and “melts” them into a unit. These circumstances clarify

Tab. 4.2 Comparsion of experimental diffusion data of the double layers, base coat – clear coat (BC-CC) and base coat with Al flakes – clear coat (BCs-CC), with the diffusion calculations across the experimental data of the single layers based on the unidirectional sorption; an overlap of the data ranges is marked grey.

Parameter	Type of double layer	upper limit BC-CC	lower limit BC-CC	mean BC-CC	upper limit BCs-CC	lower limit BCs-CC	mean BCs-CC
Normal IF diffusion coefficient / m²/s	experimental data	8.6E-12	2.1E-12	5.4E-12	1.7E-11	2.6E-13	8.6E-12
	based on single layer	1.1E-12	6.4E-13	8.8E-13	3.5E-13	3.0E-13	3.2E-13
In plane IF diffusion coefficient / m²/s	experimental data	9.1E-13	3.3E-13	6.2E-13	3.9E-13	1.3E-13	2.6E-13
	based on single layer	7.4E-13	4.1E-13	5.7E-13	8.7E-13	4.3E-13	6.5E-13
Normal NF diffusion coefficient / m²/s	experimental data	1.8E-13	1.6E-13	1.7E-13	1.5E-11	5.1E-13	7.5E-12
	based on single layer	5.2E-13	7.2E-13	6.2E-13	2.1E-13	2.5E-13	2.3E-13
In plane NF diffusion coefficient / m²/s	experimental data	3.2E-13	1.9E-13	2.5E-13	6.3E-14	3.5E-13	2.1E-13
	based on single layer	3.9E-13	6.4E-13	5.2E-13	4.4E-13	7.6E-13	6.0E-13

the good agreement of the ideal Fickian law and the unidirectional sorption. As a result, the normal diffusion is significantly higher than the in plane diffusion at the BC-CC system.

With the addition of the Al flakes, the normal NF diffusion data overlaps with the theory about the unidirectional sorption. However, the IF data and the in plane NF data show strong deviations. The Al flakes hinder any examination via the ideal Fickian law. Additionally, the calculation of the unidirectional sorption acts on the assumption that there is an equally in plane flux through the clear and the base coat with the Al flakes but the mean free path of the base coat is many times larger than the free path of the clear coat. Due to the EIS setup (see Figure 4.2), an equal flux through the base coat is not ensured. The Al flakes block the normal water diffusion, which is the basis for the in plane diffusion through the base coat itself. Consequently, the mainly in plane transport will occur through the clear coat, but a significant dominance of the clear coat is not reflected in the data.

In brief, both double layer systems, BC-CC and BCs-CC, show a trend to a faster normal diffusion, while the in plane diffusion is a potency slower. The ideal Fickian approach is suitable for the BC-CC system and the non-Fickian approach for the BCs-CC system by comparing the result with the theory about the unidirectional sorption. However, further investigations have to clarify the circumstances at the double layers with regard to stress, strains and plasticising to assess the results correctly.

4.4.3.2 Physicochemical aftermaths of salt water uptake

Similar to the single layers, the physicochemical aftermaths at the double layers are identified with regard to the changes in the glass transition, the stress and the strains. Furthermore, the long-term consequences are exhibited by the degree of the irreversible storage of water and the changes of the effect finish.

Figure 4.21 shows the glass transitions of the double layers in dry and wet states for the first heating up to 125 °C. It is obvious that the storage moduli and the loss moduli are significantly higher at the BC-CC compared to that at the BCs-CC, although the BC-CC has a shorter soaking time of max. 19 days than the BCs-CC with max. 23 days. The moduli increase due to the salt water ingress. This is very distinct at the BC-CC layer with a gain of the storage moduli from 1326 MPa to 2928 MPa at 0 °C. The corresponding loss moduli show their largest gain from 104 MPa to 250 MPa at around 45 °C. At the BCs-CC, the storage moduli slightly increase from 1224 MPa to 1481 MPa at 6 °C. The loss moduli

increase from 116 MPa to 171 MPa at around 30 °C with a trend to lower temperatures with the increase of the soaking time. The magnitude of the tan delta of the BC-CC layers amounts to 0.85 and shifts 5 °C forward to 69 °C from the dry state to the state after 19 days of soaking. The addition of the Al flakes causes a decrease of the tan delta with a magnitude of 0.7, whereby the amplitude shifts 4 °C forward to 63 °C.

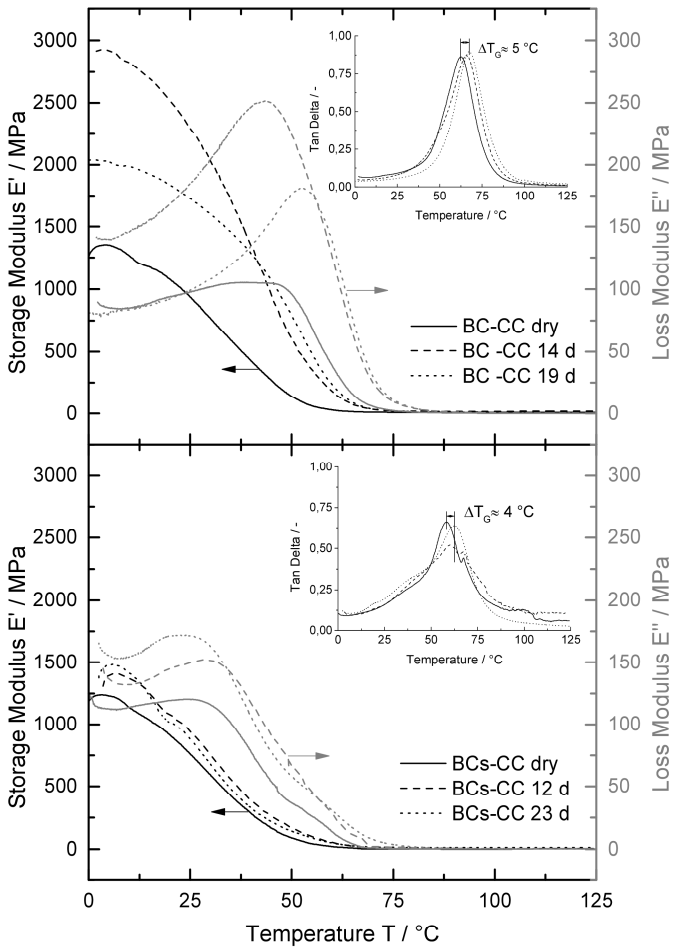

Fig. 4.21 Dynamic behaviour of the base coats (BC) and the base coats with Al flakes (BCs) covered with the clear coat (CC) after various days of soaking of 0.5 M NaCl solution; Conditions: T=0-125 °C, dT/dt=1 °C/min, f=1 Hz, averaged curves of repeat determination

Compared to the results of the single layers, the curve progression of the double layers is nearly equal to that of the clear coat. The tan delta shift of the clear coat with 5.5 °C is similar to the changes at the double layers. However, the clear coat shows no prominent signs of modulus increases after 18 days of soaking. As a result, the modulus increases have to be caused by the proven plasticising of the base coats. While the BCs shows maxima of the tan delta at higher temperatures than the pure BC (see Figure 4.9), their behaviours are converse with the clear coat at the top. This fact points to a change of the plasticising distribution.

The degree of the elasticity is displayed by the dimensionless Deborah numbers (De) in Figure 4.22. The calculations of the results are based on the given theory in the section 4.3, whereupon a heating-cooling-heating procedure is used to detect the impact of water on the entanglement behaviour of the double layers. Generally, the dry double layers are viscous with De numbers of 0.62 (BC-CC) and 0.64 (BCs-CC) but they become nearly viscoelastic with values of 0.98 (BC-CC) and 0.93 (BCs-CC) after the 2nd heating.

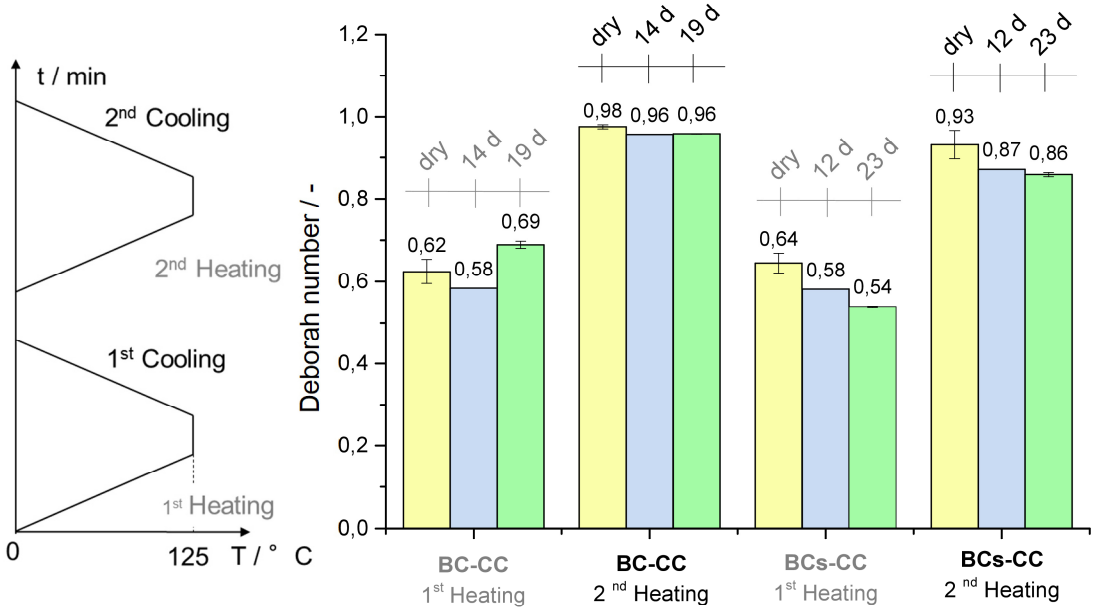

Fig. 4.22 Deborah numbers (De) measured during the first and the second heating of the base coat-clear coat (BC-CC) and the base coat with Al flakes – clear coat (BCs-CC) after various times of 0.5 M NaCl exposure, repeat determination.

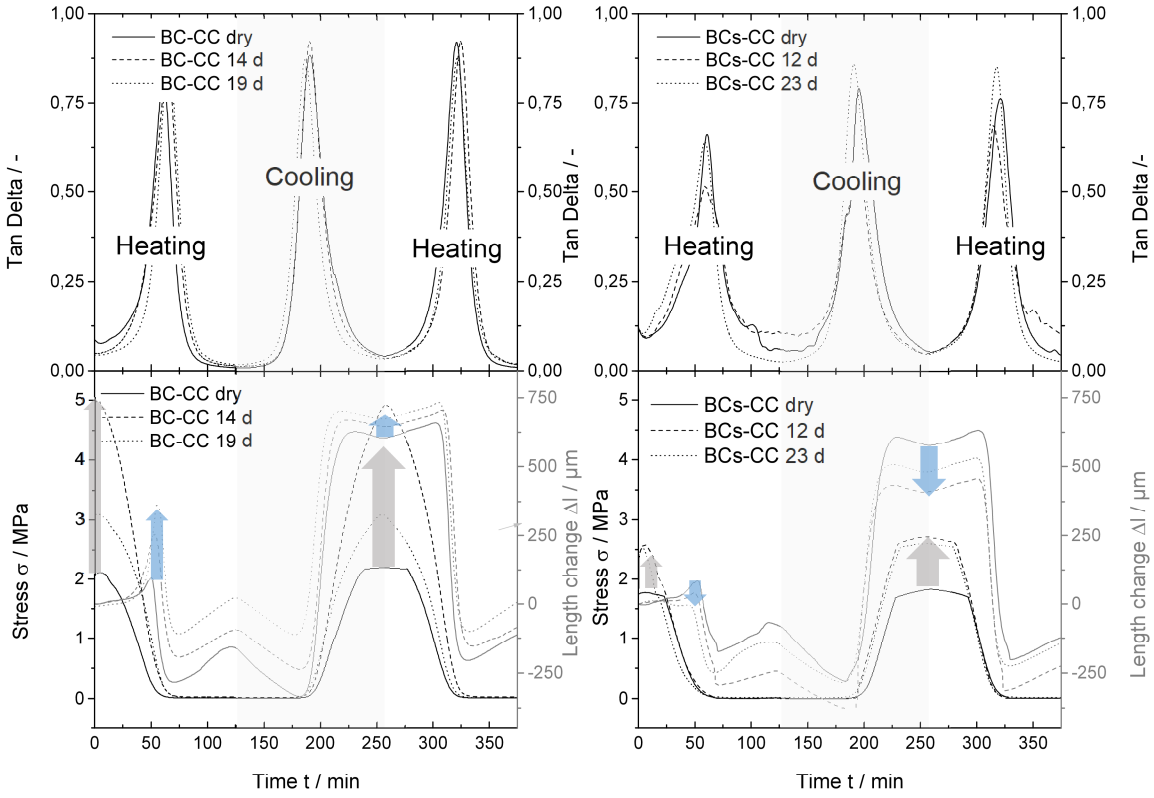

Fig. 4.23 Tan delta curves of the heating-cooling-heating cycle and the corresponding stress and length curves against the time of the double layers base coat-clear coat (BC-CC) and base coat with Al flakes-clear coat (BCs-CC), repeat determination.

Prominent differences occur by salt water with De-numbers of 0.62 (BC-CC) and 0.64 (BCs-CC). After the salt water ingress, the BC-CC layer shows nearly the equal behaviour to the dry state. However, the BCs-CC layer has a significantly viscous tendency with the increase in the soaking time. During the 1st heating, the De number decreases from 0.64 to 0.54, while the 2nd heating causes a change from 0.93 to 0.86.

With regard to the results in the section 4.4.1.3, it is known that the BCs layer contains free and bound water whereby it has to be assumed that the bound water is found as residual water after the 1st heating. This theory is supported by the decrease of the elasticity at the BCs-CC samples during the 2nd heating. The water can be bond at the Al flakes, but it can also be localised in the topmost section of the base coat due to the initial ingress from the clear coat to the first barrier of Al flakes. In contrast to BCs-CC, the BC-CC double layer responds to water reversibly as a homogeneous phase.

Moreover, the recorded stress and the length response of both double layers are illustrated in Figure 4.23 for the heating-cooling-heating cycle with time. First, the heating causes the introduction of stress. This stress is very prominent with up to 5 MPa at the wet BC-CC layers. Correspondingly, the BC-CC layers expand with a change in length of up to 250 µm. The subsequent cooling compresses the layers again. The next heating introduces the same stress as the 1st heating, however, the increase in the length is much greater with 700 µm while the water content slightly improves this trend. The layers are then more elastic. Impressively, the introduced stress is bisected by the BCs-CC layer compared to

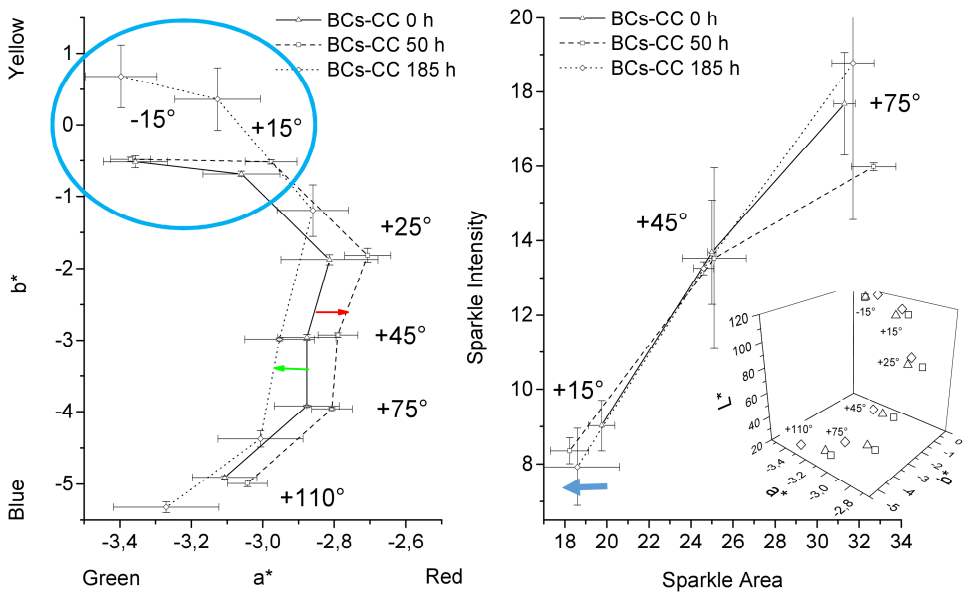

Fig. 4.24 Multi-angle spectrophotometry of the base coat with Al flakes and the clear coat cover in a dry state, after 50 h and 158 h of salt water uptake.

the BC-CC layers, while the length expansion is decreased via the water content. These converse responses correlate to the different dashpots (max. tan delta) of the double layers.

Moreover, Figure 4.24 presents the results of the multi-angle measurements at the BCs-CC layer in the dry state, after 50 h and after 185 h of salt water ingress, similar to the results at the BCs layer. A comparison of the BCs layer and the BCs-CC layer with regard to the changes of their graininess, their two tones and their sparkle grades is additionally given in Figure A4.3.1 of the Appendix. The brightness L* and colour changes a*/b* at BCs-CC layer are in the confidence interval. However, there is a distinctly yellow shift behind the gloss at -15 ° after a salt water ingress of 185 h and the sparkle area decreases in a similar way to the single BCs layer.

The visual impression of the BCs layer is lustreless while the BCs-CC layer shows a high gloss. The main gloss is produced by the clear coat. At an observation angle of -15 ° (behind the gloss), the light may impinges on the polymer-polymer interface of the BCs-CC layer. Consequently, it is likely that the interface changes due to the salt water uptake. However, the BCs-CC layer acts like a cage which stores water and stress due to the Al flakes and the polymer-polymer interface.

In brief, both double layers, BC-CC and BCs-CC, plasticise but the water ingress has different aftermaths. The BC-CC layer responds to water reversibly as a homogeneous phase which freely expanses and compresses. Conversely, the BCs-CC layer acts like a cage in which water and stress are stored. The water ingress compresses the BCs-CC layer. Free water especially is localised at the polymer-polymer interface and on the Al flakes with an irreversible value of bound water.

4.4.3.3 Relation between the adsorption coefficients SC and the physicochemical parameters

The expressiveness of the adsorption coefficient SC is assessed at the double layers, BC-CC and BCs-CC, by the comparing it with the physicochemical changes during the heating-cooling-heating cycle.

Similar to the single layers, Figure 4.25 presents the summarised results of the double layers. The corresponding data table is attached in the Appendix. The means of normal adsorption coefficients show positive deviations of the ideal Fickian law with 0.003 min^{-1} (BC-CC) and 0.016 min^{-1} (BCs-CC) while the means of the in plane adsorption coefficients are negative with -0.031 min^{-1} (BC-CC) and -0.014 min^{-1} (BCs-CC). The tension clamp used draws the layers from the in plane direction. However, the BCs-CC layer always has higher adsorption coefficients than the BC-CC layer. Interestingly, the changes in the stress, the length and the tan delta show converse behaviour to the adsorption coefficients of the two double layers during the 1st heating (blue) as was already found for the single layers other than the length changes. During the 2nd heating, the stress and the tan delta are in line with the general trend of the adsorption coefficients of the double layers (grey).

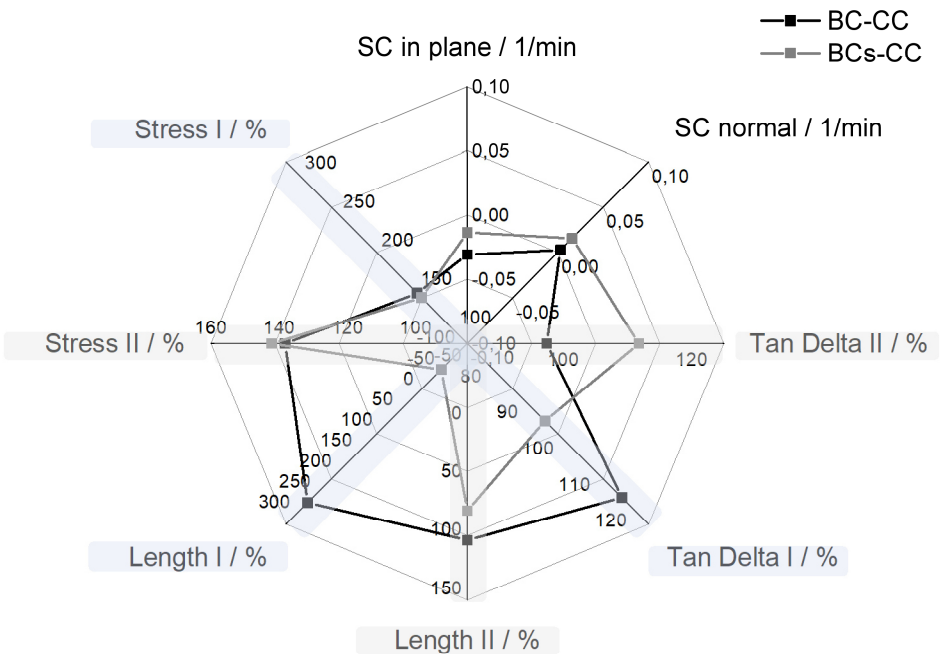

Fig. 4.25 Relation between the adsorption coefficients SC and the changes in the maximal stress, tan delta and length from the dry state to the longest salt water uptake for the first heating (I) and the second heating (II) of the double layers: Base coat – clear coat (BC-CC) and base coat with Al flakes – clear coat (BCs-CC).

As argued in the section 4.4.1.5, the main difference of the three single layers is the degree of pigmentation. While the clear coat freely expands and compresses by means of water, the coloured base coat is more restricted by the pigments and in particular, the addition of Al flakes strengthens the internal stress. The adsorption coefficients express a sum of non-Fickian activities. However, the BCs layers and the BCs-CC layers always show more positive deviations from the ideal Fickian law than the other layers (BC, CC, BC-CC), see Figure 4.7 and 4.20, which is why it has to be assumed that the increase of internal stress causes an increase in the adsorption coefficient. As a consequence, the strain of the BC, CC and BC-CC layers by water has to cause a decrease in the adsorption coefficients. Moreover, internal stress can also occur during the curing or by the clear coat as a response to the swelling of the base coat [3]. These causes may have a smaller impact on the layer system than the stress which is introduced by the Al flakes. Additionally, the De decrease causes a changing of the stress and tan delta trends at the BC-CC and BCs-CC layers upon 2nd heating. The BCs-CC layer is then more viscous than the BC-CC layer due to the irreversible amount of bound water. However, bound water in the BCs layer attenuates the increase of the adsorption coefficient because bound water has a lower permeability constant (ε_W=60) than free water (ε_W=78.3) [45]. The tan delta acts conversely to the increase of water which increases the adsorption coefficients and is also driven by the stress and strains present.

Ultimately, the investigations at the double layers support the relation of the adsorption coefficients to the internal stress and the tan delta which conversely correlates to the water content. However, it has to be considered that the results give a more distinct picture about the stress and strain behaviour than it would be at supported layer because the experiments were performed at free films and related to the adsorption coefficients measured at supported coatings.

4.4.3.4 Conclusion of multilayers

The double layer systems, BC-CC and BCs-CC, show a trend to a faster normal diffusion while the in plane diffusion is a potency slower during the salt water ingress. Both double layers plasticise but the BC-CC layer responds to water reversibly as a homogeneous phase which freely expands and compresses. Due to this, the ideal Fickian approach is applicable to the BC-CC layer. In contrast, the BCs-CC layer acts like a cage in which water and stress are stored. The water ingress compresses the BCs-CC layer, see Figure 4.26. Free water especially exists localised at the polymer-polymer interface and at the Al flakes with an irreversible value of bound water. The non-Fickian approach best describes the water diffusion at the BCs-CC layer. The results support the relation of the adsorption coefficients to the internal stress and the tan delta, which conversely correlates with the water content. Due to the non-Fickian circumstances at the BCs-CC layer, the theory about the unidirectional sorption is only applicable to the BC-CC layer.

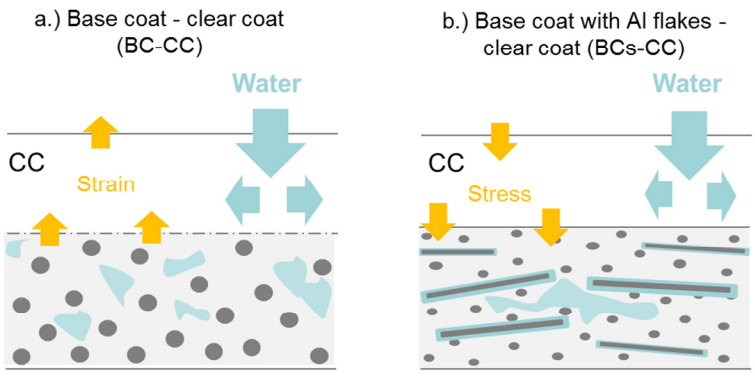

Fig. 4.26 Model of the physicochemical circumstances at the double layers, base coat – clear coat (BC-CC) and the base coat with Al flakes – clear coat (BCs-CC), during salt water uptake

4.5 Conclusion

In this study, the direction-driven nature of the water diffusion is investigated at the pigment E-coat, a base coat (BC) without and with Al flakes (BCs) and a clear coat (CC) with regard to Fickian and non-Fickian circumstances. The E-coats show neither a plasticising nor anisotropy through the layer during the salt water uptake. However, the interfacial activities are prominent, while substrate ions can have the potential to increase the cross-linking at the interface due to their dissolution during the deposition. Conversely, the base coats react via plasticising and an anisotropy. The coloured base coat (BC) has a faster normal diffusion, which is rooted in its opened pores that act as an entrance for the salt water. The addition of the Al flakes blocks the normal diffusion, making normal diffusion then ten times slower compared with the base coat without the Al flakes. At the clear coat (CC), no significant plasticising is proven which is why the Fickian and the non-Fickian laws are equally suitable for the present isotropic diffusion.

Moreover, the in plane diffusion of water is compared with the in plane ion diffusion in a wet-dry-wet cycle. The results show that an initial salt water uptake leads to the fast saturation of the clear coat (CC) while the ions diffuse a potency slower than the water. After a drying section followed by a subsequent initiation of salt water, the ions diffuse faster and in a way that is comparable to that of water due to a damage caused by the first wetting. However, later on, the ions are blocked around two potencies because new hydrophilic channels through the clear coat have to be formed by water.

By pointing out the role of polymer-polymer interfaces, the double layer systems, base coat – clear coat (BC-CC) and base coat with Al flakes – clear coat (BCs-CC), show a trend to a faster normal diffusion, while the in plane diffusion is a potency slower during the water ingress. Both double layers plasticise but the BC-CC layer responds to water reversibly as a homogeneous phase which freely

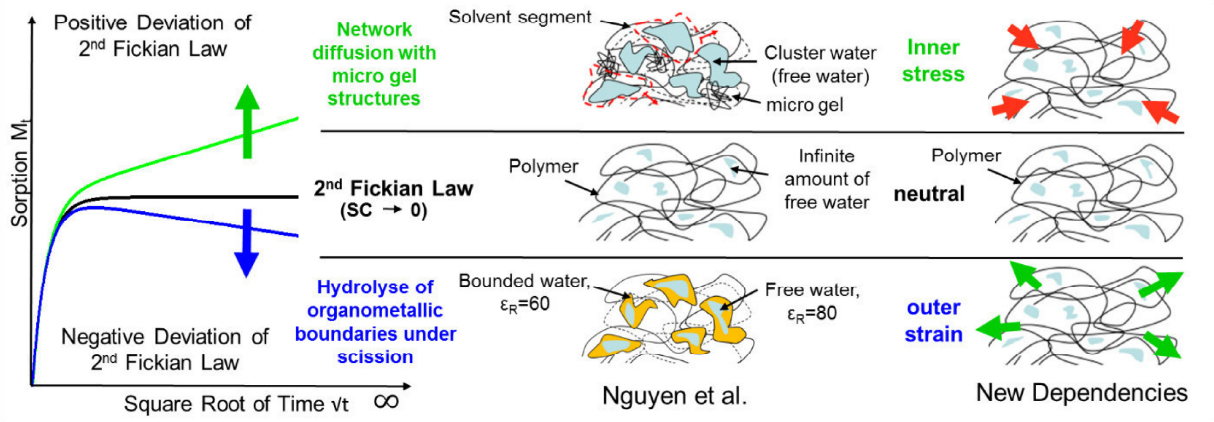

Fig. 4.27 Diagram showing the water sorption into a polymeric matrix under ideal Fickian and non-Fickian circumstances and the meaning of the adsorption coefficient SC as the deviation of the ideal Fickian law.

expands and compresses. Due to this, the ideal Fickian approach is applicable to the BC-CC layer. In contrast, the BCs-CC layer acts like a cage in which water and stress are stored. The water ingress compresses this double layer. Free water especially is localised at the polymer-polymer interface and at the Al flakes with an irreversible value of bound water. The non-Fickian approach best describes the water diffusion at the BCs-CC layer. Due to the non-Fickian circumstances at the BCs-CC system, the theory about the unidirectional sorption is only applicable to the BC-CC double layer.

Based on the generated data, the adsorption coefficients SC of the non-Fickian law are related to various parameters to estimate the physicochemical expressiveness of this coefficient. At the single and double layers, the adsorption coefficient relates to the internal stress and the tan delta, which conversely correlates with the water content. Consequently, the non-Fickian approach of Nguyen and co-workers [45] is complemented by the inner stress as a positive deviation and the outer strain as a negative deviation of the 2nd Fickian law, see Figure 4.27.

References

[1] S. Granick, S. C. Bae, Open Questions about polymer interfacial diffusion – viewpoint, J. Poly. Phys. 44 (2006) 3434.

[2] K. E. Miller, R. H. Krueger, J. M. Torkelson, Mobility-sensitive fluorescence probes for quantitative monitoring of water sorption and diffusion in polymer coatings, J. Poly. Sci. Part B 33 (1995) 2343.

[3] V. Bankh, H. P. Huinink, O. C. G. Adan, S. J. F. Erich, L. G. J. van der Ven, NMR imaging of water uptake in multilayer polymeric films: stressing the role of mechanical stress, Macromolecules 43 (2010) 3382.

[4] K. N. Allahar, B. R. Hinderliter, D. E. Tallman, G. P. Bierwagen, Water transport multilayer organic coatings, J. Electrochem. Soc. 155 8 (2008) F201.

[5] A. Miszczyk, T. Schauer, Electrochemical approach to evaluate the interlayer adhesion of organic coatings, Prog. Org. Coat. 52 (2005) 298.

[6] V. Upadhyay, K. N. Allahar, G. P. Bierwagen, Environmental humidity influence on a topcoat/Mg-rich primer system with embedded electrodes, Sensors and Actuators B 193 (2014) 522.

[7] G. P. Bierwagen, X. Wang, D. Tallmann, In-situ study of coatings using embedded electrodes for ENM measurements, Prog. Org. Coat. 46 (2003) 163.

[8] D. Vesely, Diffusion of liquids in polymers, Intern. Mater. Rev. 53 5 (2008) 299.

[9] P. Carbonini, T. Monetta, L. Nicodemo, P. Mastronardi, B. Scatteia, F. Bellucci, Electrochemical characterisation of multilayer organic coatings, Prog. Org. Coat. 29 (1996) 13.

[10] J. Vogelsang, W. Strunz, Electrochemical investigations of organic, corrosion protective barrier coatings – limiting factors of small signal perturbation techniques, Mater. Corros. 52 (2001) 462.

[11] EN ISO 16773-2:2007

[12] J. E. B. Randles, Kinetics of rapid electrode reactions, Discuss. Faraday Soc. 1 (1947) 11.

[13] K. P. Menard, Dynamic mechanical analysis: a practical introduction, 2nd Edition, CRC Press, Boca Raton, 2008.

[14] S. Rosen, Fundamental principles of polymeric materials, 2nd Edition, Wiley, New York, 1993.

[15] W. C. Elmore, Electrolytic polishing, J. Appl. Phys. 10 (1940) 724.

[16] J. Edwards, The mechanism of electropolishing of copper in phosphoric acid solutions, J. Electrochem. Soc. 100 (1953) 189C, 223C.

[17] C. Wagner, Contribution to the theory of electropolishing, J. Electrochem. Soc. 101 (1954) 225.

[18] M. Sargeson, Developments in the synthesis and reactivity of encapsulated metal ions, Pure Appl. Chem. 58 11 (1986) 1511.

[19] H. D. Busch, A. L. Vance, A. G. Kolchinski, Molecular template effect: Historical view, principles, and perspectives, Comprehensive Supramolecular Chemistry, 9 (1996) 1.

[20] U. Poth, Autolacke formulieren: Chemie, Physik, Praxis, Vincentz, Hannover, 2007.

[21] G. Williams, Cr(VI)-free corrosion protection of galvanised steel by coatings containing novel smart-release pigments, CoSi 2016, Noordwijk, The Netherlands.

[22] T. G. Fox, Influence of diluent and of copolymer composition on the glass temperature of a polymer system, Bull. Amer. Phys. Soc. 1 (1956) 123.

[23] N. Ramesh, P. K. Davis, J. M. Zielinski, R. P. Danner, J. L. Duda, Application of free-volume theory to self-diffusion of solvents in polymers below the glass transition temperature: A review, J. Polym. Phys. Part B 49 (2011) 1629.

[24] J. A. McMillan, S.C. Los, Vitreous Ice: Irreversible transformations during warm-up, Nature 206 (1965) 806.

[25] D. H. Rasmussen, A. P. MacKenzie, The glass transition in amorphous water. Application of the measurements to problems arising in cryobiology, J. Phys. Chem. 75 (1971) 967.

[26] N. Amirshaqaqi, M. Salami-Kalajahi, M. Mahdavian, Investigation of corrosion behaviour of aluminium flakes coated by polymeric nanolayer: Effect of polymer type, Corros. Sci. 87 (2014) 392.

[27] M. Jalili, M. Rostami, B. Ramezanzadeh, Surface modification of aluminium flakes with amino trimethylene phosphonic acid: Studying the surface characteristics and corrosion behaviour of the pigment in the epoxy coating, Corrosion 71 5 (2015) 628.

[28] D. E. Wurster, S. Bhattacharjya, D. R. Flanagan, Effect of curing on water diffusivities in acrylate free films as measured via a sorption technique, AAPS PharmSciTech 8 (2007) E152.

[29] Z. W. Wicks, J. Frank, N. Jones, S. P. Pappas, D. A. Wicks, Organic Coatings, Science and Technology, 3rd Edition, Wiley, New York, 2007.

[30] R. F. Boyer, Dependence of mechanical properties on molecular motion in polymers, Polymer. Eng. Sci. 8 3 (1968) 161.

[31] R. Vlasak, I. Kueppel, G. Grundmeier, Combined EIS and FTIR–ATR study of water uptake and diffusion in polymer films on semiconducting electrodes, Electrochim. Acta 52 (2007) 8075.

[32] E. L. Koehler, The influence of contaminants on the failure of protective organic coatings on steel, Corros. Nace 33 6 (1977) 209.

[33] R. G. Kelly, J. R. Scully, D. W. Shoesmith, R. G. Buchheit, Electrochemical techniques in corrosion science and engineering, New York, Marcel Dekker, 2003.

[34] H. Kaesche, Die Korrosion der Metalle – Physikalisch-chemische Prinzipien und aktuelle Probleme, Heidelberg, Springer 2011.

[35] T. Nguyen, J. B. Hubbard, J. M. Pommersheim, Unified model for the degradation of organic coatings on steel in a neutral electrolyte, J. Coat. Technol. 68 (1996) 45.

[36] S. R. Taylor, F. Contu, R. Santhanam, P. Suwanna, The use of cationic fluoroprobes to characterize ionic pathways in organic coatings, Prog. Org. Coat. 73 (2012) 169.

[37] S. Morsch, S. Lyon, P. Greensmith, S. D. Smith, S. R. Gibbon, Mapping water uptake in organic coatings using AFM-IR, Faraday Discuss. 180 (2015) 1.

[38] H. Leidheiser, R. D. Granata, R. Turoscy, Alkali metal ions as aggressive agents to polymeric corrosion protective coatings, Corrosion 43 (1987) 296.

[39] W. S. Tait, K. A. Handrich, Cation enhancement of internally coated metal container corrosion failure, Corrosion 50 (1994) 373.

[40] M. Dornbusch, S. Kirsch, C. Henzel, C. Deschamps, S. Overmeyer, K. Cox, M. Wiedow, U. Tromsdorf, M. Dargatz, U. Meisenburg, Characterization of the water uptake and electrolyte uptake of organic coatings and the consequences by means of electrochemical impedance spectroscopy and UV-vis spectroscopy, Prog. Org. Coat. 89 (2015) 332.

[41] Q. Zhou, Y. Wang: Comparison of clear coating degradation in NaCl solution and pure water, Prog. Org. Coat. 76 (2013) 1674.

[42] C. Moreno, S. Hernández, J.J. Santana, J. González-Guzmán, R.M. Souto, S. González, Characterization of water uptake by organic coatings used for the corrosion protection of steel as determined from capacitance measurements, Int. J. Electrochem. Sci. 7 (2012) 8444.

[43] C. Moreno, S. Hernández, J.J. Santana, J. González-Guzmán, R.M. Souto, S. González, Determination of water transport properties of organic coatings with EIS, Int. J. Electrochem. Sci. 7 (2012) 7390.

[44] J. Crank, The mathematics of diffusion, Clarendon Press, Oxford, 1975.

[45] V. N. Nguyen, F. X. Perrin, J. L. Vernet, Water permeability of organic/inorganic hydrid coatings prepared by sol-gel method: A comparison between gravimetric and capacitance measurements and evaluation of non-Fickian sorption models, Corros. Sci. 47 (2005) 397.

5 Overall conclusion and outlook

The omnipresence of paints and adhesives in contact with metals requires a detailed knowledge of the water diffusion and the ionic pathways through their polymer networks and along their interfaces, addressing specific developments to improve the corrosion and de-adhesion resistance.

The E-coat-metal interface in particular is of paramount importance to the automotive industry. The transport behaviour and the film formation of the E-coat conspicuously depend on the type of the substrate. During deposition, the substrates dissolve due to the extremely cathodic polarisation under highly alkaline conditions, which is why the E-coat is contaminated by the solvated metals. Steel, HDG steel and AlMg(Mn) were tested, whereby the highest E-coat contamination is found on steel. Interestingly, the interfacial ion transport at steel is slower compared to HDG steel, too. This effect becomes noticeable after incubation, see Figure 5.1. The duration of the incubation is mainly determined by the metal. The high resistance of HDG steel causes a delay of the interfacial transport of a week compared to that of steel. Pigmentation is also prominent in the findings. The ion transport at the clear E-coat starts slightly earlier and is five times faster than the ion transport at the pigment E-coat.

Conversely to steel and HDG steel, AlMg(Mn) shows the main ion flux in parallel to the interface through the E-coat. However, aggressive media cause hydrogen-induced crevice corrosion, which illustrates the interfacial pH-changes in a humid oxygen-deficient atmosphere. An acidic Mg dealloying or an alkaline galvanic coupling at the Al_6MnFe particles weaken the aluminium oxide until it breaks down. Then, the interface shows sulphate ions and undermining processes, whereby the acidic-induced ion transport is many times faster than the alkaline-introduced one. As a result, the transport at the insulating aluminium

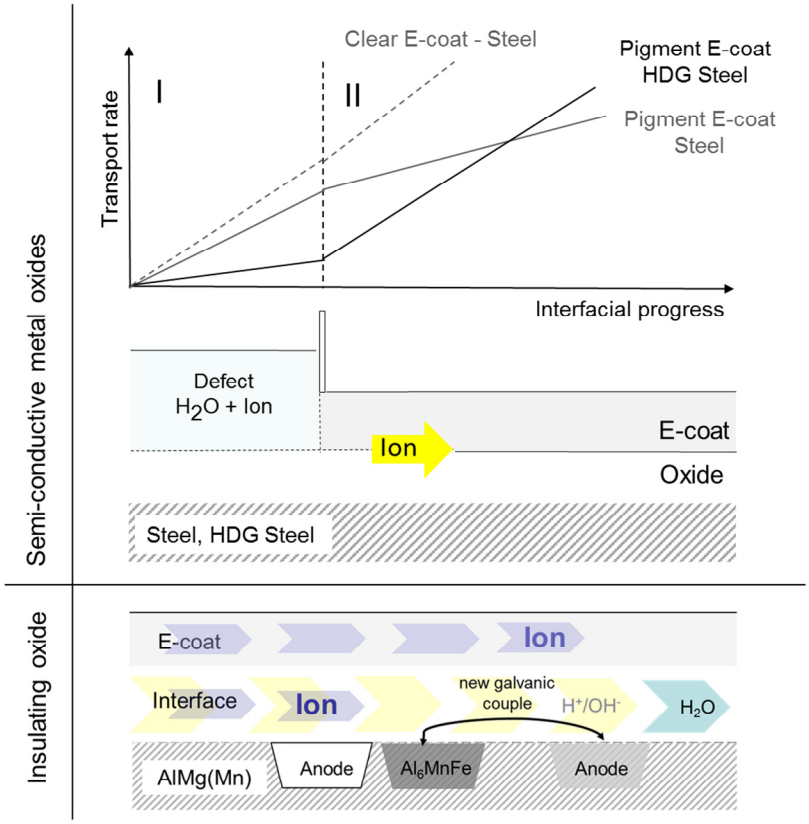

Fig. 5.1 Interfacial results of the E-coat: progress of the cathodic undermining at steel and HDG steel, (I) incubation (II) ion transport, and transport model for the insulating AlMg(Mn) oxides

oxide is driven by two transport mechanisms, through the polymer layer in parallel to the interface and at the interface itself. When the aluminium oxide is intact and the transport is completely driven in parallel to the interface, two effects are found:

- The protonation of the interfacial amine groups of the E-coat (pH=2) and
- The change in the termination of the aluminium oxide (pH=12).

Since charge carriers have no bearing on the Galvani potential of the intact aluminium oxide, the measurable Volta potential is dominated by this interfacial dipole alone. With regard to this, the Volta potentials show a linear gain from -1.7 V up to 0.8 V with an increase in the pH-value. It is assumed that the interfacial dipole changes from ionic bonds to hydrogen bonds, resulting in a charge transfer at the aluminium oxide and this is reflected by the Volta potential signal.

At the Ti/Zr-based conversion layers, the Volta potential has no significant merit of information about the interfacial processes. The pH-activities along the conversion layers are dominated by the flux through the E-coat in parallel to the interface. No interfacial ions are observed but the bond strength of the amines changes and this is in line with the performance of the conversion layer under the chosen pH-conditions, e.g. pit sealing or flushing out of polymer compounds. The protection barrier of the conversion layers at the AlMg(Mn) becomes apparent due to the decrease of the potential gradient from 2.5 V to 0.2 V, by means of an interfacial pH-change from 12 to 2.

With reference to the water diffusion to the surface normal, the E-coated steel shows the slowest water diffusion, followed by HDG steel and AlMg(Mn), see Figure 5.2 (a-c). The high iron content of around 20 at% seem to protect the E-coat against the water ingress, while a blocking of the ion ingress is probably due to osmotic forces. The normal and the in plane water diffusion are uniform/isotropic. The E-coat matrix reveals a slight Young's modulus drop and increased disorder in the pigment-polymer network on rough substrates after 50 days of salt-water uptake. Further signs of plasticising are not observed, but these circumstances already require non-Fickian treatment.

At a clear coat (CC, Figure 5.2 d), neither plasticising nor any anisotropy are proven, which is why the ideal Fickian and the non-Fickian law are equally suitable for carrying out the determination. In the in plane direction, the first salt water ingress leads to a fast saturation while the ions diffuse a potency slower than the water. After a drying section followed by a subsequent initiation of salt water, the ions diffuse faster and in a way that is comparable to water due to the water-induced damage caused by the first wetting. However, when the ions have to enter a new territory, the ions are blocked around two potencies, because new hydrophilic channels through the clear coat have to be formed by water.

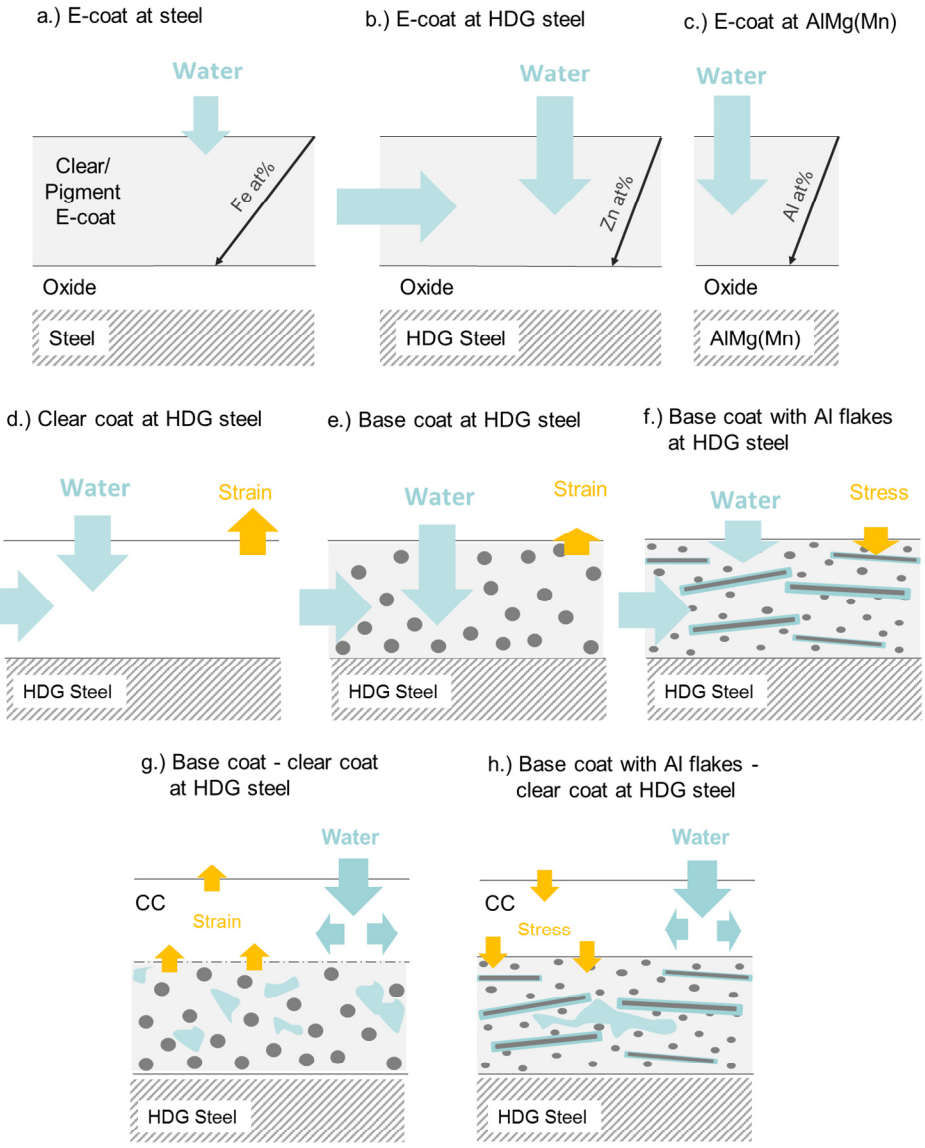

Fig. 5.2 Overview of the normal and the in plane water diffusion through various single and multilayers

With the degree of pigmentation, the limitation of polymer coatings increase to compensate the water ingress by expansion or swelling. As a consequence, the strains decrease and the internal stress increase, as presented at the clear coat, a coloured base coat (BC) and the base coat with aluminium flakes (BCs) (Figure 5.2 d-f). The internal stress causes a positive deviation of the water sorption from the ideal Fickian law, which is why such circumstances have to be expressed by a non-Fickian approach.

Moreover, the base coats plasticise and show the direction-driven nature of the water diffusion. The coloured base coat has a faster normal diffusion than the clear coat. Its opened pores are the point of entrance for the salt water. The addition of the aluminium flakes blocks the normal diffusion while the normal diffusion is then ten times slower than it is compared with the base coat without aluminium flakes.

By pointing out the role of polymer-polymer interfaces, the double layer systems, base coat – clear coat (BC-CC) and base coat with Al flakes – clear coat (BCs-CC), show a trend to faster normal water diffusion, while the in plane diffusion is a potency slower (Figure 5.2 g-h). Both double layers plasticise, but the BC-CC layer reversibly responds to water as a homogeneous phase which freely expands and compresses. In contrast, the BCs-CC layer acts like a cage in which water and stress are stored. The water ingress compresses this double layer. Free water in particular exists at localised points at the polymer-polymer interface and at the aluminium flakes with an irreversible value of bound water. Neither the ideal Fickian law nor the theory of unidirectional sorption are applicable in this case.

These results are the product of several method developments which show the uniqueness of this work and allow the quantification and assessment of the water and ion transport through polymer networks and along their interfaces. For example:

- Electrochemical impedance methods for the normal and in plane water diffusion with Fickian and non-Fickian treatment,
- Electrochemical impedance method with embedded electrodes to detect the in plane ion diffusion in a wet-dry-wet cycle,
- Scanning Kelvin probe approach and the coupling with confocal Raman spectroscopy to detect the pH-activities at the insulating aluminium oxide across the interfacial dipole,
- Dynamic-mechanical method to quantify the stress and strains at soaked multilayers and to calculate the dimensionless Deborah number as a degree of elasticity.

The collective information on the substrate dependencies and the rate-determined water and ion pathways through the polymer-metal systems offers new opportunities for paint and adhesive developments.

The results of the clear and the pigment E-coat on steel in particular were unforeseeable. It is assumed that alkaline solvated iron forms a complex with the amines as ligands. This complex changes the E-coat distribution in favour of specific macrocyclic compounds, such as polyoxometalates, which decrease the interfacial ion transport and the normal water diffusion. The principle of this effect can be used to specifically increase the cross-linking at the polymer-metal interface. It can be immediately adapted for various other polymer-metal systems of the transport, bond or electronic industry in order to block the water and ion transport and to improve their corrosion and de-adhesion resistance.

A2 Interface and volume transport on technical E-coats: A comparison of steel, hot-dip galvanised steel and AlMg(Mn)

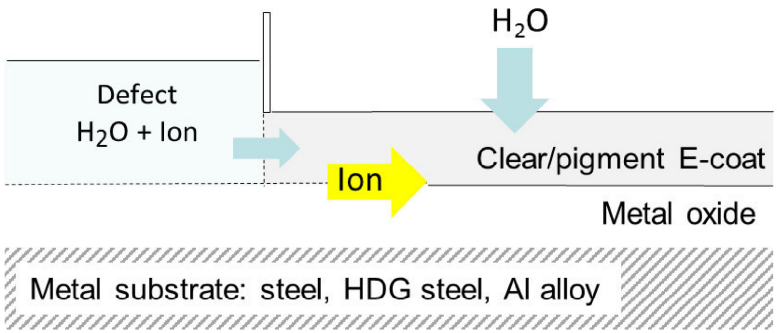

A2.1 EDX spectra of the clear and pigment E-coats and near the E-coat-substrate interfaces

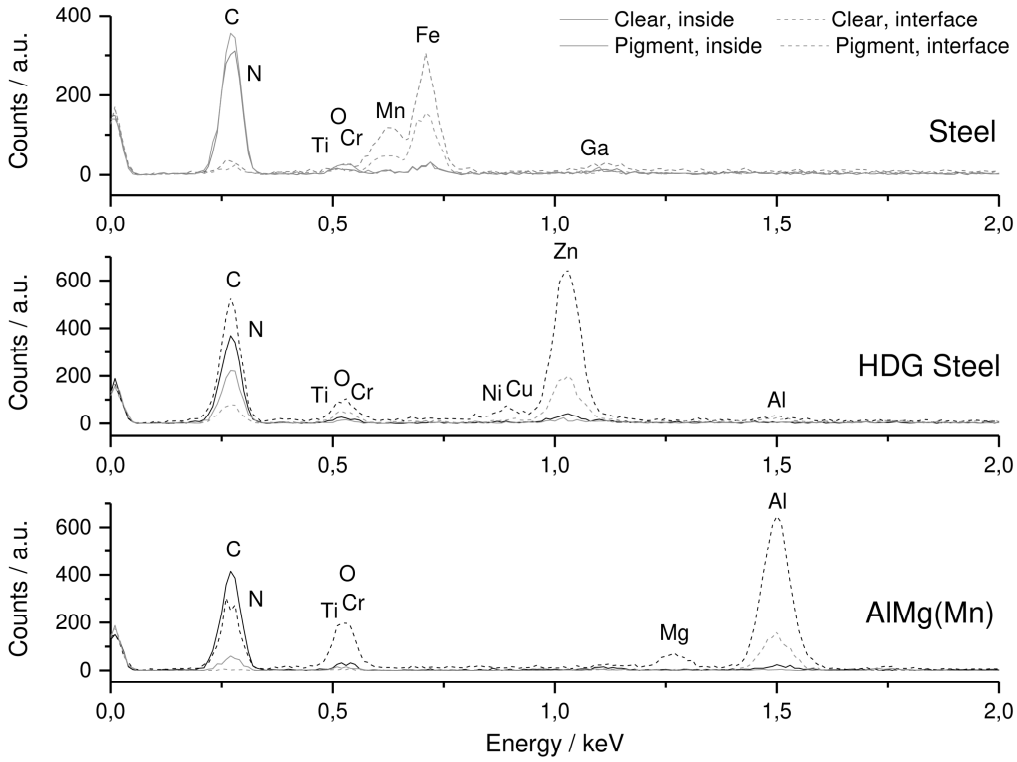

Fig. A2.1.1 EDX spectra of the coated steel, HDG steel and AlMg(Mn) in the polymer network (inside) and near the polymer-metal interface (interface)

The results of the EDX line scan spectra are shown in Figure A2.1.1 for each type of sample. The polymer contains carbon (K_α=0.277 keV), nitrogen (K_α=0.392 keV) and oxygen (K_α=0.525 keV) as the main elements. The pigment coating adds titanium (L_α=0.452 keV) in small amounts. The steel samples have a major peak at 0.705 keV of the Fe(L_α)-line with manganese as a peak shoulder of iron (L_α=0.637 keV) and chromium at 0.573 keV. In the HDG steel spectra, the L_α-line of zinc dominates at 1.012 keV, accompanied by several alloying elements like nickel, aluminium and chromium. The aluminium substrate contains mainly aluminium, shown as K_α-line at 1.486 keV and magnesium at K_α=1.253 keV.

A2.2 Validation of raw EIS data and the applied Randle circuit

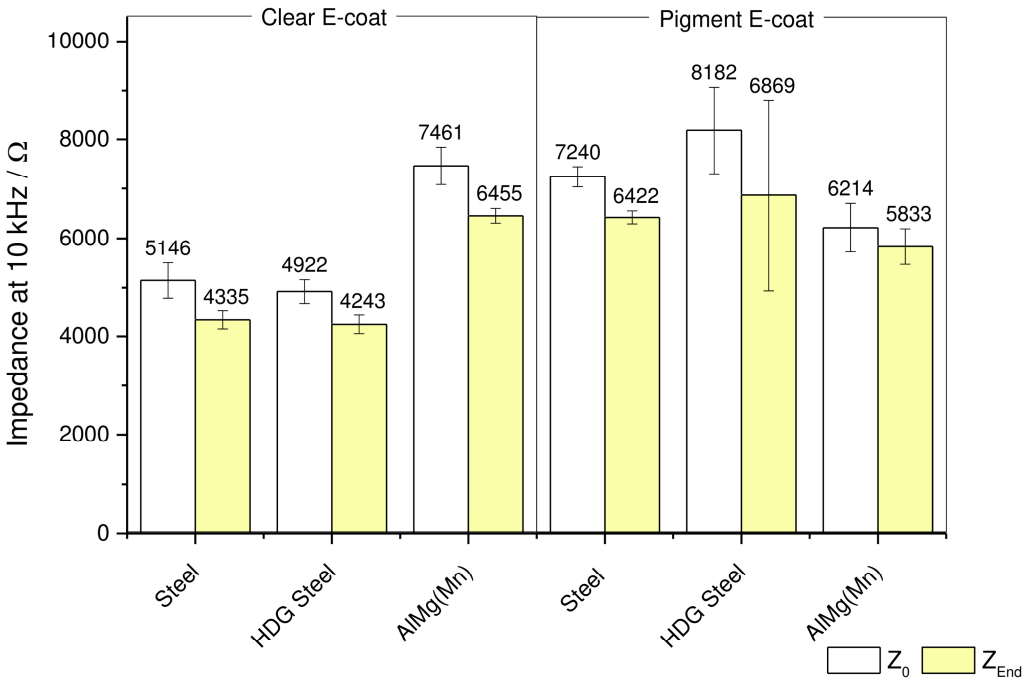

Fig. A2.2.1 Raw impedance data of the different substrates coated with clear and pigment E-coats at 10 kHz

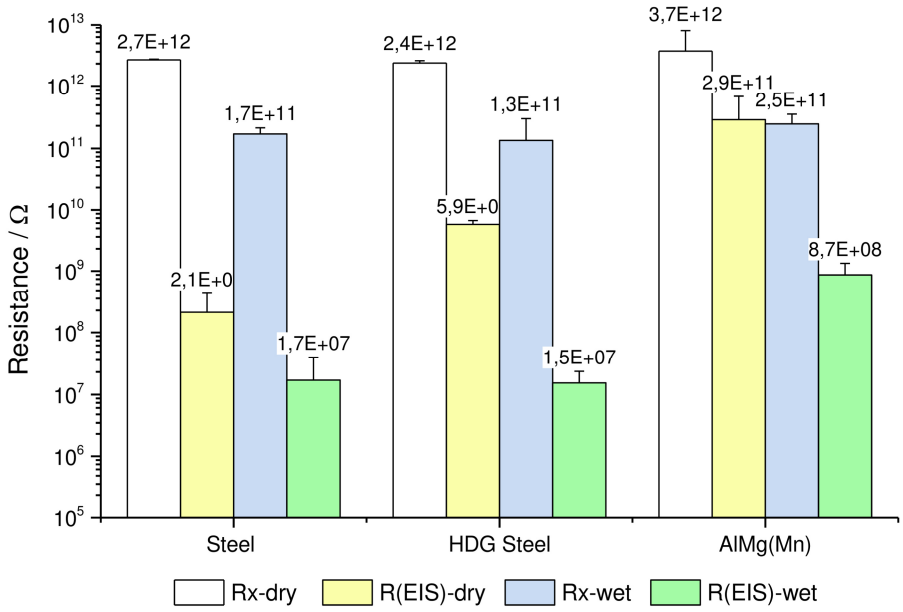

Fig. A2.2.2 Comparison of the independent resistance, R_x, with the resistance, R_{Coat}, of the Randle circuit from 100 mHz to 100 kHz for clear-coated steel, HDG steel and AlMg(Mn) samples as repeat determination.

Figure A2.2.1 provides an impression about the reproducibility of the threefold measurement by the impedance data at 10 kHz for clear and the pigment E-coats and their different substrates at the beginning and the end of the measurement. Due to the water uptake, the impedance values decrease, and this tendency can always be proven in the face of the standard deviations. The error bars overlap on HDG steel and AlMg(Mn) coated with the pigment E-coat, the other sample series show no overlapping error bars. The independent resistance measurements (R_x) on the clear E-coat further support these trends compared to the resistances of the RC circuit from 100 mHz to 10 kHz, as seen in Figure A2.2.2. The applied Randle circuit is proven.

A2.3 Fitting details of Fickian and Non-Fickian approaches

Tab. A2.3.1 Diffusion intervals and the raw fitting data of the ideal Fickian approach based on $y(t)=y_\infty+A_1\exp(t/b_1)+A_2\exp(t/b_2)$

Coating	Substrate	y_∞	A_1	t_1	A_2	t_2	Chi²	R^2	D / m² s^{-1}	Mean D / m² s^{-1}	SD D / m² s^{-1}
Clear E-coat	Steel	1,01	-1,00	-1,10	-0,11	-10,79	9,68E-05	1,00	1,68E-13	1,52E-13	2,16E-14
		1,00	-0,25	-7,91	-0,81	-1,23	1,61E-05	1,00	1,37E-13		
	HDG Steel	1,00	-0,15	-6,90	-0,94	-0,74	7,17E-05	1,00	3,75E-13	3,06E-13	9,76E-14
		0,98	-0,87	-0,93	-0,20	-8,17	7,02E-05	1,00	2,37E-13		
	AlMg(Mn)	0,99	-0,18	-3,10	-0,91	-0,68	3,52E-05	1,00	4,59E-13	2,95E-13	2,31E-13
		1,01	-1,03	-1,24	-0,13	-14,28	3,86E-04	0,99	1,32E-13		
Pigment E-coat	Steel	1,03	-0,92	-5,95	-0,17	-0,87	3,62E-04	0,99	2,72E-13	1,92E-13	1,14E-13
		1,02	-0,26	-1,41	-0,77	-4,89	1,69E-04	1,00	1,11E-13		
	HDG Steel	0,97	0,00	3,10	-1,03	-1,10	9,38E-05	0,98	1,90E-13	1,70E-13	2,77E-14
		1,04	-0,86	-1,17	-0,27	-10,69	7,49E-05	1,00	1,51E-13		
	AlMg(Mn)	0,90	-0,75	-0,73	-0,24	-2,27	4,10E-03	0,83	4,24E-13	2,73E-13	2,13E-13
		0,83	0,03	15,85	-1,03	-1,29	6,94E-04	0,10	1,23E-13		

Tab. A2.3.2 Diffusion and SC intervals incl. the raw fitting data of the Non-Fickian approach based on $y(t)=y_\infty+A_1\exp(t/b_1)+A_2\exp(t/b_2)+SC\cdot t$

Coating	Substrate	y_∞	A_1	t_1	A_2	t_2	Chi²	R^2	D / m² s^{-1}	Mean D / m² s^{-1}	SD D / m² s^{-1}	SC / min^{-1}	Mean SC / min^{-1}	SD SC / min^{-1}
Clear E-coat	Steel	1,07	-0,82	-1,26	-0,30	-11,16	1,57E-05	1,00	1,30E-13	1,53E-13	3,31E-14	-0,002	0,000	0,002
		0,97	-0,98	-1,09	-0,09	-5,93	9,63E-05	1,00	1,76E-13			0,001		
	HDG Steel	0,94	-0,91	-0,71	-0,13	-3,66	6,93E-05	1,00	4,12E-13	3,63E-13	6,91E-14	0,002	0,003	0,001
		0,89	-0,21	-2,86	-0,77	-0,84	6,41E-05	1,00	3,14E-13			0,004		
	AlMg(Mn)	0,98	-0,88	-0,66	-0,21	-2,59	3,41E-05	1,00	4,92E-13	3,65E-13	1,80E-13	0,000	0,002	0,002
		0,91	-0,53	-1,30	-0,53	-1,31	4,00E-04	0,99	2,38E-13			0,003		
Pigment E-coat	Steel	1,03	-0,69	-5,41	-0,35	-1,74	1,71E-04	1,00	7,37E-14	1,27E-13	7,51E-14	0,000	-0,006	0,008
		1,34	-0,25	-1,07	-1,16	-8,84	3,20E-04	0,99	1,80E-13			-0,011		
	HDG Steel	0,94	-0,13	-1,03	-0,88	-1,03	1,10E-04	0,98	3,79E-13	2,81E-13	1,38E-13	0,002	-0,023	0,035
		1,62	-0,85	-1,05	-3,86	-54,18	5,54E-05	1,00	1,84E-13			-0,048		
	AlMg(Mn)	0,81	-0,37	-0,80	-0,53	-0,80	1,85E-04	0,99	6,36E-13	4,48E-13	2,65E-13	0,010	0,008	0,003
		0,84	-0,50	-1,25	-0,50	-1,25	7,21E-04	0,98	2,60E-13			0,005		

A3 Interfacial behaviour along the AlMg(Mn)/E-coat interface

Excursion:

PH-behaviour of the E-coat interface with chromate-free conversion layers

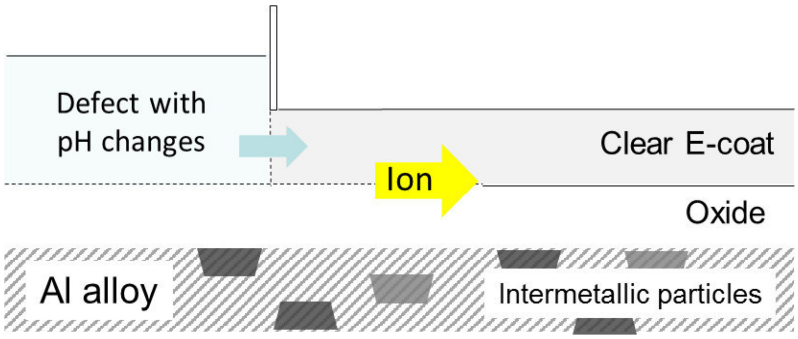

A3.1 Interfacial changes in humid oxygen-deficiency

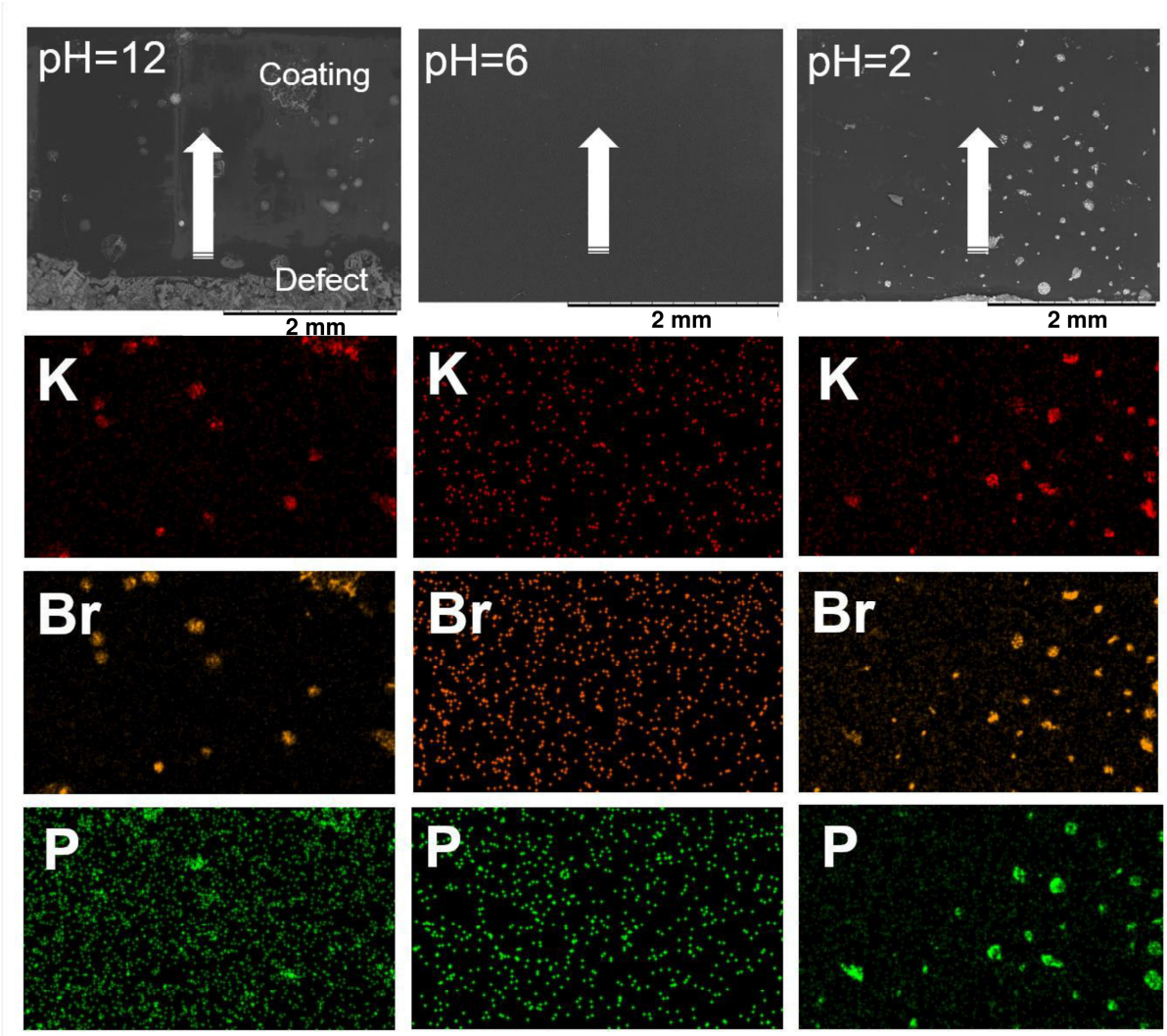

Fig. A3.1.1 SEMs/EDX mappings of the clear E-coated AlMg(Mn) with defect buffers of a pH=12 (PO_4^{3-}/HPO_4^{2-}) plus 1 M KBr, 6 (HPO_4^{2-}/$H_2PO_4^-$) plus 1 M KBr and 2 ($H_2PO_4^-$/H_3PO_4) plus 0.5 M KBr, stored in humid oxygen-deficiency for 650 h, excepting pH=2 with 100 h

A3.2 Neutral concentration-dependent sub-surface flux

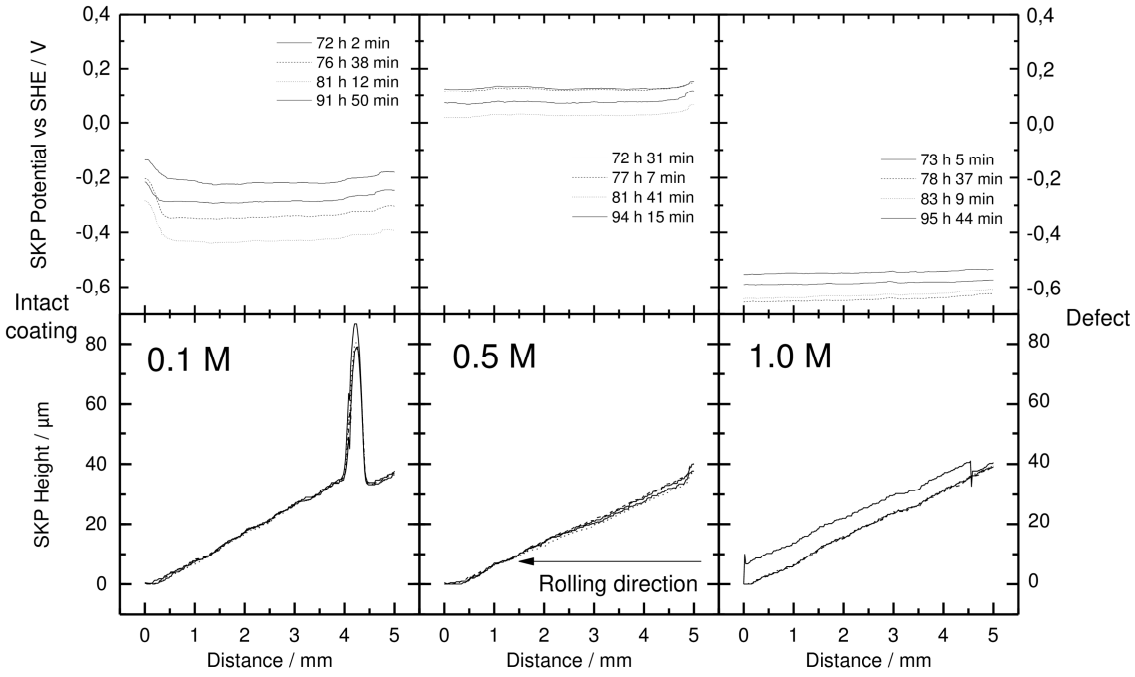

Fig. A3.2.1 Potential and height scans of the AlMg(Mn) alloy covered with a 10 µm thick E-coat between 72 h and 95 h after the buffer addition pH=6, rH=90-92 %, O_2≤3 %

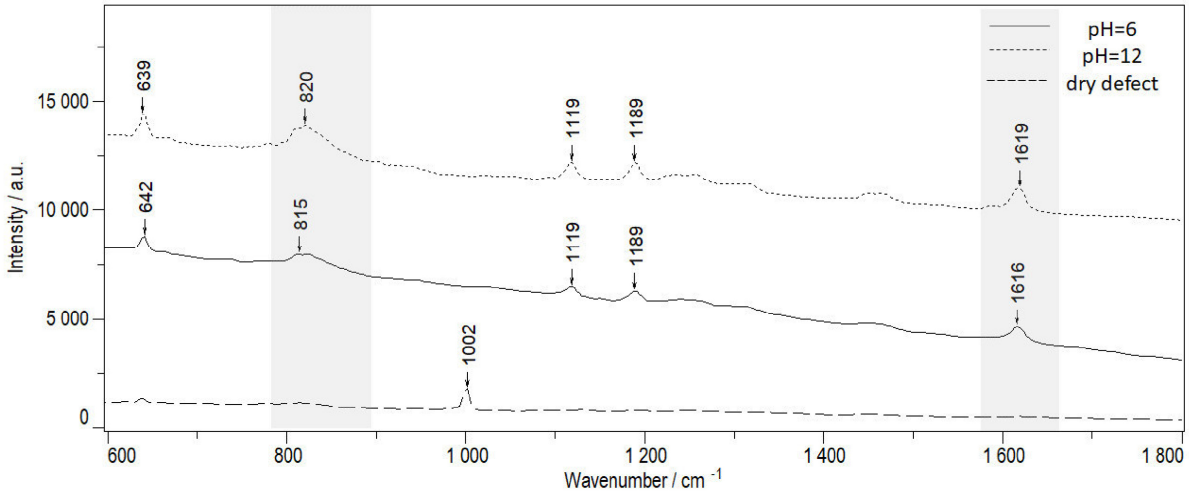

Fig. A3.2.2 Confocal Raman spectra of the clear E-coated AlMg(Mn) with substrate-deep defect filled with pH=6 ($HPO_4^{2-}/H_2PO_4^-$) and added with 1 M Na_2SO_4 after ~250 h stored in humid oxygen deficiency; spectral resolution: 0.6 cm^{-1}

A3.3 Chromate-free conversion layers applied by Henkel

Tab. A3.3.1 Details of the different chromate-free pre-treatments at the AlMg(Mn) substrate done by Henkel

Bath	Function	Product	Conc. / %	Time /s	Temperature /°C	A Ti-based layer with inhibitor	B Zr-based layer with SA	C Zr-Polymer based layer
1	Cleaning	BONDERITE C-AK 1563 BONDERITE C-AD 5003	2.5 0.25	300	60	X	X	X
2	Rinsing	Water		60	RT	X	X	X
3	Deoxidation	BONDERITE C-IC 3610	1.0	60	30	X	X	
4	Rinsing	Water		60	RT	X	X	X
5	Rinsing	De-ionised water				X	X	X
6A	Passivation	BONDERITE M-NT 160	0.5	60	30		X	
6B		BONDERITE M-NT 4850-2	0.5	60	30			X
6C		BONDERITE M-NT 2040 R2	1.5	60	30	X		
7	Rinsing	Water		60	RT	X	X	X
8	Rinsing	De-ionised water		60	RT	X	X	X
9	Drying			600	70	X	X	X

A3.4 Volta potentials of the E-coat-covered conversion layers at the AlMg(Mn) during an acidic and alkaline sub-surface flux in humid oxygen-deficiency

pH=2

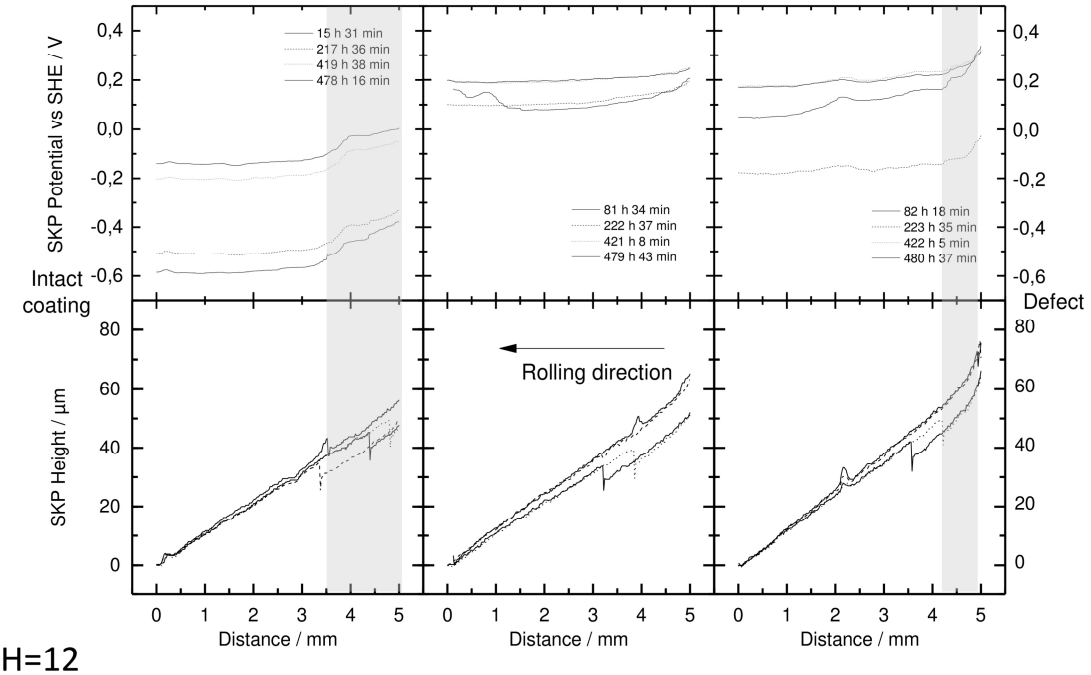

pH=12

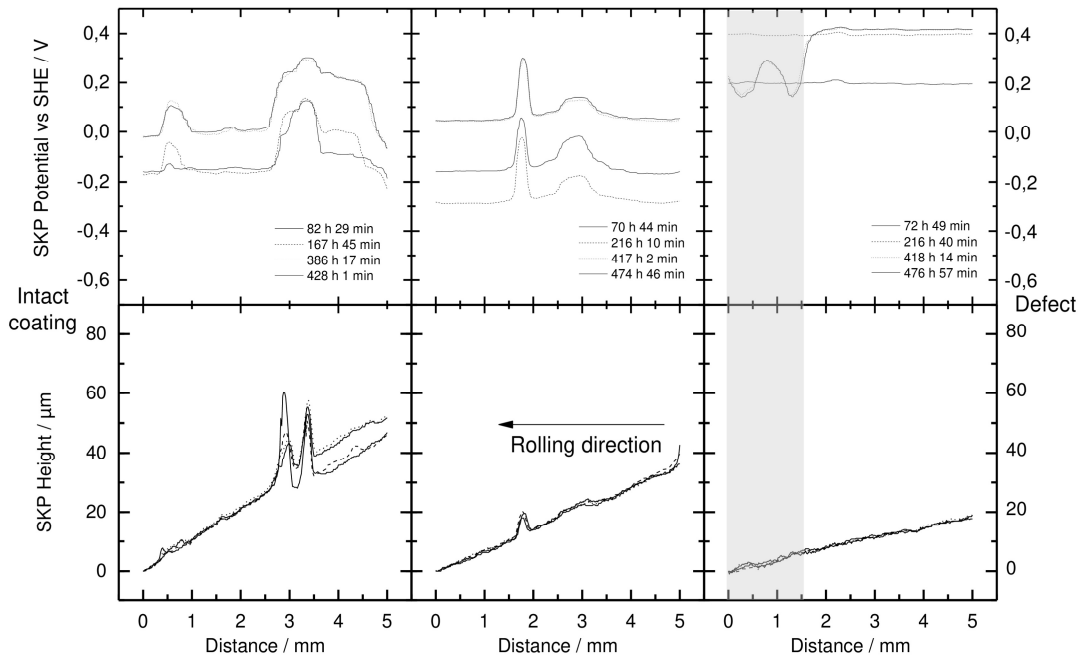

Fig. A3.4.1 Potential and height scans of the pre-treated AlMg(Mn) alloy covered with a 10 µm thick E-coat during an acidic and an alkaline sub-surface flux in humid nitrogen ambience; A) Ti plus inhibitor, B) Zr plus SA, C) Zr plus Polymer.

A3.5 Structural changes of the E-coat-covered conversion layers at the AlMg(Mn) after an acidic and alkaline sub-surface flux

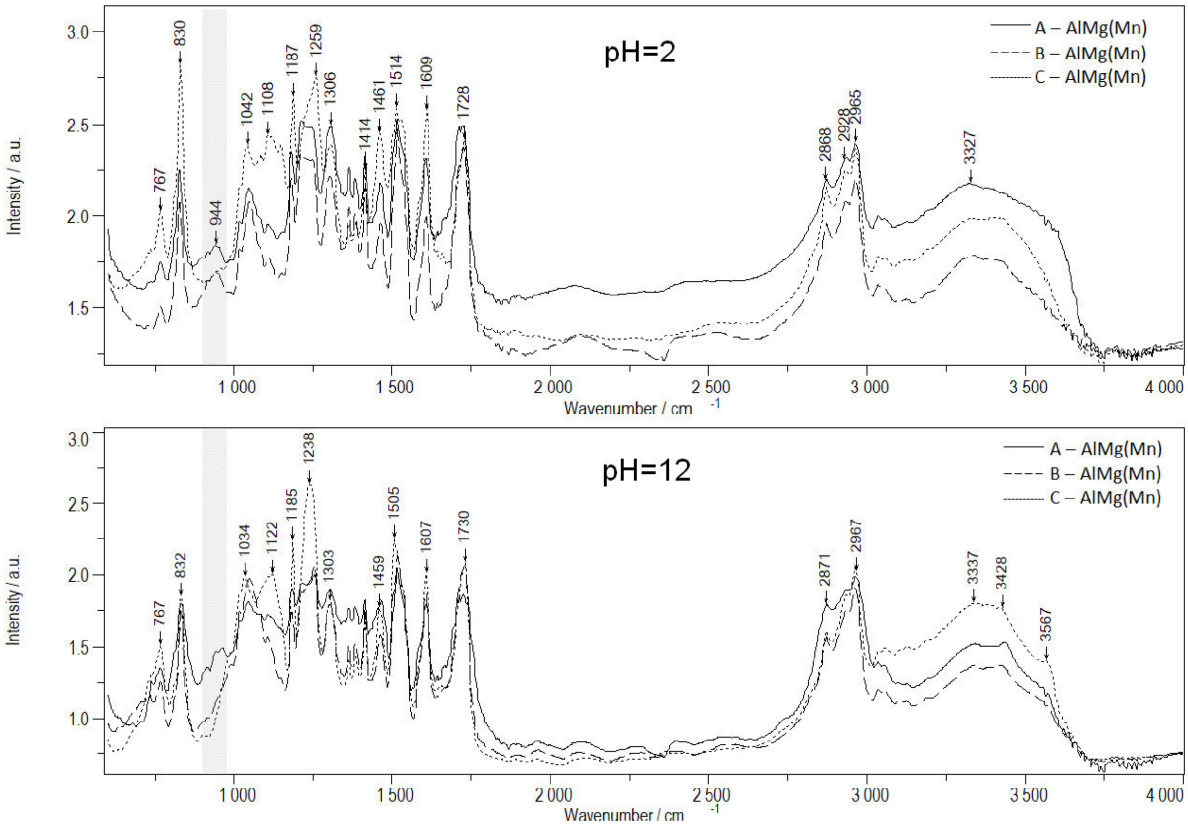

Fig. A3.5.1 IR-reflection spectra of the intact areas of the pre-treated AlMg(Mn) alloy covered with a 10 µm thick E-coat after an acidic and an alkaline sub-surface flux; A) Ti plus inhibitor, B) Zr plus SA, C) Zr plus Polymer; average of min. three spots, spectral resolution: 4 cm^{-1}

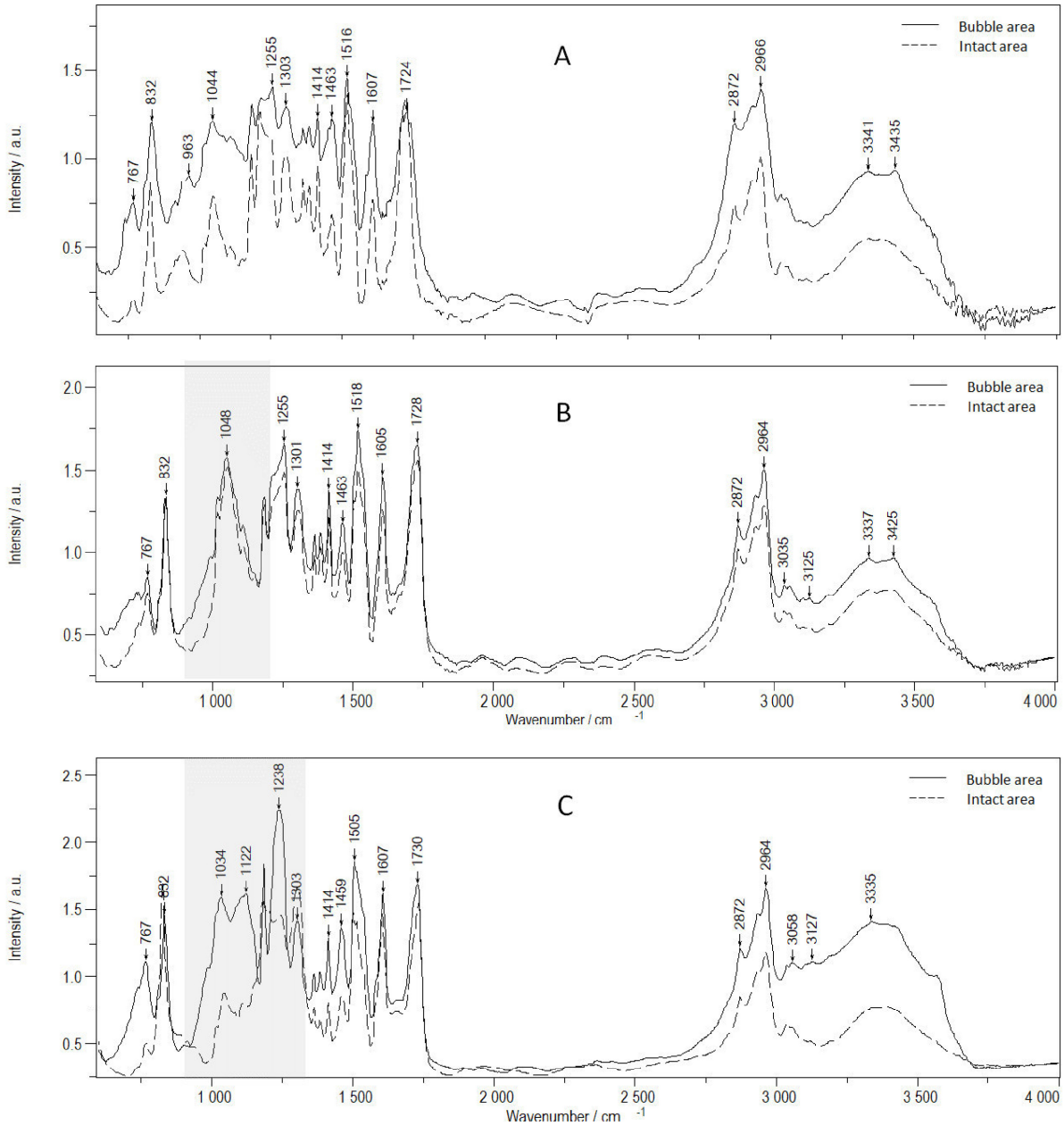

Fig. A3.5.2 Comparison of the IR-reflection spectra of the bubble and intact areas of the pre-treated AlMg(Mn) alloy covered with a 10 µm thick E-coat after **an alkaline sub-surface flux**; A) Ti plus inhibitor, B) Zr plus SA, C) Zr plus Polymer; average of min. three spots, spectral resolution: 4 cm^{-1}

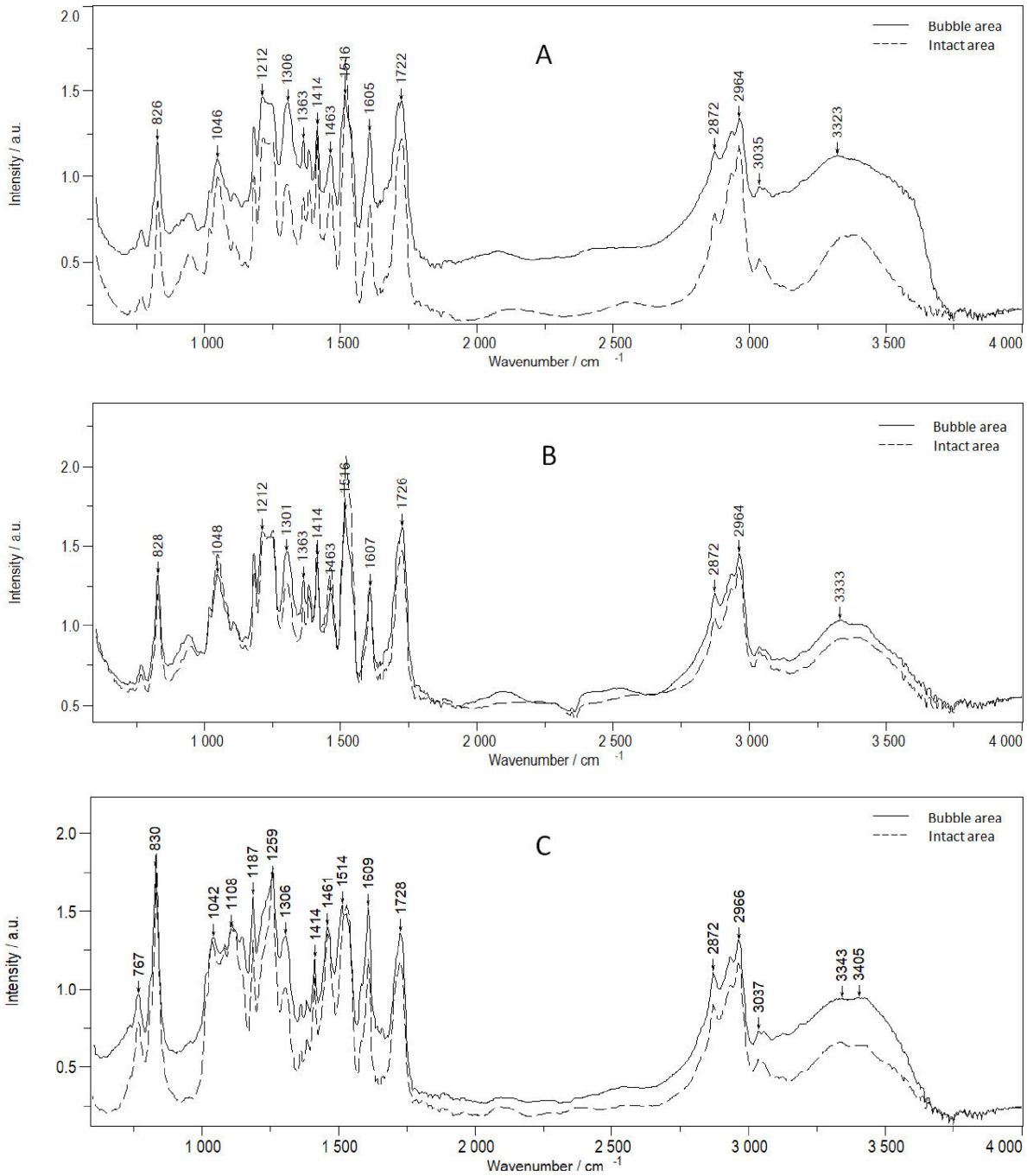

Fig. A3.5.3 Comparison of the IR-reflection spectra of the bubble and intact areas of the pre-treated AlMg(Mn) alloy covered with a 10 µm thick E-coat after **an acidic sub-surface flux**; A) Ti plus inhibitor, B) Zr plus SA, C) Zr plus Polymer; average of min. three spots, spectral resolution: 4 cm^{-1}

A3.6 FIB cuts of the E-coat-covered conversion layers at the AlMg(Mn) after the acidic and alkaline sub-surface flux

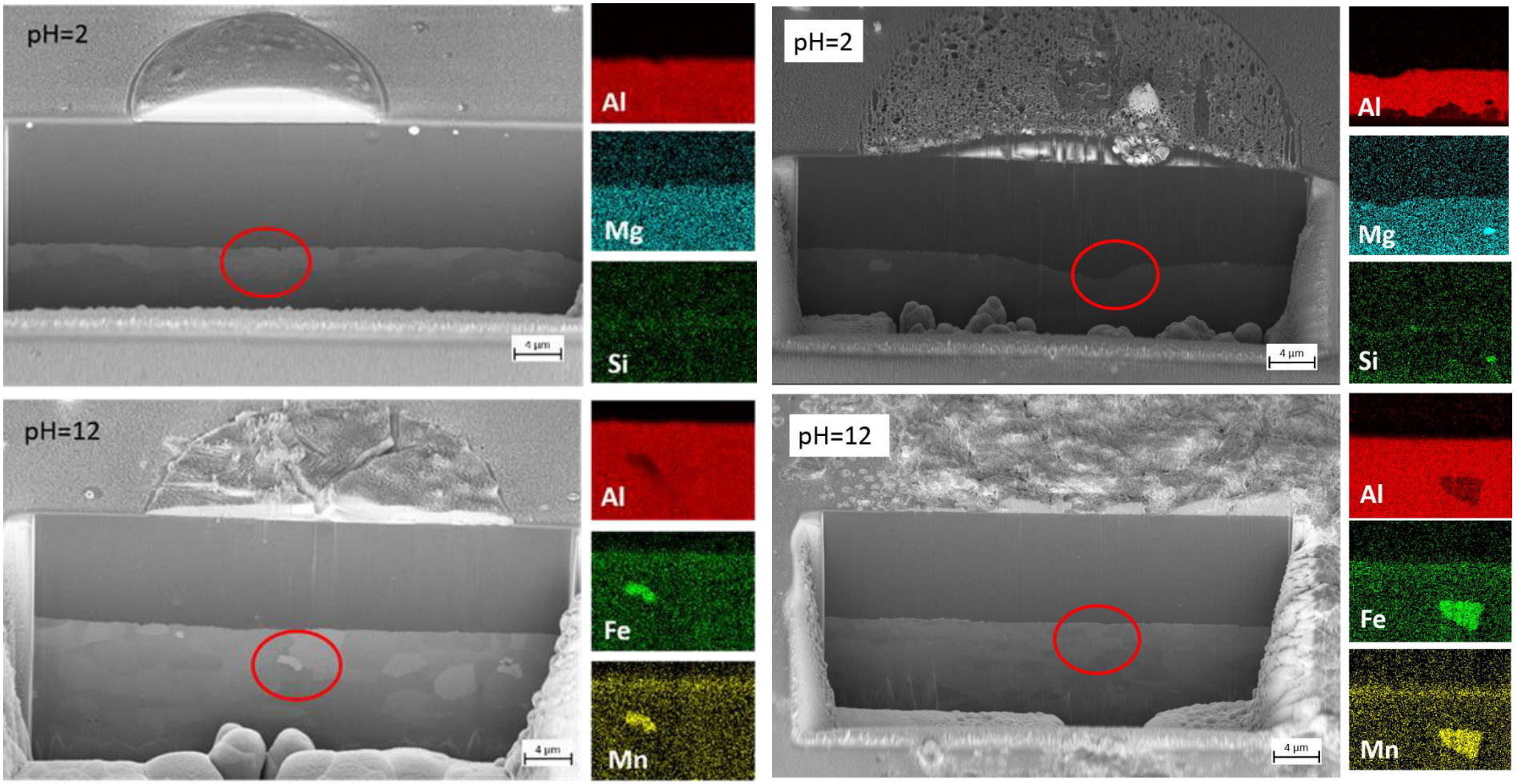

Fig. A3.6.1 FIB-cuts at the bubbles of the Ti-based conversion coating with the inhibitor (left) and the Zr-based conversion coating with the SA (right) after the acidic and alkaline sub-surface flux

A4 Normal diffusion vs in plane diffusion:

Single layer, multilayer and their peculiarities

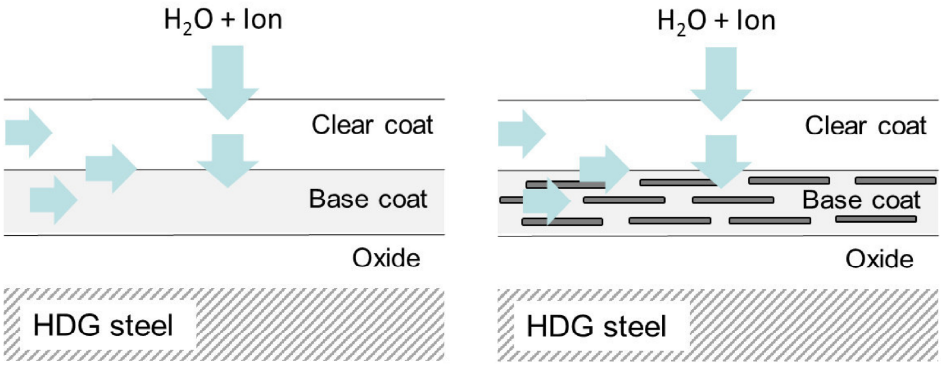

A4.1 Structural characteristic of the pigment E-coat, the base coats and the clear coat

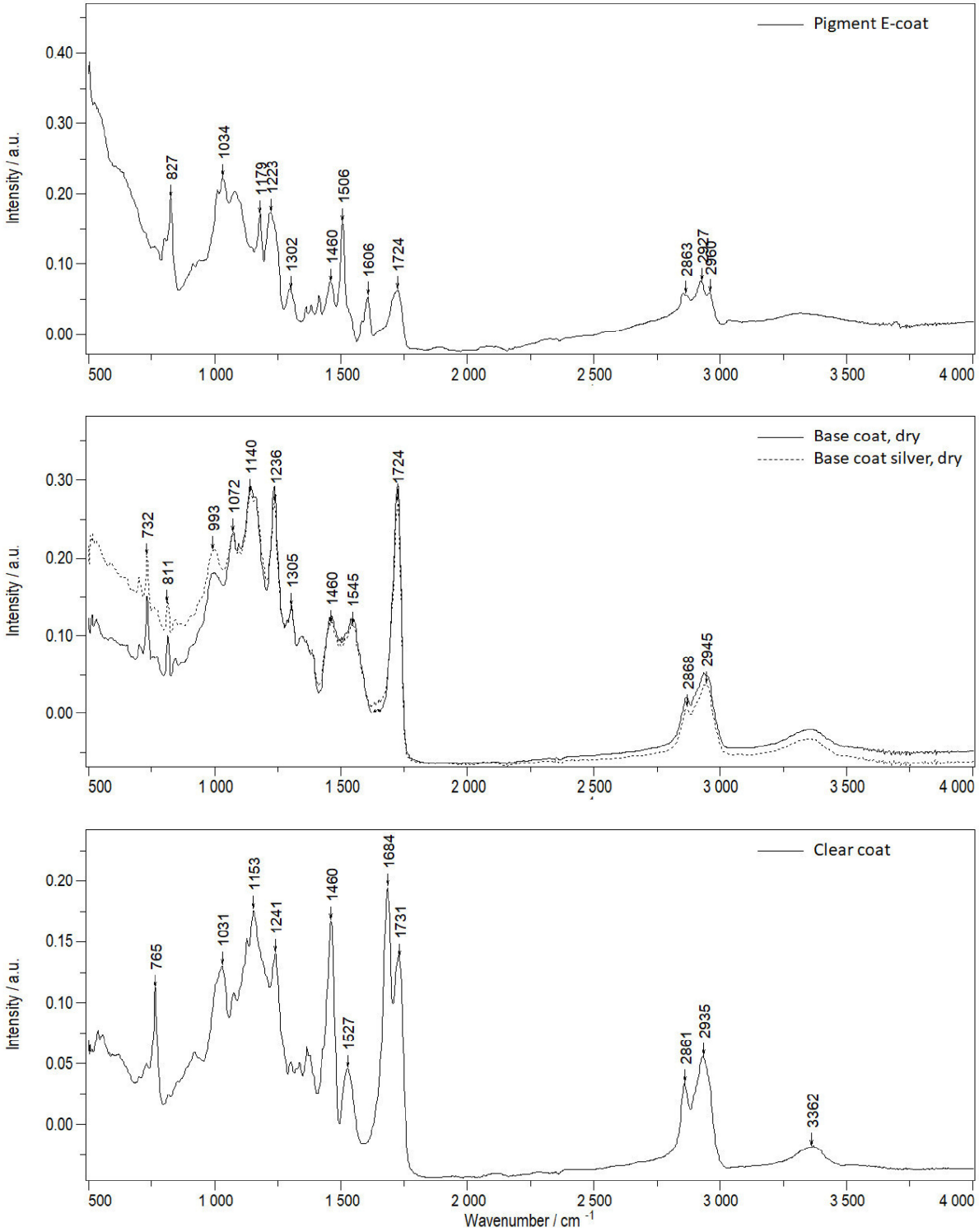

Fig. A4.1.1 IR spectra of the pigment E-coat, the base coat (BC), the base coat with Al flakes (BCs) and the clear coat in a dry state at the HDG steel, spectral resolution: 4 cm^{-1}

A4.2 Direction-driven water diffusion at various single layers

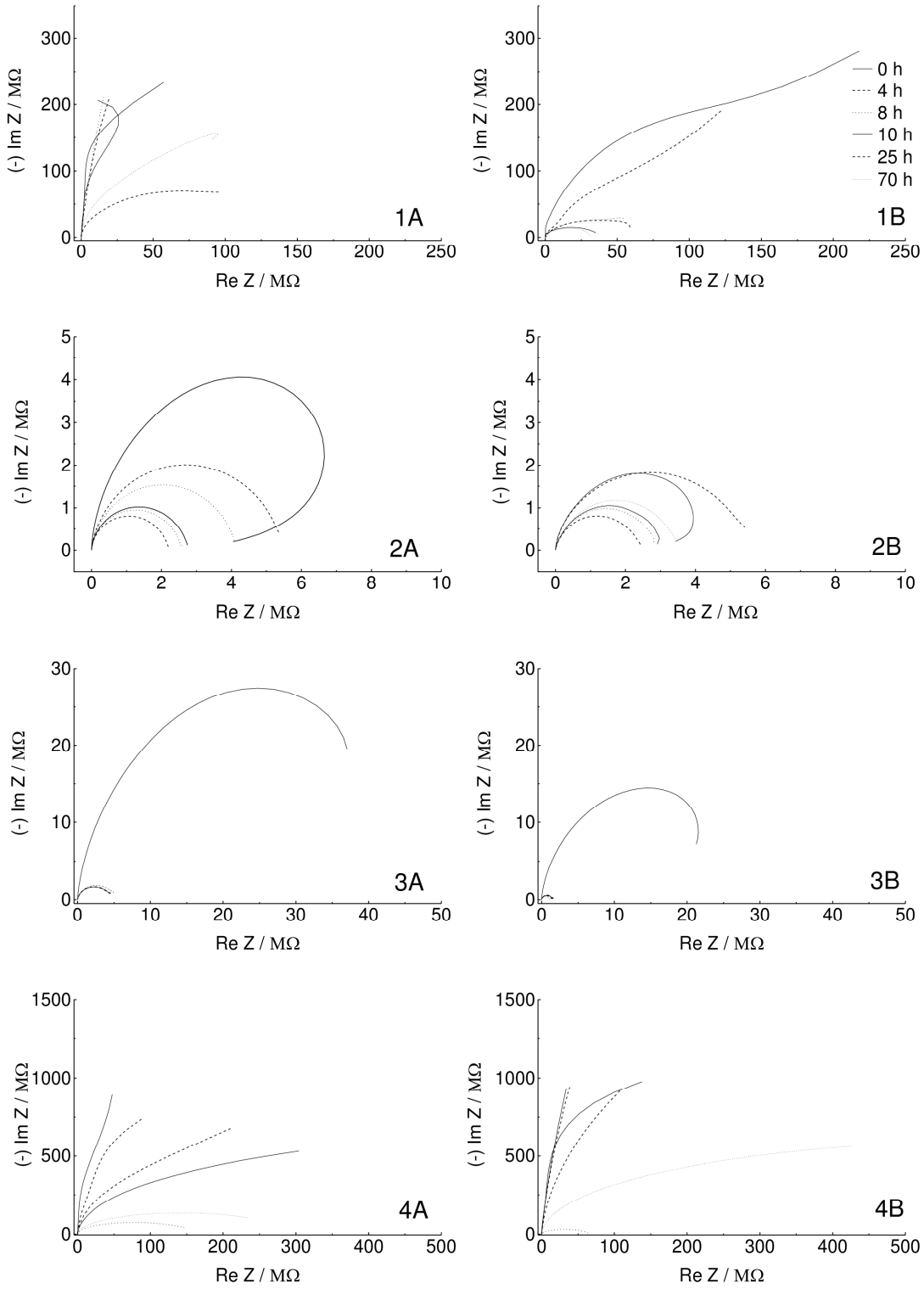

Fig. A4.2.1 Nyquist plots of the E-coat (1), the base coat (2), the base coat with Al flakes (3) and the clear coat (4) at HDG steel during the electrolyte ingress up to 70 h measured in normal (A) and in plane direction (B), frequency range: 10 kHz to 100 mHz, start: OCP, amplitude: 20 mV

Tab. A4.2.1 Normal direction: diffusion intervals and the raw fitting data of the ideal Fickian approach based on $y(t)=y_\infty+A_1\exp(t/b_1)+A_2\exp(t/b_2)$

Coating	y_∞	A_1	t_1	A_2	t_2	Chi	R^2	D / m² s^{-1}	Mean D / m² s^{-1}	SD D / m² s^{-1}
Pigment E-coat	0,97	0,00	3,10	-1,03	-1,10	9,38E-05	0,98	1,90E-13	1,70E-13	2,77E-14
	1,04	-0,86	-1,17	-0,27	-10,69	7,49E-05	1,00	1,51E-13		
Base coat	0,99	-0,53	-0,32	-0,56	-1,02	9,64E-05	0,99	2,13E-12	1,54E-12	8,32E-13
	0,95	-0,50	-0,65	-0,50	-0,65	8,74E-04	0,95	9,50E-13		
Base coat silver	1,00	-0,39	-2,84	-0,66	-0,92	3,98E-05	1,00	2,66E-13	2,52E-13	1,93E-14
	0,95	-0,46	-1,02	-0,56	-2,18	5,14E-05	1,00	2,39E-13		
Clear coat	0,98	-0,59	-0,75	-0,59	-0,75	7,79E-04	0,96	7,26E-13	6,01E-13	1,78E-13
	0,98	-0,59	-0,92	-0,59	-0,92	2,01E-03	0,91	4,75E-13		

Tab. A4.2.2 In plane direction: diffusion intervals and the raw fitting data of the ideal Fickian approach based on $y(t)=y_\infty+A_1\exp(t/b_1)+A_2\exp(t/b_2)$

Coating	y_∞	A_1	t_1	A_2	t_2	Chi²	R^2	D / m² s^{-1}	Mean D / m² s^{-1}	SD D / m² s^{-1}
Pigment E-coat	1,04	-0,09	-23,27	-1,03	-1,13	2,10E-04	0,99	1,60E-13	1,17E-13	6,10E-14
	0,94	-0,95	-1,68	-0,07	-9,59	1,13E-04	1,00	7,41E-14		
Base coat	0,95	-0,52	-0,59	-0,52	-0,59	4,04E-04	0,98	1,18E-12	1,06E-12	1,66E-13
	0,92	-0,96	-0,66	-0,04	-0,66	1,11E-03	0,94	9,43E-13		
Base coat silver	1,02	-0,38	-2,29	-0,74	-0,52	1,48E-04	0,99	7,75E-13	1,12E-12	4,89E-13
	0,53	-0,31	-0,53	-0,31	-0,53	5,22E-02	0,95	1,47E-12		
Clear coat	0,99	-0,51	-0,88	-0,51	-0,88	3,09E-04	0,99	5,25E-13	3,88E-13	1,93E-13
	0,90	-0,53	-1,27	-0,53	-1,27	7,77E-04	0,99	2,52E-13		

Tab. A4.2.3 Normal: water diffusion and SC intervals incl. the raw fitting data of the Non-Fickian approach based on $y(t)=y_\infty+A_1\exp(t/b_1)+A_2\exp(t/b_2)+SC\cdot t$

Coating	y_∞	A_1	t_1	A_2	t_2	Chi²	R^2	D / m² s^{-1}	Mean D / m² s^{-1}	SD D / m² s^{-1}	SC / min^{-1}	Mean SC / min^{-1}	SD SC / min^{-1}
Pigment E-coat	0,94	-0,13	-1,03	-0,88	-1,03	1,10E-04	0,98	3,79E-13	2,81E-13	1,38E-13	0,002	-0,023	0,035
	1,62	-0,85	-1,05	-3,86	-54,18	5,54E-05	1,00	1,84E-13			-0,048		
Base coat	1,32	-0,84	-0,35	-0,61	-1,30	5,83E-05	1,00	1,74E-12	1,74E-12	5,39E-15	-0,003	-0,009	0,008
	1,37	-0,72	-0,35	-0,77	-1,37	5,19E-05	1,00	1,74E-12			-0,014		
Base coat silver	1,06	-0,80	-1,04	-0,30	-4,86	3,44E-05	1,00	1,97E-13	1,85E-13	1,72E-14	-0,003	-0,002	0,001
	0,98	-0,68	-1,16	-0,36	-3,07	4,52E-05	1,00	1,73E-13			-0,002		
Clear coat	1,19	-0,26	-10,90	-1,14	-0,68	5,88E-04	0,97	4,36E-13	3,64E-13	1,01E-13	-0,009	-0,011	0,004
	1,49	-0,58	-16,28	-1,13	-0,83	8,12E-04	0,96	2,92E-13			-0,014		

Tab. A4.2.4 In plane: water diffusion and SC intervals incl. the raw fitting data of the Non-Fickian approach based on $y(t)=y_\infty+A_1\exp(t/b_1)+A_2\exp(t/b_2)+SC\cdot t$

Coating	y_∞	A_1	t_1	A_2	t_2	Chi²	R^2	D / m² s^{-1}	Mean D / m² s^{-1}	SD D / m² s^{-1}	SC / min^{-1}	Mean SC / min^{-1}	SD SC / min^{-1}
Pigment E-coat	0,96	-0,52	-1,14	-0,52	-1,14	2,10E-04	0,99	3,10E-13	2,22E-13	1,25E-13	0,002	0,002	0,000
	0,90	-0,49	-1,74	-0,49	1,74	1,17E-04	1,00	1,33E-13			0,002		
Base coat	1,31	-0,02	6,49E+04	-1,35	-0,67	1,07E-04	0,99	4,50E-13	6,68E-13	3,07E-13	-0,003	-0,009	0,008
	0,99	-0,63	-1,43	-0,81	-0,51	1,09E-04	0,99	8,85E-13			-0,014		
Base coat silver	1,10	-0,83	-0,58	-0,36	-3,78	1,28E-04	1,00	6,17E-13	7,55E-13	1,95E-13	-0,005	0,009	0,019
	0,54	-0,29	-0,67	-0,29	-0,67	9,18E-04	0,97	8,93E-13			0,022		
Clear coat	1,06	-0,25	-0,43	-0,86	-1,22	1,56E-04	0,99	1,21E-12	7,28E-13	6,88E-13	-0,010	-0,006	0,005
	0,92	-0,54	-1,30	-0,54	-1,30	7,72E-04	0,99	2,41E-13			-0,002		

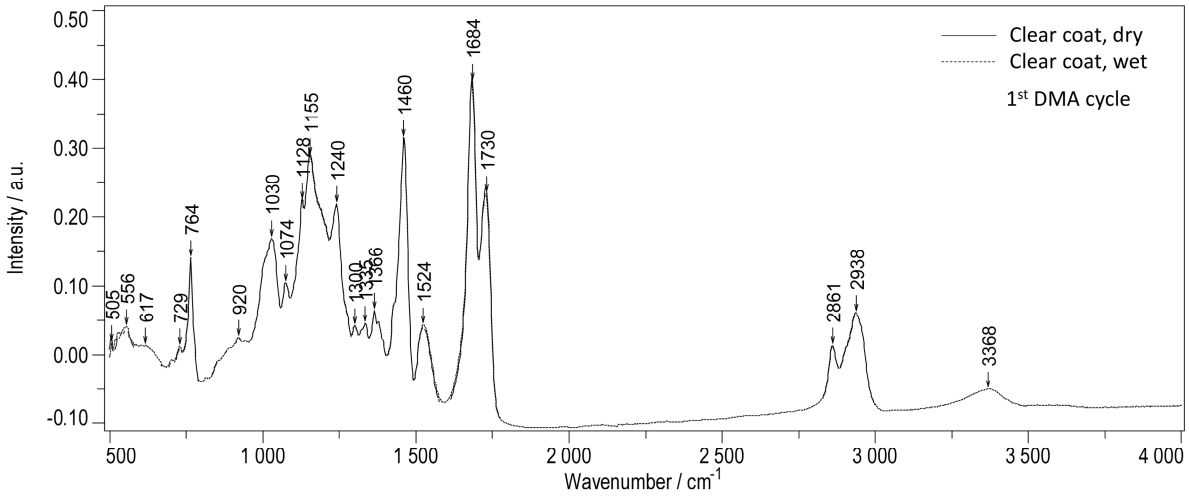

Fig. A4.2.2 IR-ATR spectra of the clear coat in the dry and wet state after the first heating up to 125 °C, spectral resolution: 4 cm^{-1}

Tab. A4.2.5 Raw data of Fig. 4.12: Relation between the adsorption coefficients SC and the changes of the maximal stress, tan delta and length from the dry state to the longest salt water uptake for the base coat (BC), the base coat with Al flakes and the clear coat films (CC)

Type of Film	BC	BCs	CC
SC_{normal} / min^{-1}	-0.009	-0.002	-0.011
$SC_{in\ plane}$ / min^{-1}	-0.009	0.009	-0.006
Stress dry / MPa	0.29	1.01	2.81
Stress[1] / %	240	308	109
Length dry / µm	666	128	530
Length[1] / %	175	80	64
Tan Delta dry / -	0.37	0.27	0.91
Tan Delta[1] / %	84	90	81

[1)] Averaged relation to the dry layer

A4.3 Direction-driven water diffusion at polymer-polymer interfaces

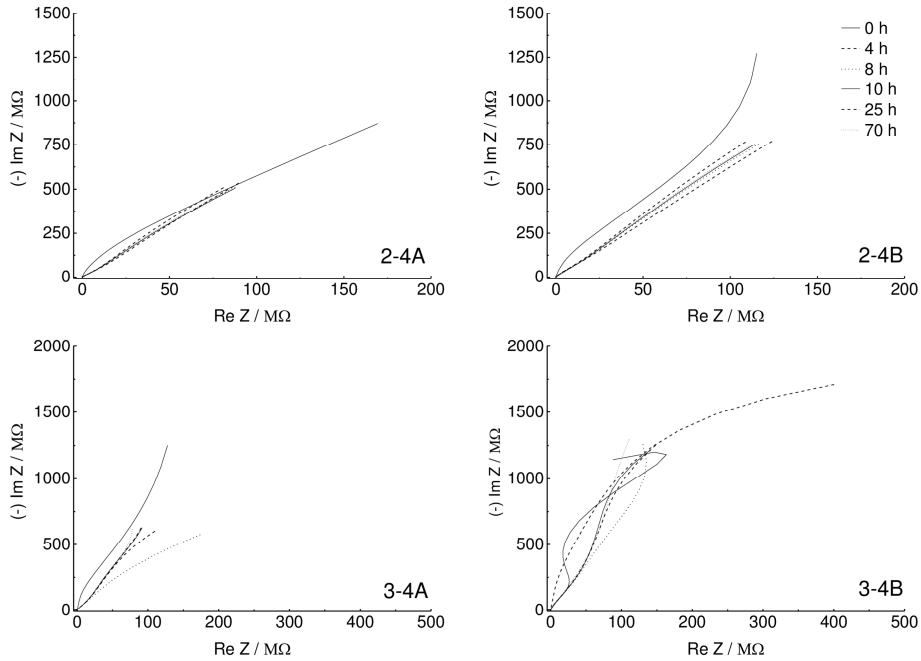

Fig. A4.3.1 Nyquist plots of the double layers: base coat – clear coat (2-4) and base coat with Al flakes – clear coat (3-4) during the electrolyte ingress up to 70 h measured in normal (A) and in plane direction (B), frequency range: 10 kHz to 100 mHz, start: OCP, amplitude: 20 mV

Tab. A4.3.6 Normal and in plane water diffusion intervals of the double layers and their raw fitting data of the ideal Fickian approach based on $y(t)=y_\infty+A_1\exp(t/b_1)+A_2\exp(t/b_2)$

Coating	y_∞	A_1	t_1	A_2	t_2	Chi²	R^2	D / m² s^{-1}	Mean D / m² s^{-1}	SD D / m² s^{-1}
Normal: Base coat -Clear coat	0,99	0,57	-0,34	-1,54	-0,77	6,30E-05	1,00	2,10E-12	5,37E-12	4,63E-12
	0,97	0,25	-0,16	-1,19	-0,91	2,81E-04	1,00	8,64E-12		
Normal: Base coat silver -Clear coat	1,00	-0,29	-0,11	-0,80	-1,04	7,08E-05	1,00	1,70E-11	8,60E-12	1,18E-12
	3951,27	-0,78	-0,89	-3950,56	-111964,51	3,17E-04	0,99	2,55E-13		
In plane: Base coat -Clear coat	0,97	-0,54	-0,67	-0,54	-0,67	7,54E-04	0,98	9,14E-13	6,23E-13	4,13E-13
	1,24	-0,30	-7,84E+114	-1,02	-0,78	6,79E-04	0,99	3,31E-13		
In plane: Base coat silver -Clear coat	0,95	-0,49	-1,76	-0,49	-1,76	3,25E-04	0,99	1,31E-13	2,60E-13	1,82E-13
	1,00	-0,87	-0,73	-0,23	-4,02	2,82E-04	0,99	3,89E-13		

Tab. A4.3.7 Normal and in plane water diffusion and SC intervals of the double layers incl. their raw fitting data of the Non-Fickian approach based on $y(t)=y_\infty+A_1\exp(t/b_1)+A_2\exp(t/b_2)+SC\cdot t$

Coating	y_∞	A_1	t_1	A_2	t_2	Chi²	R^2	D / m² s^{-1}	Mean D / m² s^{-1}	SD D / m² s^{-1}	SC / min^{-1}	Mean SC / min^{-1}	SD SC / min^{-1}
Normal: Base coat - Clear coat	0,98	0,48	-18,03	-1,54	-1,13	2,26E-04	1,00	1,60E-13	1,71E-13	1,57E-14	-0,008	0,003	0,016
	1,00	0,42	-6,00	-1,55	-1,07	3,74E-04	0,99	1,82E-13			0,014		
Normal: Base coat silver - Clear coat	1,03	-0,80	-1,12	-0,31	-0,12	6,30E-05	1,00	1,45E-11	7,50E-12	9,89E-12	-0,004	0,016	0,028
	0,71	-0,39	-0,89	-0,39	-0,89	3,18E-04	0,99	5,09E-13			0,035		
In plane: Base coat - Clear coat	1,30	0,22	-2,50	-1,62	-0,84	4,18E-04	0,99	3,22E-13	2,54E-13	9,62E-14	-0,014	-0,031	0,024
	1,24	0,22	-2,42E+21	-1,51	-1,04	1,74E-04	1,00	1,86E-13			-0,048		
In plane: Base coat silver - Clear coat	1,33	-0,66	-2,53	-0,67	-2,53	1,60E-04	1,00	6,34E-14	2,07E-13	2,03E-13	-0,047	-0,014	0,048
	0,97	-0,93	-0,76	-0,13	-1,91E+04	2,00E-04	1,00	3,51E-13			0,020		

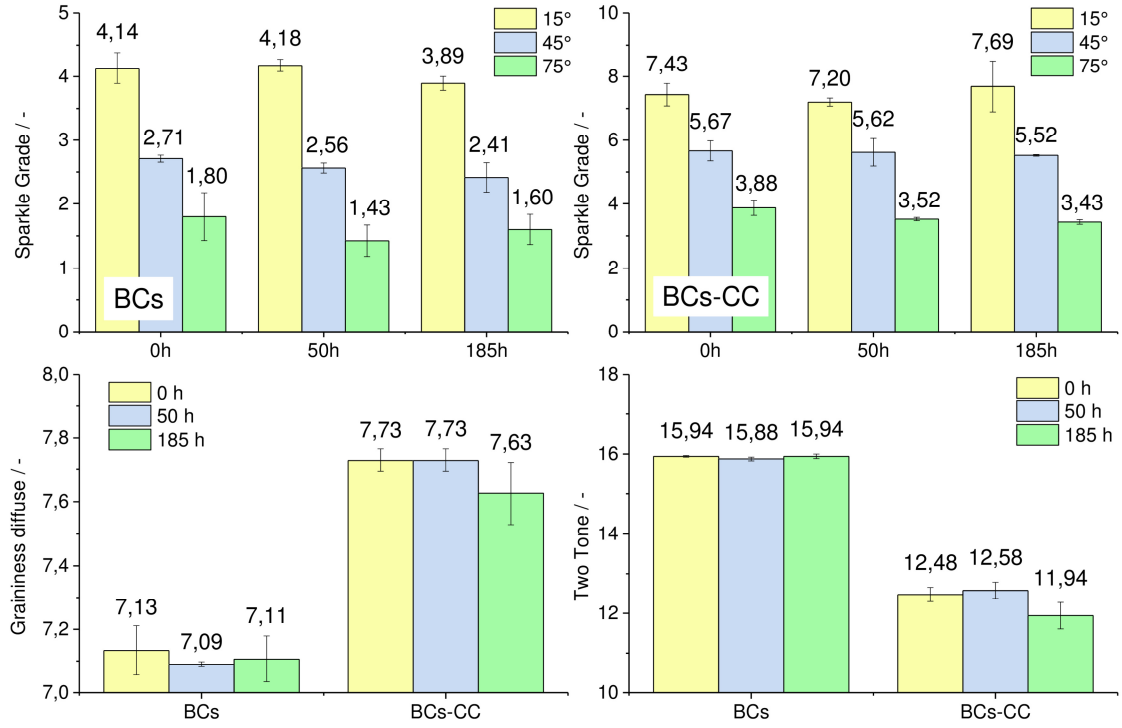

Fig. A4.3.1 Sparkle grades, graininess and two tones of the base coat with Al flakes (BCs) and this base coat covered with the clear coat (BCs-CC) in the dry state, after 50

Tab. A4.3.8 Raw data of Fig. 4.23: Relation between the adsorption coefficients SC and the changes of the maximal stress, tan delta and length from the dry state to the longest salt water uptake for the first heating (I) and the second heating (II) of the base coat – clear coat (BC-CC) and the base coat with Al flakes – clear coat (BCs-CC)

Type of Double layer	BC-CC		BCs-CC	
SC_{normal} / min^{-1}	0.003		0.016	
$SC_{in\ plane}$ / min^{-1}	-0.031		-0.014	
Stress dry / MPa	2.03	2.20	1.80	1.83
Stress[1] / %	150	142	144	138
Length dry / µm	92	659	84	632
Length[1] / %	268	109	-57	84
Tan Delta dry / -	0.76	0.91	0.66	0.76
Tan Delta[1] / %	118	97	96	112

[1)] Averaged relation to the dry layer